TUNING THE MESOMORPHIC PROPERTIES OF PHENOXY-TERMINATED SMECTIC LIQUID CRYSTALS

by

Matthew Thompson

A thesis submitted to the Department of Chemistry

In conformity with the requirements for

the degree of Doctor of Philosophy

Queen's University

Kingston, Ontario, Canada

August, 2015

Abstract

A new type of liquid crystal display using surface stabilized ferroelectric liquid crystals (SSFLCs) has faster switching times than conventional nematic displays. The application of SSFLCs in large LCD devices such as TVs has been hindered due to a layer contraction at the smectic A-smectic C transition. The layer contraction leads to buckling of the smectic layers and results in zigzag defects. These zigzag defects degrade optical quality of ferroelectric liquid crystal (FLC) films. So-called 'de Vries-like' liquid crystals with a smectic A-smectic C layer contraction of less than 1% have been sought to address the problem.

In the first section of this thesis, we show that one can tune mesomorphic properties in 2-phenylpyrimidine liquid crystals by addition of a nanosegregating phenoxy end group. In this study, it was shown that nanosegregation can be used to exaggerate the difference in mesophase properties in sterically equivalent isomers. The study also showed that the effect of nanosegregration is not always Smectic C promoting and that, although it may decrease orientational order, it is not the only prerequisite to 'de Vries-like' properties in calamitic mesogens. Next, we investigated the phenoxy end group through substituent effects. In this study, it was discovered that the SmC phase can be promoted through increased intermolecular interactions that decrease out of layer fluctuations.

We also showed that phenoxy-terminated mesogens exhibit extremely low optical tilt angles for the SmC phase, on the order of ~10 degrees, which were not consistent with the observed layer spacing obtained from X-ray diffraction experiments. In attempts to determine their true optical tilt angle, these mesogens were doped with chiral dopants and electro-optical switching experiments showed higher optical tilt angles. The phenoxy-terminated mesogens were shown to

have a high pre-tilt angle due to surface interactions with the glass slide. The increased optical tilt angle allows for the possibility of using these compounds in SSFLC devices.

Finally, we investigated the possibility of using SmC-N materials for use as an alignment pathway in SSFLC devices. The fluorophenoxy end group was added to a fluorenone core and were then analyzed for optical tilt angle through the use of chiral dopants for potential use in SSFLC devices.

Acknowledgements:

First, I would like to thank Dr. Robert P. Lemieux for his mentorship and guidance during my time at Queen's University. I would also like to thank Dr. Frank Giesselmann and his group for hosting me at the University of Stuttgart in Germany. I would also like to thank all of my Lemieux group lab mates: Dr. Qian Cui, Dr. Qingxiang Song, Ian Rupar, Dr. Tamer Andrea, Dr. V. Jayalakshmi, Dr. Chris Schubert, and Dr. Kirk Mulligan. I would also like to thank the undergraduate students in the Lemieux lab: Rosemary Bakhurst, and Daphne Cheung. I would also like to thank Carolyn Carkner for her support of my PhD Thesis. I would also like to thank members of my supervisory committee: Dr. Ralph Whitney and Dr. Stan Brown for freely offering their time during the course of my PhD. I would also like to thank the support staff who have kept the chemistry department running: Françoise Sauriol in the NMR facility, Ed Maracle, and Robin Roberts in the electronics shop, Kim Mackinder in the science store, Annette Keyes, Meredith Richards, Michelle Boutilier, Pam Bandy-Dafoe in the main office. I would like to thank my TA supervisors: Igor Kozin, Jasan Vhalakis, John Carran, and David Zechel for making teaching an enjoyable experience at Queen's University. Finally, I would like to thank my family, especially my parents, for always being there for me, without their endless support this degree would not be possible.

Statement of Co-Authorship and Originality:

All of the experimental work presented in this thesis was performed by the author under the supervision of Dr. R. P. Lemieux in the Department of Chemistry, Queen's University, unless otherwise noted. Small-angle X-ray scattering experiments were performed by Matthew Thompson, Nadia Kapernaum, and Andreas Bogner at the University of Stuttgart.

Original work presented includes: the synthesis and physical characterization of novel phenoxy-, methylphenoxy- and fluorophenoxy-terminated 2-phenylpyrimidine liquid crystals (**QL11, QL12, QL20, QL21, QL22, QL23** and **QL27**), and fluorophenoxy-terminated fluorenone liquid crystals (**QL29)**; physical characterization of various liquid crystal phases including polarized optical microscopy and differential scanning calorimetry, measurement of optical tilt angle, and investigation of a binary mixtures of various liquid crystals. Precursor compounds to **QL29** were synthesized by Rosemary Bakhurst, **QL12-10/5** was synthesized by Carolyn Carkner and computational chemistry calculations were completed by Carolyn Carkner (Mosey Group) in the Department of Chemistry at Queen's University.

Table of Contents:

List of Tables:

List of Figures:

List of Abbreviations:

Å	Angstrom
AC	Alternating current
(aq)	Aqueous
α	Susceptibility coefficient
Ar	Aromatic
B3LYP	Becke's three parameter hybrid functional using the Lee, Yang and Parr correlation functional (density functional theory method)
C_2	C2 rotational symmetry
C_2h	C2 rotational symmetry with horizontal mirror plane
CF_3	Trifluoromethyl
CN	Cyano
CH_3	Methyl
c	Electroclinic coupling constant
CP	Crossed polarizers
Cr	1st Crystal phase
Cr’	2nd Crystal phase (If applicable)
χ	2D Wide-angle X-ray scattering intensity distribution.
1D	1-Dimensional
2D	2-Dimensional
d_A	Layer spacing in the SmA phase
d_{AC}	Layer spacing at the SmA-SmC Transition

d_c	Layer spacing in the SmC phase
d(T)	Layer spacing at a given temperature T
DC	Direct current
DIAD	Diisopropyl azodicarboxylate
DSC	Differential scanning calorimetry
e_c	Electroclinic coefficient
EI	Electron impact ionization
ESI	Electrospray ionization
E	Electric field
Γ	Ferroelectric torque
Γ^{ε}	Dielectric torque
h	Hours
HCl	Hydrochloric acid
HRMS	High resolution mass spectrometry
I	Intensity
Iso, I	Isotropic liquid
k	Kilo
kJ	Kilojoule
kcal	Kilocalorie
J	Coupling constant
L	Molecular length
L_{eff}	Effective molecular length
LC	Liquid crystal

LCD	Liquid crystal device
LRMS	Low resolution mass spectrometry
$MgSO_4$	Magnesium sulfate
MS	Mass spectrometry
MHz	Megahertz
mp	Melting point
mol	Mole
MP_2	Second order Moller-Plesset perturbation theory
N	Nematic
n	Director
N*	Chiral nematic
NMR	Nuclear magnetic resonance
OLF	Out-of-Layer fluctuations
PPh_3	Triphenylphosphine
2-PhP	2-Phenylpyrimidine
5-PhP	5-Phenylpyrimidine
R	Reduction factor
R_1	Rubbing direction 1
R_2	Rubbing direction 2
ROF_i	Rotational orientation factor
S_2	Orientational order parameter
SAXS	Small-angle X-ray scattering
Sm	Smectic

SmA	Smectic A
SmB	Smectic B
SmC	Smectic C
SmF	Smectic F
SmI	Smectic I
SmX*	Smectic X* (X means unknown)
SSFLC	Surface stabilized ferroelectric liquid crystal
T	Temperature
T_{AC}	Temperature at the SmC-SmA transition
θ	Tilt angle, Angle of incidence.
θ_{opt}	Optical tilt angle
THF	Tetrahydrofuran
THP	Tetrahydropyran
μm	Micrometer
WAXS	Wide-angle X-ray scattering

Liquid Crystal Code Names:

QL11-*m*/*n*

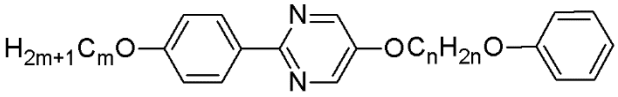

QL12-*m*/*n*

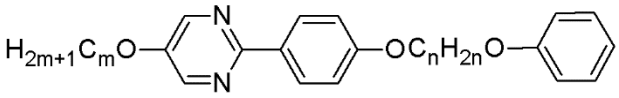

QL20-*m*/*n*

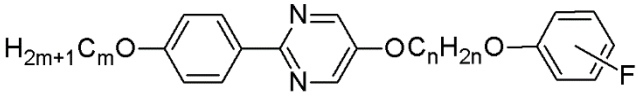

QL21-*m*/*n*

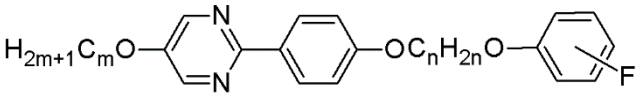

QL22-*m*/*n*

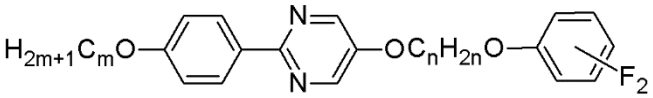

QL23-*m*/*n*

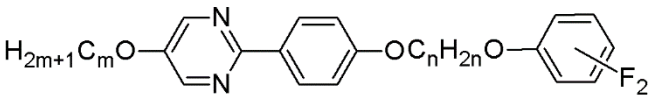

QL27-*m*/*n*

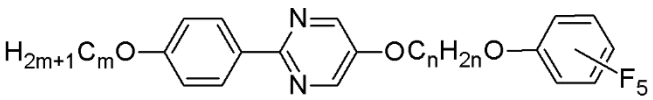

QL29-*m*/*n*

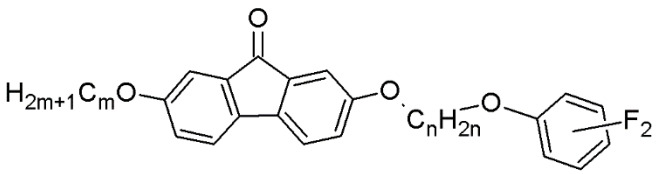

QL30-*m*/*n*

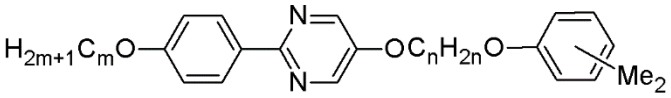

QL31-*m*/*n*

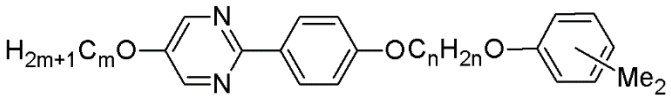

Chapter 1: Introduction

Typically, students are taught that there are only three distinct phases of matter: Solid, Liquid and Gas. Solids have a high degree of translational, rotational, positional and directional order. On the other hand, isotropic liquids and gases are completely disordered. In some materials, there are phases which do not exhibit a high degree of translational, rotational, positional and directional order, but these same materials are not completely disordered. These in-between phases are defined as mesophases. Compounds that exhibit these mesophases are either called soft crystals if they are more ordered and thus more crystal-like, or liquid crystals (LCs) if they are less ordered and more liquid-like. Liquid crystal phases, unlike soft crystals, exhibit long-range ordering while keeping their fluid-like properties.

Liquid crystalline phases were first observed by an Austrian botanist named Reinitzer in 1888.[1] Since then, liquid crystals have been studied on academic and industrial levels. Liquid crystals are best known for their applications in liquid crystal displays (LCD). Liquid crystals have dominated the market because of their ability to be easily customized. It is important to note that liquid crystals can also be used for a wide variety of applications such as liquid crystal thermometers[2], optical imaging and recording[3], photovoltaics[4], and synthetic medical applications.[5]

Twisted nematic liquid crystals have dominated the LCD market since the discovery of cyanobiphenyl nematic mesogens by G.W. Gray.[6] Gray's nematic liquid crystal **5CB** (Figure 1-1) was the first stable, room temperature mesogen to have optimal properties for display applications. While twisted nematic LCD devices have been commercialized, they are not, theoretically, the best liquid crystal mesophase for display applications. Twisted nematic devices tend to have a slow

switching time and a narrow viewing angle. To address problems with power consumption, switching time and viewing angle, a new type of LCD device has been developed: the Surface Stabilized Ferroelectric Liquid Crystal (SSFLC) device based on chiral Smectic C (SmC*) liquid crystals. This thesis focuses on the origin of Smectic C phase formation in calamitic liquid crystals in terms of the van der Waals interactions and molecular functionalization required for the Smectic C phase, and the further investigation of so-called 'de Vries-like' properties for SSFLC applications. In this work, we studied the interplay between core-core interactions and interaction of end-groups at layer interfaces and their effect on mesomorphic properties. In addition, we discovered and investigated an easily customized nanosegregating end-group to better understand the role of nanosegregation in mesomorphic properties and its role in 'de Vries-like' behavior.

1.1 Introduction to Liquid Crystals

There are two main types of liquid crystals, which are called lyotropic and thermotropic liquid crystals. Lyotropic liquid crystals are formed when combined with a solvent; these mesophases are concentration and temperature dependent. Lyotropic liquid crystals can be found in soap and in many biological systems, including cell membranes.[7] In such systems, amphiphilic molecules are solvated, which imposes order into the system, often by virtue of hydrophobic/hydrophilic forces. Lyotropic liquid crystals will not be discussed further in this thesis. The second type of liquid crystals are called thermotropic liquid crystals, which exhibit mesomorphic properties that are solely dependent on temperature. Thermotropic liquid crystals can be either enantiotropic or monotropic. Enantiotropic mesophases are observed on heating and cooling and are thermodynamically stable. Monotropic mesophases are not thermodynamically stable and they appear only on supercooling below the melting point of the compound. Examples of common lyotropic and thermotropic liquid crystals are shown in Figure 1-1.

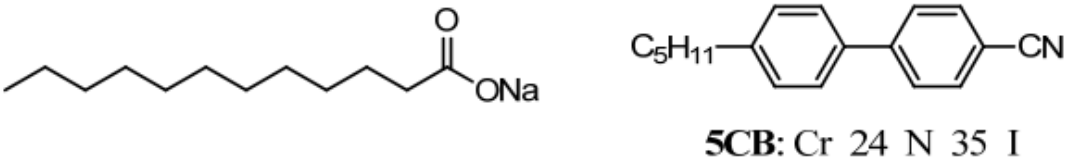

Figure 1-1: Sodium dodecanoate, a common lyotropic liquid crystal found in soap (left) and 4'-pentylbiphenyl-4-carbonitrile (right), a common thermotropic mesogen.

Thermotropic mesogens are generally characterized by their molecular shape. There are four main shape classes of thermotropic mesogens, which are shown in Figure 1-2. The molecular shape of liquid crystals is important for two reasons. The first reason is that the shape of the materials affects how the mesogens pack, which affects what mesophase is observed. The second reason is shape anisotropy, which reduces the symmetry of non-covalent interactions, resulting in unique properties such as birefringence and dielectric anisotropy. The first class of liquid crystals is calamitic liquid crystals; formed by mesogens that are rod-like in shape, with a rigid aromatic core and one or two alkyl chains. Calamitic liquid crystals tend to form smectic (Sm) and nematic (N) mesophases, which will be described later in the thesis. The second class of mesogen is called discotic liquid crystals; formed by molecules that are disk-like in shape, with circular aromatic cores and alkyl chains extending away from the core.

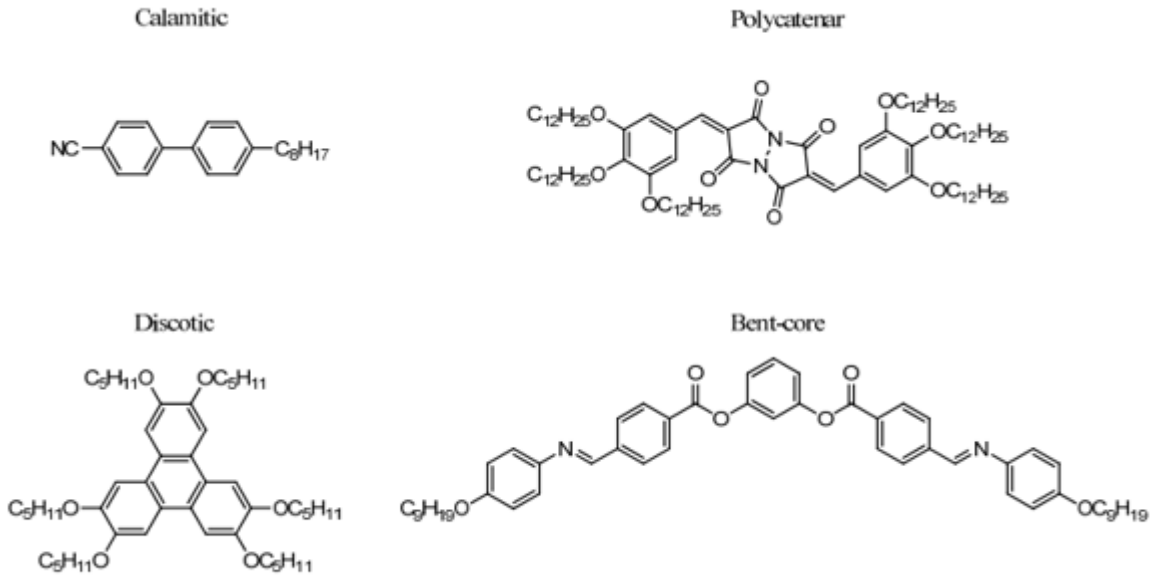

Figure 1-2: Examples of calamitic, polycatenar, discotic, bent-core mesogens.

These mesogens normally form columnar mesophases in which mesogens self-assemble into columns by stacking on top of each other. The third class of liquid crystals is polycatenar liquid crystals, which are formed by mesogens that have rod-like cores but have multiple alkyl chains which extend in multiple directions relative to the long axis of the molecule. Polycatenar liquid crystals are typically thought of as a hybrid of disc-like and rod-like liquid crystals, but normally exhibit columnar mesophases. Discotic and polycatenar liquid crystals are generally investigated for their potential in photovoltaics applications. The fourth class of liquid crystals is bent-core liquid crystals, which are formed by rod-like mesogens commonly described as banana shaped. These mesogens tend to form smectic phases. This thesis focuses on thermotropic calamitic mesogens.

1.2 Thermotropic Calamitic Mesogens

Calamitic liquid crystals are formed by rod-shaped mesogens. The typical structure of a calamitic mesogen is shown in Figure 1-3. Calamitic mesogens tend to have a scaffolding of two or more aromatic rings (Ar) with one or two aliphatic side chains or alicyclic groups at positions R1 and R2. While calamitic mesogens do not require linking groups X, Y, and Z, typically linking groups can be added between the aromatic rings or the aromatic rings and the aliphatic side chain(s). Common linking groups in calamitic liquid crystals include ester, ether, imine, ethenyl, ethynyl, methyleneoxy, or dimethylene groups.[8] Linking groups may extend the length of the molecule and distinctly modify mesomorphic properties without changing the overall rod-like shape of the mesogen.

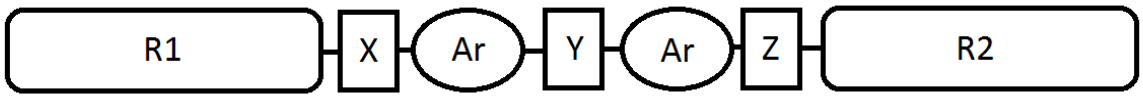

Figure 1-3: The general structure of a calamitic mesogen.

Calamitic mesogens can be modified in a variety of ways. Simple modifications can be achieved through substitution of terminal groups, linking groups, lateral groups, or aliphatic side chain groups. Lateral substitution can be achieved by the addition of substituents on the Ar groups (Figure 1-3), while terminal and aliphatic side chain substitution can be accomplished through substitution of the X, Y, Z, R1 and R2 positions. A wide variety of substituents have been used to modify mesomorphic properties including but not limited to CN, F, Cl, Br, NO_2, and CH_3.[9,10] Modification of the mesogens using these substituents affect not only mesomorphic properties,

such as melting point and clearing point but also physical properties such as dielectric anisotropy, optical anisotropy and visco-elastic properties.

Thermotropic calamitic mesogens exhibit a wide variety of mesomorphic properties. As previously stated, they form two main types of mesophases. The first is the nematic phase, which is described as a group of molecules that, on the time average, are oriented in one direction, referred to as the director **n**, without forming layers. The second type of mesophase are called smectic phases, which are described by molecules having orientational order, like the nematic phase, but the molecules are also organized into layers. There are many different types of smectic mesophases including the smectic A (SmA), smectic C (SmC), smectic I (SmI), smectic F (SmF), and smectic B (SmB) phases. The different designations of the smectic phases describe the internal ordering of the molecules within the smectic layers. The three most commonly observed and most important mesophases used in liquid crystal display (LCD) applications are the nematic (N), smectic A (SmA) and smectic C (SmC) mesophases. The ordering of these three phases are described schematically as groups of hard spherocylinders in Figure 1-4.

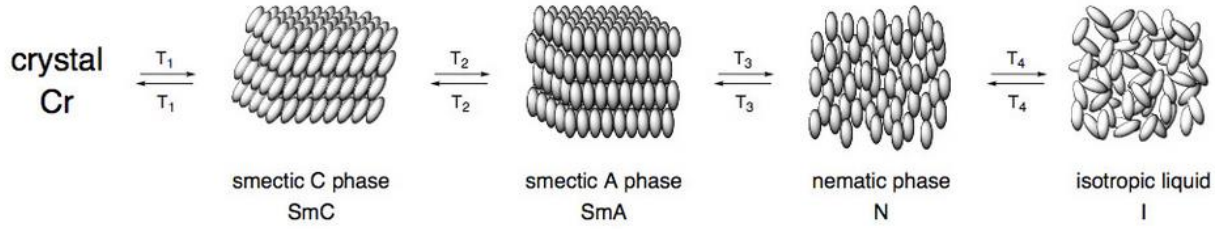

Figure 1-4: Schematic of liquid crystal mesophases as hard spherocylinders.

1.2.1 The Nematic Phase

Nematic liquid crystals are currently used in a wide variety of LCD applications.[11] The nematic phase is a mesophase in which molecules are oriented in one direction. These molecules are aligned on the time average along the director (**n**). The lack of translational order in the nematic phase results in a relatively low viscosity and fluid behavior. The ordering of the nematic phase is characterized by an orientational order parameter (S_2). The order parameter S_2 is a measure of the orientational order about the director **n** according to equation (eq. 1-1), where θ is the angle formed by the long axis of a single molecule and the director **n**, which represents the average direction of all of long molecular axes.[12]

$$S_2 = \frac{1}{2} < 3\,cos^2\theta - 1 > \qquad \text{(eq. 1-1)}$$

The orientational order parameter, S_2 ranges from 0 to 1: if the orientational order parameter is 1, the molecules are perfectly ordered along the director (**n**); if the orientational order parameter is 0, the molecules are completely disordered. Typically the orientational order parameter for the nematic phase is between 0.4 and 0.7.[11] The nematic phase is easily characterized by texture analysis using polarized optical microscopy (POM), as shown in Figure 1-5. The nematic phase shows distinct textures when viewed on an untreated glass slide under a polarized optical microscope, including a Schlieren texture that exhibits brushes and point defects, and a planar 'marble' texture.

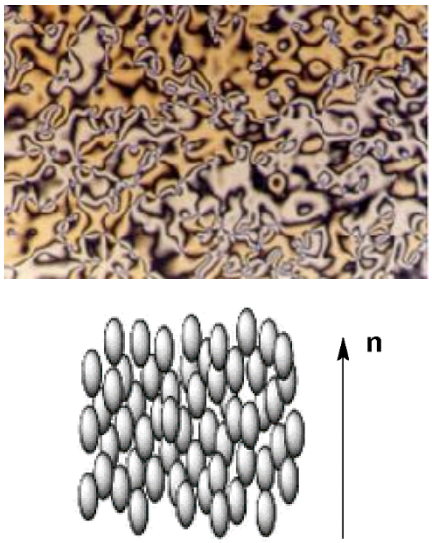

Figure 1-5: Polarized photomicrograph of a Schlieren texture characteristic of the nematic phase.

1.2.2 The Smectic A Phase

In the smectic A phase, mesogens are oriented along a director (**n**) and are organized in diffuse layers; the director **n** is parallel to the layer normal **z**. Although molecules in the smectic layers have some degree of translational order, they are rotationally disordered about **n**. The increase in translational order causes the smectic A phase to be more viscous than the nematic phase. The orientational order parameter S_2 for a conventional Smectic A phase is ~0.7-0.8.[11] The smectic A phase is characterized by the formation of focal-conic fan textures and dark homeotropic domains when viewed by polarized optical microscopy. In these homeotropic domains, the molecules are oriented vertically on the glass slide and do not exhibit birefringence. In a planar orientation, the molecules exhibit birefringence and form a focal-conic fan texture due to the

formation of layers (Figure 1-6). Birefringence is an optical phenomenon which will be discussed later in the thesis.

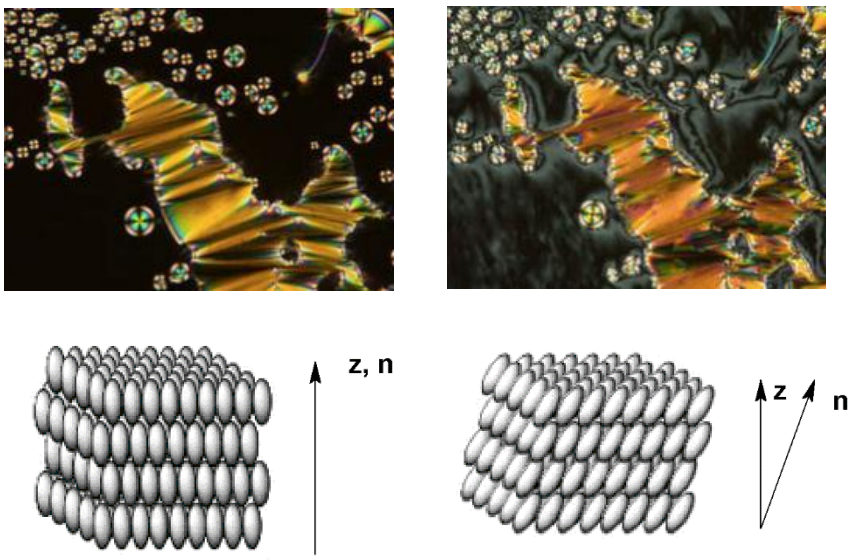

Figure 1-6: Polarized photomicrographs of fan texture below and homeotropic domains characteristic of the SmA phase (left) and broken fans and Schlieren textures characteristic of the SmC phase (right)

1.2.3 The Smectic C Phase

The smectic C phase is a tilted form of the smectic A phase. The SmC phase exhibits orientational order about the director **n** and has a layered structure like the SmA phase, but the director **n** is tilted at an angle θ with respect to the layer normal **z**. The tilt of the SmC phase is dependent on temperature and increases with decreasing temperature. The Smectic C phase can be identified under polarized optical microscopy by its characteristic Schlieren and broken fan textures. The grey Schlieren texture arises from the homeotropic domains of the SmA phase when the molecules are aligned vertically on the slide; as the temperatures decreases, the molecules tilt and the Schlieren becomes more pronounced as the molecules become more birefringent. The

broken fan texture is formed from the fan texture of the SmA phase due to the formation of tilt domains of opposite orientation; when the SmC phase forms directly from isotropic liquid or nematic phase, the fan texture is the same as that of the SmA phase.

1.3 Origin of Tilt in the Smectic C Phase

The origin of tilt in the Smectic C phase has been described by a variety of models over the years.[13,14,15] It is important to note that the different theories that have been proposed do not necessarily contradict each other and that one theory alone may not be enough to describe the origins of tilt. It is generally thought that several of the factors postulated in the following models should be considered in describing the origins of the tilted SmC phase.

1.3.1 The McMillan Model

The earliest description of the origin of tilt in the SmC phase tilts was by McMillan, who proposed that the SmC phase arises due to dipole-dipole interactions of polar groups such as ethers or esters which link the core to the side chains.[13] The hypothesis was based on the observation that 4,4'-di-n-alkoxyazoxybenzene mesogens form SmC phases, but 4,4'-di-n-alkylazoxybenzene mesogens do not.[16] McMillan proposed that the rotational order about **n** increases with decreasing temperature and results in a coupling of so-called "outboard dipoles" that creates an induced torque causing tilt in the SmC phase, as shown in Figure 1-7; however, it was later shown that the model is not general after subsequent discoveries that "outboard dipoles" are not required for the formation of the Smectic C phase in a variety of compounds.[17]

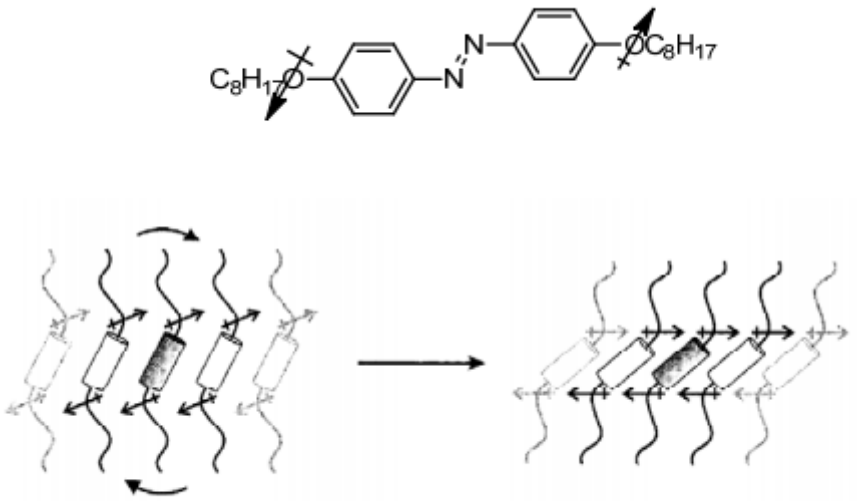

Figure 1-7: Schematic representation of the McMillan Model of the origin of the tilted SmC phase.

1.3.2 The Wulf Model

According to the Wulf model, the predominant interactions in the SmC phase are steric interactions and depend on packing forces.[14] The Wulf model neglects the "outboard dipole" arguments of the McMillan model and argues that simple molecular shape and rotational freedom of each molecule drives the tilt in the SmC phase. In this model, the average molecular shape of the SmA phase is defined as cylinders, which is representative of the fact that molecules in the SmA phase can rotate around their long axes freely. On cooling into the SmC phase, molecular rotation around the long axis is hindered due to packing forces and steric interactions. In such a system, the shape of a rod-like mesogen is represented by a zigzag shaped bent cylinder, which corresponds to the lowest energy conformation in a rod-like mesogen. Wulf then compares the lowest energy conformation of packing zigzags, which involve tilting the molecular long axes, as shown in Figure 1-8.

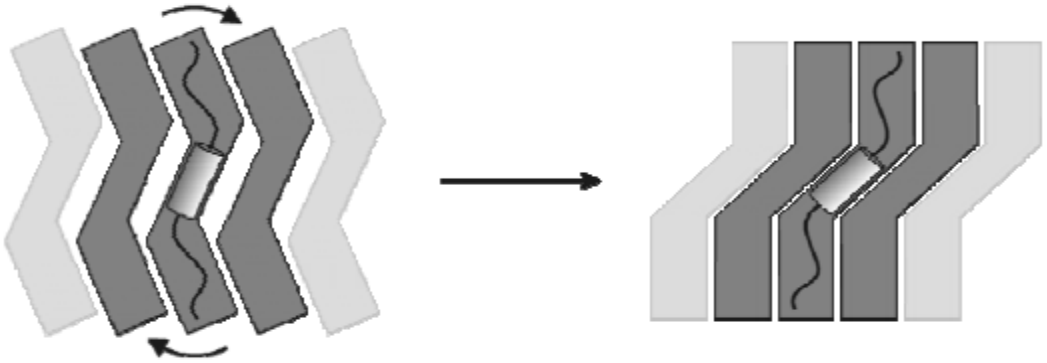

Figure 1-8: Schematic representation of the Wulf model of the origins of tilt in the SmC phase.

1.3.3 The Entropic Pressure Model

Recently, the Boulder group led by Clark and Walba proposed that the driving force for tilting in the SmC phase is due to "entropic pressure", which is the force exerted on alkyl chains by the other alkyl chains in opposition to the favourable van der Waals interactions of the aromatic cores, and the effect of alkyl chain extension on conformational degrees of freedom.[15] Tilting also increases the average cross-section of the core, which would increase the amount of van der Waals interactions in the system and compensates for the entropy loss due to a suppression of out-of-layer fluctuations (vide infra) and increase in rotational order about **n,** as shown in Figure 1-9.

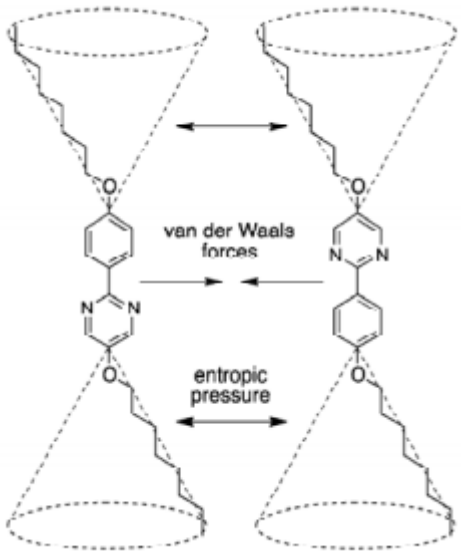

Figure 1-9: Schematic representation of the Entropic Pressure model on the origins of the tilted SmC phase. The conformational space of the aliphatic chains is approximated by conical volumes.

The entropic pressure model suggests that there is a balance between core-core interactions and conformational disorder of the alkyl chains, and this balance is observed through the molecular tilt as increased alkyl chain length.[18] The evidence of this model is shown by the lengthening of alkyl chains favouring the SmC phase over the SmA phase due to conformational disorder of the alkyl chains.[19] The longer the alkyl chain, the more conformational degrees of freedom are available than from a shorter alkyl chain. The longer alkyl chain therefore occupies more conformational space and forces the rigid aromatic cores farther apart in the diffuse lamellar structure of an orthogonal SmA phase.[15] According to the entropic pressure model, free energy can be minimized when tilting in the SmC phase and by a balance between the entropic pressure caused by conformation disorder of the alkyl chains and the van der Waals interactions of the aromatic cores.

1.4 Structure-Mesomorphic Property Relationships

In SSFLC device applications, the main mesomorphic properties to be optimized are mesophase temperature range, viscosity, optical tilt angle, birefringence, helical pitch, spontaneous polarization, and bookshelf geometry (vide infra). An important part of the design of Smectic C liquid crystals materials for SSFLC applications is creating a library of compounds with complementary properties. Typically, liquid crystal materials for SSFLC applications are mixtures of liquid crystal compounds to achieve optimized device characteristics. Hence, it is important to understand structure-property relationships in developing new materials for SSFLC material mixtures.

1.4.1 Structural Elements and Their Effect on Mesomorphic Properties

Studies have shown that tuning mesomorphic properties can be achieved primarily by varying core-core interactions and alkyl chain lengths.[20,21,22] In recent years, studies have also shown that another factor affecting properties is the use of end-groups on the alkyl chains.[18,22] In varying the functionalization at the end of the alkyl chain, one can promote different mesophase characteristics while maintaining the same aromatic structural core and alkyl chain lengths, which allows for unique optimization of properties for a given mesophase. It is important to consider the promotion of liquid crystal phases as a delicate balancing act for two reasons. The first is that liquid crystals are not restricted to forming one mesophase, and when one seeks to promote a particular mesophase, it is common to see other mesophases appear. The second reason is that, if one attempts to promote more ordered mesophases, a soft crystal or crystalline phases may result; However, attempting to promote less ordered phases can result in an isotropic liquid phase instead of the desired mesophase.

1.4.1.1 Core-Core Interactions

Typically, the core of a thermotropic calamitic mesogen contains two to three aromatic rings in a linear geometry. The core of a liquid crystal is the dominant structural element in selecting mesogen characteristics. The structure of the core can be customized by varying attributes such as planarity, dipole moment, and polarizability, which allows for a wide variety of cores to be considered in liquid crystal synthesis depending on what type of mesomorphic properties are required for the device. Studies of the aromatic core subunit in liquid crystals have shown that mesomorphic properties are incredibly sensitive to structural variations.[8] For instance, a subtle change such as substituting a 2-phenylpyrimidine (2-PhP) core with a 5-phenylpyrimidine (5-PhP) core can change the mesophase from SmC to SmA, as shown in Figure 1-10.[23] Aromatic fluoro substitution is a powerful approach to tune the mesomorphic properties of nematic and ferroelectric liquid crystals for display applications because of their unique combination of small size, low polarizability, high polarity, and high chemical stability.[8] Lateral fluoro substituents on aromatic cores have been widely used in the development of nematic liquid crystals with high negative dielectric anisotropy for vertically aligned nematic (VAN) display applications, and achiral SmC liquid crystals with low viscosity and high resistivity. Notably, the development of difluoroterphenyl mesogens by Gray *et al.* proved to be a major innovation in LCD technology that also demonstrated how mesomorphic properties can be drastically modified by changing the positions of fluoro substituents on the terphenyl core (vide infra).[24,25]

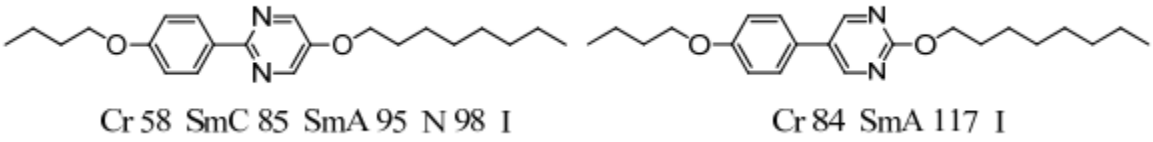

Figure 1-10: Two isomers **2-PhP-4/8** and **5-PhP-4/8**, and their mesomorphic properties.

While modification of calamitic liquid crystals can be accomplished with a wide variety of substituents, such as CH_3, OCH_3, Cl, Br, CN, and NO_2, the most common substituent is fluorine. The fluorine group is interesting due to its unique polar and steric properties. The fluorine group is the second smallest atom substituent next to hydrogen, which minimizes steric changes. Substituents such as carbon, nitrogen, and oxygen tend to require other bonded atoms that give them much larger sizes compared to fluorine. While fluorine is the smallest substituent, it is also a highly electronegative element (3.98), which shows in the large C-F dipole moment (1.41D), that allows for specific control of dielectric anisotropy.[8] The fluorine group also has a very low polarizability compared to hydrogen and the other halogens. The lower polarizability of the fluorine group may cause a decrease in strength of intermolecular dispersive forces relative to the parent system. The C-F bond also has a bond dissociation energy of 115.7 kcal/mol, which contributes to a high degree of stability.

The tuning of mesomorphic properties using a fluorine group is highly dependent on its location on the aromatic core. A single fluoro terminal substitution was first studied in 1925 by Bergt.[26] Terminally substituted cores with cyano, nitro, and fluoro groups were assumed to increase the clearing point of liquid crystals by virtue of their high polarity. The research showed that terminally substituted cores with cyano, nitro and fluoro groups promote the nematic phase, and that terminally substituted cores with cyano and nitro groups have higher clearing points than

the respective liquid crystal parent compounds. However, the fluoro substituent does not stabilize the mesophase particularly well, as shown in Table 1-1. The noted difference between the cyano, nitro and fluoro substituents is the low polarizability of the latter. Although the terminal fluoro group increases the positive dielectric anisotropy, it does not significantly increase the polarizability anisotropy, thus destabilizing the mesophases. The single fluoro substituent also does not significantly increase the length to width ratio of the molecule, which is a major factor in stabilizing mesophases.

Table 1-1: The effect of a terminal substituent on mesomorphic properties.[8]

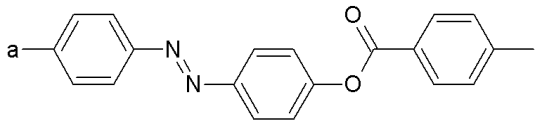

Substituent	Transition Temperatures ($\circ C$)				
a	Cr		N		I
F	•	156	•	222	•
CN	•	169	•	312	•
NO_2	•	180	•	289	•

The introduction of a second fluoro group lateral to the terminal position of the aromatic core, as shown in Figure 1-11, tends to further decrease the melting and clearing points while only slightly increasing the dielectric anisotropy.[27] Introduction of a third fluoro group further increases the positive dielectric anisotropy due to the symmetric nature of the two lateral fluoro groups. Another option for adding additional fluoro groups to a mesogen is to add a fluorinated alkyl or

alkoxy chain as end-group. The addition of small alkyl terminal groups on the mesomorphic core such as -CF_3, -OCF_2H, -and OCF_3 further increases the positive dielectric anisotropy, although the addition of these fluoro groups causes an increase in the clearing point and promotes the formation of smectic mesophases due to an increase in the length to width ratio of the mesogen.[28,29]

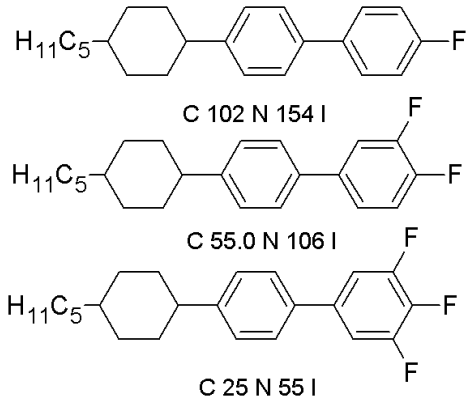

Figure 1-11: The effect of terminal fluorination on mesomorphic properties.[27]

In 1954, Gray reported the first examples of laterally substituted LCs with simple 4-alkoxy benzoic acids.[30] Lateral substitution of liquid crystalline compounds has been widely investigated. In calamitic liquid crystals, any lateral branching of the mesomorphic core disrupts intermolecular packing interactions. The size of the substituent is one of the most important factors in lateral substitution of liquid crystals, as expressed in terms of van der Waals volume.[30] The fluoro substituent is unique because its small size allows for minimal disruption of interactions due to sterics.[8] A laterally fluorinated core is therefore reasonably stable and can be used to promote liquid crystallinity better than other larger substituents.[31] A lateral fluoro substituent also allows access to materials with lower melting and clearing points, and with negative dielectric

anisotropy.[32] The effect of larger lateral halogen substituents includes a decrease of both the stability of smectic phases and a decrease of melting and clearing points, as shown in Table 1-2.[9]

Mesomorphic properties are also highly affected by the position of the fluoro substituents. If the fluoro group is located near the terminal end of the aromatic core, called outer-edge substitution, the fluoro group can fit into the free volume between the alkyl chain and the core, thus reducing the disruption in packing interactions significantly. A fluoro substituent near the center of the core, called inner-core substitution, tends to increase packing disruptions and thus greatly destabilizes liquid crystalline mesophases, particularly in smectic materials.[33,34]

Terphenyl smectogens provide a unique opportunity to examine the effect of lateral fluorination in calamitic liquid crystals.[24] The terphenyl scaffold has very high polarizability and length to width ratio, thus allowing for multiple fluoro substituents with different substitution patterns without completely destabilizing the mesophases.[34] As previously described, there are two main types of fluoro substitution, inner-core substitution and outer-edge substitution. Single fluoro substitution in the inner-core causes disruption in side-by-side packing arrangements, which tends to suppress smectic phases and promote the nematic phase instead.

Table 1-2: The effect of steric bulk due to lateral substitution on mesomorphic properties.[9]

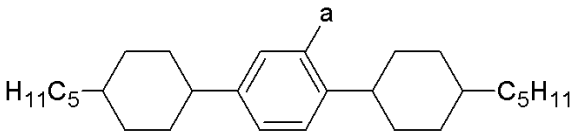

Substituent	Transition Temperatures ($\circ C$)							van der Waals Volume (Å)
a	Cr		Sm		N		I	
H	●	50	●	196	●		●	3.4
F	●	61	●	79	●	143	●	5.8
Cl	●	46	●		●	96	●	12
Br	●	41	●		●	81	●	14.4
CN	●	63	●	43	●	80	●	14.7

Inner-core fluoro group(s) also increase the dihedral angle between aromatic rings, which decreases the polarizability of the liquid crystal core, and reduces both melting and clearing points compared to the parent system. Lateral fluoro substitution can reduce the symmetry of the mesogen, which tends to favour the formation of a tilted SmC phases over the orthogonal SmA phase.[34] The dissymmetric fluoro effect can be enhanced when a fluoro group is added to the terphenyl scaffold that has an ether linking group, which increases the lateral dipole moment that tends to favor the smectic C phase, which is demonstrated in Figure 1-12.

Figure 1-12: The effect of lateral fluoro substitution the mesomorphic properties of terphenyl mesogens.[8]

When the fluoro group is positioned farther away from the ether linking group on the terphenyl scaffold, the stability of the smectic C phase increases. Two inner-core fluoro substituents further enhance the nematic character in terphenyl liquid crystals due to increased twisting, and a decrease in packing interactions that destabilizes the smectic phases. An increase in alkyl chain length can stabilize smectic phases; a strategy used in LC synthesis to increase the length to width ratio of the mesogen. When both fluoro groups are at the outer edge of the core, the increase in molecular width is less pronounced than in inner-core substitution due to the available free volume, as previously described. The strong transverse dipole moment and increased packing interactions in outer-edge substituted terphenyl mesogens compared to the inner-core substitution help stabilize the smectic phases, particularly the tilted SmC phase. The addition of three fluoro groups on terphenyl mesogens causes a decrease in the stability of smectic mesophases and favours the nematic phase, but decreases both melting point and clearing points by a significant amount.[8]

1.4.1.2 Alkyl Chain Odd-even Effect

The alkyl chain length also plays an important role in defining mesomorphic properties. Varying the alkyl chain length can affect properties such as temperature range, mesophase observed, and viscosity.[35] The alkyl chain length affects the degree of nanosegregation of the crystal-like cores and fluid-like alkyl chains. The length-to-width ratio (aspect ratio) plays a major role in controlling packing forces. One of the most important factors to consider when varying alkyl chain length is the odd-even effect, which is manifested by adding a single methylene unit onto an alkyl chain and the resulting effect on the alkyl chain volume.

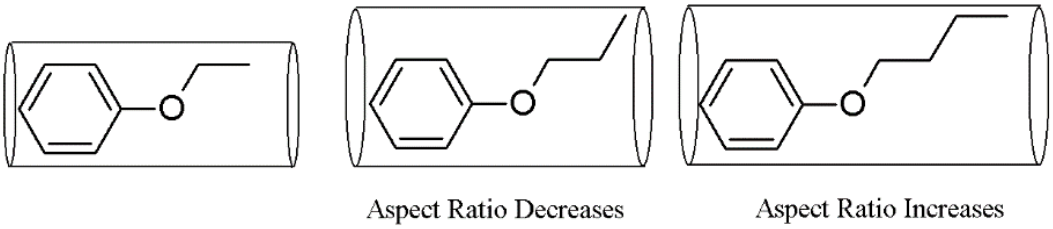

Figure 1-13: Pictorial representation of the odd-even effect by single additions of a methylene unit.

As shown in Figure 1-13, adding methylene groups to an even numbered alkoxy chain results in a decrease in aspect ratio, whereas addition to an odd-numbered alkoxy chain increases the aspect ratio. In these cases, it is observed that the addition of a methylene group will cause changes to molecular interactions and packing forces depending on the change in aspect ratio and orientation of end-groups of the liquid crystal mesogen.[35] For example a well-studied mesogenic scaffold **2-PhP-*m/n***, gives insight into the mesogenic modifications by alkyl chain length. A homologous series of **2-PhP-*5/n*** is shown in Figure 1-14, which shows the structure property

relationship of alkyl chain length, as previously described, and the odd-even effect in the melting point.[36]

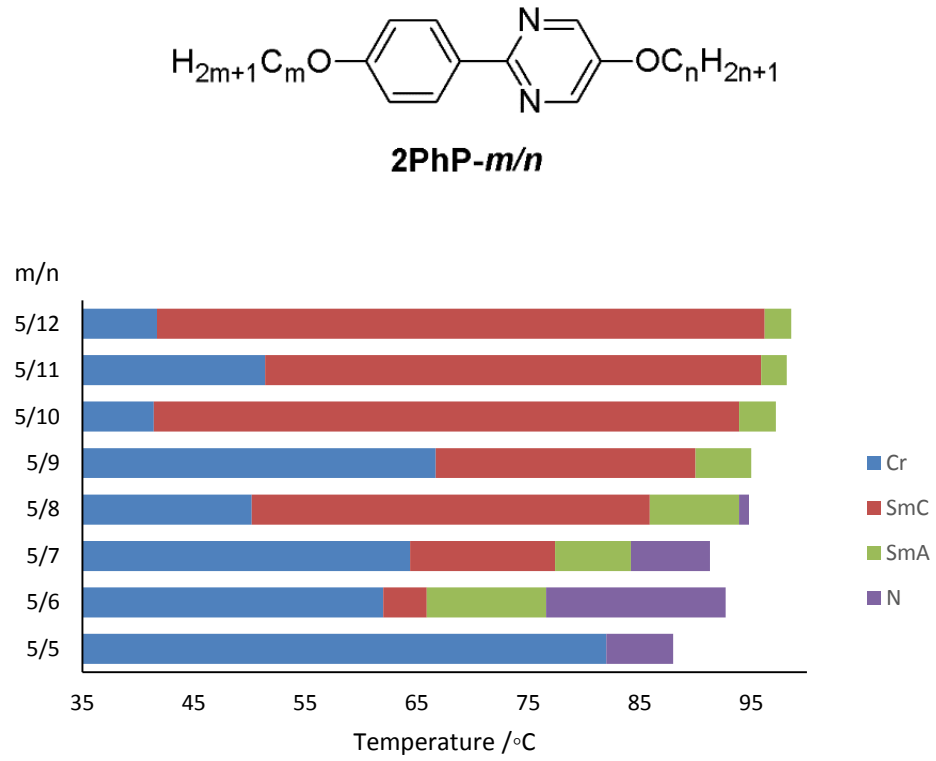

Figure 1-14: Phase transition temperature of a homologous series of **2PhP-5*/n***, demonstrating the effect of varying the alkyl chain length on the melting point.[36]

1.4.1.3 Alkyl Chain End-groups

Alkyl chain end-groups have been found to have a significant effect on liquid crystal properties, such as mesophase temperatures, observed mesophases, anisotropy and a variety of other important properties.[18] In recent studies, the Lemieux group and Goodby groups have shown that using specific end-groups can change the overall properties of liquid crystal molecules and promote critical liquid crystal properties that were previously thought to be dominated by core-

core interactions.[37,38,39,40,41] Some end-groups synthesized by the Lemieux group and the Goodby group, are shown in Figure 1-15.

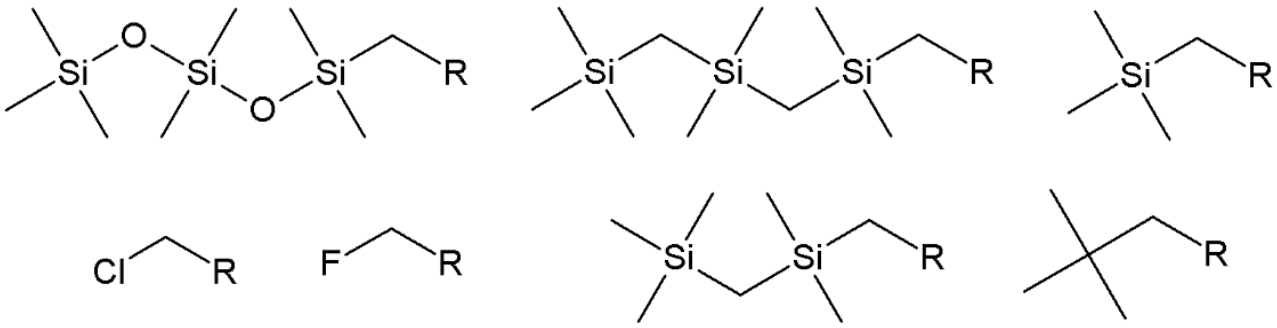

Figure 1-15: End-groups used to vary mesomorphic properties of cores.

Recent work by Goodby *et al.*, has shown that the incorporation of branched terminal chains (bulky end-groups) can thermally stabilize the SmC phase by reducing free volume, however if the end-group is too bulky, the stability of the SmC phase is greatly reduced, and in some cases the molecules were found to have no mesomorphic properties.[41]

Siloxane and carbosilane end-groups promote the formation of smectic phases by virtue of nanosegregation.[42] Nanosegregation is a fundamental part of mesophase formation.[43] As previously discussed, without the nanosegregation between the cores and the alkyl chains, smectic liquid crystals would not exist. In current studies, it has been found that nanosegregation can be enhanced by adding an end-group that is incompatible with both the alkyl chain and aromatic cores.[39] When adding a nanosegregating end-group, one can essentially achieve a three part system, which increases lamellar order. The corresponding smectic mesophase tends to form intercalated bilayers, as shown in Figure 1-16,[42] which suppresses the formation of the nematic phase and promotes the formation of the smectic phases.

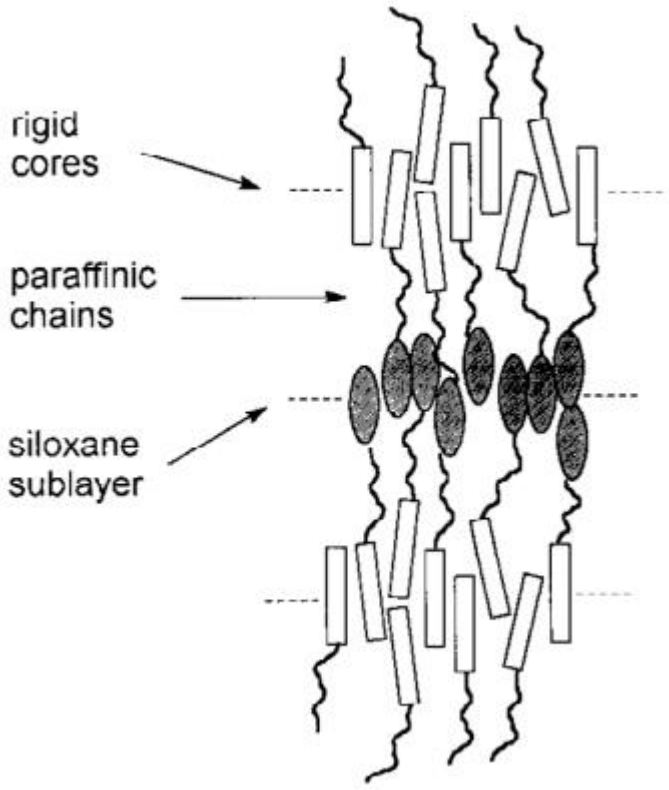

Figure 1-16: Nanosegregation in smectic liquid crystals with oligosiloxane end-groups.[42]

To build a typical triblock mesogen, alkyl chain end-groups may include fluorocarbon, carbosilane, or siloxane groups as nanosegregating elements. Carbosilanes and siloxanes have decreased rotational energy about the Si-O or Si-C bonds as shown in Figure 1-17. The decreased energy barrier of rotation allows for the chain to rotate more freely with respect to the alkyl chain, thus causing them to nanosegregate.[42] On the other hand, perfluorinated alkyl chains are more rigid than the corresponding alkyl (C-H) chains have a higher rotational energy barrier and thus a narrowing of the alkyl chain cone; this is commonly known as the fluorophobic effect. Mesogens containing carbosilane and siloxane end-groups tend to have higher viscosity than their parent compound, which affects switching time and alignment in SSFLC applications. Although

mesogens with perfluorinated alkyl chains have lower viscosity, they are difficult to align in cells with rubbed polyimide substrate.

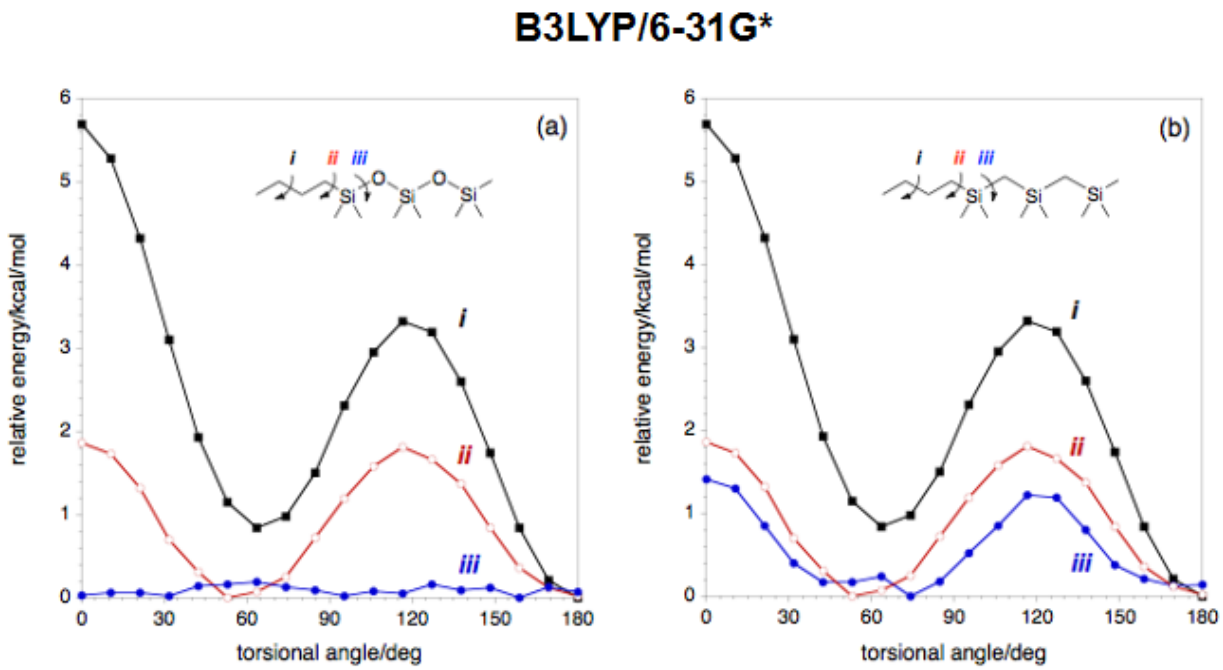

Figure 1-17: Conformational energy profiles of a C-C bond (**i**), a C-Si bond (**ii**), and a Si-O bond (**iii**).

The use of aromatic end-groups in the rational design of new smectic liquid crystals may hold significant potential because non-covalent arene-arene interactions can be finely tuned by aromatic substitution although there are only a few reports of arene terminated mesogens in the literature. The first of these reports, by Gray *et al.*, focused on the homologous series of phenyl-terminated alkyl 4-(benzylideneamino)cinnamates and revealed alternations in the nematic-isotropic transition temperatures and entropy of transition with increasing length and parity of the phenyl-terminated alkyl chain that are significantly more pronounced than those normally observed in the absence of a phenyl end-group, as shown in Figure 1-18.[44]

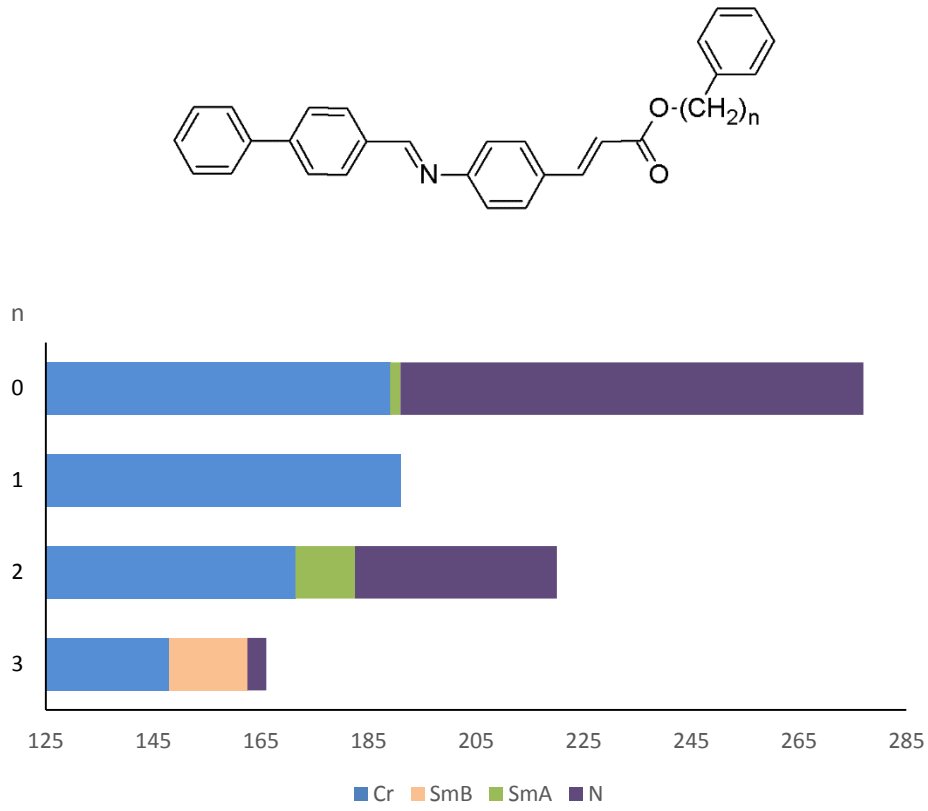

Figure 1-18: Mesomorphic properties of phenyl-terminated alkyl 4-(benzylideneamino)cinnamates.

As noted in a recent review by Imrie *et al.*, this behavior is similar to that observed with liquid crystal dimers, and arene-terminated mesogens may therefore be considered as structural intermediates between conventional liquid crystal monomers and dimers.[45]

1.4.2 Nematic Promoting Factors

Nematic liquid crystals are characterized by a low orientational order and a lack of nanosegregating elements. Nematic mesogens tend to have small alkyl chain lengths (1-5 carbon units) and weakly interacting cores to prevent core segregation and the formation of layers.[36] An example of a N-promoting core is cyanobiphenyl, which has a non-planar structure that prevents

strong core-core interactions in the liquid crystal phase. The cyano unit is critical for the formation of the nematic phase because it increases the polarizability anisotropy of the core.[6] The cyanobiphenyl can only accommodate one alkyl chain, thus limiting any lamellar order promoted by nanosegregation of the alkyl chains from the cores. As long as the alkyl chain length remains relatively short, smectic phases can be avoided.

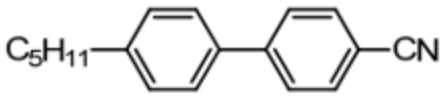

Cr 24 N 35 I

1.4.3 SmA Promoting Factors

Smectic mesophases are promoted through an increase in lamellar order and a high degree of polarizability. The smectic A phase is promoted primarily by amphilicity and is thought to be favoured over the SmC phase due to entropic factors. Amphilicity in thermotropic liquid crystals is caused by a balance between core-core interactions and alkyl chain fluidity. The liquid crystalline cores cause arene-arene interactions to drive the system towards crystalline behavior, while the alkyl chains drive the system towards fluid like properties, which results in liquid crystalline properties. The main entropic factor is out-of-layer fluctuations (OLF), which allow molecules to propagate between layers of the SmA phase, as shown in Figure 1-19. Because of the OLF mobility in the SmA phase, enthalpic contributions to the free energy of the system from core-core interactions are reduced.

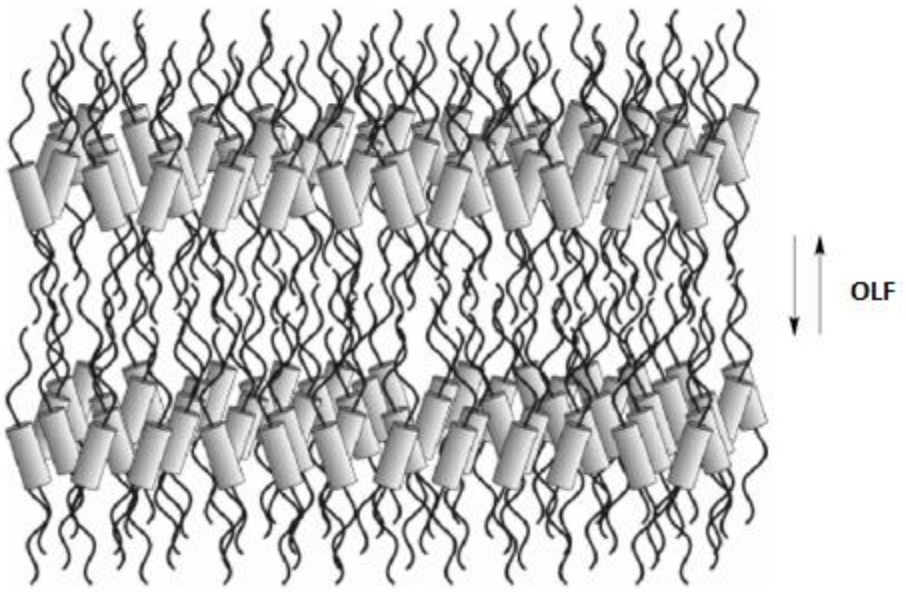

Figure 1-19: Schematic representation of the SmA phase and out-of-layer fluctuations.

Hence, in order to promote the smectic A phase, one must have lamellar order without overly strong core-core interactions that would suppress out-of-layer fluctuations. These types of liquid crystals tend to have medium sized alkyl chain lengths (5-8 carbon units). Promoting the smectic A mesophase can also be accomplished by increasing the alkyl chain lengths of a nematic mesogen and by improving core-core interactions of a weakly nanosegregating nematic promoting core, as shown in Figure 1-20 and Figure 1-21.[6]

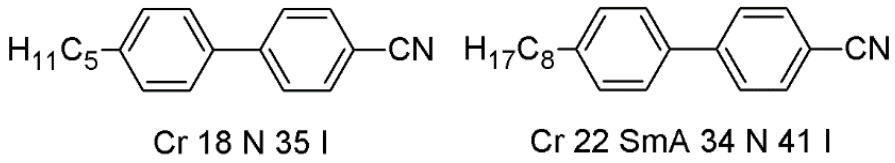

Figure 1-20: 4-pentyl-4'-cyanobiphenyl and 4-heptyl-4'-cyanobiphenyl.

Improving core-core interactions for SmA promotion is generally accomplished by increasing the polarizability of a non-planar core, and thus increasing the amphiphilicity of the system. While the nematic phase can be promoted with biphenyls, an example of a Smectic A promoting core is 5-phenylpyrimidine because of the increase of polarizability from a biphenyl core while keeping the aromatic rings in a non-planar orientation, limiting core-core interactions allowing for out-of-layer fluctuations.[46]

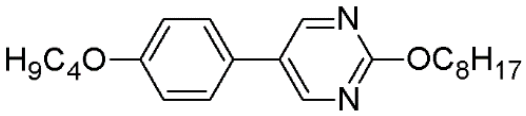

Cr 84 SmA 117 I

Figure 1-21: Phase transitions of **5-PhP-4/8**, a SmA promoter.

The SmA phase may also be promoted through the use of alkyl chain end-groups. The effect of the chloro end-group was originally attributed to polar interactions at the layer interface; however, this was recently ruled out by Rupar *et al.* in a study of sterically equivalent series of chloro-terminated 2-phenylpyrimidine mesogens (Figure 1-22).[18]

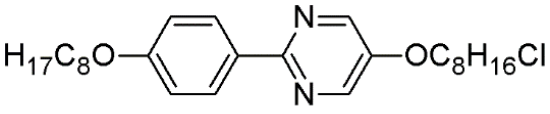

QL8-8/8 Cr 67 SmA 105 Iso

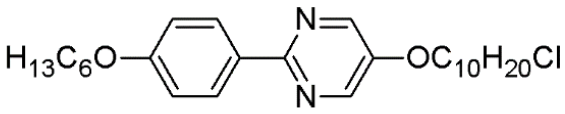

QL8-6/10 Cr 67 SmA 95 I

Figure 1-22: Two chloro-terminated SmA mesogens.

Instead, the evidence suggests that the SmA promoting effect is caused by the electron-withdrawing effect of the chloro end-group on the alkoxy chain, which reduces electrostatic

repulsion between alkyl chains, as shown in Figure 1-23. The reduced electrostatic repulsion of the alkyl chains allow the cores to move closer together without having to tilt, which would be costly in terms of entropy.[18]

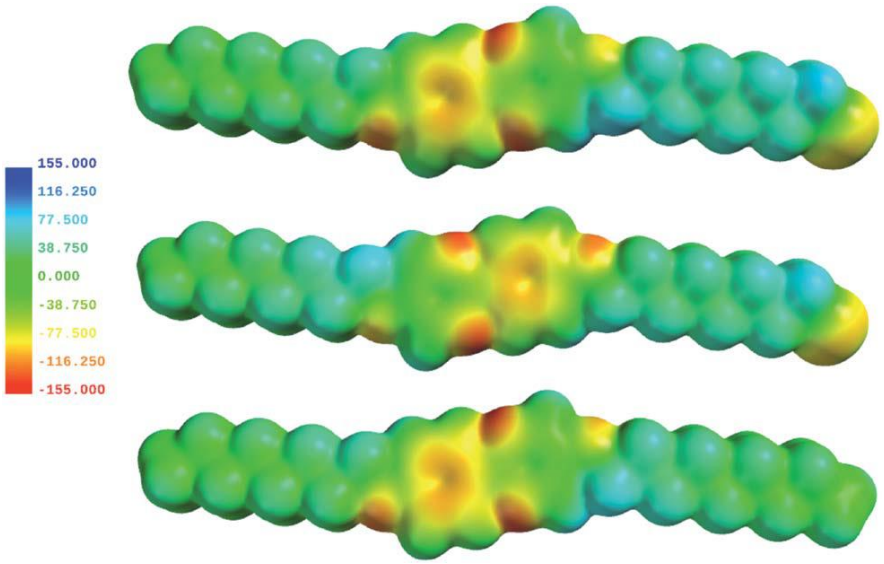

Figure 1-23: B3LYP/6-31G* level calculations of the electrostatic potential isosurfaces of **2-PhP-8/8** and the two chloro-terminated **2-PhP-8/8** isomers.[18]

1.4.4 SmC Promoting Factors

Structural factors promoting the smectic C phase include a planar core structure that has a high polarizability, and strong core-core interactions to suppress the SmA phase. Two examples of SmC mesogens are shown in Figure 1-24. The smectic C phase can typically be promoted with an increase of alkyl chain lengths (8-12 carbons), which reduces core-core interactions due to entropic pressure and favours tilting to maximize core-core interactions. The increase in lamellar order with longer alkyl chain lengths is accompanied by a decrease in out of layer fluctuations. The smectic C mesophase can also be promoted by strengthening core-core interactions. Typical

SmC cores are planar and highly polarizable; for example 2-phenylpyrimidine. The smectic C phase can also be promoted through the use of nanosegregating alkyl chain end-groups. Alkyl chain end-groups such as a trisiloxane or tricarbosilane can be used to increase nanosegregration of the mesogen, thus causing the promotion of the SmC phase at shorter chain lengths. Nanosegregation suppresses out-of-layer fluctuations and reduces the entropic cost of molecular tilt.[39]

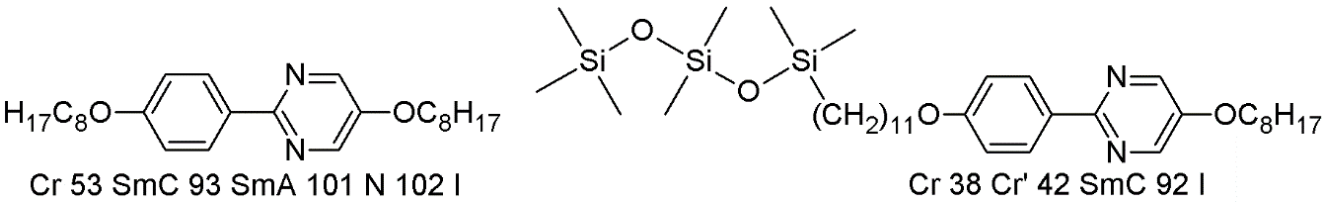

Figure 1-24: **2PhP-8/8** and **TriSi-2PhP5-11/8**: Two common SmC mesogens.[39]

1.5 The Chiral SmC* Phase

The liquid crystals that have been discussed so far are achiral. Chiral liquid crystals have unique properties because of the loss of symmetry in the bulk phase. There are two different ways to promote chiral mesomorphic behavior. The first is to synthesize a chiral mesogen and the second is to add a chiral dopant to an achiral liquid crystal. Chiral dopants can be used in very small quantities to induce chirality in the bulk of the liquid crystal phases and do not necessarily have to be mesogenic themselves.

The chiral smectic A phase is comparable to the achiral smectic A phase with respect to molecular orientation. On the other hand, the chiral smectic C phase in the bulk is characterized by a helical structure in which the director **n** precesses about **z** from one layer to the next, as shown

in Figure 1-25. The SmC* helix is characterized by a pitch that is normally on the order of a few microns. Another manifestation of chirality at the macroscopic level in the SmC* phase is spontaneous polar ordering.

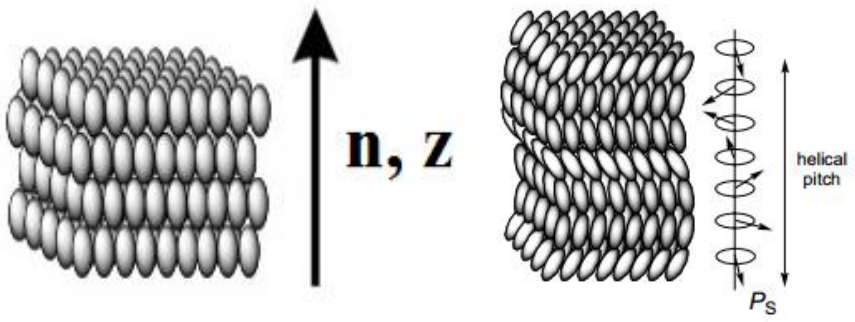

Figure 1-25: The graphical representation of the bulk SmA* phase (left) transitioning into the bulk helical SmC* phase, in which the helical pitch causes a net spontaneous polarization of 0. (right)

1.5.1 The Molecular Origins of P_s

Thus far, the spontaneous polarization has been defined using mesogens as hard spherocylinders. While it is convenient to think of liquid crystals as hard spherocylinders, they lack the molecular definition required to understand the molecular origins of P_s. Walba and Clark developed the Boulder model in 1986 to describe the molecular-level behaviour leading to spontaneous polarization. The model allows for general predictions of sign and relative magnitude of P_s for chiral SmC* materials.[47,48]

The Boulder model uses conformational analysis to predict the direction and relative magnitude of polarization in materials. The model assumes that molecules in the SmC* phase are oriented with the side-chains in fully extended all-*anti* conformations, resulting in a zigzag geometry.[49,50]

This orientational ordering is modeled by a mean-field potential with a bent cylinder (zigzag) shape often referred to as a binding site by analogy with host-guest chemistry. The binding site is assumed to have the same basic shape for all SmC materials, and is mirror symmetric even for the chiral SmC* phase with the chiral guest in the binding site, as shown in Figure 1-26.

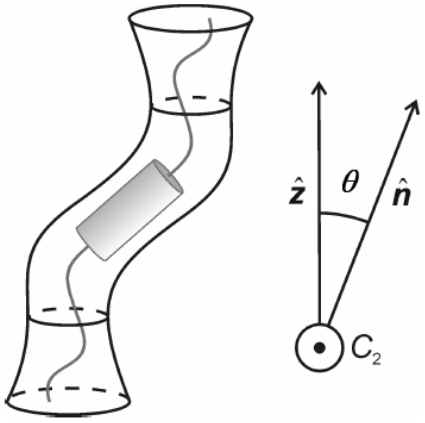

Figure 1-26: A bent-cylinder binding site proposed in the Boulder model, specifying the direction of the layer normal, the director and the C_2 rotational axis.

The transverse molecular dipoles contribute to the spontaneous polarization in a smectic C* phase provided that the dipolar groups are located near a stereogenic center. According to the Boulder model, the sign and magnitude of the spontaneous polarization can be determined by examining the predominant conformation of the chiral segment and its associated dipolar group.[47] The spontaneous polarization can be expressed in terms of molecular dipoles according to equation 1-2.[47]

$$P_S = \sum_i \frac{D_i \mu_{\perp i} ROF_i}{\varepsilon} \qquad \text{(eq. 1-2)}$$

where ε is the dielectric constant for the material and, for the *i*th conformation, D_i is the molecular number density, $\mu_{\perp i}$ is the component of the dipole moment along the C_2 axis, and ROF_i is the rotational orientation factor which is a measure of the degree of rotational order imposed on the zigzag conformation by the binding site.[47]

An important part of the equation is the *ROF*. The *ROF* does not equal zero for polar functional groups that are sterically coupled to the stereocenter. If the polar functional group is not coupled to the sterogenic center and there is no orientational bias, the *ROF* equals 0 and will not contribute to spontaneous polarization of the material.[47]

For example, the Boulder model has been shown to predict the sign of the polarization induced by 4-octyloxyphenyl-4((2S)-oct-2-yloxy)benzoate. In this particular case, it can be noted that there are several polar groups that could contribute to the overall spontaneous polarization, including two ethers and an ester group. It can be seen that the octyloxy and the ester functional groups are too far away from the stereogenic center to contribute to the spontaneous polarization. We can then analyze each stable conformer, which shows that there are three different co-planar staggered conformations about the C2-C3 bond. Since one of the three dipole moments lies in the tilt plane it cannot contribute to the spontaneous polarization. If we analyze the remaining two conformers, as shown in Figure 1-27, we can see that one of the two conformers is more energetically stable due to the anti relationship between the methyl group at the stereogenic center and the alkyl side chain. In this case, a negative spontaneous polarization results due to this favoured conformation, which agrees with experimental results.[47]

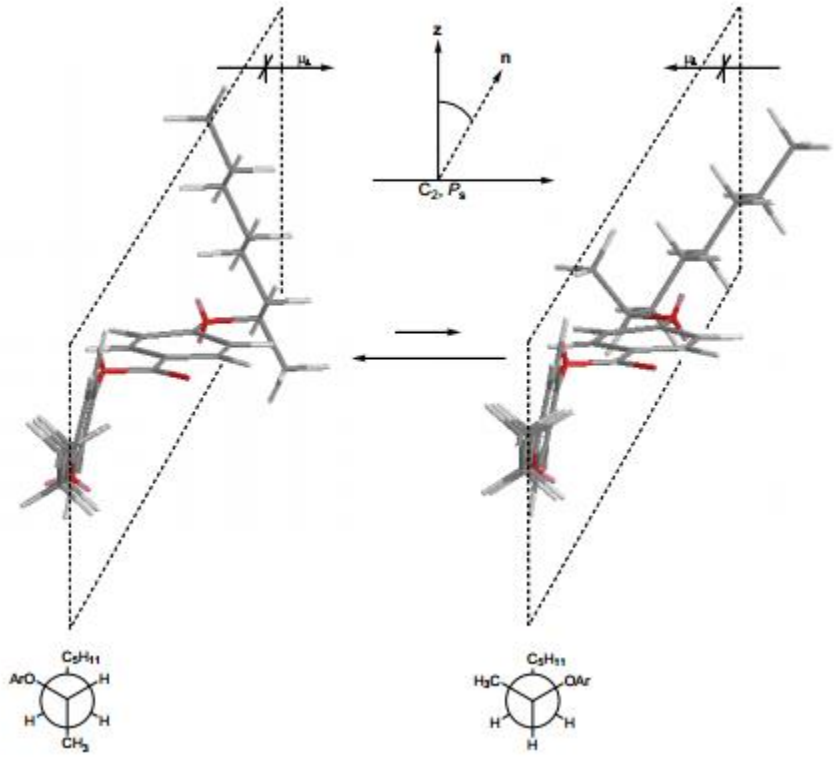

Figure 1-27: Conformations contributing to the spontaneous polarization of 4-octyloxyphenyl-4((2S)-oct-2-yloxy)benzoate. The dashed box is representative of the tilt plane. The transverse dipole moment direction is represented by the arrow, pointing from the negative to the positive direction, which is consistent with the physics convention for dipole moments.[47]

1.5.2 Surface Stabilization of the Smectic C* Phase

In 1980, Clark and Lagerwall showed that it was possible to unwind the SmC* helix by surface stabilization.[51] To unwind the helix, the SmC* phase must be aligned in between two glass slides that are separated by a distance equal or less than the helical pitch of the SmC* material, which is typically a few microns, and that have a parallel rubbed polymer film as alignment substrate. In this surface-stabilized state, shown in Figure 1-28, the SmC* phase exhibits a net spontaneous polarization, which can be coupled to an applied electric field (vide infra).[51] Because

of the surface stabilization, the surface stabilized SmC* phase shows hysteresis under an AC field and thus behaves like a ferroelectric. It is therefore referred to as a surface stabilized ferroelectric liquid crystal (SSFLC).

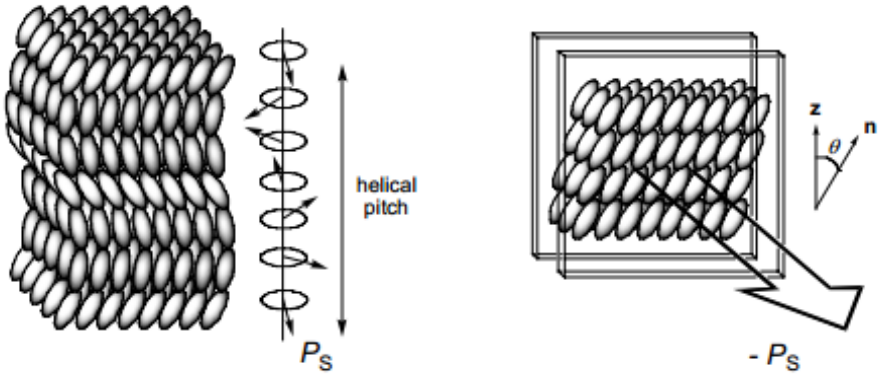

Figure 1-28: The SmC* Helices in the bulk (left). The surface stabilized SmC* phase due to planar boundary conditions (right).

The property of spontaneous polar order was first predicted by Meyer in 1976 based on a simple symmetry argument.[52] Spontaneous electric polarization in the SmC* phase can be observed due to the increase of rotational order and decrease is symmetry from the achiral SmC phase. The achiral SmC phase has C_2h symmetry, and the reflection symmetry operation (σ) causes a bulk directional polarization of zero along the C_2 axis. The chiral SmC phase loses the reflection symmetry, as shown in Figure 1-29, causing the C_2 axis to become polar.[52]

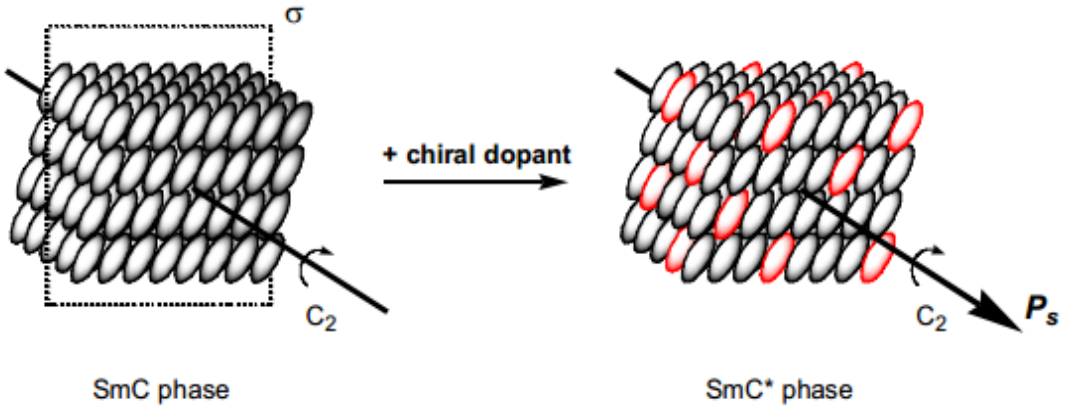

Figure 1-29: The reduction in symmetry of the SmC phase to the SmC* phase on the addition of a chiral dopant.

The lack of reflection symmetry and the corresponding conformation bias of polar groups coupled to a stereocenter gives rise to a spontaneous polarization P_s along the C_2 axis. This polarization is intrinsic to each SmC* layer, but the bulk SmC* phase has a no net spontaneous polarization P_s due to the formation of the helical structure, as shown in Figure 1-28.

1.6 Electro-optics of Liquid Crystal Films

Liquid crystals are anisotropic in nature, which results in an optical property called birefringence. Because of birefringence, liquid crystals uniformly aligned can rotate planar polarized light and therefore allow for light transmission when positioned between crossed polarizers depending on the orientation of the director **n** relative to the polarizers. When the director orientation can be changed by application of an electric field *E*, a liquid crystal film can act as an electro-optical light shutter.[11]

1.6.1 Birefringence

Due to the uniaxial symmetry around **n** in N and SmA liquid crystals, many physical properties such as refractive index, dielectric permittivity, magnetic susceptibility, viscosity and conductivity have different values parallel to the director **n** and perpendicular to it. The optical anisotropy of liquid crystals can be described by a spherocylinder which has two principle refractive indices. These indices are commonly referred to as the ordinary refractive index n_o and the extraordinary refractive index n_e. The ordinary refractive index is measured for the light wave where the vector vibrates perpendicular to the optical axis. The extraordinary refractive index is measured through the electron vector which vibrates along the optical axis, as shown in Figure 1-30.[11]

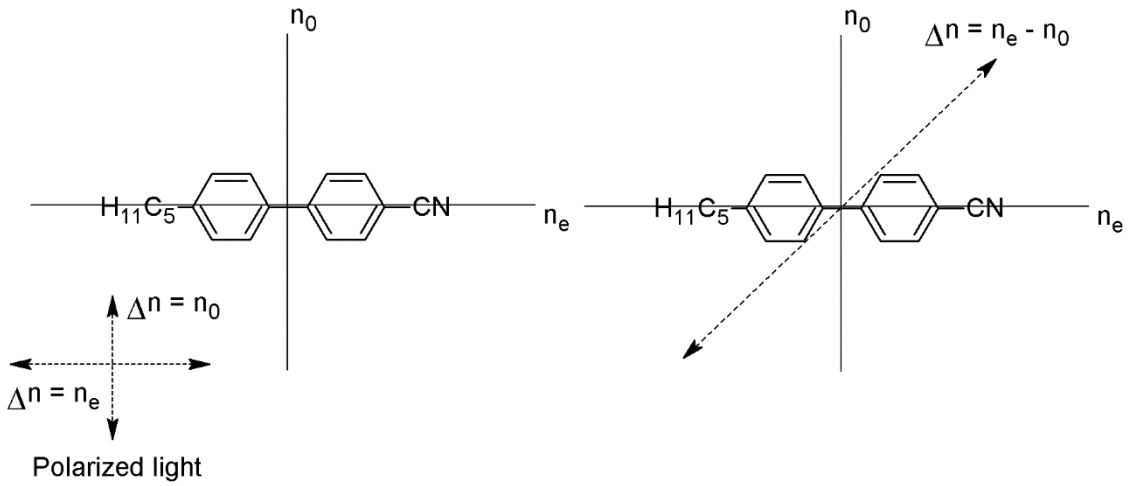

Figure 1-30: Origin of optical birefringence in **5CB**, a calamitic liquid crystal.

. The two different refractive indices lead to a special property called birefringence. Birefringence (Δn) is expressed through equation 1-3.

$$\Delta n = n_e - n_o \qquad \text{(eq. 1-3)}$$

When plane polarized light interacts with a liquid crystal it is split into an ordinary and extraordinary waves depending on the angle of incidence. The light travels at different speeds through the material and emerges with some phase differences that depend on the thickness of the birefringent material. A birefringent molecule in between crossed polarizers is shown in Figure 1-31.[53]

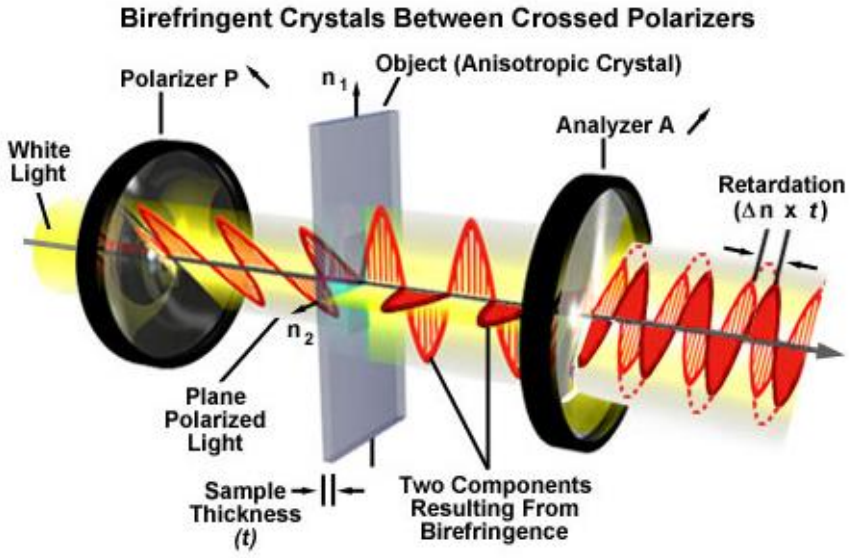

Figure 1-31: A birefringent sample interacting with plane polarized light, splitting the plane polarized light into two components resulting in a retardation of light exiting the analyzer.[53]

1.6.2 Dielectric Anisotropy

The electric permittivity of a material is a constant of proportion between electric displacement and electric field intensity and is determined by the ability of a material to polarize in response to an applied electric field. In most cases, the electric permittivity is measured relative

to the electric permittivity of free space (8.85×10^{-12} Fm^{-1}). The relative electric permittivity of a material is then expressed as the dielectric constant of the material, ε. Given the cylindrical symmetry of liquid crystal materials, the two different dielectric constants can be simplified as $\varepsilon_{\parallel}$ and $\varepsilon_{\perp}$, in which $\varepsilon_{\parallel}$ is the dielectric constant parallel and $\varepsilon_{\perp}$ is the dielectric constant perpendicular to the long axis of the molecule. The two dielectric constants can then be used to calculate the dielectric anisotropy of the material as shown in equation 1-4.[11]

$$\Delta\varepsilon = \varepsilon_{\parallel} - \varepsilon_{\perp} \qquad \text{(eq. 1-4)}$$

The dielectric anisotropy can have a positive or negative value depending on whether the dielectric permittivity is stronger perpendicular or parallel to the long axis of the molecule. The interactions and alignment of liquid crystals with an applied electric field depend on the strength of the electric field and magnitude and sign of the dielectric anisotropy of the material.[11]

1.6.3 The Freedericksz Transition

The Freedericksz transition is an electro-optical spatial transformation of a liquid crystalline material with high positive dielectric anisotropy and is not to be confused with a phase transition.[54] The Freedericksz transition is described by a uniform molecular director distortion within an applied electric or magnetic field. The distortion arises from the alignment of the dipole moment of a molecule with the direction of the applied field. The distortion is field dependent and, as the field increases, the molecules gradually rotate until the director is aligned with the field. The transition is typically observed in planar aligned cells in which the field is applied in the vertical

direction, which causes the liquid crystal sample to adopt a homeotropic configuration, as shown in Figure 1-32.[54]

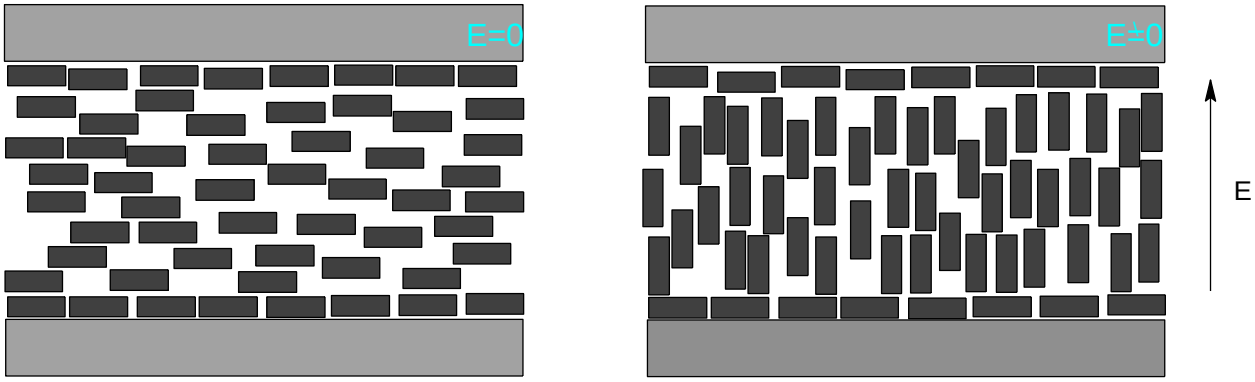

Figure 1-32: A graphical representation of the Fredericksz transition of nematic liquid crystal mesogens. Planar aligned molecules are shown on the left in the absence of an applied field. On the right, the molecules are placed in an applied field and react to the applied field by aligning their dipoles in the direction of the applied field.

1.6.4 Soft Mode Electroclinic Effect in the Chiral SmA* Phase

Garoff and Meyer observed that an electric field E applied parallel to SmA* layers induces a uniform molecular tilt θ relative to the layer normal **z** in a direction orthogonal to E; this effect is called the electroclinic effect.[55,56] The electroclinic effect is a pre-transitional electro-optical phenomenon that is observed near the SmA*-SmC* phase transition in the presence of an applied field. The electroclinic effect is due to pretransitional tilt fluctuations in the orthogonal SmA* phase as the temperature approaches the transition point T_{AC}; the field E couples with the transient polarization P_s to produce an induced tilt θ, as shown in Figure 1-33.

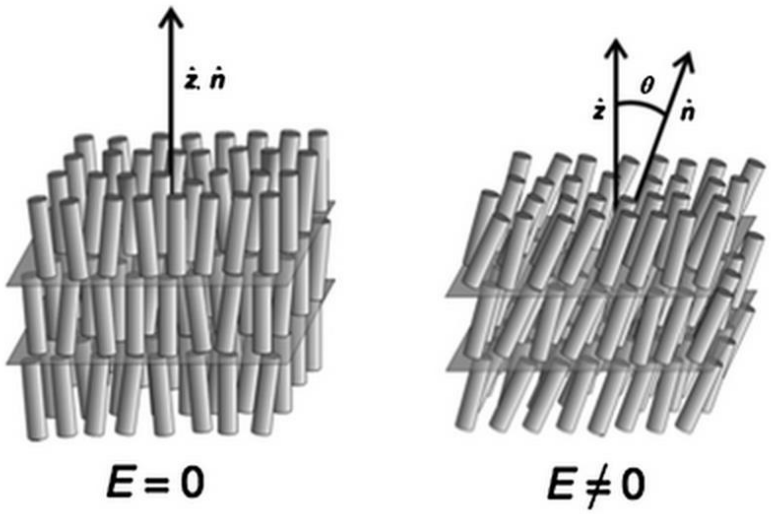

Figure 1-33: As the temperature approaches T_{AC}, random tilt fluctuations in the smectic layers are observed (left). On application of an applied field, the random tilt fluctuations align in a single direction. (right).

For small induced tilt angles, the induced tilt angle θ is directly proportional to the strength of the applied field E as expressed by equation 1-5.

$$\theta = e_c E \qquad \text{(eq. 1-5)}$$

where e_c is the electroclinic coefficient and is inversely proportional to the reduced temperature as expressed by equation 1-6.

$$e_c = \frac{c}{\alpha(T - T_c)} \qquad \text{(eq. 1-6)}$$

where c is the electroclinic coupling constant between θ and E, and α is a susceptibility coefficient which is independent of chirality.[55,56,57]

1.6.5 Goldstone Mode Switching in Ferroelectric Liquid Crystals

In the previous section, the origins of spontaneous polarization in the chiral SmC* phase were discussed. In the surface-stabilized state of the SmC* phase, the ferroelectric properties allow for the tilt orientation to be switched from $+\theta$ to $-\theta$ by rotation around the SmC* cone angle because of the coupling of P_s with the applied electric field E.

A SSFLC can be turned into a light shutter between crossed polarizers. By aligning the smectic C* director with one polarizer, a dark state can be produced. By applying an electric field, the director can be switched from $+\theta$ to $-\theta$, and light can pass through the crossed polarizers provided that θ is not 45°. The two most important properties of this SSFLC device are that it has fast switching times on the order of microseconds and it is theoretically bistable. Switching from $+\theta$ to $-\theta$ by rotating about the tilt cone in the SmC* phase is known as Goldstone mode switching, as shown in Figure 1-34.

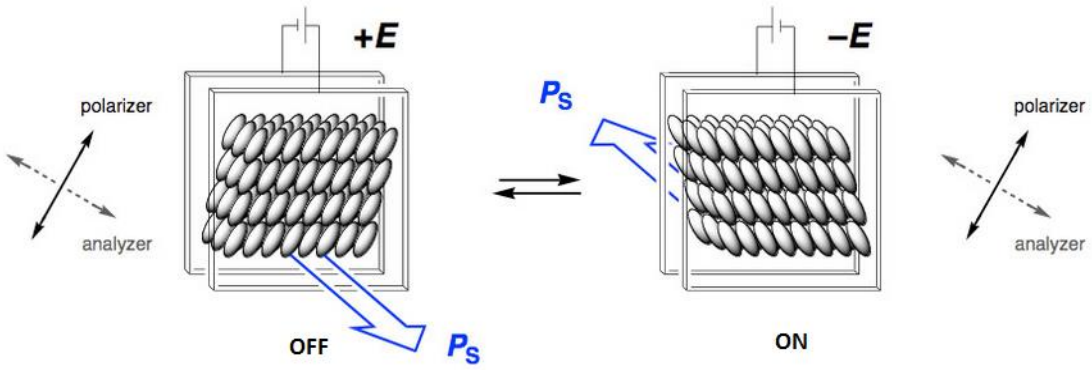

Figure 1-34: Switching of a SSFLC between crossed polarizers.

If we imagine that the ferroelectric liquid crystal (FLC) is in a stable state in a small DC field, as shown in Figure 1-35; we may then switch to the second state by reversing the polarity of the applied electric field *E*.

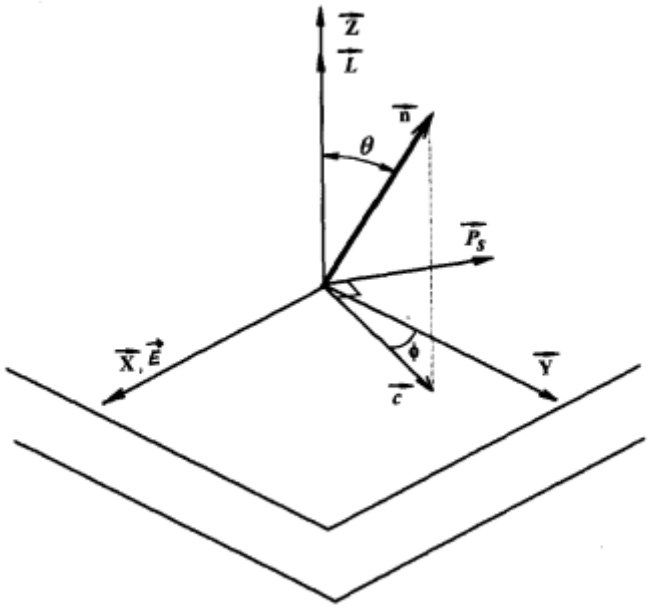

Figure 1-35: Local symmetry of the SmC* phase in the X,Y,Z coordinate system; where **n** is the molecular director; **L** is the smectic layer normal; **c** is a projection of **n** on the smectic layer plane; $\mathbf{P_s}$, spontaneous polarization vector; $\boldsymbol{\theta}$, molecular tilt angle, $\boldsymbol{\phi}$, azimuthal angle; X-Y, smectic layers; **E** is the electric field applied along **x**.[58]

In this case the director rotates around **L**, at a constant tilt angle θ and assumes an orientation that is opposite in position to the cone, or it can be described as the azimuthal angle ϕ changing from ϕ to $\phi + \pi$. The change in azimuthal angle ϕ can then be translated into the bulk of the sample and the entire macroscopic polarization $\mathbf{P_s}$ is coupled with *E* to give an effective driving torque for switching as expressed in equation 1-7.[58]

$$\mathbf{P_s} \times \mathbf{E} = P_s E \sin\phi \qquad \text{(eq. 1-7)}^{58}$$

In Goldstone mode switching described above, the layer normal **L** and the tilt angle θ between the director **n** and the layer normal **L** do not change during application of an electric field parallel to the layers.

1.7 Optimal SSFLC Devices

There are many requirements for a "working" SSFLC device. The most important requirements are a broad temperature range of the SmC* phase, low viscosity, an optical tilt angle of 22.5 degrees, long helical pitch, spontaneous polarization on an order of 20 – 30 nC/μm^2, uniform alignment, and bookshelf geometry. A tilt angle of 22.5 degrees produces an angular change of 45 degrees upon Goldstone mode switching, which is optimal to achieve maximum contrast between crossed polarizers, an example of SSLFC switching contrast is shown in Figure 1-36.

a) 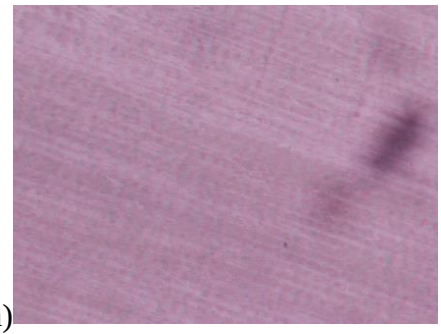 b) 

Figure 1-36: Polarized photomicrographs of a SSFLC switching between light (a) and dark (b) states.

1.7.1 Spontaneous Polarization, Viscosity and Switching Times

Typical switching times for SSFLCs devices are on the order of microseconds. The fast switching time of the SmC* mesophase is dependent on the spontaneous polarization P_s, rotational viscosity, and the applied electric field. To optimize SSFLC devices, spontaneous polarization should be maximized while viscosity should be minimized. However, viscosity generally scales with P_s due to increased intermolecular interactions. A P_s value of 20-30 nC/um^2 normally gives optimum switching times in SSFLC devices.

1.7.2 Helical Pitch

To unwind the helix in the chiral Smectic C* phase and achieve a surface-stabilized state, the distance between the two glass slides must be smaller than the SmC* helical pitch. Typical helical pitch values for FLC device mixtures are between 1 and 5 μm, but should be as long as possible. The larger the helical pitch the larger the distance that can be accommodated between the two glass slides of the cell. Optimizing the helical pitch of a SSFLC mixture is extremely important for device design. Bistability will be lost if the helical pitch is shorter than the cell width, which is discussed in the next section.

1.7.3 Bistability, Bookshelf Geometry and Uniform Alignment

Unlike devices based on nematic liquid crystals, SSFLC devices are bistable. Bistability is defined by having two energetically equivalent switching states, which allow images to be stable in the absence of an applied field. A bistable SSFLC device requires the molecules to be in a bookshelf geometry and uniformly aligned. If the helix is not completely unwound, bistability will be reduced and the orientation of the director will change when the field is turned off. If the SmC*

phase is not aligned properly, the director and the tilt of the domains will not produce a uniform light shutter, as there will be multiple randomly distributed domains creating more than two switching states. To achieve proper alignment of a Smectic C* phase, it is common to cool down from the N* phase into the SmA* phase and then cool further into the Smectic C* phase. The process of cooling through the higher temperature phases allows the molecules to align their director uniformly throughout the cell and then the molecules will tilt in one direction creating a template for a uniform light switch.

The problem with this approach is the layer contraction that takes place upon cooling from the SmA to the SmC phase, which causes a buckling of the layers from a bookshelf geometry to a chevron geometry as shown in Figure 1-37.[59] When chevrons of opposite folds are formed, the voids create zigzag defects that decreases the optical quality of the film, as shown in Figure 1-38. Zigzag defects can be avoided by controlling the chevron fold direction with appropriate surface treatment and alignment conditions, but the chevron geometry in SSFLC displays inevitably results in lower birefringence, contrast and viewing angles relative to a bookshelf geometry. The SmC phase can also be aligned via a N to SmC transition in the presence of an applied field[60] but there are two main problems. In the case of a SmA-SmC transition the SmA phase aligns along the rubbing direction and then the director tilts in either direction. On the other hand, a N-SmC cooling sequence results in the formation of SmC layers with the director along the rubbing direction, which create one switching state with **n** along the rubbing direction being more stable than the other switching state with **n** forming an angle 2θ from the rubbing direction.

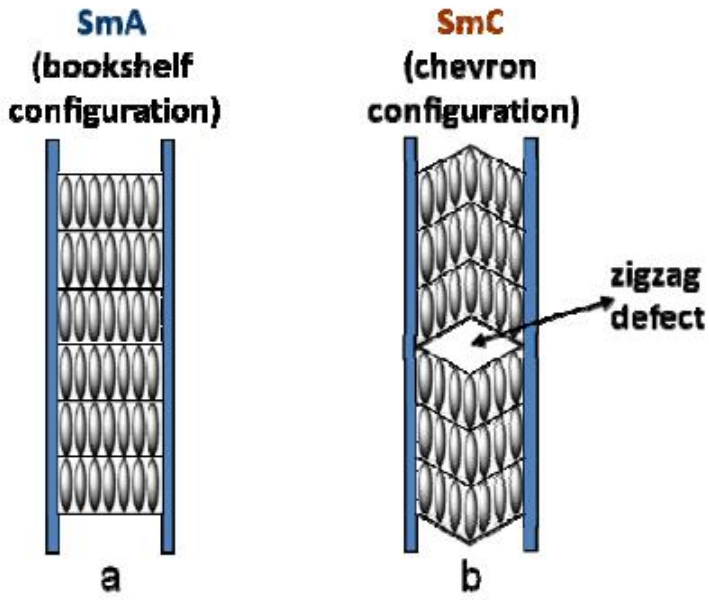

Figure 1-37: (a) A bookshelf aligned SmA* mesogen between two glass slides. (b) The SmA* phase transitioning to the SmC* phase and the formation of the chevron configuration.

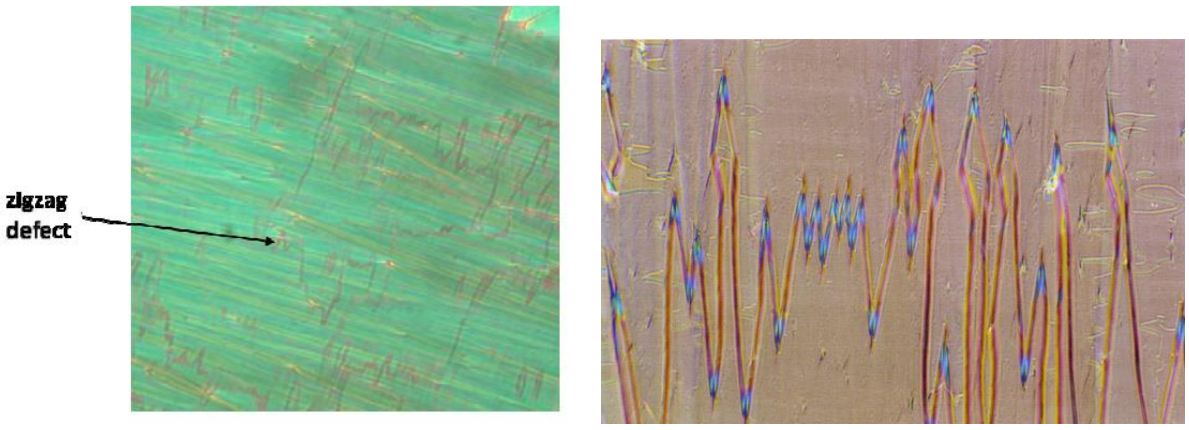

Figure 1-38: Polarized optical microscopy pictures of zigzag defects in the SmC* phase.

The disruption of bistability can be fixed through changing the cell design. In SmC-N material cells, each side (top and bottom) of the poly(imide) cell is rubbed at the switching tilt

angle with respect to each other.[61] In this case, when the mesogen is aligned with one side of the cell, it is not aligned with other, and thus bistability in these systems is restored as shown in Figure 1-39.

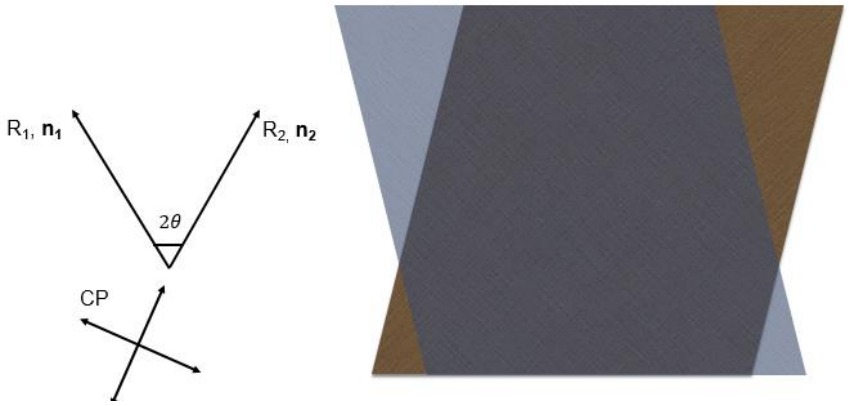

Figure 39: Diagram of a cell with two rubbing directions, R_1 and R_2, with the same surface coating on each cell surface, with the rubbing direction rotated by the switching angle (2θ) with respect to each other.

The second problem with SmC-N devices is that conventional SmC-N materials have very large tilt angles of 30 – 40 degrees, too far away from the switching angle of 22.5 degrees. The large tilt angle makes the SmC-N materials useless for display applications due to low optical contrast.[62]

1.8 'De Vries-like' Liquid Crystals

The layer contraction problem at the SmA-SmC transition in SSFLC devices has been at the forefront of research in the liquid crystal field. In conventional liquid crystals with a SmA to SmC phase transition, the layer contraction is around 7 to 10% of the layer spacing. While customization of properties in SSFLC devices can be achieved through careful consideration of dipole moment, molecular structure, and compound mixtures, solving the layer contraction

problem remains a significant challenge. One possible solution is found in so-called 'de Vries' liquid crystals which exhibit no layer contraction between the SmA and SmC phases. Perfect 'de Vries' liquid crystals have yet to be discovered but materials that approach 'de Vries' properties are known as 'de Vries-like' liquid crystals.[63] These materials undergo a SmA-SmC phase transition with a layer contraction of less than 1% while forming tilt angles on an order of 20-30 degrees. To understand how molecules can tilt in the absence of a layer contraction, a new model of the SmA-SmC transition is required.

1.8.1 Classic Rigid Rod Model

The classic rigid rod model is described by rigid spherocylinders which tilt uniformly by an angle θ upon the SmA-SmC phase transition, as shown in Figure 1-40(a). In this model, the layer spacing in the SmC phase d_c scales with the tilt angle θ, expressed by equation 1-8, where d_A is the layer spacing in the SmA phase. The layer contraction $(d_A\text{-}d_C)/d_A$ is expressed as a function of θ by equation 1-9.

$$d_C = d_A \cos\theta \qquad \text{(eq. 1-8)}$$

$$\frac{(d_A - d_C)}{d_A} = 1 - \cos\theta \qquad \text{(eq. 1-9)}$$

1.8.2 Diffuse Cone Model

The diffuse cone model provides an explanation for 'de Vries-like' behaviour.[63] According to the diffuse cone model, mesogens in the SmA phase are tilted but the azimuthal distribution is random. As a result, the system is still described as a SmA phase with the director **n** parallel to the layer normal **z** on the time average. At the SmA-SmC transition, the molecules lose their random azimuthal distribution within the layers and tilt in one direction, as shown in Figure 1-40(b). The SmA-SmC transition in the diffuse cone model has no layer contraction given that the molecules are already tilted in the SmA phase. Given that no perfect 'de Vries' material has been discovered and that contribution from rigid rod behavior is dependent on the tilt angle, a measure of 'de Vries' character was developed by Mochizuki *et al.* as the reduction factor R.[64,65]

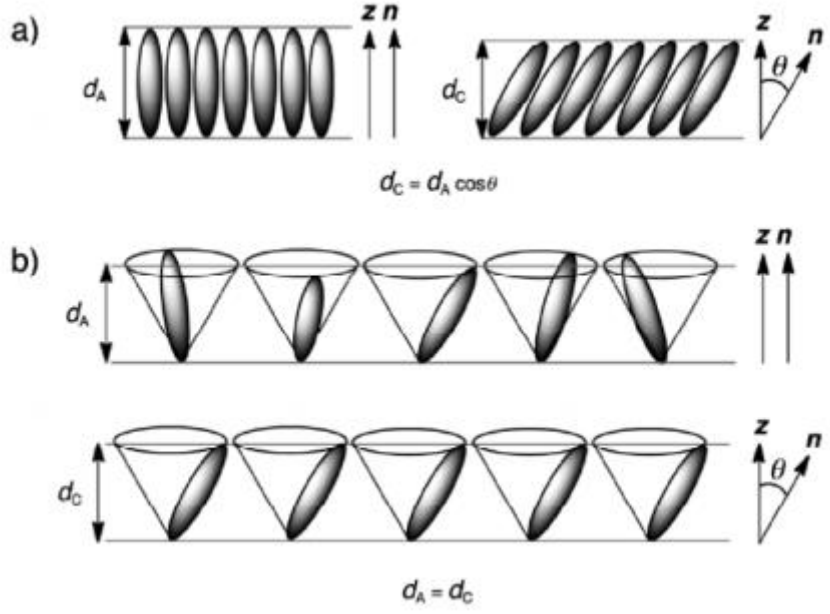

Figure 1-40: a) The classic spherocylinder rigid rod model. b) The diffuse cone model.

1.8.3 Reduction Factor

The reduction factor *R* (eq. 1.10) is a measure of 'de Vries-like' character defined as the ratio of the tilt angle $\delta(T)$ required to give a layer contraction d_C/d_{AC} at a temperature *T* below the SmA-SmC transition point T_{AC}, assuming a conventional model of hard spherocylinders, over the optical tilt angle θ_{opt}, which is measured by polarized optical microscopy.[64] According to this model, as *R* approaches 0, the material will be more 'de Vries-like'; as *R* approaches 1, the material follows the rigid rod model. Typically in 'de Vries-like' materials, there is a large negative thermal expansion in the SmA phase that continues into the SmC phase, which counter acts the large layer contraction normally observed on a SmA to SmC phase transition, and eventually restores the pre-SmA-SmC transition layer spacing.

$$R = \frac{\delta(T)}{\theta_{opt}(T)} = \frac{\cos^{-1}\left[\frac{d_C(T)}{d_{AC}}\right]}{\theta_{opt}(T)} \qquad \text{(eq. 1-10)}$$

1.8.4 Layer Spacing *d*, Orientational Order Parameter S_2, and Effective Layer Spacing L_{eff}

In the investigation of 'de Vries-like' materials, the orientational order parameter S_2 and the effective length (L_{eff}) of the liquid crystals are important parameters. The layer spacing of smectic phases is measured by small-angle X-ray scattering (vide infra), and allows for the characterization of 'de Vries-like' materials by measuring the difference between the layer spacing

at the SmA-SmC phase transition and layer spacing in the SmC phase. Typically, the layer contraction is reported at ten degrees below the SmA-SmC phase transition (T - T_{AC} = -10 K).[39] Mesogens in smectic phases can fluctuate between smectic layers, and also can fluctuate randomly about the director **n**. The latter is quantified by the orientational order parameter S_2. In conventional SmC and SmA mesophases, the orientational order parameter is relatively high at 0.7-0.8, whereas in most 'de Vries-like' liquid crystals, S_2 in the SmA phase has been reported to be in the range of 0.4 and 0.65 and increases to approximately 0.7-0.8 upon transition to the SmC phase.[37,39] The orientational order parameter can also be used to determine the effective length of the molecules within each layer. The effective length $L_{eff}(T)$, as expressed in equation 1-11 where $d(T)$ is the layer spacing at temperature T, and $S_2(T)$ is the orientational order parameter at temperature T, is a measure of the layer spacing if the mesogen has perfect orientation order (S_2 = 1). The effective length can be used to assess the degree of nanosegregation and bilayer intercalation in a smectic phase.

$$L_{eff}(T) = 3d(T)/(S_2(T) + 2) \qquad \text{(eq. 1-11)}$$

1.8.5 X-ray Scattering Experiments

Powder X-ray scattering is used to obtain a wide variety of mesomorphic data. The technique allows for the determination of smectic layer spacing, average intermolecular distance, X-ray tilt, and orientational order parameters. The analysis of X-ray scattering is based on Bragg's law, as described in Figure 1-41. Bragg's law describes the situation where X-ray scattering is

constructively interfering; it is expressed by equation 1-12, where λ is the wavelength of the X-ray beam, d is the distance between two molecules, and θ is the angle of incidence.

$$n\lambda = 2d \sin\theta \qquad \text{(eq. 1-12)}$$

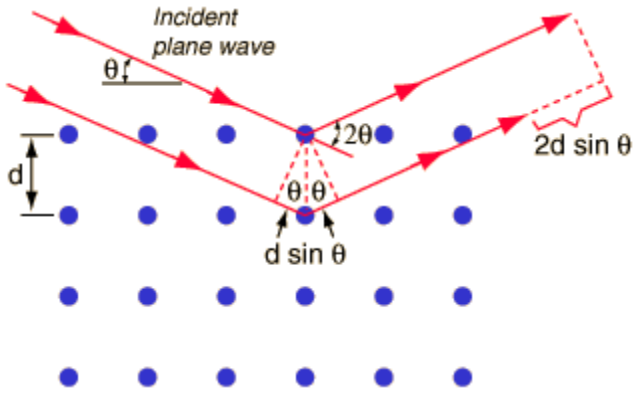

Figure 1-41: A pictorial definition of Bragg's law (equation 1-12).[66]

There are two types of powder X-ray scattering experiments, 1-dimensional (1D) and 2-dimensional (2D). 1D experiments are broken into small-angle X-ray scattering (SAXS) and wide-angle X-ray scattering (WAXS). In SAXS experiments, the layer spacing can be accurately measured using Bragg's law based on the Bragg's angle of the first order peak, as shown in Figure 1-42.[37]

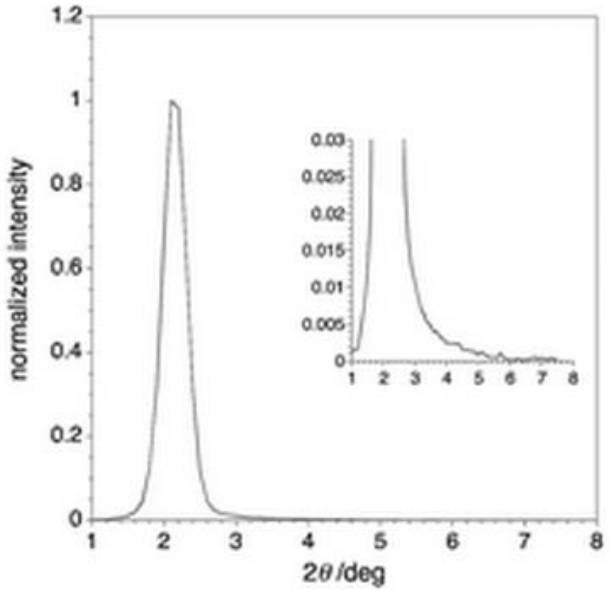

Figure 1-42: Representation of unprocessed small-angle X-ray scattering experiment data for **QL19-6.**[37]

In WAXS experiments, the average intermolecular distance can be obtained. In liquid crystals, the intermolecular distance is typically seen as a large Gaussian distributed peak in which the average intermolecular distance can be obtained by analyzing the peak maximum.[46] In 2D X-ray diffraction experiments, where the sample is aligned in a monodomain, the intermolecular distance can be more accurately probed and the wide-angle data allows one to determine the orientation of the director **n** relative to the layer normal, and measure the X-ray tilt of the SmC phase, as shown in Figure 1-43.[46] Furthermore, the examination of the shape of the wide-angle reflection of the X-ray tilt is related to the orientational order parameter S_2, as well as the effective length L_{eff} as previously described in section 1.8.4.

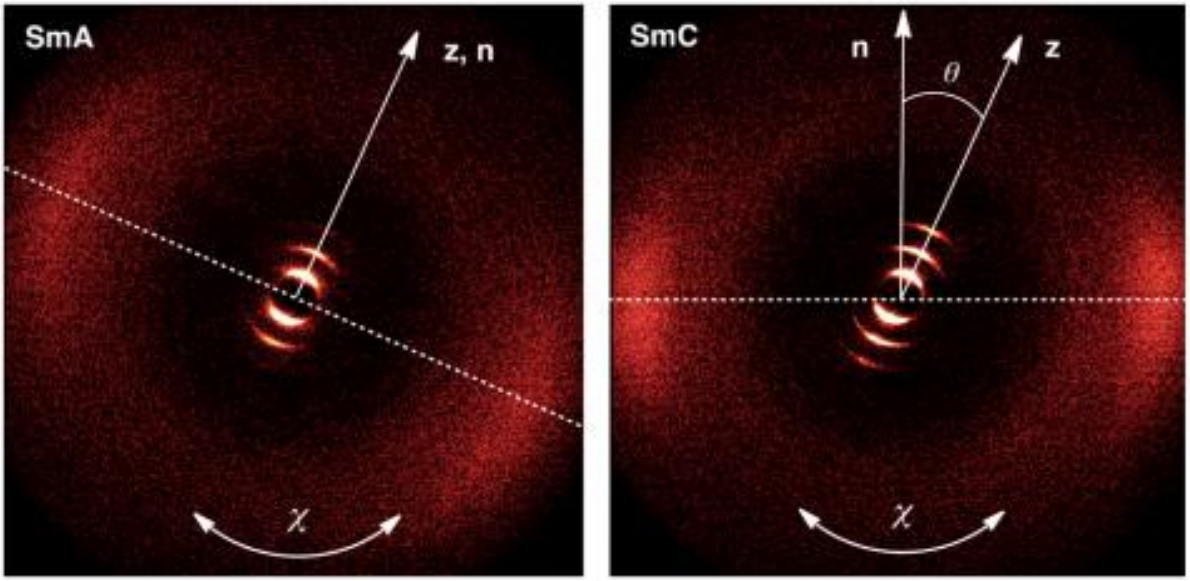

Figure 1-43: 2D X-ray scattering patterns of **QL16-6** in the SmA phase 72 degrees Celsius and in the SmC phase at 42 degrees Celsius.[46]

1.8.6 Known 'de Vries-like' Materials

While many 'de Vries-like' materials have been synthesized, as shown in Figure 1-44, the structural determinants of this effect are still not fully understood. The layer contraction of these materials is much less than those exhibited by conventional liquid crystals such as **DOBAMBC**, as shown in Figure 1-45.[67]

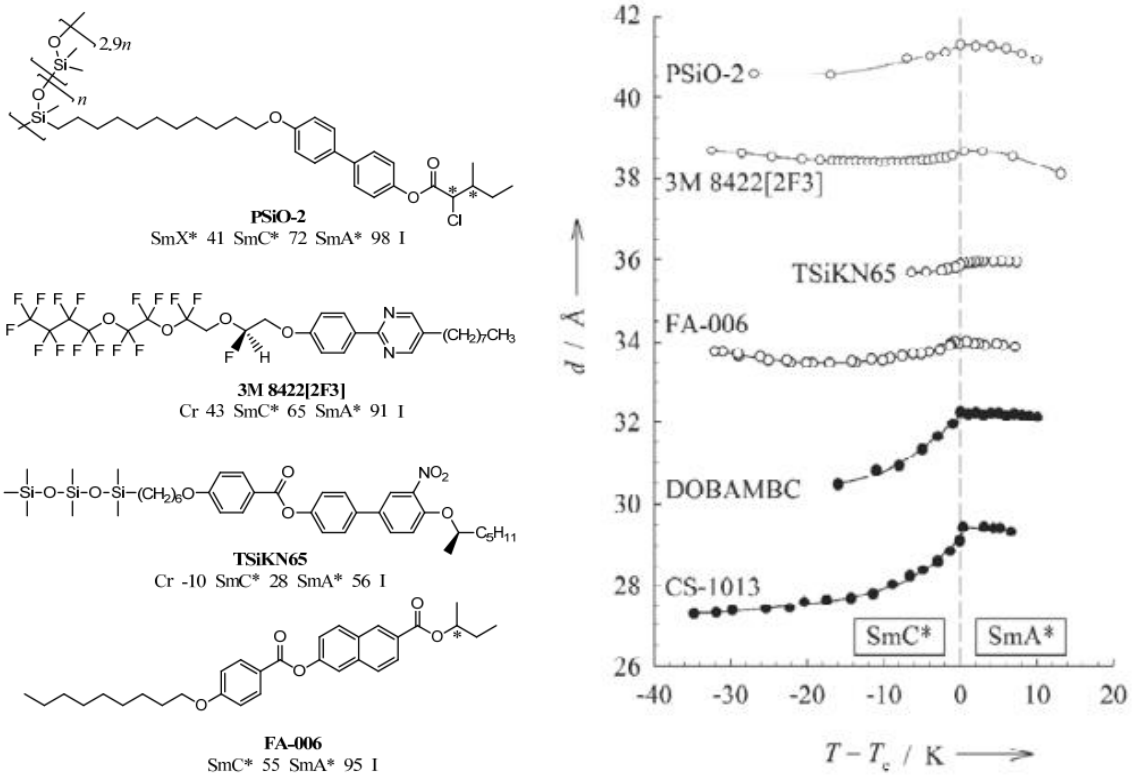

Figure 1-44: (a) Chemical structures of known 'de Vries-like' materials. (b) SAXS layer spacing *d* vs reduced temperature $T - T_c$ for several 'de Vries-like' materials in relation to conventional material **DOBAMBC** and conventional mixture **CS-1013**. [67]

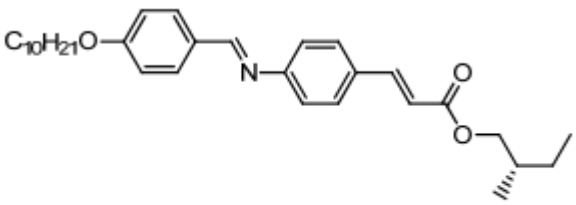

DOBAMBC
Cr 76 SmC* 95 SmA 117 I

Figure 1-45: The chemical structure of **DOBAMBC**, a conventional liquid crystal material with a SmA-SmC transition.

In previous years, the Lemieux group developed a design strategy for liquid crystals based on achieving a balance between SmA and SmC promoting elements. For example, materials such as **QL6** and **QL16**, shown in Figure 1-46, feature a carbosilane end-group that promotes a SmC phase by virtue of nanosegregation, and a chloro-terminated alkyl chain or a 5-phenylpyrimidine core as smectic A promoting elements. *R* values for **QL6-6** and **QL16-6** are 0.20 and 0.17, respectively, and the corresponding layer contractions are 0.4% and 0.5%, respectively.[37,39,46]

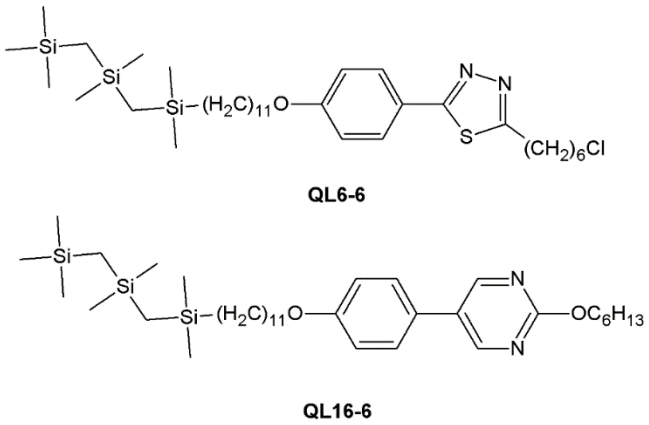

Figure 1-46: Molecular structures of **QL6-6** and **QL16-6**[37,39]

In a paper by Mulligan *et al.*, a homologous series of carbosilane mesogens were synthesized, in which the length of the carbosilane end-group was varied, as shown in Figure 1-47.[37] The paper suggests that 'de Vries-like' properties strongly depend on the degree of nanosegregation and the lamellar ordering imposed by the carbosilane end-group, which was accomplished through the synthesis of 5-phenyl-1,3,4-thiadiazole mesogens with chloro terminated alkoxy chains (**QL13-*n***, **QL18-*n***, and **QL19-*n***). The data shows that increasing the length of the nanosegregating carbosilane end-group, from monocarbosilane to tricarbosilane, 'de Vries-like' character increases and can be measured by the reduction factor, *R*, as shown by the

change in layer spacing in Figure 1-47. The decrease in reduction factor is consistent with the increase in nanosegregation and quality of lamellar ordering in these mesogens.[37]

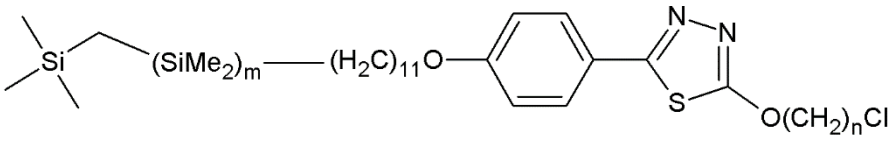

m = 2 : **QL13-n**
m = 1 : **QL18-n**
m = 0 : **QL19-n**

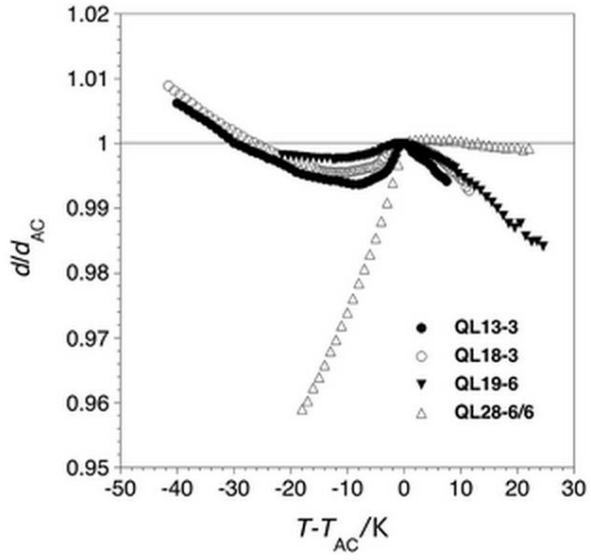

Figure 1-47: Small-angle X-ray scattering layer spacing vs. reduced temperature data for **QL13-3**, **QL18-3**, **QL19-6** and **QL28-6/6**[37]

Smectic monodomain 2D X-ray scattering experiments show that the orientational order parameter S_2 increases with increased nanosegregation of the carbosilane end-group, as shown in Figure 1-48. While the change in S_2 between the parent mesogen, 2-(6-chlorohexyloxy)-5-(4-hexyloxyphenyl)-1,3,4-thiadiazole (**QL28-6/6**) and the monocarbosilane mesogen (**QL19-6**) is relatively small, S_2 decreases substantially between **QL19-6** and dicarbosilane mesogen (**QL18-**

3), with a corresponding increase in end-group nanosegregation. The increase in S_2 in these mesogens supports the hypothesis that 'de Vries-like' behavior in these materials arises from a combination of high lamellar order and low orientational order.[37]

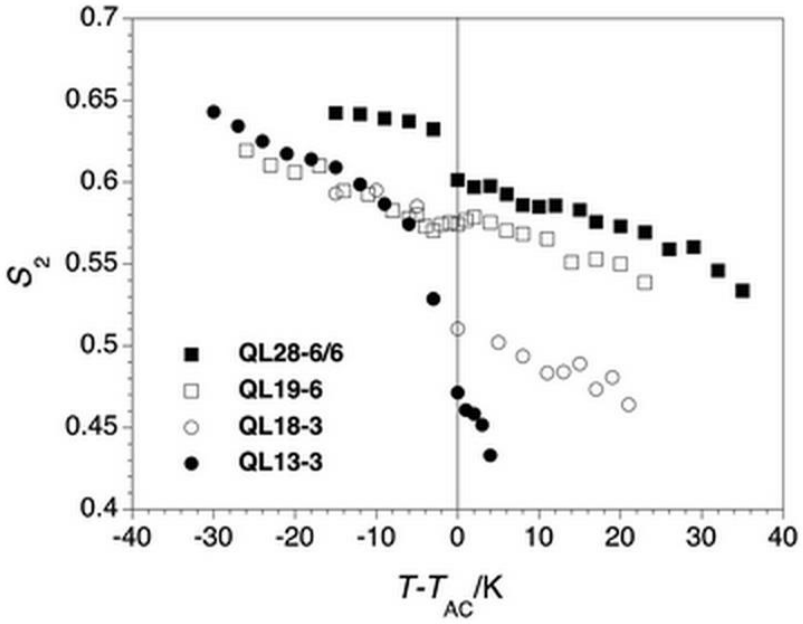

Figure 1-48: Orientational order parameter calculated by fitting intensity of χ from 2D X-ray scattering experiments of **QL13-3, QL18-3, QL19-6** and **QL28-6/6**.[37]

1.9 Project Outline

The aim of this project is to create new end-groups to promote 'de Vries-like' behavior in liquid crystals. It has been shown that nanosegregation is critical for many formations of 'de Vries-like' mesogens. We investigated nanosegregation as a means of promotion of 'de Vries-like' behaviour.

In the first section, we investigated phenoxy-terminated end-groups as a means to promote nanosegregation, as well as ‘de Vries-like’ behavior in 2-phenylpyrimidine core liquid crystals. In the second section, we investigated tuning phenoxy-terminated end-group mesogens mesophasic behehaviour through the use of substituent groups. The fluoro substituent was used in these experiments due to its limited steric change from the parent compound.

In the next section we investigated **QL23-8/8-2,6F$_2$** as a possible ‘de Vries-like’ compound. We also investigated the origins of the nematic phase in phenoxy-terminated mesogens. In the following section, we investigate the **QL22-8/8-2,6F$_2$** and **QL29-8/8-2,6F$_2$** for their possible use in SSFLC devices. In the next section, we investigate mixtures of phenoxy-terminated compounds in hopes of promoting ‘de Vries-like’ behaviour, as well as tuning mesomorphic properties of liquid crystals.

1.10 References

(1) Reinitzer, F. *Monatshefte fuer Chemie* **1888**, *9*, 421.

(2) Chaudhari, A.; Woudenber, T.; Albin, M.; Goodson, K. *Journal of Microelectromechanical Systems* **1998**, *7* (4), 345.

(3) Deniset-Besseau, A.; Peixoto, P. D. S.; Mosser, G.; Schanne-Klein, M.-C. *Optics Express* **2010**, *18* (2), 1113 .

(4) Carrasco-Orozco, M.; Tsoi, W.; O’Neill, M.; Aldred, M.; Vlachos, P.; Kelly, S. *Advanced Materials* **2006**, *18*, 1754.

(5) Chen, Y.; Ma, P.; Gui, S. *BioMed Research International*, **2014**, 1.

(6) Gray, G.; Harrison, K. J.; Nash, J. A. *Electronics Letters* **1973**, *9*, 130.

(7) Tiddy, G. J. T. *Physics Reports* **1980**, *57* (1), 1.

(8) Hird, M. *Chemical Society Reviews* **2007**, *36*, 2070.

(9) Osman, M. A. *Molecular Crystals Liqiud Crystals* **1985**, *128*, 45.

(10) Demus, D.; Demusc, H.; Zaschke, H.,. *Flussige Kristalle in Tabellen*; Deutscher Verlag für Grundstoffindustrie: Leipzig, 1974.

(11) Demus, D.; Goodby, J.; Gray, G.; Spiess, H.; Vill, V. *Handbook of Liquid Crystals, Volume 2A: Low Molecular Weight Liquid Crystals I*; 1998.

(12) Kuczyński, W.; Żywucki, B.; Małecki, J. *Molecular Crystals and Liquid Crystals* **2002**, *381* (1), 1.

(13) McMillan, W. L. *Physical Review A: Atomic, Molecular, and Optical Physics* **1973**, *8*, 1921.

(14) Wulf, A. *Physical Review A: Atomic, Molecular, and Optical Physics* **1975**, *11*, 365.

(15) Reddy, R. A.; Zhu, C.; Shao, R.; Korblove, E.; Gong, T.; Shen, Y.; Garcia, E.; Glaser, M. A.; MacLennan, J. E.; Walba, D. M. *Science* **2011**, *332*, 72.

(16) Gray, G. W.; Goodby, J. W. *Smectic Liquid Crystals: Textures and Structures*; Heyden 1984.

(17) Goodby, J. W.; Gray, G. W.; McDonnell, D. G. *Molecular Crystals and Liquid Crystals* **1977**, *34*, 183.

(18) Rupar, I.; Mulligan, K. M.; Roberts, J. C.; Nonnenmacher, D.; Giesselmann, F.; Lemieux, R. P. *Journal of Materials Chemistry C: Materials for Optical and Electronic Devices* **2013**, *1*, 3729.

(19) Hartley, C. S.; Kapernaum, N.; Roberts, J. C.; Giesselmann, F.; Lemieux, R. P. *Journal of Materials Chemistry* **2006**, *16*, 2329.

(20) Lin, H.; Lai, L; Hsieh, W. P.; Huang, W. *Liquid Crystals* **1997**, *22* (5), 661.

(21) Hu, N.; Shao, R.; Zhu, C.; Shen, Y.; Park, C.; Korblova, E.; Guerra, C.; Rego, J. A.; Hexemer, A.; Clark, N. A.; Walba, D. M. *Chemical Science* **2014**, *5* (5), 1869.

(22) Song, Q.; Nonnenmacher, D.; Giesselmann, F.; Lemieux, R. P. *Journal of Materials Chemistry C: Materials for Optical and Electronic Devices* **2013**, *1*, 343.

(23) Hegmann, T.; Meadows, M. R.; Wand, M. D.; Lemieux, R. P. *Journal of Materials Chemistry* **2004**, *14*, 185.

(24) Gray, G. W.; Hird, M.; Lacey, D. *Molecular Crystals Liqiud Crystals* **1985**, *123*, 185.

(25) Gray, G. W.; Hird, M.; Toyne, K. J. *Molecular Crystals Liqiud Crystals* **1991**, *204*, 43.

(27) Balkwill, P.; Bishop, D.; Pearson, A.; Sage, I. *Molecular Crystals Liqiud Crystals* **1985**, *123*, 1.

(26) Bergt, K. PhD Thesis, **1925**.

(28) Pavluchenko, A. I.; Smirnova, N. I.; Petrov, V. F.; Fialkov, Y. A.; Shelyazhenko, A.; Vagupolsky, S. V. *Molecular Crystals Liqiud Crystals* **1991**, *209*, 225.

(29) Kirsch, P. *Modern Fluoroorganic Chemistry*; Wiley-VCH: Weinheim, 2004.

(30) Gray, G. W.; Jones, B. *Journal of the Chemical Society* **1954**, *76*, 2556.

(31) Kelly, S. M.; Schad, H. *Helvetica Chimica Acta* **1984**, *67*, 1580.

(32) Schad, H.; Kelly, S. M. *Journal of Chemical Physics* **1984**, *81*, 1514.

(33) Chan, L.K.M.; Gray, G. W.; Lacey, D.; Toyne, K. J. *Molecular Crystals Liqiud Crystals* **1988**, *158B*, 209.

(34) Chan, L.K.M.; Gray, G. W.; Lacey, D. *Molecular Crystals Liqiud Crystals* **1985**, *123*, 185.

(35) Senthil, S.; Rameshbabu, K.; Wu, S.-L. *Journal of Molecular Structure* **2006**, *783* (1-3), 215.

(36) Kouji, O.; Makoto, U.; Shinichi, S.; Kautoshi, M. 5-Alkoxy-2-(4-alkoxyphenyl)pyrimidine, method for its preparation and use. 0313991A2, 1989.

(37) Mulligan, K. M.; Bogner, A.; Song, Q.; Shubert, P. J.; Giesselmann, F.; Lemieux, R. P. *Journal of Materials Chemistry C* **2014**, *2*, 8270.

(38) Song, Q.; Bogner, A.; Giesselmann, F.; Lemieux, R. P. *Chemical Communications* **2013**, *49*, 8202.

(39) Song, Q.; Nonnenmacher, D.; Giesselmann, F.; Lemieux, R. P. *Journal of Materials Chemistry C* **2013**, *1*, 343.

(40) Song, Q.; Nonnenmacher, D.; Giesselmann, F.; Lemieux, R. P. *Chemical Communications* **2011**, *47* (16), 4781.

(41) Mandle, R. J.; Davis, E. J.; Voll, C.-C. A.; Lewis, D. J.; Cowling, S. J.; Goodby, J. W. *Journal of Materials Chemistry C* **2015**, *3*, 2380.

(42) Ibn-Elhaj, M.; Skoulios, A.; Guillon, D.; Newton, J.; Hodge, P.; Coles, H. J. **1995**, *19*, 373.

(43) Tschierske, C. *Isreal Journal of Chemistry* **2012**, *52*, 935.

(44) Goodby, J. W.; Gray, G. W. *Journal de Phsique Colloques* **1976**, *37* (C3), 17.

(45) Imrie, C. T.; Henderson, P. A. *Chemical Society Reviews* **2007**, *36*, 2096.

(46) Schubert, C. P.; Bogner, A.; Porada, J. H.; Ayub, K.; Andrea, T.; Giesselmann, F.; Lemieux, R. P. *Journal of Materials Chemistry C* **2014**, *2*, 4581.

(47) Walba, D. M.; Vohra, R.T.; Clark, N.A.; Handschy, M. A.; Xue, J.; Parmar, D. S.; Lagerwall, S. T. *Journal of the American Chemical Society* **1986**, *108*, 7424.

(48) Walba, D. M.; Mallouck, T. E. In *In Advances in the synthesis and Reactivity of Solids*; JAI Press, Ltd: Greenwich, CT, 1991; Vol. 1, pp 173.

(49) Samulski, E. T.; Dong, R. Y. *Journal of Chemical Physics* **1982**, *77* (10), 5090.

(50) Samulski, E. T. *Israel Journal of Chemistry* **1983**, *23* (3), 597.

(51) Clark, N. A.; Lagerwall, S. T. *Applied Physics Letters* **1980**, *36*, 899.

(52) Meyer, R.B.; Liebert, L.; Strzelecki, L.; Keller, P. *Journal de Physique, Lettres* **1975**, *36*, L69.

(53) Abramowitz, M.; Davidson, M. W., http://www.olympusmicro.com/primer/lightandcolor/birefringence.html. Date Access: May 25 2015.

(54) Brochard., F.; Leger, L.; Meyer, R.B. *Journal de Physique Colloques* **1975**, *36* (C1), 209.

(55) Garoff, S.; Meyer, R.B. *Physical Review Letters* **1977**, *38*, 848.

(56) Garoff, S.; Meyer, R. B. *Physical Review A* **1979**, *19*, 338.

(57) Glogarova, M.; Destrade, C.; Marcerou, J. P.; Bonvent, J. J.; Nguyen, H. T. *Ferroelectrics* **1991**, *121*, 285.

(58) Kalmykov, Y. P.; Vij, J. K. *Liquid Crystals* **1994**, *17* (5), 741.

(59) Rieker, T. P.; Clark, N. A.; Smith, G. S.; Parmer, D. S.; Sirota, E. B.; Safinya, C. R. *Physical Review Letters* **1987**, *59*, 2658.

(60) Hotta, A.; Hasegawa, R.; Takatoh, K. *Japanese Journal of Applied Physics* **2004**, *43* (9A), 6243.

(61) Chen, H-M. P.; Lin, C-W.; Invited paper Liquid Crystals XIV; Department of Photonics and Display Institute, **2010**.

(62) Cluzeau, P.; Ismaili, M.; Anakkar, A.; Foulon, M.; Babeau, A.; Nguyen, H. T. *Molecular Crystals Liquid Crystals* **2001**, *362*, 185.

(63) De Vries, A. *Journal of Chemical Physics* **1979** *70*, 2705.

(64) Takanishi, Y.; Ouchi, Y.; Takezoe, H.; Fukuda, A.; Mochizuki, A.; Nakatsuka, M. *Japanese Journal of Applied Physics* **1990**, *29* (6), L984.

(65) Radcliffe, M. D.; Brostrom, M. L.; Epstein, K. A.; Rapparport, A. G.; Thomas B. N.; Clark, N. A. *Liquid Crystals* **1999**, *26*, 789.

(66) Bragg's Law Picture http://hyperphysics.phy-astr.gsu.edu/hbase/quantum/bragg.html. Accessed June 15, 2015.

(67) Lagerwall, S. T.; Giesselmann, F. *ChemPhysChem* **2006**, *7*, 20.

Chapter 2: The Effect of Phenoxy End-group in 5-Alkoxy-2-(4-alkoxyphenyl)pyrimidine Liquid Crystals.

Previous work has shown that nanosegregation is crucial to the formation of 'de Vries-like' liquid crystals.[1,2] In this study, we sought to expand the library of 'de Vries-like' materials by evaluating a new class of nanosegregating end-groups. In order to provide a foundation for our investigation of aromatic end-groups as nanosegregating units in smectogenic materials, we synthesized two sterically equivalent series of phenoxy-terminated 5-alkoxy-2-(4-alkoxyphenyl)pyrimidine liquid crystals **QL11-*m/n*** and **QL12-*m/n***, where m+n = 16. Not only do these two series allow us to determine if the phenoxy end-group can be used as a nanosegregating element for 'de Vries-like' liquid crystals, they also allow for the investigation of the mesomorphic properties of phenoxy-terminated mesogens in terms of proximity of the end-group to the core.

The phenylpyrimidine core has been used as a scaffold in many FLC mixtures and thus provides a useful benchmark for evaluating the impact of the aromatic end-group as a structural modifier of conventional FLC components.[3] Unlike the more common homologous series in which the length of a mesogen is gradually increased by adding methylene units to one or both alkyl chain(s), mesogens in sterically equivalent series have the same molecular length but vary in terms of the relative lengths of the alkyl chains. Such a series make possible the investigation of the interplay between core-core interactions and the effect of the phenoxy end-groups on lamellar ordering.

2.1 Synthesis and Characterization

The two series **QL11-*m/n*** and **QL12-*m/n*** were prepared by sequential alkylations of commercially available 2-(4-hydroxyphenyl)pyrimidin-5-ol with appropriate 1-bromoalkane and

phenoxy terminated 1-bromoalkane via nucleophilic substitution reactions, or with the appropriate alkan-1-ol and phenoxy-terminated alkan-1-ol via Mitsunobu reactions, as shown in Scheme 2-1. The latter approach was preferred by virtue of shorter reaction times and higher yields. The new compounds were recrystallized from acetonitrile and hexanes, and their mesomorphic properties were analyzed by polarized optical microscopy and differential scanning calorimetry. Phase transition temperatures are listed in Table 2-1.

Table 2-1: Phase transition temperatures (°C) and enthalpies of transition (KJ mol^{-1}, in parenthesis) measured by DSC for compounds **QL11-*m/n*** and **QL12-*m/n***

Compound	Cr		Cr′		SmC		SmA		N		I
QL11-4/12	•	83 (42)					•	78 (8.5)[a]			•
QL11-5/11	•	74 (48)					•	70 (8.2)[a]			•
QL11-6/10	•	86 (56)					•	85 (12)[a]			•
QL11-7/9	•	72			•	61 (<0.1)[a,b]	•	76 (48)[c]			•
QL11-8/8	•	79 (49)			•	80 (<0.1)[b]	•	95 (13)			•
QL11-9/7	•	81			•	75 (<0.1)[a,b]	•	84 (71)[c]			•
QL11-10/6	•	85 (2.0)	•	95 (44)	•	83 (<0.1)[a,b]	•	106 (15)			•
QL11-11/5	•	80 (47)					•	86 (8.5)			•
QL11-12/4	•	127 (68)					•	116 (11)[a]			•
QL12-4/12	•	83 (7.7)	•	88 (45)							•
QL12-5/11	•	80 (65)									•
QL12-6/10	•	92 (61)									•
QL12-7/9	•	79 (12)	•	82 (50)							•
QL12-8/8	•	93 (65)					•	81 (1.0)[a]	•	86 (3.5)[a]	•
QL12-9/7	•	72 (41)									•
QL12-10/6	•	87 (48)			•	84 (<0.1)[a,b]	•	93 (8.4)			•
QL12-11/5	•	80 (58)					•	76 (8.3)[a]			•
QL12-12/4	•	96 (52)			•	100 (<0.1)[b]	•	101 (11)			•

Notes: [a]Monotropic mesophase.
[b]Transition temperature measured by polarized microscopy.
[c]Total enthalpy for both transitions due to incomplete resolution of the peaks.
A bullet indicates the presence of the phase shown in the column heading (Cr, Cr', SmC, SmA, N, I).

The SmA phase formed by some of the isomers in series **QL11-*m/n*** and **QL12-*m/n*** was identified by the formation of characteristic fan textures and dark homeotropic domains on cooling from isotropic liquid, whereas the SmC phase was identified on cooling from the SmA phase by the appearance of weakly birefringent Schlieren textures in the homeotropic domains together with

the conversion of fan textures to characteristic broken fan textures, as shown in Figure 2-1(a) and (b).

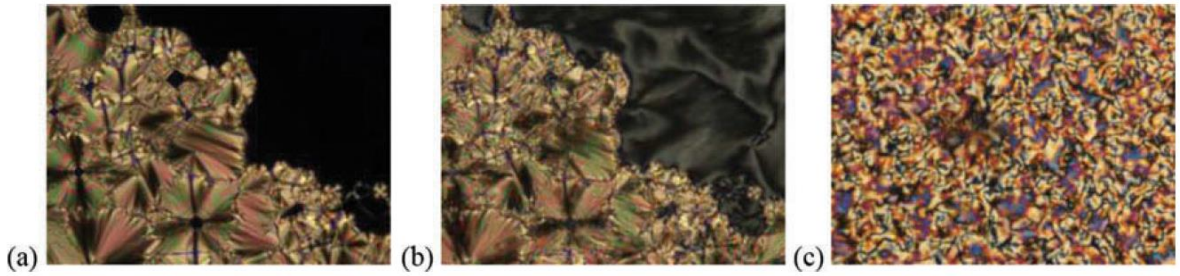

Figure 2-1: Polarized photomicrographs viewed on cooling from the isotropic phase of (a) **QL11-10/6** at 99°C (SmA), (b) **QL11-10/6** at 75°C (SmC) and (c) **QL12-8/8** at 85°C (N).

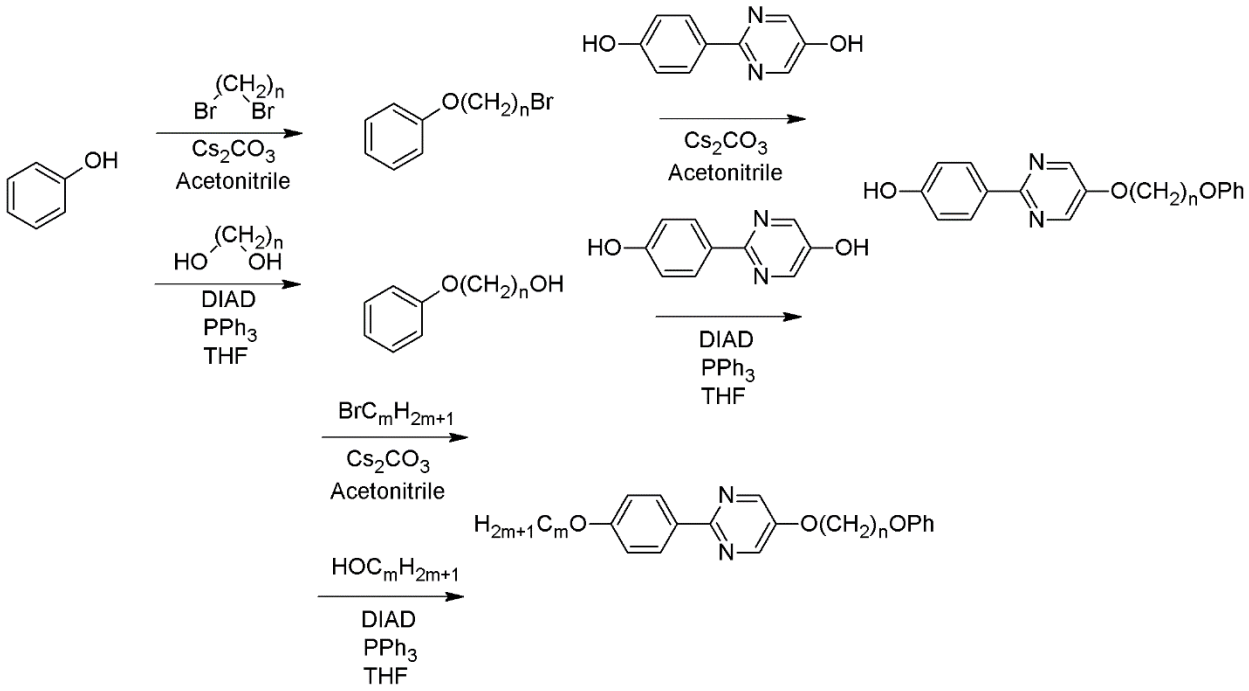

Scheme 2-1: Synthesis of **QL11-*m/n***.

The two sterically equivalent series exhibit strikingly different mesomorphic properties, as shown in Figure 2-2. Compounds in the **QL11** series, with the phenoxy terminated alkoxy chain tethered to the pyrimidine ring, exhibit a richer mesomorphism, with five isomers forming

enantiotropic smectic phases, and all nine isomers showing monotropic smectic phases on cooling. Within the five isomers that exhibit enantiotropic phases, four of the compounds (n = 6-9) have a SmC-SmA transition. On the other hand, only two isomers in series **QL12-*m/n*** form enantiotropic smectic phases, and five isomers show no mesomorphic properties at all – two isomers (**QL12-10/6** and **QL12-12/4**) form SmA and SmC phases on cooling and another (**QL12-8/8**) forms nematic and SmA phases on cooling.

On further examination of the mesomorphic properties of these two sterically equivalent series, a strong odd-even effect of the SmA-Iso transition temperature is present in the **QL11** series. This pronounced odd-even effect is consistent with those previously observed with phenyl-

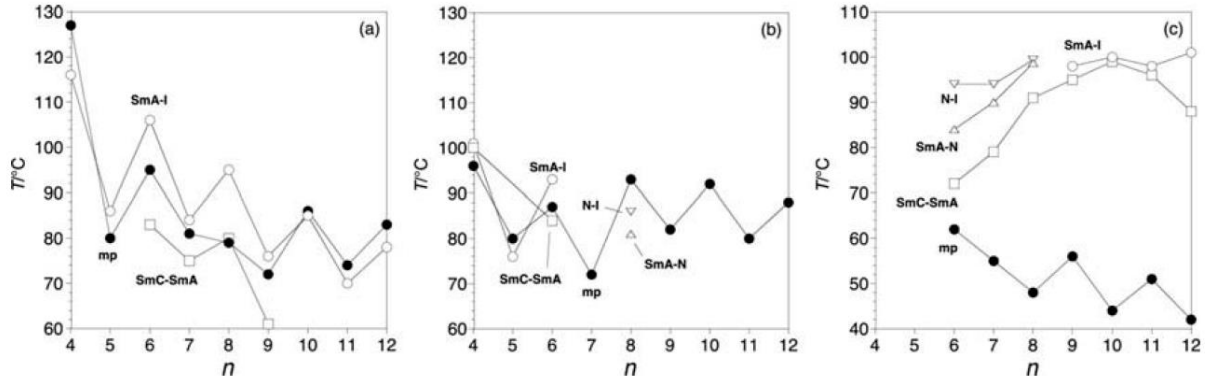

Figure 2-2: Phase transition temperatures as a function of the chain length *n* in the sterically equivalent series (a) **QL11-*m/n***, (b) **QL12-*m/n*** and (c) **2PhP-*m/n***: melting point (●), SmC-SmA (□), SmA-isotropic (○), SmA-nematic (Δ) and nematic-isotropic (▽) transitions. The data for **2PhP-*m/n*** were obtained from the patent literature.

terminated mesogens.[4,5] A comparison of the mesomorphic properties in series **QL11-*m/n*** and **QL12-*m/n*** with those of the parent isomers **2PhP-*m/n*** (*m* + *n* = 16) shows that the addition of a phenoxy end-group at either end of the 5-alkoxy-2-(4-alkoxyphenyl)pyrimidine scaffold causes a significant increase in melting point and inhibits – at least partially – the mesomorphism of these materials. In most cases the broad enantiotropic SmC phase formed by the parent isomers, **2PhP-**

m/n, is completely suppressed by the addition of a phenoxy end-group. Interestingly, of all the chain length combinations in the two series, only **QL11-10/6** and **QL12-10/6** have similar mesomorphic properties. In these experiments, it is apparent that the three pairs of isomers in which the phenoxy end-group is most distant from the core (n = 10-12) are also similar by virtue of their lack of mesomorphic properties; the **QL11** isomers only form narrow monotropic smectic mesophases, whereas the **QL12** isomers do not show mesomorphic behavior. The second-order SmA-SmC phase transitions were not detected by DSC and the transition temperatures were measured by POM on cooling based on the appearance of the Schlieren textures. The nematic phase formed by **QL12-8/8** produced a Schlieren texture on cooling from the isotropic liquid phase, as shown in Figure 2-1(c), which turned into a fan texture and homeotropic domains upon transition to the SmA phase.

2.2 X-ray Scattering Experiments

In order to investigate the smectic layer structure formed by these compounds, we carried out small-angle X-ray scattering (SAXS) and monodomain 2D X-ray scattering analyses on the representative materials **QL11-10/6** and **QL12-10/6**, which both form an enantiotropic SmA phase and monotropic SmC phase. The smectic layer spacing *d* was derived from the first-order scattering peak at small-angle according to Bragg's law (eq. 1-12) and plotted as a function of temperature *T* on cooling from the isotropic liquid phase. As shown in Figure 2-3, we were able to measure *d*(*T*) on cooling in both the SmA and SmC phases for **QL11-10/6**, but only in the SmA phase for **QL12-10/6** as the material crystallized before the SmA-SmC phase transition temperature was reached. The layer spacing in the SmA phase is the same for the two isomers within experimental error (±0.1 Å) and does not vary significantly with temperature; the average *d* value of 34.0 Å is 2.3 Å shorter than the length L of a fully extended molecular model (Figure

2-7) minimized at the B3LYP/6-31G* level. Such a discrepancy is normally ascribed to orientational fluctuations (vide infra). The decrease in layer spacing on cooling **QL11-10/6** into the tilted SmC phase results in a maximum layer contraction of 1.0% at 10 K below the SmA-SmC transition temperature ($T - T_{AC} = -10$ K), which is normally found to be evidence of a 'de Vries-like' liquid–crystal (vide infra).

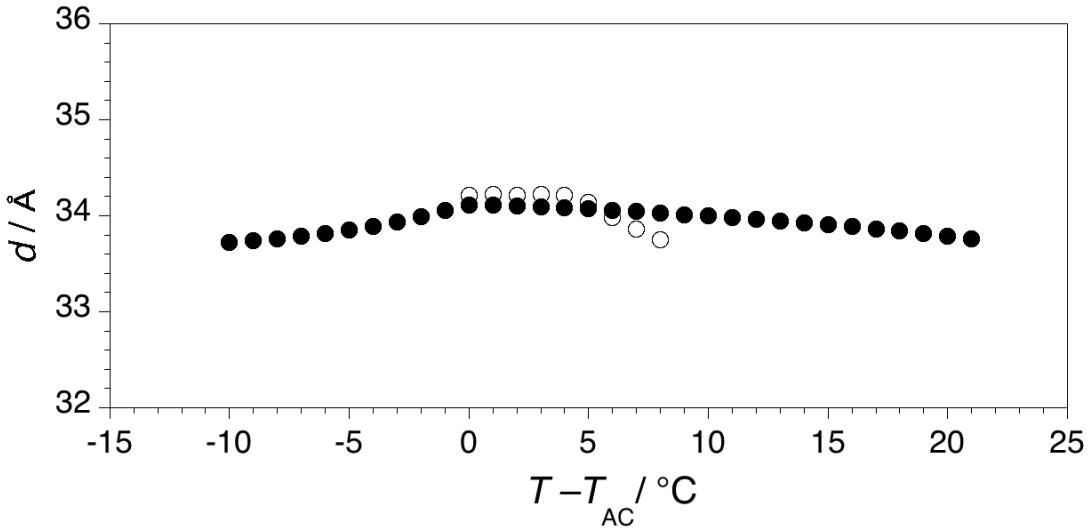

Figure 2-3: Smectic layer spacing d versus reduced temperature $T - T_{AC}$ for **QL11-10/6** (●) and **QL12-10/6** (○).

In order to model the SmA layer formed by **QL11-10/6** and **QL12-10/6**, the effective length L_{eff} of the molecules forming the smectic layers was derived from the layer spacing d and the orientational order parameter S_2 according to equation (1-1). S_2 values of a smectic monodomain were measured as a function of T by 2D X-ray scattering. A 2D X-ray scattering pattern of compound **QL12-10/6** obtained from a single SmA domain is shown in Figure 2-4. A monodomain was obtained by cooling from an isotropic liquid to a smectic phase and moving the X-ray beam to probe the sample for a suitable domain by analyzing the spectra visually to find the

most condensed small-angle X-ray pattern, as shown along **z** in Figure 2-4a. After locating a suitable monodomain, the scan time is increased to get a precise spectra, as shown in Figure 2-4a.

a) 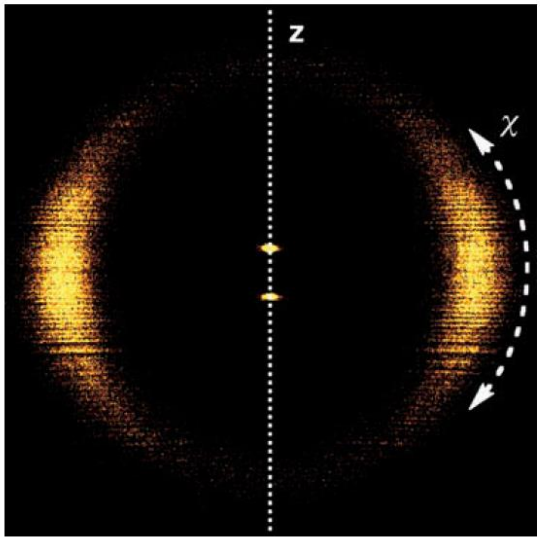

b) 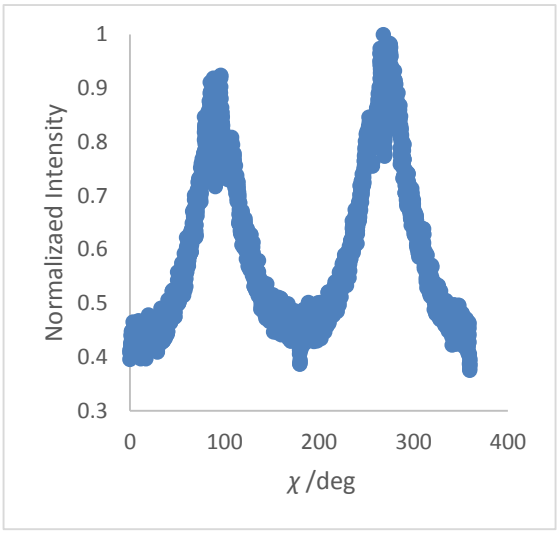

Figure 2-4: a) 2D X-ray scattering pattern from a SmA monodomain formed by **QL12-10/6**. b) Integrated normalized intensity of the wide-angle scattering χ of **QL12-10/6**.

The 2D pattern features a sharp small-angle scattering along the layer normal **z** corresponding to the layer periodicity and a diffuse wide-angle scattering along an axis that is orthogonal to small-angle scattering, with a maximum corresponding to a mean intermolecular distance of 4.4 Å. The breadth of the wide-angle scattering intensity *I* along the azimuthal angle χ is inversely related to the orientational ordering of the mesogens, and S_2 values are obtained by integrating the wide-angle scattering intensity along χ and analyzing the resulting intensity profile (Figure 2-4b) according to the method of Davidson *et al.* Davidson shows that the mere fit of the intensity around χ to equation 2-1 allows access to an approximation of the order parameter.[6]

$$I(\theta) = f_0 + \frac{2}{3} f_2 \cos^2\theta + \frac{8}{15} f_4 \cos^4\theta + \frac{16}{35} f_6 \cos^6\theta + \frac{128}{315} f_8 \cos^8\theta + \cdots \qquad \text{(eq. 2-1)}^6$$

Where f_0 is negligible in the case of a very oriented phase, such as a SmA monodomain.[6] As shown in Figure 2-5, orientational order in the SmA phase of **QL11-10/6** and **QL12-10/6** is relatively invariant of temperature, with average S_2 values of 0.58 and 0.57, respectively.

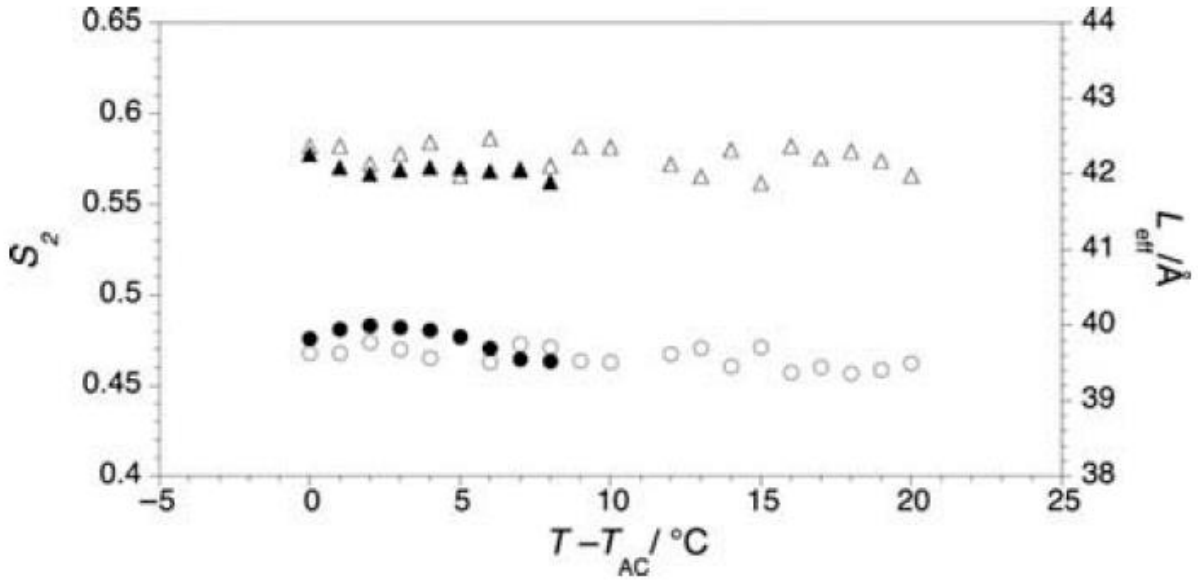

Figure 2-5: Orientational order parameter S_2 (triangles) and effective molecular length L_{eff} (circles) versus reduced temperature $T - T_{AC}$ measured in the SmA phase formed by **QL11-10/6** (open symbols) and **QL12-10/6** (filled symbols).

These values are the same within experimental error (±0.02) and are smaller than S_2 values typical of a conventional SmA phase (0.7–0.8), but still significantly larger than those measured for 'de Vries-like' materials such as **QL1-7** (S_2 = 0.38–0.43).

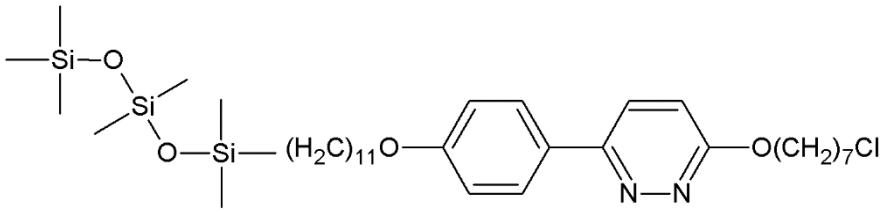

QL1-7

The effective molecular lengths are calculated using equation (1-11) and the corresponding *d* values measured by SAXS to give average L_{eff} values for **QL11-10/6** and **QL12-10/6** of 39.6 and 39.8 Å, respectively, which are the same within experimental error (±0.4 Å). The difference between L_{eff} and the calculated molecular length *L* of **QL11-10/6** (36.3 Å) is ca. 3.5 Å, which is the approximate length of the terminal phenyl ring according to the model shown in Figure 2-6.

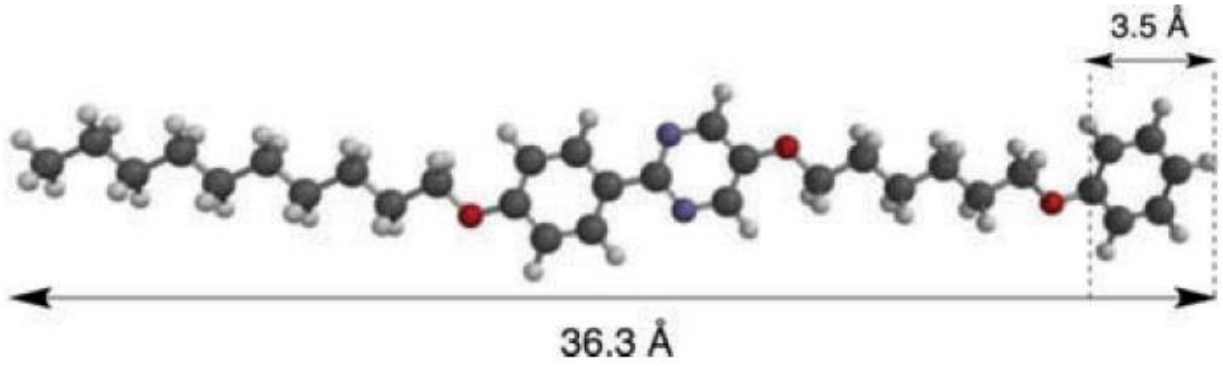

Figure 2-6: Molecular model of **QL11-10/6** minimized at the B3LYP/6-31G* level (Spartan'14,Wavefunction Inc.).

If we take into account conformational fluctuations of the alkyl chains and assume that the mesogen molecular length on the time average is somewhat less than that calculated for a fully extended molecular model, these results suggest that mesogens in the SmA phase are organized in intercalated bilayers with the phenoxy end-groups nanosegregated, as shown schematically in Figure 2-7. Such a model is consistent with the SmC-suppressing effect of the phenoxy end-group

in relation to the parent series **2PhP-*m/n*** as attractive van der Waals interactions between phenoxy end-groups would be maximized by out-of-layer fluctuations between smectic layers, which are less hindered in the orthogonal SmA phase.

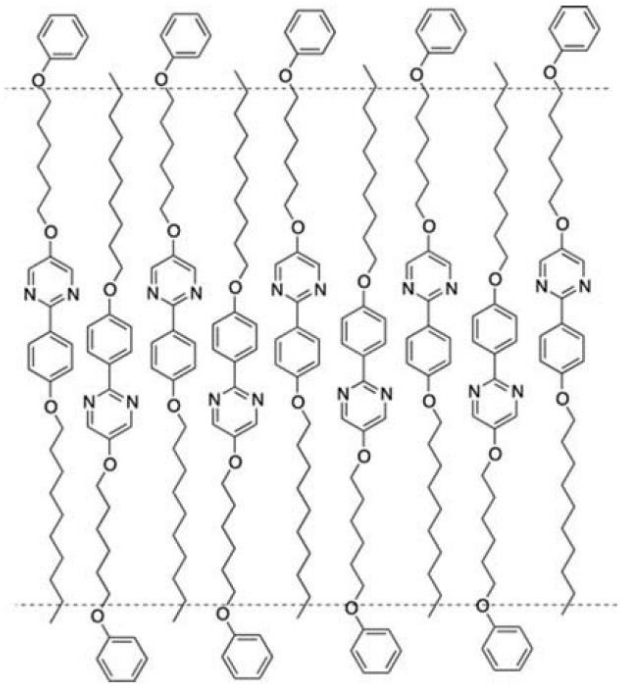

Figure 2-7: Schematic representation of the intercalated bilayer structure proposed for the SmA phase formed by **QL11-10/6.**

2.3 Optical Tilt Angle Measurements

Optical tilt angles (θ_{opt}) in the SmC phase of **QL11-8/8** were first measured by POM in the absence of an electric field as half the angle of rotation between dark states in domains of opposite tilt orientation with the samples aligned in ITO glass cells with a cell gap of 4 μm and a low pretilt (< 1°) rubbed polyimide alignment substrate. The results of these experiments showed an unusually low tilt of 6° at $T - T_{AC}$ = -10 K in comparison to the conventional mesogen **2PhP-8/8**, as shown in Figure 2-8, and 2-9. The unusually small θ_{opt} value of 8° at $T - T_{AC} = -10$ K, might explain the layer contraction of 1.0% based on a conventional model of smectic layers without having to

invoke ‘de Vries-like’ behavior. The small tilt angle in the SmC phase is also consistent with the weak birefringence of the Schlieren texture observed by POM.

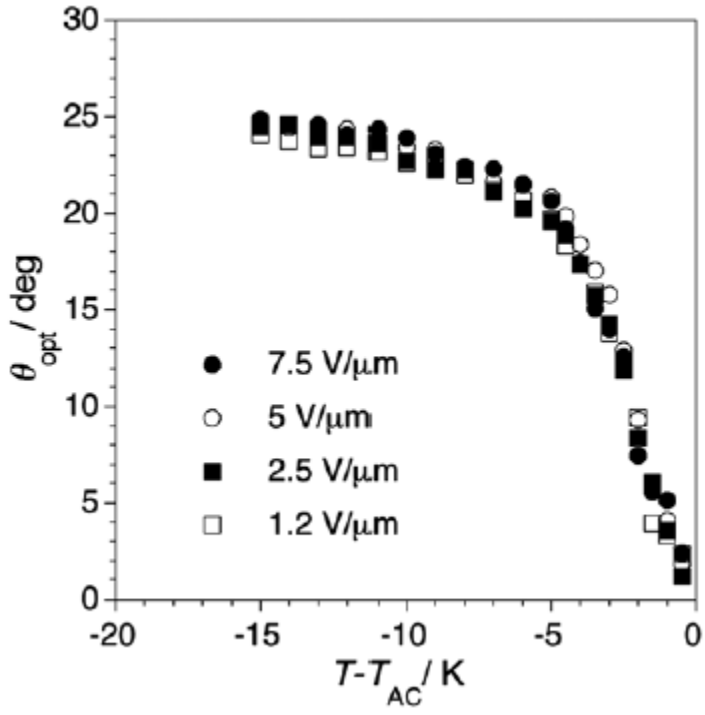

Figure 2-8: Optical tilt angle vs. reduced temperature measured electro-optically by POM in the SmC* phase for **2-PhP-8/8** (5 mol%). The data were acquired on cooling from the isotropic liquid phase.

To assess the validity of these measurements, a sample of **QL11-8/8** was doped with the chiral additive **MDW797** (2-5 mol%) and tilt angles θ_{opt} were measured electro-optically by switching the ferroelectric SmC* phase between opposite tilt orientations as SSFLC films aligned in the same glass cells, as shown in Figure 2-9. Unlike the conventional **2-PhP-8/8** mesogen, shown in Figure 2-10, the θ_{opt} (T) profile of **QL11-8/8** shows a dependence on the applied field E, and reaches a saturation point at 15 V/μm. The increase in tilt angle with increased applied field persists well below the SmA-SmC transition, which is inconsistent with an electroclinic effect.

This effect is also inconsistent with an electroclinic effect due to a decrease in the saturation voltage with increased concentration of chiral dopant.

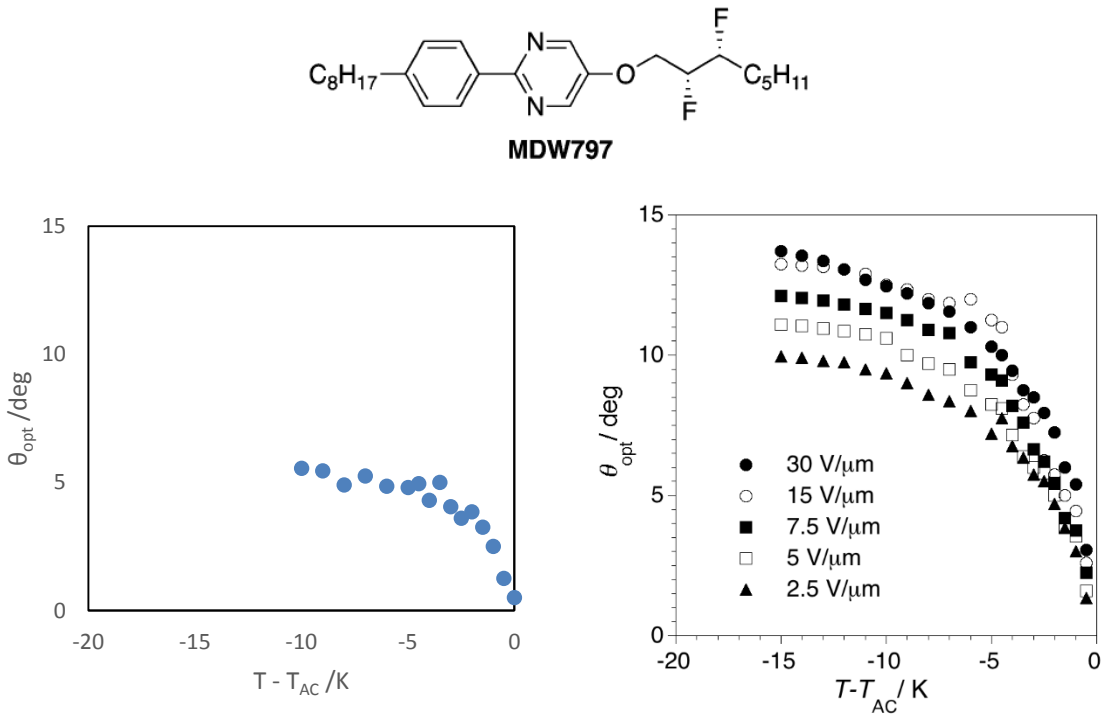

Figure 2-9: Optical tilt angle vs. reduced temperature measured electro-optically by POM in the SmC* phase for **QL11-8/8** (5 mol%) The data were acquired on cooling from the isotropic liquid phase.

These results suggest that the phenoxy end-groups cause an appreciable pretilt θ of the director **n** about the tilt cone in the SmC* phase. As shown in Figure 2-10, this pretilt should give an optical tilt angle θ_{opt} that appears by POM to be less than the actual tilt angle in the absence of an applied field. With the electro-optical measurements of θ_{opt} (T), the ferroelectric torque Γ produced by the coupling of E to the spontaneous polarization P_{S} induced by **MDW797**, which drives the Goldstone mode switching, should also work against the pretilt elasticity to bring the director **n** in the tilt plane **xz** at the saturation voltage. Hence, the optical tilt angle of **QL11-8/8** at

$T - T_{AC}$ = -10 K is in fact 13 degrees and not 8 degrees. The corresponding R value for the **QL11-8/8** at T_{AC} – 10 K is 0.63, which indicates that **QL11-8/8** does not behave fully as a rigid rod, but is also not a 'de Vries-like' material either.

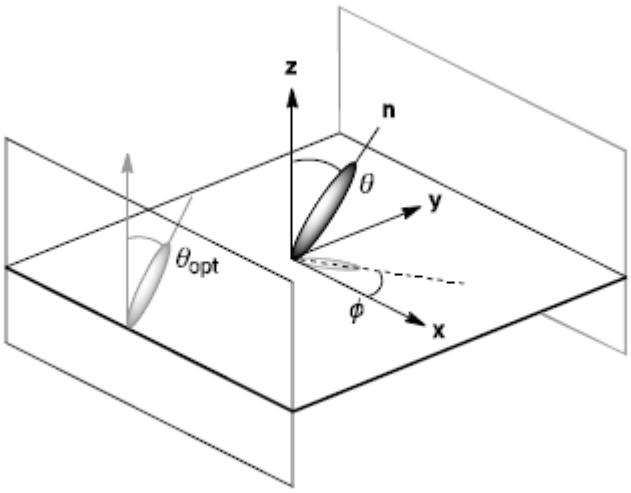

Figure 2-10: Local symmetry of the SmC* phase in a surface-stabilized configuration between two glass slides. The mesogen is represented by a hard spherocylinder oriented along the director **n**; its projection in the tilt plane **xz** is shown in grey.

2.4 Molecular Modeling

Drawing any structure–property relationship based on modelling of intermolecular spatial correlations can only be done at a first-order of approximation given the relatively high degree of orientational fluctuations in the SmA phase formed by these compounds. Given this caveat, and considering the unique similarity of the mesomorphic properties of **QL11-10/6** and **QL12-10/6** (Figure 2-2), it may be reasonable to assume that, in the intercalated bilayers formed by these two isomers according to Figure 2-8, the phenylpyrimidine cores are approximately 'in register', and that core–core interactions should therefore be invariant of core orientation. Furthermore, the interplay between phenoxy nanosegregation and core–core interactions may be revealed by

comparing the mesomorphic properties of isomeric pairs with *m/n* = 8/8 and 12/4, in which inverting the core orientation has opposite effects. As shown in Table 2-1, **QL11-8/8** and **QL12-12/4** both form enantiotropic SmA and SmC phases, whereas **QL11-12/4** and **QL12-8/8** form monotropic SmA and nematic phases. This suggests that inverting the core orientation in **QL11-8/8** causes a weakening of core–core interactions in an intercalated bilayer structure, whereas the opposite effect is apparent upon inverting the core orientation in **QL11-12/4.** If we assume that the phenylpyrimidine cores in the intercalated bilayers formed by the 10/6 isomers are in register, an inspection of molecular models according to Figure 2-11 suggests that the cores would be offset by ca. 50% in intercalated bilayers formed by the 8/8 or 12/4 isomers, which would bring either the pyrimidine rings (**QL11-8/8** and **QL12-12/4**) or phenyl rings (**QL11-12/4** and **QL12- 8/8**) approximately in register. To model these interactions, we performed calculations of potential energies of association ΔE for antiparallel dimers of the model compound 5-methoxy-2-(4-methoxyphenyl)pyrimidine (**2PhP-1/1**) in which the starting point for each optimization was a dimer with either the pyrimidine or phenyl rings 'in register'. The dimer structures were optimized at the MP2/6-31+G(d,p) level of theory, followed by single-point energy calculations at the MP2/6-311++G(d,p) level using the Gaussian 09 software package. As shown in Figure 2-11, the offset imposed at the start of each dimer optimization is closely maintained in the final structures. The potential energy of association was calculated in each case as the difference between the energy of the dimer and twice the energy of the monomer.

Figure 2-11: Antiparallel dimer structures of **2PhP-1/1** optimized at the MP2/6-31+G(d,p) level, with the pyrimidine rings (left) and the phenyl rings (right) 'in register'.

According to these calculations, the dimer with the pyrimidine rings 'in register' is more stable than the dimer with the phenyl rings 'in register' by 0.7 kcal mol−1 (ΔE = −25.6 kcal mol^{-1} vs. −24.9 kcal mol^{-1} , respectively), which is consistent with the observed mesomorphic properties in relation to the proposed intercalated bilayer model.

2.5 References

(1) Mulligan, K. M.; Bogner, A.; Song, Q.; Shubert, P. J.; Giesselmann, F.; Lemieux, R. P. *Journal of Materials Chemistry C.* **2014**, *2*, 8270.

(2) Song, Q.; Nonnenmacher, D.; Giesselmann, F.; Lemieux, R. P. *Journal of Materials Chemistry C* **2013**, *1*, 343.

(3) Wand, M. D.; Walba, D. M. Ferroelectric Liquid Crystals Compounds Containing Chiral Haloalkyoxy Tails Units and Compositions Containing Them. US5051506 A, 1991.

(4) Kuczyński, W.; Żywucki, B.; Małecki, J. *Molecular Crystals and Liquid Crystals* **2002**, *381* (1), 1.

Chapter 3: Tuning the Mesomorphic Properties of Phenoxy-terminated 5-Alkoxy-2(4-alkoxyphenyl)pyrimidine Liquid Crystals: The Effect of Fluoro Substitution

In this chapter, we report a detailed study of the effect of fluoro substitution on the mesomorphic properties of the phenoxy-terminated liquid crystals **QL11-*m/n*** and show how such substitutions may provide a predictable means of tuning the properties of FLC mixtures in a synthetically convenient manner. We will address how changing the position of a single fluoro substituent on the phenoxy end-group of **QL11-*m/n*** can affect its mesomorphic properties, and provide an explanation for the substituent effects in terms of arene-arene interactions at the smectic layer interfaces and their possible influence in promoting or suppressing out-of-layer fluctuations. We also show how mesomorphic properties can be further tuned by difluoro and perfluoro substitution.

3.1 Synthesis and Characterization

The compounds **QL20-*m/n*-*x*F, QL22-8/8-*x,y*F2** and **QL27-8/8**, were prepared by sequential alkylations of 2-(4-hydroxyphenyl)pyrimidin-5-ol with the appropriate fluorophenoxy-terminated 1-bromoalkane and 1-bromoalkane via nucleophilic substitution reactions, as shown in Scheme 3-1.

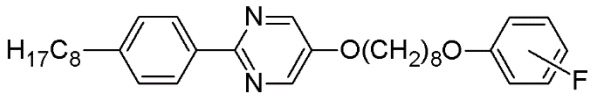

QL20-8/8-xF

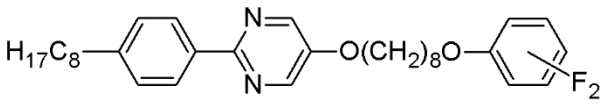

QL22-8/8-x,yF_2

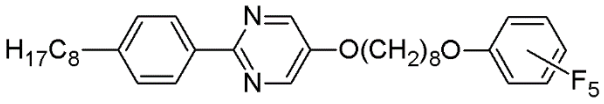

QL27-8/8

The new compounds were recrystallized from acetonitrile and hexanes, and their mesomorphic properties were characterized by polarized optical microscopy (POM) and differential scanning calorimetry. Phase transition temperatures and enthalpies of transition are listed in Table 3-1.

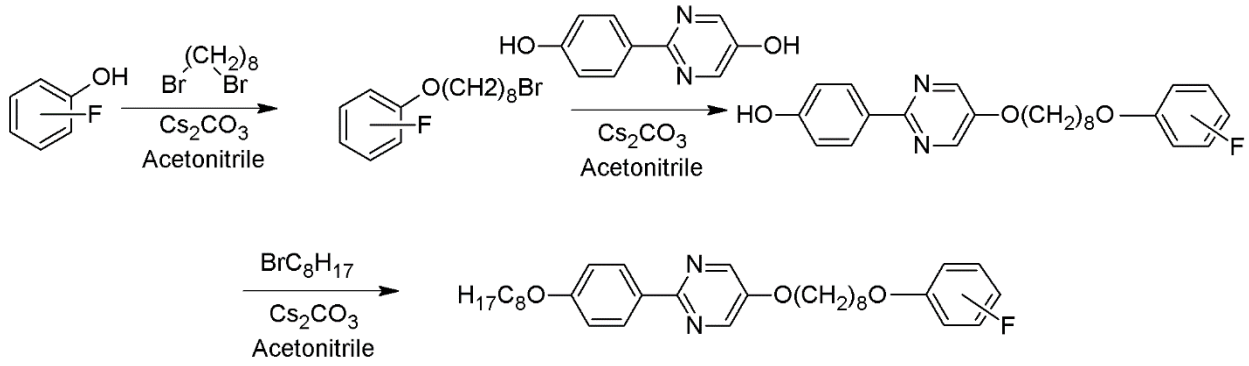

Scheme 3-1: Synthesis of **QL20-8/8-xF**.

Table 3-1: Transition temperatures (°C) and enthalpies of transitions (kJ mol^{-1}, in parentheses) for compounds **QL20-*m*/*n*-*x*F**, **QL22-8/8-*x*,*y*F$_2$** and **QL27-8/8** measured by DSC.

Compound	Cr		SmC		SmA	N		I
QL20-8/8-2F	•	66 (56)	•	80 (< 0.1)[a]	•		83 (9.3)	•
QL20-8/8-3F	•	81 (42)	(•	72 (< 0.1))[a,c]	•		96 (12)	•
QL20-8/8-4F	•	82 (46)			•		102 (10)	•
QL20-10/6-2F	•	72 (37)	•	85 (< 0.1)[a]	•		88 (9.2)	•
QL20-10/6-3F	•	87 (50)	(•	75 (< 0.1))[a,c]	•		106 (12)	•
QL20-10/6-4F	•	93 (41)			•		114 (12)	•
QL20-12/4-2F	•	91	(•	85 (< 0.1))[a,c]	•		93 (49)[b]	•
QL20-12/4-3F	•	120 (52)			(•		116 (8.5))[c]	•
QL20-12/4-4F	•	120 (51)			•		133 (13)	•
QL22-8/8-2,3F$_2$	•	81 (63)	(•	78 (< 0.1))[a,c]	•		88 (11)	•
QL22-8/8-2,4F$_2$	•	62 (56)	(•	61 (< 0.1))[a,c]	•		92 (10)	•
QL22-8/8-2,5F$_2$	•	75 (42)	•	76 (< 0.1)[a]	•		87 (10)	•
QL22-8/8-2,6F$_2$	•	36 (22)	•	68 (2.5)		•	75 (1.7)	•
QL22-8/8-3,4F$_2$	•	78 (51)			•		98 (8.9)	•
QL22-8/8-3,5F$_2$	•	88 (52)			•		95 (12)	•
QL27-8/8	•	36 (19)	•	65 (< 0.1)[a]	•		92 (9.3)	•

[a] Transition temperature measured by polarized microscopy. [b] Total enthalpy for both transitions due to partial resolution of the peaks. [c] Monotropic mesophase.

The SmA phase was identified by the formation of characteristic fan textures and dark homeotropic domains on cooling from the isotropic liquid phase, as shown in Figure 3-1(a); for the applicable compounds, the SmC phase was identified on further cooling from the SmA phase by the appearance of Schlieren textures in the homeotropic domains and the transition of fan textures to characteristic broken fans textures, as shown in Figure 3-1(b). The nematic phase formed by **QL22-8/8-2,6F$_2$** was identified by the formation of a marbled texture with high birefringence, which turned into Schlieren and fan textures upon transition to the SmC phase, as shown in Figures 3-1(c) and 3-1(d). The absence of broken fans is characteristic of a SmC phase formed via a first order SmC-N transition.[1]

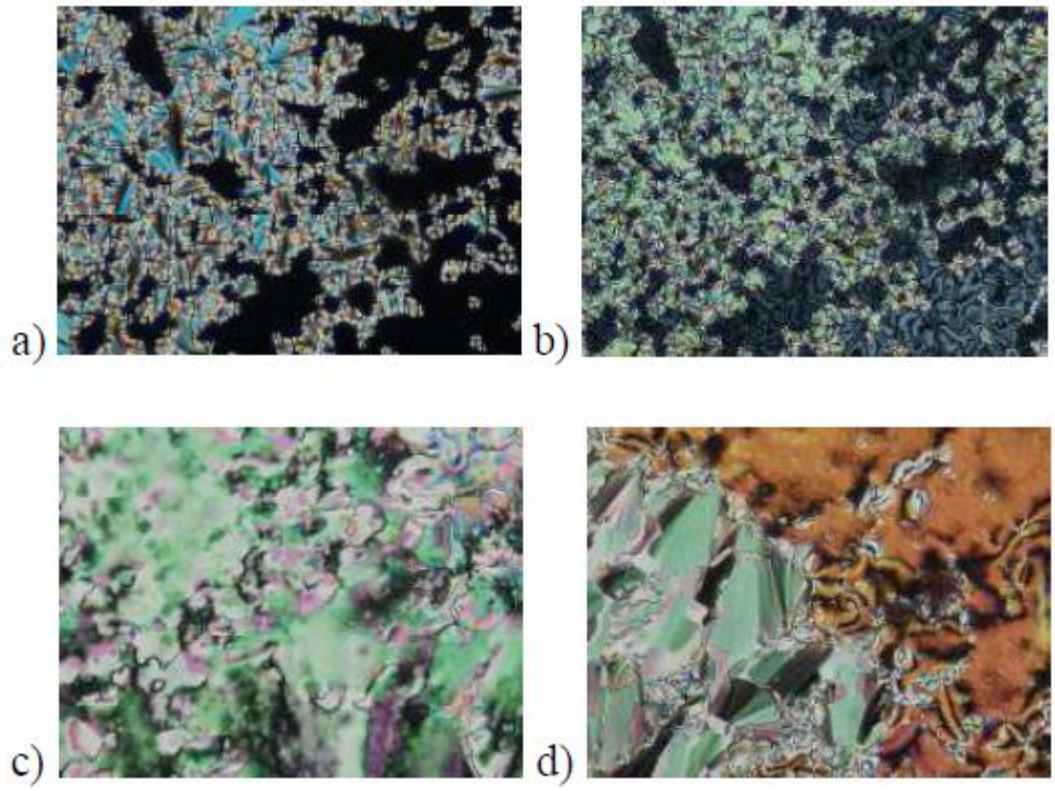

Figure 3-1: Polarized photomicrographs of (a) **QL20-8/8-2F** in the SmA phase at 82 °C, (b) **QL20-8/8-2F** in the SmC phase at 69 °C, (c) **QL22-8/8-2,6F$_2$** in the N phase at 73 °C, and (d) **QL22-8/8-2,6F$_2$** in the SmC phase at 67 °C, all obtained on cooling from the isotropic liquid phase.

In the monofluoro series **QL20-*m/n*-*x*F**, we chose to examine the same three representative isomers featured in Chapter 2, which reflect the interplay between core-core interactions and the nanosegregation imposed by the phenoxy end-groups. Modeling of intermolecular correlations in the SmA phase formed by the parent isomers **QL11-*m/n*** based on measurements of *d* spacing and orientational order parameters S_2 suggest that the phenylpyrimidine cores are approximately in register in the intercalated bilayer structure formed by **QL11-10/6**, and partially offset to bring the pyrimidine rings in register in the case of **QL11-8/8**, and the phenyl rings in register in the case of **QL11-12/4**. As shown in Figure 3-2, the trend in mesomorphic properties observed with the three **QL11-*m/n*** isomers, i.e., the increase in melting point and reduction in mesomorphic character

with decreasing length *n* of the phenoxy-terminated alkoxy chain, is also observed with compounds **QL20-*m/n*-*x*F**, which suggests that a similar intercalated bilayer structure is formed in their smectic phases.

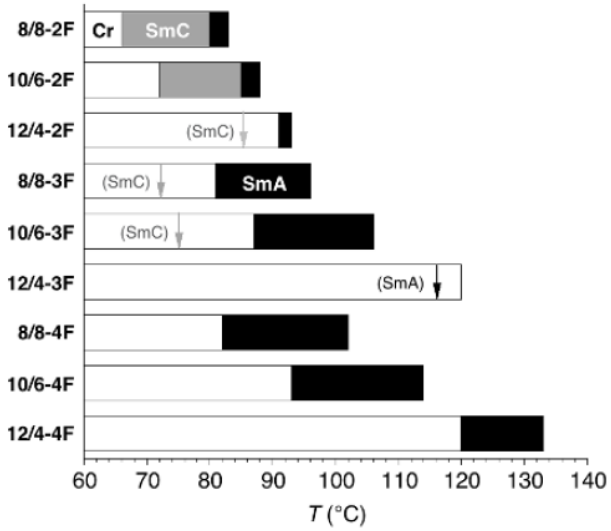

Figure 3-2: Mesophases formed by the phenoxy-terminated derivatives **QL20-*m/n*-*x*F**. The arrows represent monotropic phase transitions.

Far more interesting is the effect of changing the position of the fluoro substituent from the *ortho* to the *para* position on the phenoxy end-group. Notwithstanding that all nine monofluoro derivatives form a SmA phase, including **QL20-12/4-3F**, which forms a SmA phase on cooling only (monotropic), the effect of the *ortho*-fluoro substituent is distinct and twofold: (i) it causes an appreciable decrease in melting point and (ii) it promotes the formation of a SmC phase, even with the 12/4 isomer as a monotropic phase. On the other hand, the *para*-fluoro substituent stabilizes the SmA phase and completely suppresses the formation of the SmC phase, even on cooling. The effect of the *meta*-fluoro substituent appears to be somewhere in between those of *ortho* and *para* to the extent that it is negligible. Indeed, the mesomorphic properties of the three *meta*-fluoro isomers are nearly identical to those of the parent isomers **QL11-*m/n***.

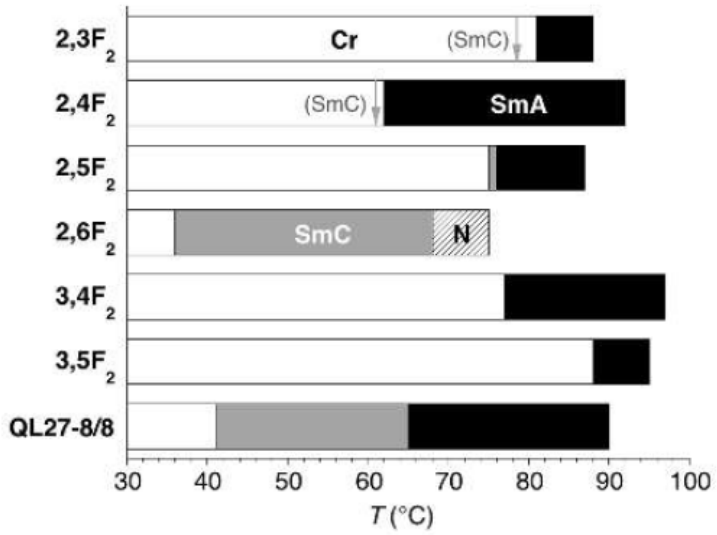

Figure 3-3: Mesophases formed by the phenoxy-terminated derivatives **QL22-8/8-*x*,*y*F2** and **QL27-8/8**. The arrows represent monotropic phase transitions.

In the difluoro substituted series **QL22-8/8-*x*,*y*F2**, the opposing substituent effects appear to balance one another, except in one unusual case. As shown in Figure 3-3, the 2,3-, 2,4- and 2,5-regioisomers form SmA and SmC phases, although the SmC phase is monotropic in two cases. Perhaps coincidentally, the mesomorphic properties of the 2,5-regioisomer, in which the two fluoro substituents are in direct opposition, are almost identical to those of the unsubstituted analogue **QL11-8/8**. In the absence of an *ortho*-fluoro substituent, as in the 3,4- and 3,5-regioisomers, only a SmA phase is formed. On the other hand, having fluoro substituents at both *ortho* positions results in the formation of a nematic phase and a very broad SmC phase; this is a less common phase sequence that may have interesting implications in terms of chevron-free SSFLC devices (vide infra). In the case of the perfluorinated derivative **QL27-8/8**, we observed broad SmA and SmC phases and a significant lowering of the melting point, which is consistent with a report by Itahara on the effect of a perfluorophenoxy end-group on mesomorphic properties

of a homologous series of 4-alkoxy-4'-cyanobiphenyl nematogens.[3] On cooling from the isotropic liquid phase, the SmC phase of **QL27-8/8** persisted at temperatures as low as 2 °C due to substantial supercooling.

3.2 Optical Tilt Angle Measurements

Optical tilt angles (θ_{opt}) in the SmC phase were first measured by POM in the absence of an electric field, as previously described in chapter 2, and gave unusually small θ_{opt} (T) values as well. The samples were then doped with the chiral additive **MDW797** (2-5 mol%) and tilt angles were measured electro-optically by switching the SmC* phase between opposite tilt orientations. For example, measurements of θ_{opt} for **QL20-8/8-2F** and **QL20-10/6-2F** were in the range of 6-8° at a reduced temperature of 10 K below the SmA-SmC phase transition point (T–T_{AC} = –10 K). As previously described with compound **QL11-8/8**, the $\theta_{opt}(T)$ profiles of **QL20-8/8-2F**, **QL20-10/6-2F**, **QL20-10/6-3F** and **QL22-8/8-2,6F2**, showed a pronounced dependence on the applied field E, as shown in Figure 3-4.

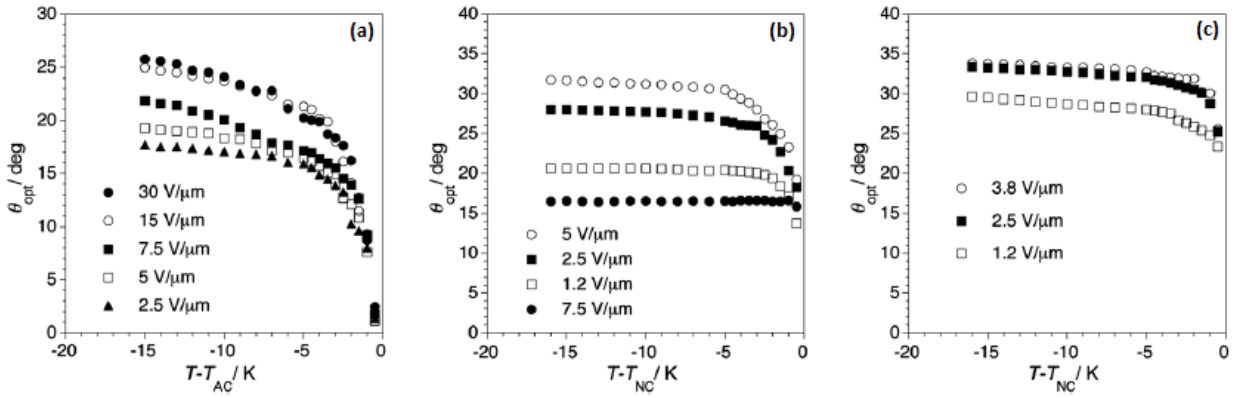

Figure 3-4: Optical tilt angle *vs.* reduced temperature measured electro-optically by POM at various electric fields in the SmC* phase for three mesogens doped with the chiral additive **MDW797** (*x* mol%): (a) **QL20-10/6-2F** (5 mol%), (b) **QL22-8/8-2,6F2** (2 mol%) and (c) **QL22-8/8-2,6F2** (5 mol%).

For example, the optical tilt of **QL20-10/6-2F** gradually increases with E and reaches a saturation point at 15 V/μm. The increase in θ_{opt} with E persists well below the SmA-SmC transition point T_{AC} and is therefore inconsistent with an electroclinic effect, which is only observed in the near vicinity of T_{AC}. The saturation voltage decreases with increasing dopant concentration—from 2 to 5 mol%—and a saturation of $\theta_{opt}(E)$ is observed in all cases except for **QL22-8/8-2,6F$_2$** with 2 mol% of **MDW797**, as shown in Figure 3-4(c). The optical tilt of this SmC* mixture increases with E up to 5 V/μm, and then decreases by approximately 50% with a further increase in E to 7.5 V/μm. However, this effect vanishes with a higher dopant concentration of 5 mol%, and a saturation of $\theta_{opt}(E)$ is observed at 2.5 V/μm. These results are also consistent with the phenoxy end-group causing an appreciable pretilt θ of the director **n** about the tilt cone in the SmC* phase, as previously described in section 2.3 and Figure 2-10.

The θ_{opt} (E) behaviour described in Figure 3-4(c) could be explained by competing ferroelectric torque Γ and dielectric torque Γ^{ε}, with the latter dominating at higher E and driving the director **n** away from the tilt plane. In the SmC* phase, the **z** component of the dielectric torque Γ^{ε} working on the azimuthal angle ϕ is proportional to E^2 and the dielectric anisotropy and/or dielectric biaxiality of the liquid crystal, whereas the ferroelectric torque Γ is proportional to E and P_S. A higher concentration of **MDW797** (5 mol%) would restore the dominance of the ferroelectric torque by virtue of a higher P_S and thus allow tilt saturation to be achieved. The fact that this behavior is only observed with **QL22-8/8-2,6F$_2$** is consistent with molecular models suggesting that the two *ortho*-fluoro substituents should increase the positive dielectric anisotropy of the liquid crystal.

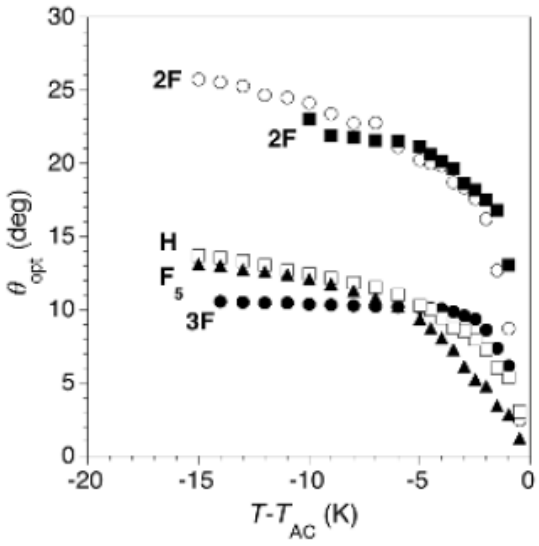

Figure 3-5: Optical tilt angle *vs.* reduced temperature measured electro-optically by POM at 15 V/μm in the SmC* phase for five mesogens doped with the chiral additive **MDW797** (5 mol%): **QL11-8/8** (□), **QL20-8/8-2F** (■), **QL20-10/6-2F** (○) **QL20-10/6-3F** (●) and **QL27-8/8** (▲). The data were acquired on cooling from the isotropic liquid phase.

As shown in Figure 3-5, the SmC promoting effect of the *ortho*-fluoro substituent is seen in the larger optical tilt angles of 23° and 24° at $T–T_{AC}$ = –10 K for **QL20-8/8-2F** and **QL20-10/6-2F**, respectively; these are more than twice the optical tilt angles measured at the same reduced temperature for the unsubstituted mesogen **QL11-8/8**, the *meta*-fluoro derivative **QL20-10/6-3F** and the perfluoro derivative **QL27-8/8**, in which the opposing effects of *ortho*- and *para*-fluoro substituents appear to cancel out. Further evidence of this SmC-promoting effect is provided by the step-like function $\theta_{opt}(T)$ profile of **QL22-8/8-2,6F$_2$** as seen in Figure 3-6(d), which is typical of liquid crystals with a first-order SmC-N phase transition, showing a tilt angle of 33° at $T – T_{AC}$ = –10 K.

3.3 Small-angle X-ray Scattering

The three fluorinated mesogens forming enantiotropic SmA and SmC phases over appreciable temperature ranges were analyzed by small-angle X-ray scattering as a function of temperature to determine the extent of smectic layer contraction on transition from the orthogonal SmA to the tilted SmC phase. The smectic layer spacing *d* was derived from the first order scattering peak at small-angle on heating from the crystalline phase according to Bragg's law, except for the non-fluorinated mesogen **QL11-8/8**, which was analyzed on cooling from the isotropic phase due to the narrow temperature range of the SmC phase on heating. As shown in Figure 3-6, the profiles of relative layer spacing d/d_{AC} *vs.* reduced temperature show a substantial degree of layer contraction upon transition to the SmC phase at T_{AC}, which is typically observed with conventional smectic liquid crystals. The difference in layer contraction between the two *ortho*-fluorinated mesogens and the non-fluorinated mesogen **QL11-8/8** can be accounted for by the difference in tilt angle θ_{opt}. Indeed, the reduction factor *R* values calculated at $T - T_{AC} = -10$ K for these three compounds range from 0.80 to 0.87, which are the same within experimental error (assuming errors of ± 0.1 Å for SAXS and ± 1° for θ_{opt} measurements), and suggest the absence of 'de Vries-like' properties. The $d/d_{AC}(T)$ profile of the perfluorinated mesogen **QL27-8/8** is very similar to that of **QL11-8/8**, and gives a *R* value approaching 1 at $T - T_{AC} = -10$ K.

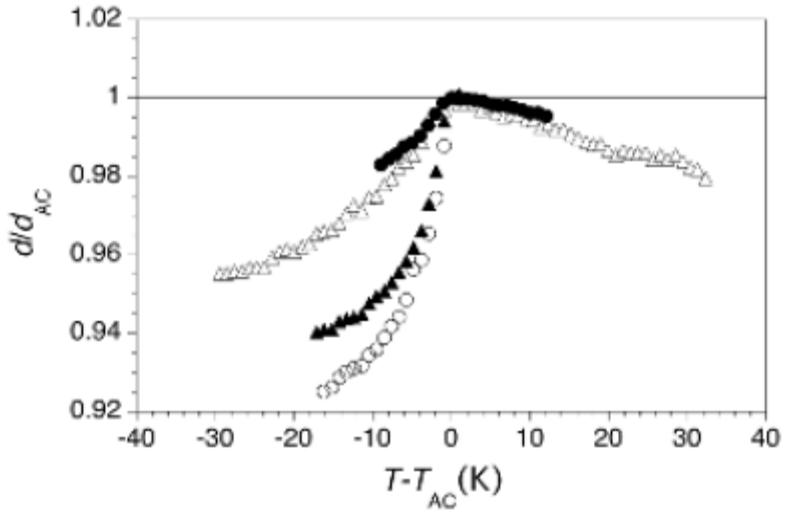

Figure 3-6: Relative smectic layer spacing *vs.* reduced temperature for **QL11-8/8** (●), **QL20-8/8-2F** (▲), **QL20-10/6-2F** (○) and **QL27-8/8** (Δ). The data were acquired on heating from the crystalline phase except for **QL11-8/8**.

3.4 Modeling of End-group Interactions

To understand the effect of fluoro substitution on the mesomorphic properties reported herein, we sought to model the interactions of phenoxy end-groups at the interface of smectic layers by calculating changes in the potential energy of association ΔE for non-covalent dimers of fluoro-substituted *n*-butyloxybenzene molecules in parallel and antiparallel geometries. At a first-order of approximation, these two geometries model the non-covalent interactions of phenoxy end-groups within a smectic layer and between layers through out-of-layer fluctuations, respectively, as shown in Figure 3-7. The assumption underlying this modeling exercise is that the suppression of out-of-layer fluctuations due to attractive non-covalent interactions between phenoxy end-groups in a parallel geometry should favour the SmC phase by reducing the entropic cost of molecular tilt. On the other hand, attractive non-covalent interactions between phenoxy end-groups

in an antiparallel geometry would require out-of-layer fluctuations, which would be maximized in the orthogonal SmA phase, as illustrated in Figure 3-7.

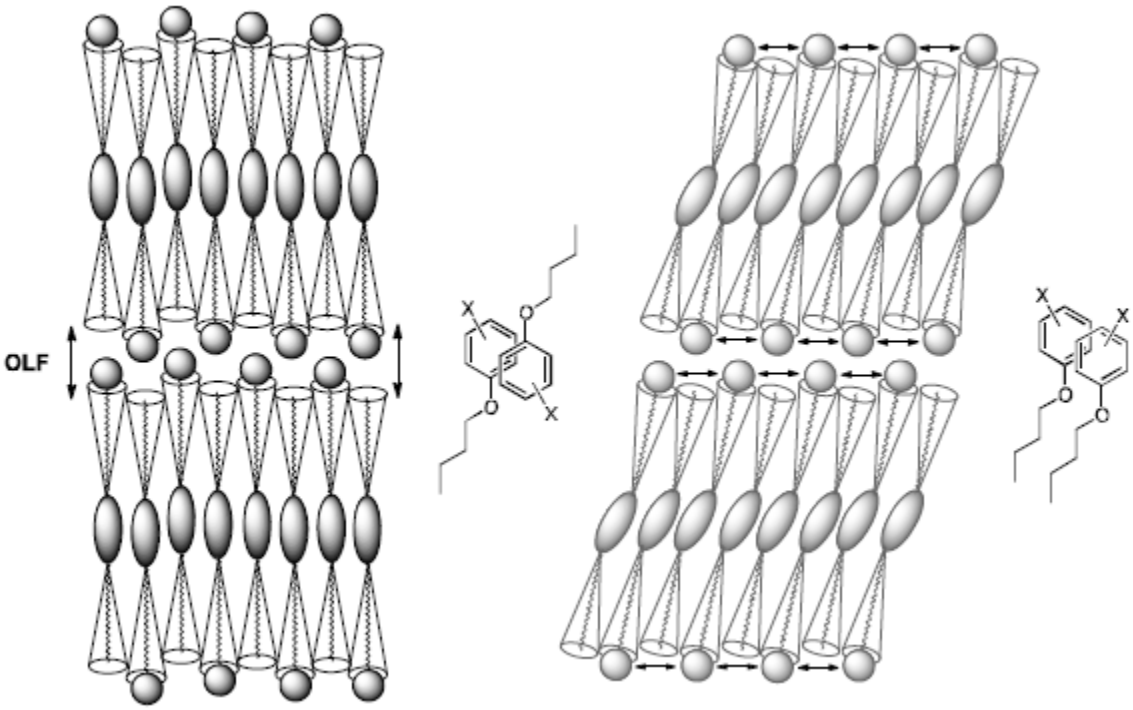

Figure 3-7: Models of phenoxy end-group interactions in antiparallel and parallel geometries in relation to structures of the SmA (left) and SmC phases (right).

Calculations were performed with starting dimer geometries in which the two molecules are oriented either parallel or antiparallel and the aromatic rings are perfectly superposed; with the *ortho*- and *meta*-fluoro derivatives, separate starting geometries with the fluoro substituents oriented in the same (*syn*) or opposite (*anti*) directions were also considered. The potential energy of the geometry minimization was performed at the MP2/6-31+G** level using the Gaussian 09 software package, and the resulting energies were corrected for basis set superposition error (BSSE) by performing single point calculations at the MP2/6-311++G** level on the equilibrium geometry with the keyword COUNTERPOISE. In each case, the association energy ΔE was

calculated as the difference between the BSSE-corrected energy of the associated dimer and twice the energy of one molecule obtained from a single-point calculation at the MP2/6-311++G** level. In all cases, the parallel or antiparallel orientations imposed at the start of the minimizations were closely maintained in the final structures, as shown by four representative examples in Figure 3-8. The resulting ΔE values are listed in Table 3-2.

Table 3-2: Potential energies of association ΔE for unsubstituted and fluoro-substituted *n*-butyloxybenzene dimers in parallel and antiparallel geometries.[a]

	ΔE (kcal mol^{-1})[b]			
X	*Parallel-Syn*	*Parallel-Anti*	*Antiparallel-Syn*	*Antiparallel-Anti*
H	–6.8		–6.5	
2F	–6.2	–7.5	–4.3	–6.5
3F	–6.2	–6.8	–6.3	–6.4
4F	–8.1		–9.2	

[a] Based on BSSE-corrected energies obtained at the MP2/6-311++G**//MP2/6-31+G** level of theory. [b] Calculated as the difference between the BSSE-corrected energy of the associated dimer and twice the energy of one molecule obtained at the MP2/6-311++G**//MP2/6-31+G** level.

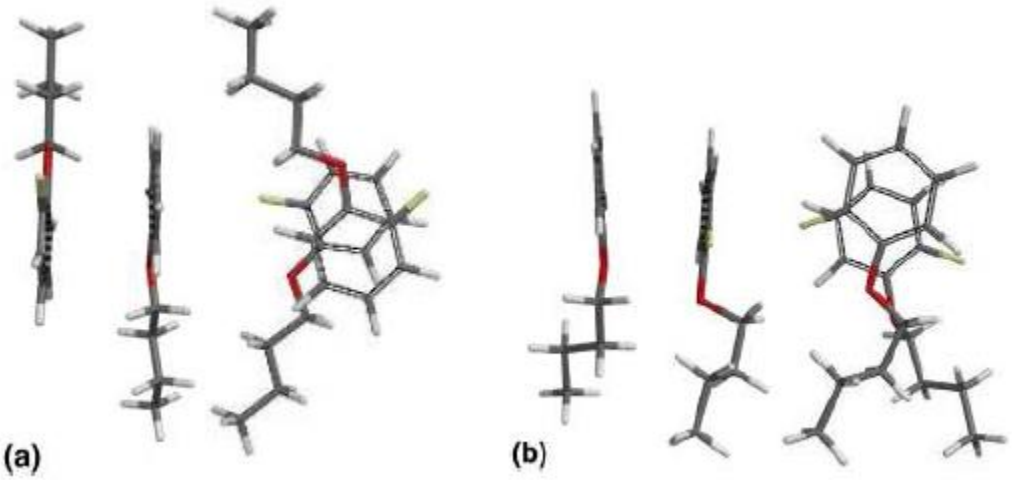

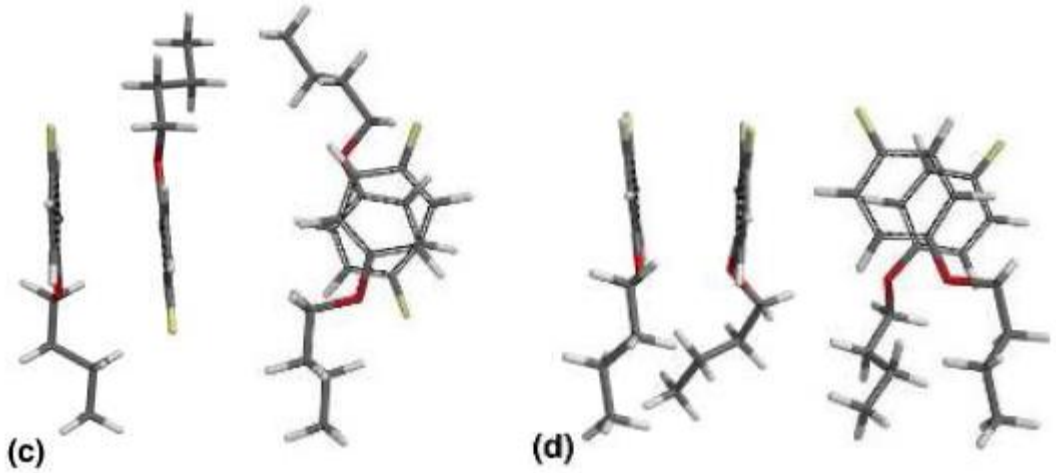

Figure 3-8: Dimer geometries minimized at the MP2/6-31+G** level as side and front views: (a) 2-fluoro-1-(*n*butyloxy)benzene (*antiparallel-anti*), (b) 2-fluoro-1-(*n*-butyloxy)benzene (*parallel-anti*), (c) 4-fluoro-1-(*n*butyloxy)benzene (*antiparallel*), and (d) 4-fluoro-1-(*n*-butyloxy)benzene (*parallel*).

Notwithstanding the usual caveats about drawing correlations between calculated energies of non-covalent interactions in the gas phase and bulk properties in the condensed phase, the trend in relative ΔE values between the most stable parallel and antiparallel geometries of fluoro-substituted *n*-butyloxybenzene dimers is consistent with the observed substituent effects based on the notion that attractive in-layer interactions between phenoxy end-groups should promote the formation of a SmC phase, and that attractive out-of-layer interactions between phenoxy end-groups should promote the formation of a SmA phase. Hence, the difference in association energy $\Delta\Delta E$ between the parallel and antiparallel *anti* geometries of the *ortho*-fluoro dimer is 0.97 kcal/mol in favour of the parallel geometry, whereas the corresponding energy difference $\Delta\Delta E$ for the *para*-fluoro dimer is 1.1 kcal/mol in favour of the antiparallel geometry. The $\Delta\Delta E$ for the *meta*-fluoro dimer and unsubstituted dimer are smaller (~0.3 kcal/mol), although opposite geometries are favoured, which may be consistent with the fact that a *meta*-fluoro substituent has a negligible effect on the smectogenic properties of phenoxy-terminated mesogens, and that the more subtle

energetic preference for phenoxy end-group interactions in either a parallel or antiparallel geometry may not be strong enough to affect the inherent balance between SmA and SmC phases formed by these materials.

3.5 Potential Applications

The phenoxy-terminated surface stabilized liquid crystal mesogens show a high dependence of the optical tilt θ_{opt} on the applied field, which allows for the tunability of θ_{opt} similar to the electroclinic effect and may be used as an analog light shutter. The optimal optical tilt angle of 22.5 degrees can be obtained by varying E in these systems. In previously reported SmC-N materials the tilt angle is commonly ~40 degrees which decreases their value in device applications.[2] In the case of **QL22-8/8-2,6F2**, a SmC-N liquid crystal was synthesized that has an optical tilt angle of around ~22° at $T - T_{AC} = -10$ under the conditions of $E = 0$. At relatively low applied fields, $E < 2$ V/μm, the material can still be switched and optimal switching angles can be maintained. **QL22-8/8-2,6F2** is deficient due to its high positive dielectric anisotropy which can cause distortions to the SmC phase under high applied fields.

3.6 References:

(1) Demus, D.; Goodby, J.; Gray, G.; Spiess, H.; Vill, V. *1 Handbook of Liquid Crystals, Volume 2A: Low Molecular Weight Liquid Crystals I*; 1998.

(2) Cluzeau, P.; Ismaili, M.; Anakkar, A.; Foulon, M.; Babeau, A.; Nguyen, H. T. *Molecular Crystals Liquid Crystals* **2001**, *362*, 185.

(3) Itahara, T. *Liquid Crystals*, **2005**, *32*, 115.

Chapter 4: Substituent Effects in Phenoxy-terminated 5-Alkoxy-2(4-alkoxyphenyl)pyrimidine Liquid Crystals with Inverted Geometries

In Chapter 2, the mesomorphic properties of phenoxy-terminated liquid crystals were presented and discussed. The data suggest that the phenoxy end-group nanosegregates at the layer interface, which causes 2-phenylpyrimidine cores to be offset from their most stable geometries of association. The phenoxy-terminated mesogens showed an increased SmC thermal stability when *m*/*n* is equal to 8/8. In Chapter 3, we investigated the effect of fluoro substituents on the phenoxy end-group, and showed that the SmC phase is promoted by an *ortho*- fluoro substituent on the phenoxy end-group. Two main questions arise from this work. The first question is whether core-core interactions or end-group interactions are the dominant influence on mesomorphic properties. The second question is what causes the nematic phase formed by **QL22-8/8-2,6F2**. The interplay between core-core and end-group interactions may be assessed through the synthesis and characterization of the inverted series of these mesogens, as well as the synthesis of the 2,6-dimethylphenoxy end-group mesogen to investigate changes in sterics, arene-arene interactions, and molecular geometry.

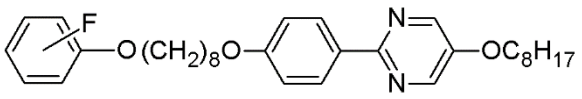

QL21-8/8-x,yF_2

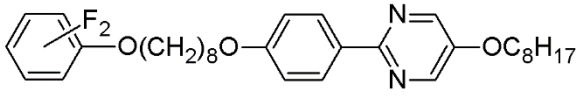

QL23-8/8-x,yF_2

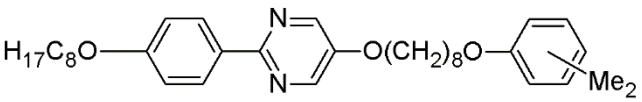

QL30-8/8-x,yMe_2

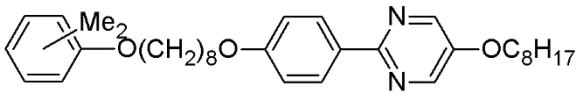

QL31-8/8-x,yMe_2

4.1 Synthesis and Characterization

The **QL21-8/8-*x*F**, and **QL23-8/8-*x*,*y*F2** series, and the **QL30-8/8-*x*,*y*Me2**, and **QL31-8/8-*x*,*y*Me2** mesogens were prepared by sequential alkylations of 2-(4-hydroxyphenyl)pyrimidin-5-ol with the appropriate fluorophenoxy-terminated or dimethylphenoxy-terminated 1-bromooctane and 1-bromooctane via nucleophilic substitution reactions, as shown in Scheme 4-1. The new compounds were recrystallized from acetonitrile, methanol, and hexanes, and their mesomorphic properties were characterized by polarized optical microscopy (POM) and differential scanning calorimetry. Phase transition temperatures and enthalpies of transitions are listed in Table 4-1.

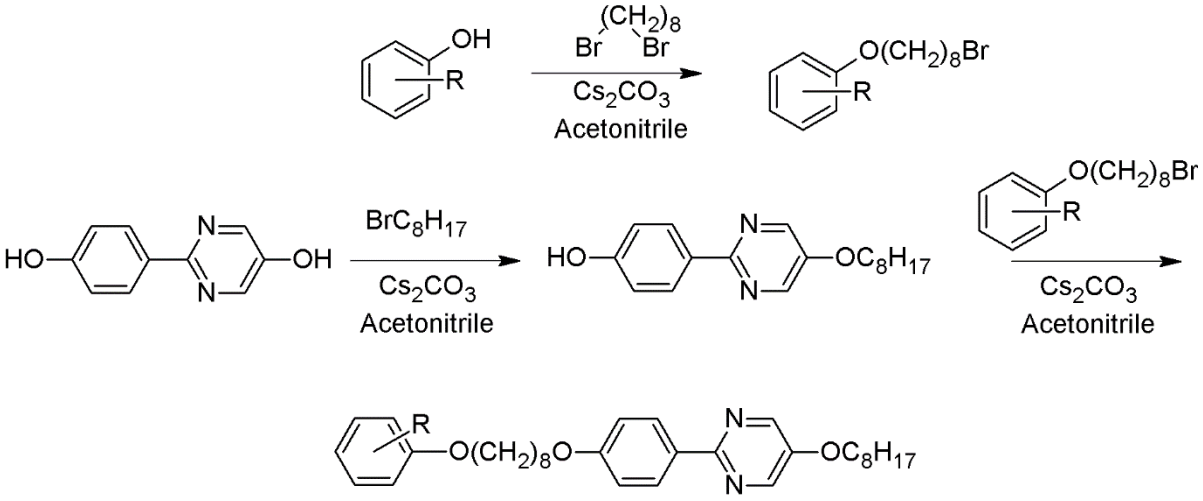

Scheme 4-1: Synthesis of inverted geometry 2PhP core liquid crystals **QL21**, **QL23, and QL31.**

Table 4-1: Transition temperatures (°C) and enthalpies of transitions (kJ mol^{-1}, in parentheses) for compounds **QL20-8/8-*x*F**, **QL21-8/8-*x*F**, **QL22-8/8-2,6F$_2$**, **QL23-8/8-2,6F$_2$**, **QL27-8/8**, **QL30-8/8-2,6Me$_2$**, and **QL31-8/8-2,6Me$_2$** measured by DSC.

Compound	Cr		SmC		SmA		N		I
QL20-8/8-2F	●	66(56)	●	80(<0.1)	●			83(9.3)	●
QL21-8/8-2F	●	61(64)	●	71(<0.1)	●			78(3.6)	●
QL20-8/8-3F	●	81(42)	(●	72(<0.1)	●			96(12)	●
QL21-8/8-3F	●	85(45)			(●	85(7.3)			●
QL20-8/8-4F	●	82(46)			●			102(10)	●
QL21-8/8-4F	●	87(76)			●	96(2.7)	●	97(4.4)	●
QL22-8/8-2,6F$_2$	●	36(22)	●	68(2.5)			●	75(1.7)	●
QL23-8/8-2,6F$_2$	●	39(56)	●	50(<0.1)	●	66(1.0)	●	77(2.4)	●
QL30-8/8-2,6Me$_2$	●	46(71)	●	47(<0.1)	●	65(1.5)	●	70(2.8)	●
QL31-8/8-2,6Me$_2$	●	62(58)	(●		●	67(0.6)	●	72(2.7)	●
QL27-8/8	●	36(19)	●	65(<0.1)	●			92(9.3)	●

The nematic phase of **QL23-8/8-2,6F$_2$** was characterized by the formation of a marbled texture with high birefringence as shown in 4-1a. The SmA phase was identified by the formation of characteristic fan textures and dark homeotropic domains on cooling from the isotropic liquid phase, as shown in Figure 4-1b, and the SmC phase was identified on further cooling from the SmA phase by the appearance of Schlieren textures in the homeotropic domains and the conversion of fan textures to characteristic broken fan textures, as seen in 4-1c.

a) 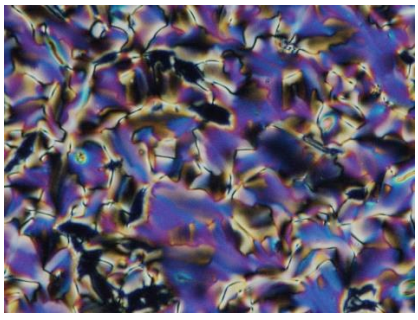 b) 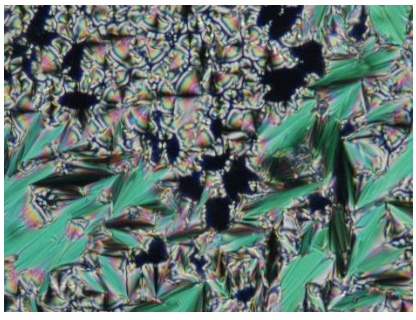

c) 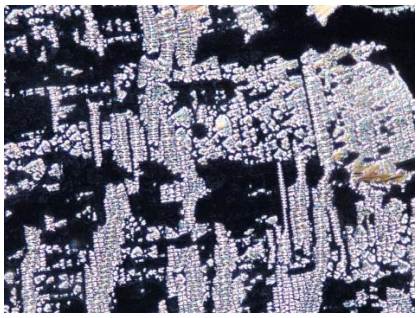

Figure 4-1: Photomicrographs of **QL23-8/8-2,6F$_2$** (a) 68°***C*** nematic phase on cooling (b) 64°***C*** SmA phase on cooling (c) 32°***C*** SmC phase on cooling on a rubbed slide.

4.2 The Balance between Core-core and End-group Interactions

In Figure 4-2, the mesomorphic properties of **QL21-8/8-*x*F**, **QL23-8/8-*x*,*y*F$_2$**, **QL30-8/8-Me$_2$** and **QL31-8/8-Me$_2$** are compared to those of **QL20-8/8-*x*F** and **QL22-8/8-*x*,*y*F$_2$**, as well as the parent mesogen **QL11-8/8.**

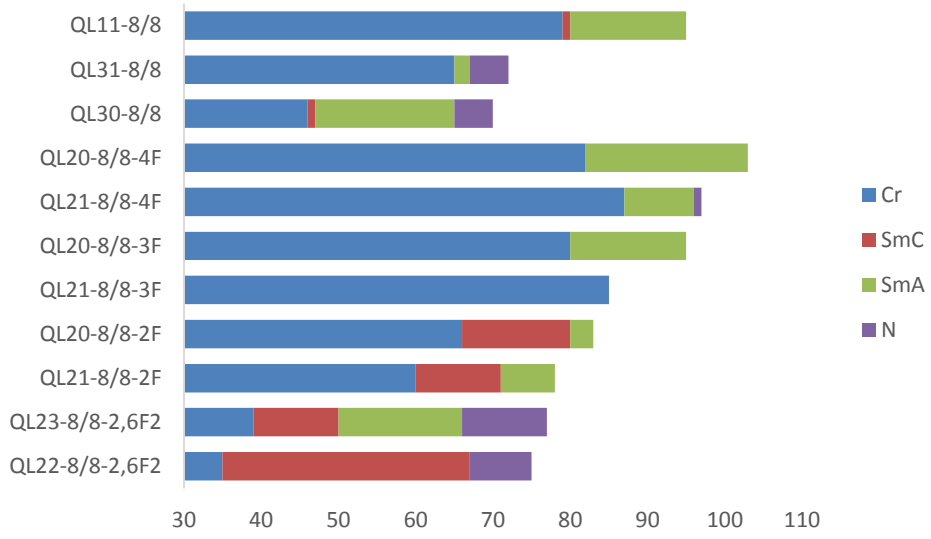

Figure 4-2: Mesophases formed by the phenoxy-terminated derivatives **QL20-8/8, QL21-8/8**, **QL22-8/8**, **QL23-8/8**, **QL30-8/8**, and **QL31-8/8**.

In this comparison, we find that the *ortho*-fluoro phenoxy end-group promotes the SmC phase regardless of core orientation. Nevertheless, the effect of core-core interactions can still be observed through the stabilization of the SmC phase in **QL20-8/8-2F** compared to **QL21-8/8-2F**. In **QL21-8/8-3F**, the SmC phase is suppressed, and the SmA phase is monotropic, whereas **QL20-8/8-3F** forms a SmA and a monotropic SmC phase. These two isomers show similar trends to their parent compounds **QL11-8/8** and **QL12-8/8**. The subtle change in mesomorphic properties shows that core-core interactions in the 3F isomers can still have a significant effect on the mesophase properties, but that end-group interactions still dominate the mesomorphic properties. The *para*-fluoro substituent strongly promotes the SmA phase, but a narrow nematic phase can be observed near the clearing point of **QL21-8/8-4F**, which will be discussed later in this chapter. Overall the phenoxy end-group appears to promote a strong degree of lamellar order in 2-phenylpyrmidine liquid crystals.

4.3 Powder X-ray Scattering Experiments

Overall, the two geometries of monofluoro mesogens **QL20** and **QL21** have relatively similar mesomorphic properties. However, **QL23-8/8-2,6F$_2$** is unique among phenoxy-terminated mesogens because it shows an increase in layer spacing in the SmC phase as it approaches the crystallization point, as shown in Figure 4-3. Typically, mesogens which show an increase in layer spacing on cooling in the SmC phase do so by virtue of an increase in orientational order. The increase in S_2 offsets the layer contraction due to molecular tilt, which corresponds to an overall layer spacing increase in the SmC phases. However, the $d(T)$ profile of **QL23-8/8-2,6F$_2$** clearly shows a decrease in layer spacing in the SmA phase on cooling towards the SmC phase.

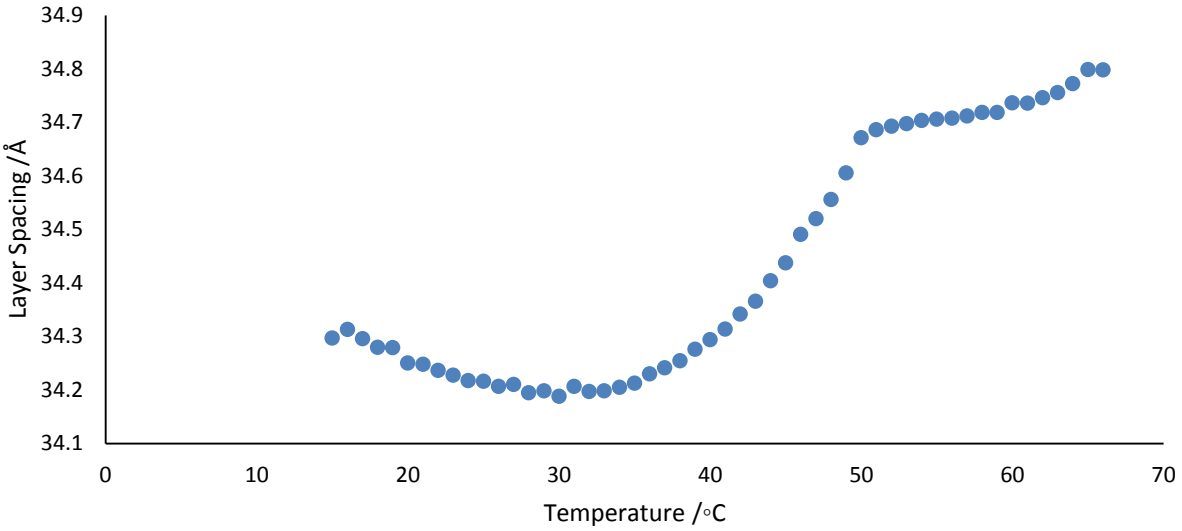

Figure 4-3: Layer spacing vs Temperature measured by SAXS for cooling from the isotropic phase of **QL23-8/8-2,6F$_2$** taken from cooling from the isotropic phase.

Another unusual feature of **QL23-8/8-2,6F$_2$** is that it shows a second order scattering peak at small-angle, as shown in Figure 4-4. A detectable second-order Bragg reflection peak is typically observed with mesophases with a high degree of lamellar order or increased nanosegregation, as in 'de Vries-like' materials such as the carbosilan-terminated mesogens discussed previously.

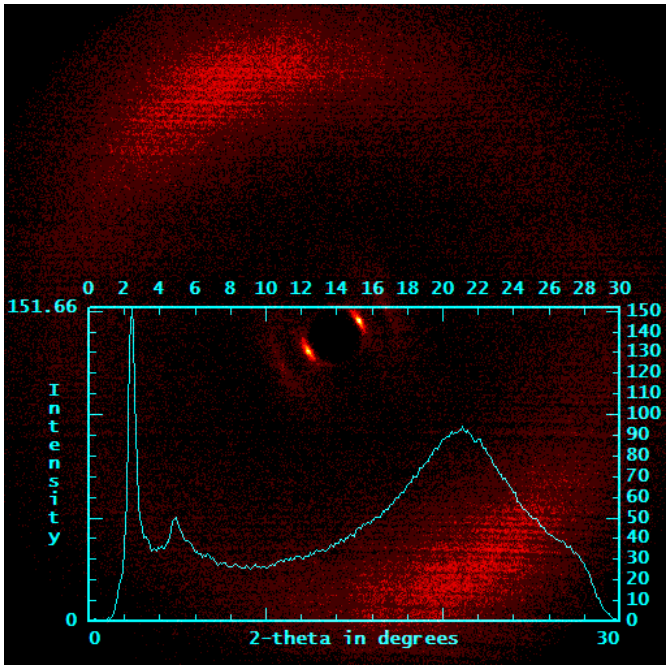

Figure 4-4: 2D X-ray mono domain of **QL23-8/8-2,6F2** in the SmA phase.

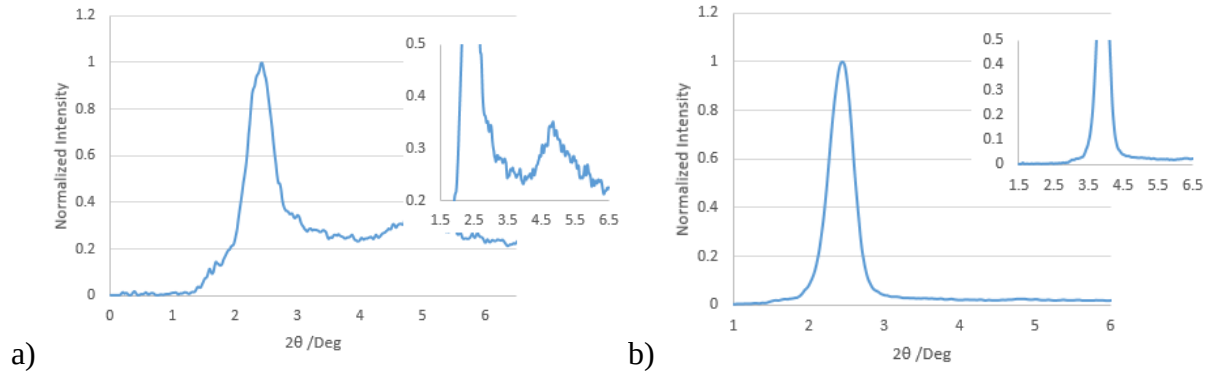

a) b)

Figure 4-5: Normalized intensity profiles of the small-angle X-ray scattering profile taken by 2-D X-ray scattering techniques for (a) **QL23-8/8-2,6F2**, and (b) **QL21-8/8-4F.**

While this mesogen may be a candidate as 'de-Vries-like', the saturated tilt angle measured with an applied field of 15 V/um on a mixture of **QL23-8/8-2,6F2** with 2% **MDW797** showed that the change in layer spacing of ~1% can be accounted for by a low tilt angle of ~ 12 degrees, as shown

in Figure 4-6. The corresponding R value at $T - T_{AC}$ = -10 K for this material is 0.58, which is an intermediate between a smectic liquid crystal behaving like rigid rods and a pure 'de Vries-like' liquid crystal.

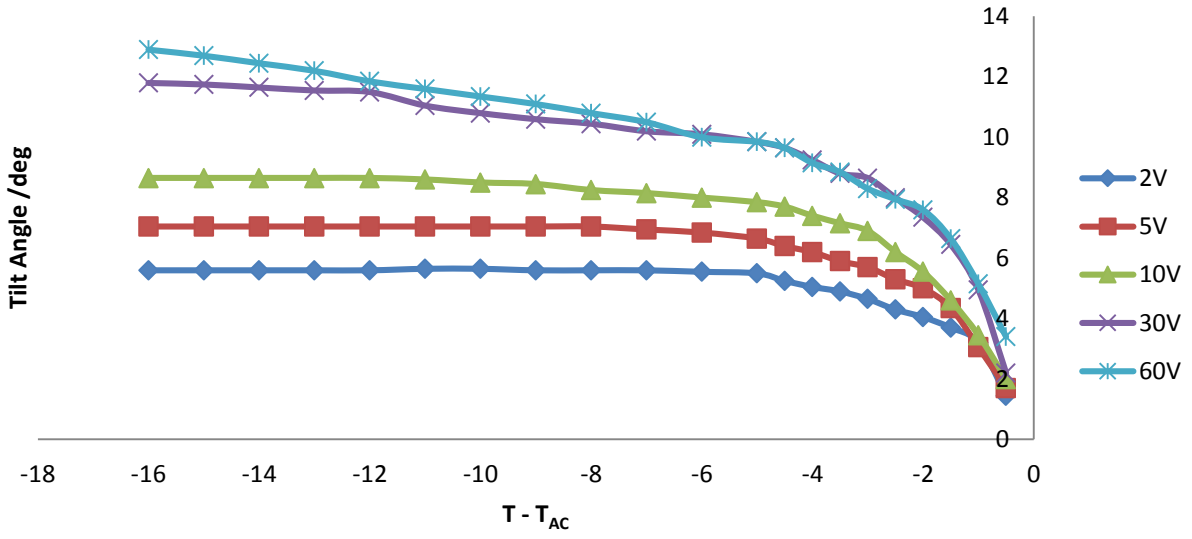

Figure 4-6: Plot of optical tilt angles θ_{opt} vs. electric field E for **QL23-8/8-2,6F$_2$** doped with 2% **MDW797** in a 4um planar aligned poly(imide) cell.

4.4 Origins of the Nematic Phase in Phenoxy-terminated Mesogens

Fluoro-substituted phenoxy end-groups have been shown as a strong promoters of lamellar order and therefore smectic phases, except for **QL21-8/8-4F**, **QL22-2,6F$_2$**, **QL23-8/8-2,6F$_2$**, and **QL29-8/8-2,6F$_2$**, which also form a nematic phase. In previous work on terphenyl mesogens, it has been shown that lateral substitution on aromatic cores promotes the nematic phase because of decreased arene-arene interactions due to increased steric hindrance between cores.[1] To determine why a nematic phase is formed by these compounds, we prepared the dimethyl analogues of the 2,6-difluoro mesogens to assess any contribution from sterics (packing forces), molecular geometry, and electronic interactions involved in the 2,6-difluorophenoxy-terminated mesogens.

The mesomorphic properties of these mesogens and enthalpies of transitions are shown in Table 4-1.

QL30-8/8-2,6Me$_2$ forms a nematic phase in both the normal and inverted geometries, albeit with a narrow temperature range, suggesting that the nematic phase may be due to large steric interactions at the layer interface between phenoxy end-groups. However, **QL22-8/8-2,6F$_2$** should have weaker steric disruptions than **QL30-8/8-2,6Me$_2$**, which suggests that the nematic phase formed by **QL21-8/8-4F, QL22-8/8-2,6F$_2$** and **QL23-8/8-2,6F$_2$** is not due only to increased steric interactions at the layer interface.

The molecular orientation of a phenoxy end-group is predicted to be coplanar with the alkoxy chain. In previous studies, the 2,6-dimethylphenoxy group has been shown to orient perpendicular to the alkoxy chain due to steric interactions between the methyl substituents and the alkoxy chain. These calculations are supported by ^{13}C NMR experiments, which show equal through-space C-F coupling with the alkyl chain carbon, which forms a triplet. This rotational restriction creates a unique situation as it would decrease the favorable intermolecular interactions at the layer interface, which could explain the decrease in lamellar order required for promotion of the nematic phase. We performed a conformational analysis at the B3LYP/6-31G* level that shows a similar conformational preference for the 2,6-difluorophenoxy end-group, as shown in Figure 4-7.

Figure 4-7: Molecular model of **QL22-8/8-2,6F$_2$** minimized at the B3LYP/6-31G* level (Spartan'14, Wavefunction Inc.) showing the orientation of the molecular dipole moment 2.8D for **QL22-8/8-2,6F$_2$**).

The mesogens can then be compared in terms of electronics. In **QL22-8/8-2,6F$_2$, QL23-8/8-2,6F$_2$** and **QL21-8/8-4F,** the molecules can be seen to have aligned dipole moments between core and end-group, which are not seen in **QL30-8/8-2,6Me$_2$** or **QL31-8/8-2,6Me$_2$**. The dipole moment of **QL-22-8/8-2,6F$_2$** is shown in Figure 4-7. If the nematic phase was due to an increased dipole moment or dipole-dipole interactions, the 2,6-dimethyl mesogens would not exhibit the nematic phase.

The formation of the SmC phase in **QL22-8/8-2,6F$_2$** can be speculated to be caused by an increase in stability of edge-to-face arene-arene interactions, due to the electron withdrawing effect of the fluoro substituents, at the layer interface. The increase in parallel interactions should increase thermal stability of the SmC phase, as shown in Chapter 3, consistent with the observed mesomorphic properties. While **QL30-8/8-2,6Me$_2$** shares the same molecular rigidity as **QL22-8/8-2,6F$_2$**, methyl substituents do not have the electron withdrawing properties of the fluoro substituent, and a SmA phase is observed.

4.5 References

(1) Hird, M., *Chemical Society Reviews* **2007**, *36*, 2070.

Chapter 5: SmC-N Liquid Crystals with Negative Dielectric Anisotropy.

In Chapter 3, a phenoxy-terminated mesogen with a SmC-N phase transition was discovered (**QL22-8/8-2,6F$_2$**). When mixed with a chiral dopant, the optical tilt angle in the SmC phase was found to be voltage dependent due to strong surface interactions of the phenoxy end-group. It was also observed that the high positive dielectric anisotropy of the 2-phenylpyrimidine core combined with the 2,6-difluorophenoxy end-group in **QL22-8/8-2,6F$_2$** caused a competition between ferroelectric and dielectric torque acting on the azimuthal cone angle(s) when the applied field was increased. In order to determine if the effect of the 2,6-difluorophenoxy end-group on mesomorphic properties is limited to the 2-phenylpyrimidine core, and to reduce the high positive dielectric anisotropy of **QL22-8/8-2,6F$_2$**, a fluorenone scaffold with a large transverse dipole moment, **QL29-8/8-2,6F$_2$**, was envisioned.

5.1 Synthesis and Characterization

The fluorenone derivatives were synthesized by protecting one of the two hydroxyl groups of 2,7-dihydroxyfluorenone with a tetrahydropyran protecting group, followed by alkylation with the appropriate 1-bromoalkane. This was followed by deprotection and subsequent alkylation with the appropriate phenoxy-terminated 1-bromoalkane. A homologous series of **QL29-m/8-2,6F$_2$** (m = 7, 8, 9 ,10) was prepared and their mesomorphic properties compared to those of the corresponding series. Mesomorphic properties were characterized by polarized optical microscopy and differential scanning calorimetry.

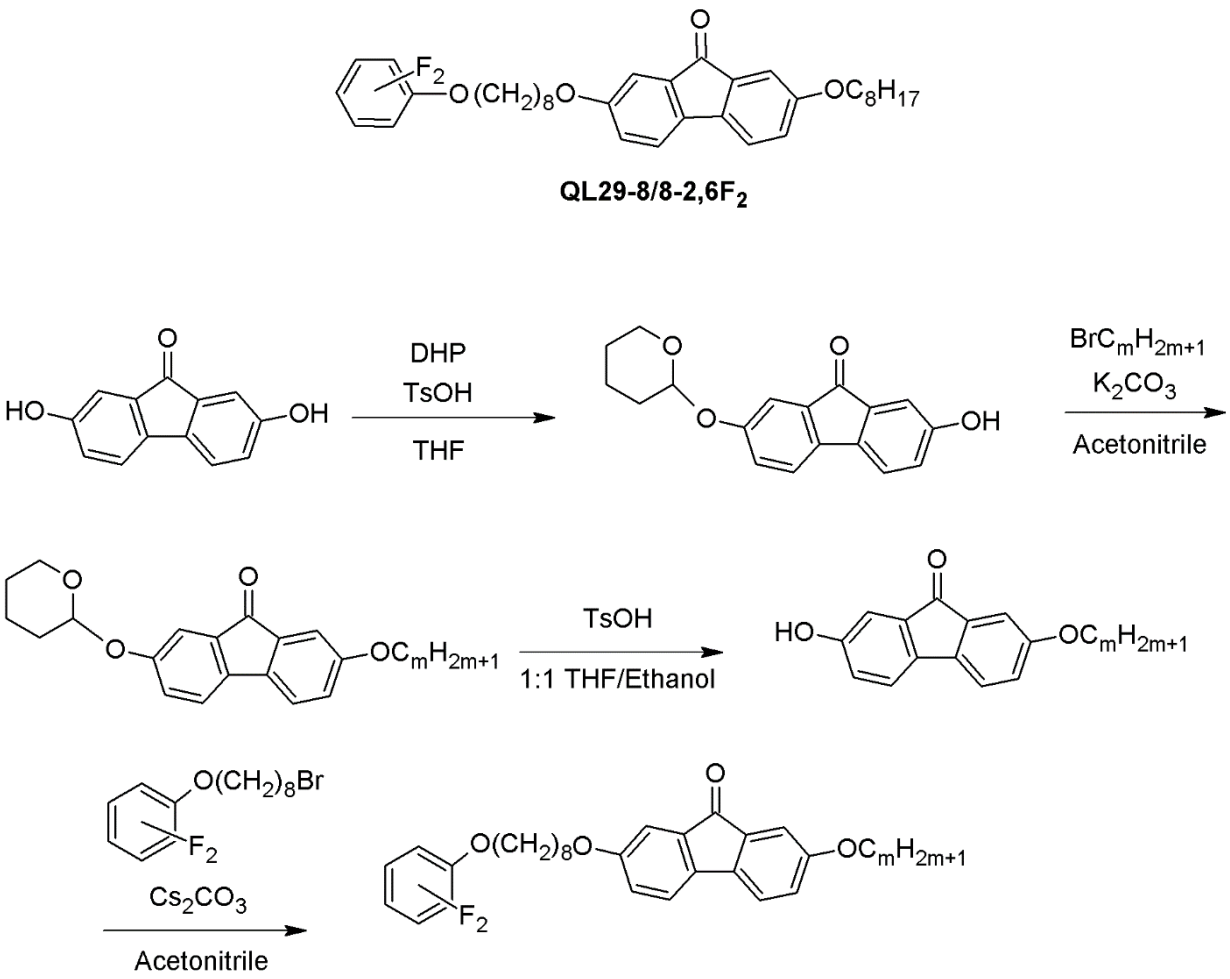

Scheme 5-1: Synthesis of fluorenone core liquid crystals **QL29-*m*/8**-2,6F_2.

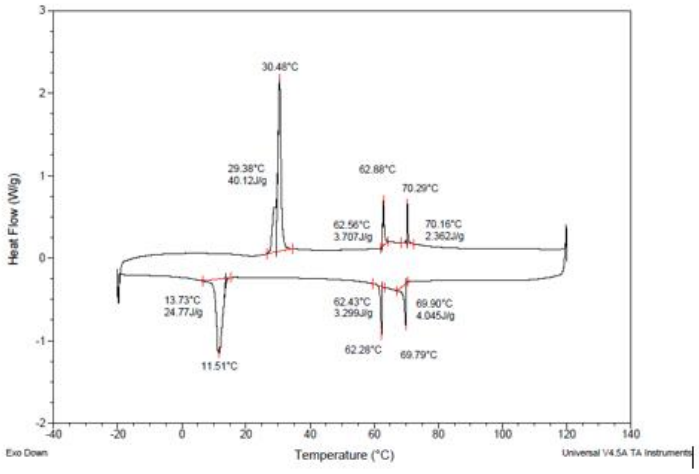

Figure 5-1: Differential Scanning Calorimetry profile for **QL22-7/8-2,6F2** showing both SmC-N and N-Iso phase transitions.

In Figure 5-1, the DSC shows both Iso-N and N-SmC transitions. In the **QL22-*m*/8-2,6F$_2$** and **QL29-*m*/8-2,6F$_2$** mesogens, the nematic phase was characterized by a marbled texture with high birefringence as shown in Figure 5-2a. The SmC phase was characterized by fan textures and a Schlieren texture, as shown in Figure 5-2b.

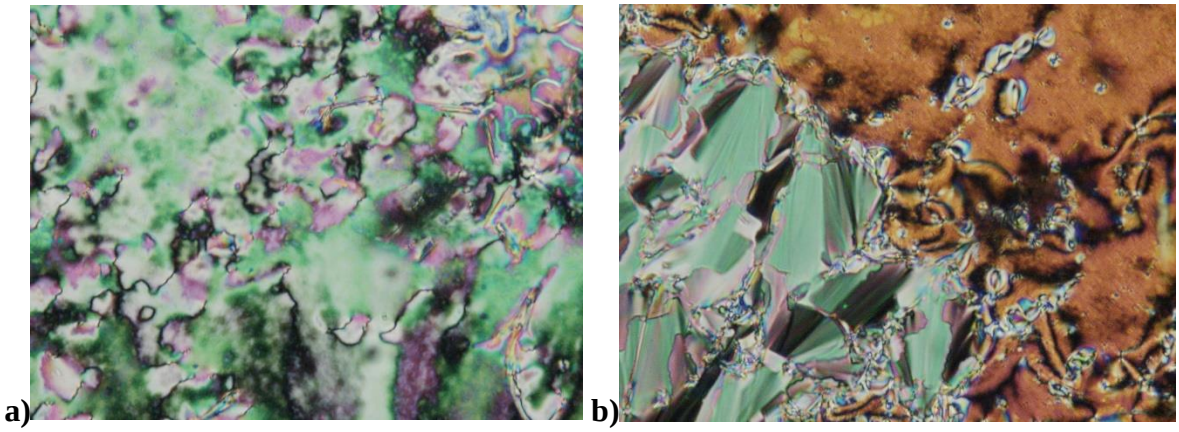

Figure 5-2: a) Nematic phase of **QL22-8/8-F$_2$** on cooling at 73 degrees Celsius b) SmC phase of **QL22-8/8-2,6F$_2$** on cooling at 63 degrees Celsius

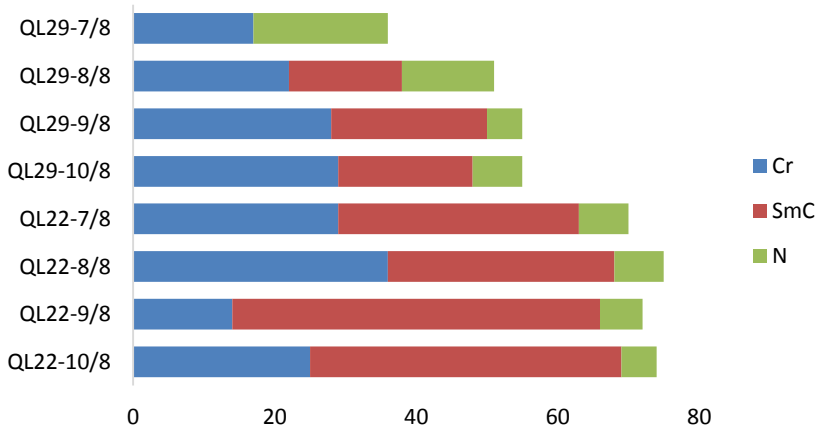

Figure 5-3: Mesomorphic properties of homologous series **of QL22-*m*/8-2,6F$_2$ and QL29-*m*/8-2,6F$_2$** measured on heating by DSC.

In Figure 5-3, the data shows that the 2,6-difluorophenoxy end-group is a strong SmC promoter in both 2-phenylpyrimidine and fluorenone derivatives, with all but one of the compounds forming enantiotropic SmC phases; **QL29-7/8-2,6F$_2$** forms a monotropic SmC phase. Not surprisingly, the increase in alkyl chain length results in an increase in the SmC phase temperature range, as well as a general decrease in nematic phase temperature range. Phase transition temperatures and enthalpies of transition are listed in table 5-1.

Table 5-1: Transition temperatures (°C) and enthalpies of transitions (kJ mol^{-1}, in parentheses) for homologous series of **QL22-*m*/8-F$_2$** and **QL29-*m*/8-F$_2$** measured by DSC.

Compound	Cr		SmC		N		I
QL22-7/8-2,6F$_2$	●	29(40)	●	63(3.7)	●	70(2.4)	●
QL22-8/8-2,6F$_2$	●	36(22)	●	68(2.5)	●	75(9.3)	●
QL22-9/8-2,6F$_2$	●	14(25)	●	66(2.8)	●	72(2.9)	●
QL22-10/8-2,6F$_2$	●	25(12)	●	69(2.5)	●	74(2.7)	●
QL29-7/8-2,6F$_2$	●	17(19)	(●	11(0.9)	●	30(1.0)	●
QL29-8/8-2,6F$_2$	●	22(22)	●	38(1.5)	●	51(2.9)	●
QL29-9/8-2,6F$_2$	●	28(14)	●	50(2.0)	●	55(0.3)	●
QL29-10/8-2,6F$_2$	●	29(15)	●	48(2.6)	●	55(3.5)	●

5.2 Optical Tilt Angle Measurements

Optical tilt angles were first measured by POM in the absence of an electric field, and gave unusually small θ_{opt} (T) values for SmC-N materials. Optical tilt angles in the SmC* phase formed by **QL22** and **QL29** derivatives were measured by POM in the presence of an electric field, as described in chapter 3 using **MDW797**, and the values were found to be consistent with conventional SmC-N materials, with θ_{opt} (E) values of approximately 30 degrees, as shown in Figure 5-4 and Figure 5-5.

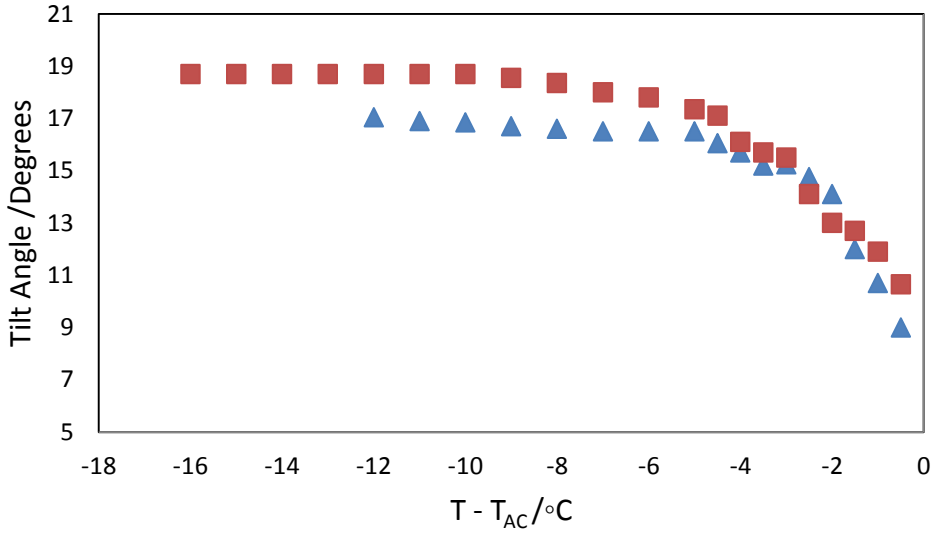

Figure 5-4: Tilt angles of **QL22-8/8-2,6F$_2$** (■) and **QL29-8/8-2,6F$_2$** (▲)SmC-N compounds in absence of applied field.

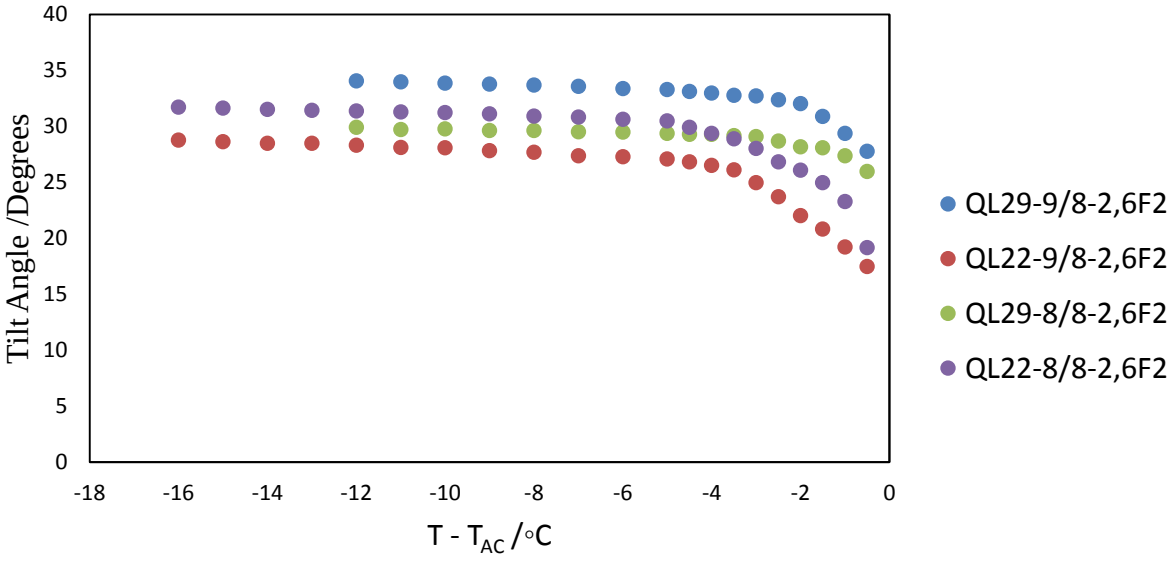

Figure 5-5: Saturated optical tilt angle measurements of **QL29-*m*/8-2,6F$_2$** and **QL22-*m*/8-2,6-F$_2$** in the presence of an applied field.

In Chapter 3, an electric field greater than 6.25 V/um was applied on **QL22-8/8-2,6F$_2$** in an aligned poly(imide) cell. In the SmC* phase, the sample switches from its planar conformation into a Schlieren texture with low birefringence, which is consistent with the effect of a dielectric torque caused by positive dielectric anisotropy of the mesogen, as shown in Figure 5-6.

Figure 5-6: Photomicrographs of **QL22-8/8-2,6F$_2$** in the SmC phase in the presence of an applied field, showing distortion of planar alignment due to high positive dielectric anisotropy of the compound.

When the applied field is decreased from E (θ_{max}), the θ_{opt} (E) of **QL22-8/8-2,6F$_2$** is tunable and dependent on the concentration of the chiral dopant and the cell thickness. In mixtures with a low concentration of chiral dopant, the competing effect of the dielectric toque prevents access to E (θ_{max}) due to large positive dielectric anisotropy. Alignment of **QL22-*m/n*-2,6F$_2$** on a poly(imide) cell requires a constant applied field during transition to the SmC* phase to prevent formation of the opposite tilt domain. The large positive dielectric anisotropy of **QL22-*m/n*-2,6F$_2$** causes a Freedericksz transition in the nematic phase, which causes the molecules to orient themselves homeotropically before the SmC*-N* phase transition. The net result is a distorted planar alignment on transition to the SmC* phase. In the case of **QL29-8/8-2,6F$_2$,** the negative dielectric anisotropy allows the use of large applied electric fields (>25V/um) for alignment and switching experiments. The change in dielectric anisotropy in the nematic phase is shown in Figure

5-7, through polarized optical micrographs of increased voltages in samples of **QL22-8/8-2,6F$_2$** and **QL29-8/8-2,6F$_2$** doped with **MDW797**.

a) 

b) 

c) 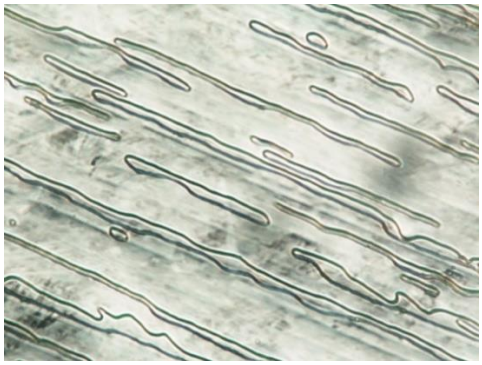

d) 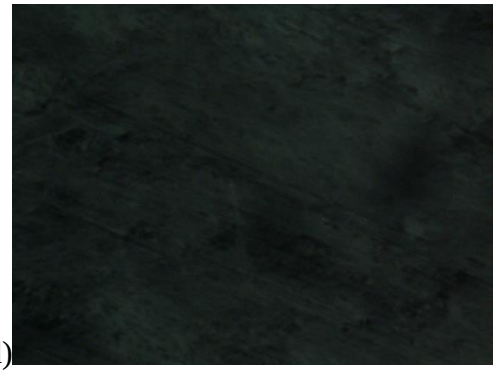

e) 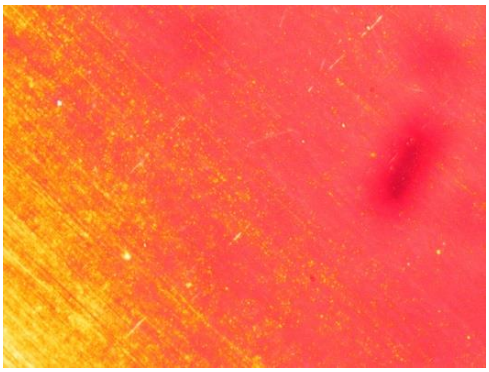

f) 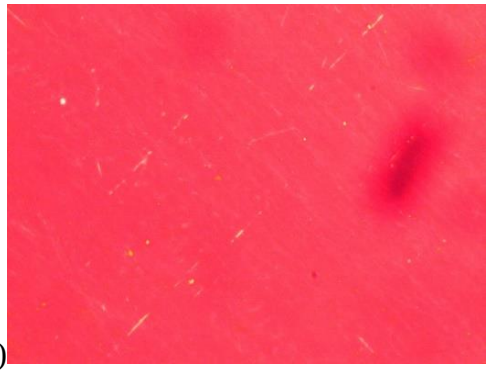

g) 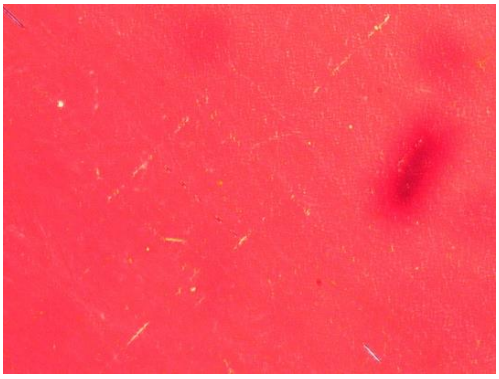 h) 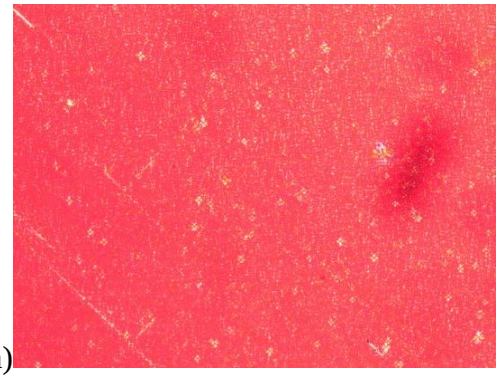

Figure 5-7: a,b,c,d) Photomicrographs of **QL22-8/8-2,6F2** in the nematic phase at $T - T_{N-I}$ = -5 K under an applied field of 0, 1, 3, 8 V/μm, respectively. e,f,g,h) Photomicrographs of **QL29-8/8-2,6F2** in the nematic phase at $T - T_{N-I}$ = -5 K under an applied field of 0, 1, 3, 8 V/μm, respectively.

In the case of **QL29-m/n-2,6F2**, a lower concentration of dopant can be used in switching experiments to tune θ_{opt} (E), as shown in Figure 5-8.

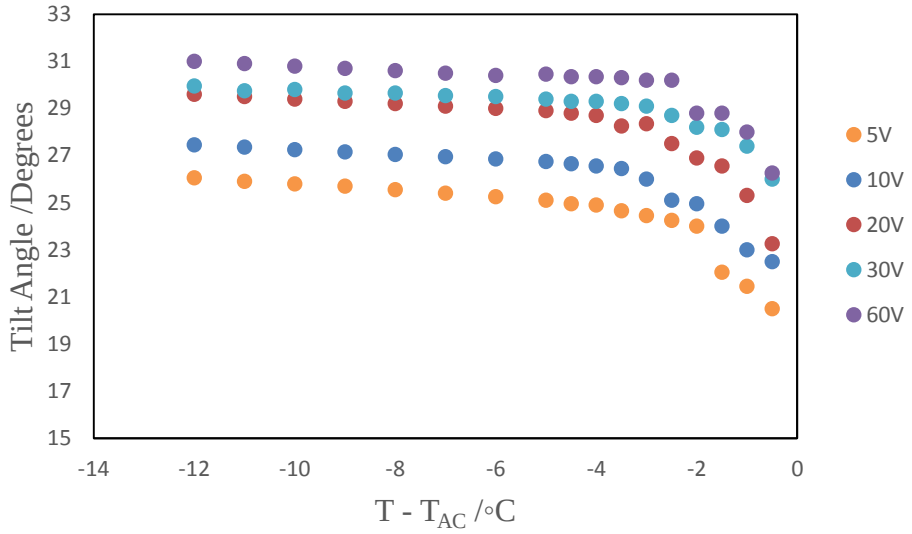

Figure 5-8: Tilt angle measurements with varying applied field for **QL29-8/8-2,6F2**

In these experiments, the data suggests that a tunable tilt angle is possible and an optimal tilt angle of 22.5 degrees can be obtained in SmC-N materials, due to the phenoxy end-group.

Although bistability is lost due to the difference in energy between the two switching states, as the director **n** is oriented along the rubbing directing and when the director **n** is oriented away from the rubbing direction.

5.3 Optical Switching Experiments

In Chapter 3, the **QL22** mesogens were found to have high positive dielectric anisotropy causing the molecules to "flip" instead of uniformly switching. While the switching of the **QL22-8/8-2,6F$_2$** mesogen had to be kept to a low voltage when using 2-5 mol% **MDW797** due to high positive dielectric anisotropy, the switching experiments worked surprisingly well. The POM pictures of the light and dark states, switching between $+\theta$ to $-\theta$, of **QL22-8/8-2,6F$_2$** are shown in Figure 5-9.

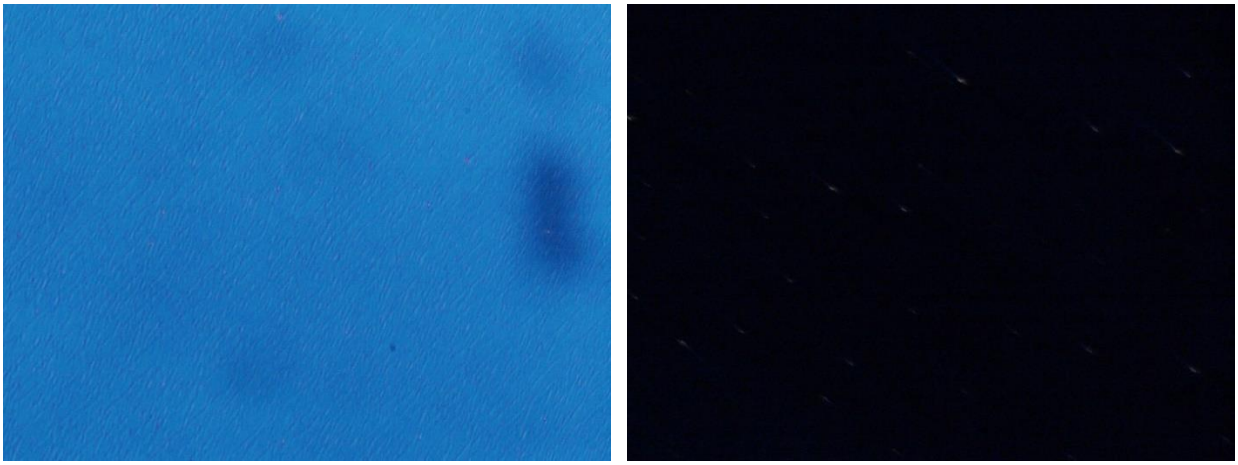

Figure 5-9: Photomicrographs of **QL22-8/8-2,6F$_2$** switching between $+\theta$ and $-\theta$ applied fields.

The **QL29-8/8-2,6F$_2$** mesogen has a negative dielectric anisotropy. The switching experiments for the **QL29** derivatives were performed for switching between $+\theta$ and $-\theta$ values in partially aligned samples to show contrast of switching states, as shown in Figure 5-10.

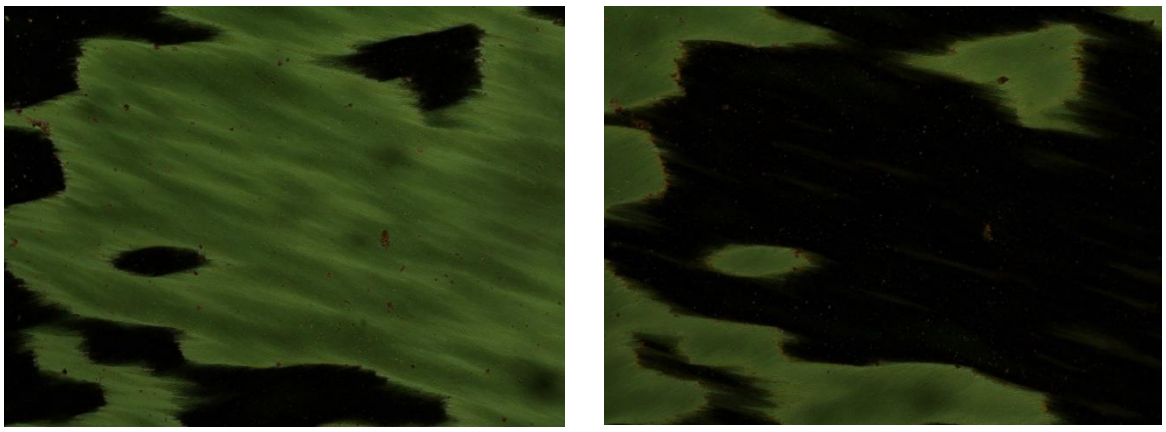

Figure 5- 10: Photomicrographs of aligned **QL29-8/8-2,6F$_2$** switching between + θ (left) and – θ (right) applied fields.

Chapter 6: Structure-Property Relationships of Phenoxy and Fluorophenoxy Mixtures

6.1 QL27-8/8 and QL11-8/8 Mixing Experiments

In order to test the validity of the interactions of the phenoxy groups within the layer structure, as well as stabilize the SmC phase in fluorophenoxy-terminated mesogens, several mixtures of phenoxy- and fluorophenoxy-terminated liquid crystals were investigated to determine if the SmC phase could be further stabilized by non-covalent interactions of the end-groups.

The first experiment involves mixing the perfluorophenoxy mesogen (**QL27-8/8**) with the phenoxy mesogen (**QL11-8/8**) which should, in principle, promote stronger in-layer interfacial interactions by virtue of the strong electrostatic attraction of perfluorophenyl and phenoxy groups and further promotion of the smectic phases, as well as nanosegregation. Hence, **QL27-8/8** and **QL11-8/8** were mixed together in various proportions to form a phase diagram shown in Figure 6-1. This phase diagram shows that the melting point is much lower when an increased percentage of **QL27-8/8** is added to the mixture.

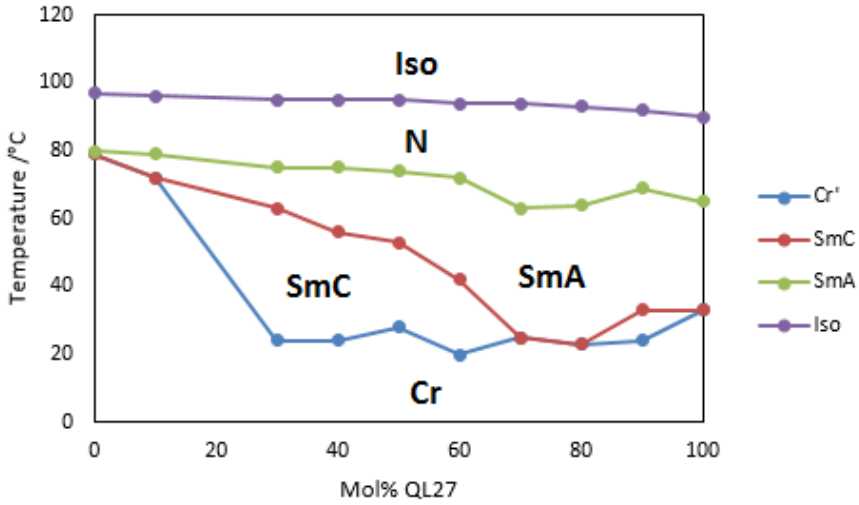

Figure 6-1: Phase diagram of a mixture of **QL11-8/8** and **QL27-8/8** taken by DSC on heating.

The phase diagram does not show a thermal stabilization of the SmC phase at 50% where arene-arene interactions of the perfluorophenoxy/phenoxy end-groups should be maximized. On closer examination of the phase transitions by DSC, as shown in Figure 6-2, the mixtures were found to be heterogeneous and exhibited two different melting peaks. These DSC peaks show that the compounds melt separately, which may be the reason there is a lack of stabilization observed in these mixtures.

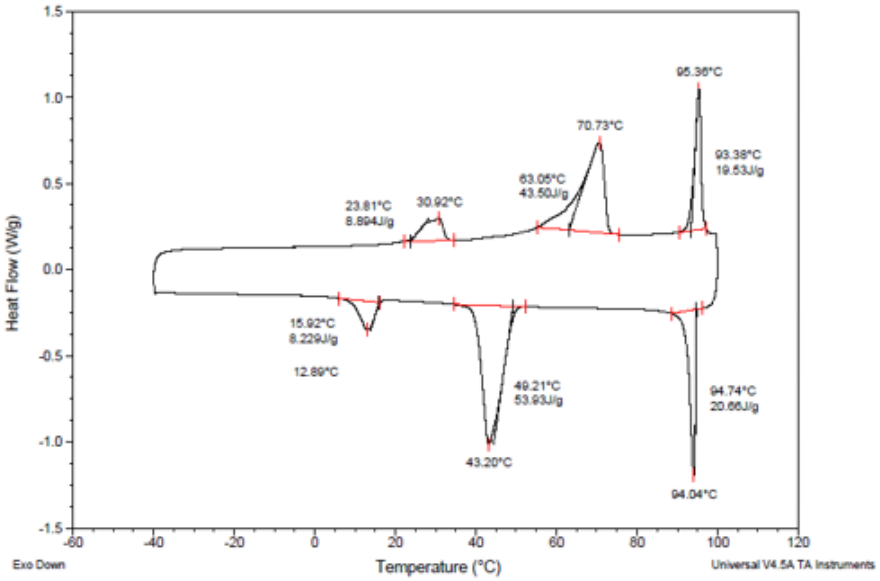

Figure 6-2: 30% **QL27-8/8** / **QL11-8/8** mixture DSC profile showing two melting and crystallization peaks.

6.2 50% QL22-8/8-2,6F$_2$ / QL23-8/8 Mixing Experiment

The **QL22-8/8-2,6F$_2$** / **QL23-8/8-2,6F$_2$** phase diagram (Figure 6-4) shows that a SmC-N phase transition can be observed in a 50:50 mixture of **QL22-8/8-2,6F$_2$ / QL23-8/8-2,6F$_2$**. This shows the potential use of these systems as room temperature SmC*-N devices. The POM pictures of the 50:50 mixture show a very light Schlieren texture, as shown in Figure 6.3.

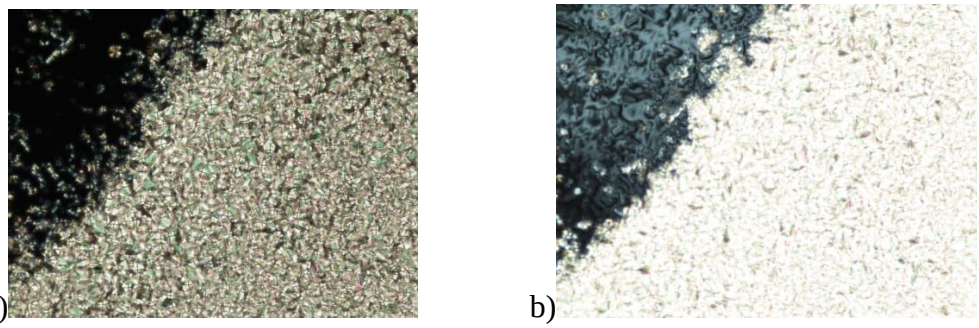

Figure 6-3: Photomicrograph of 50% **QL22-8/8-2,6F$_2$ / QL23-8/8-2,6F$_2$**. a) SmA phase b) SmC phase with increased light intensity to increase visibility of the Schlieren.

As previously stated, the high positive dielectric anisotropy of the 2-phenylpyrimidine core, combined with the 2,6-difluorophenoxy end-group renders these mesogens with SmC-N transitions useless for device applications. In this case the high dipole created by the 2,6-difluorophenoxy end-group in **QL23-8/8-2,6F2** is reduced by the dipole moment of the 2-PhP core in the opposite orientation. This decrease in dielectric anisotropic of the mixture allows for optical switching and observation of θ_{opt} (E). As described in Chapter 4, the material was doped with a chiral dopant and the minimum and maximum tilt angles were observed and are shown in Figure 6-5.

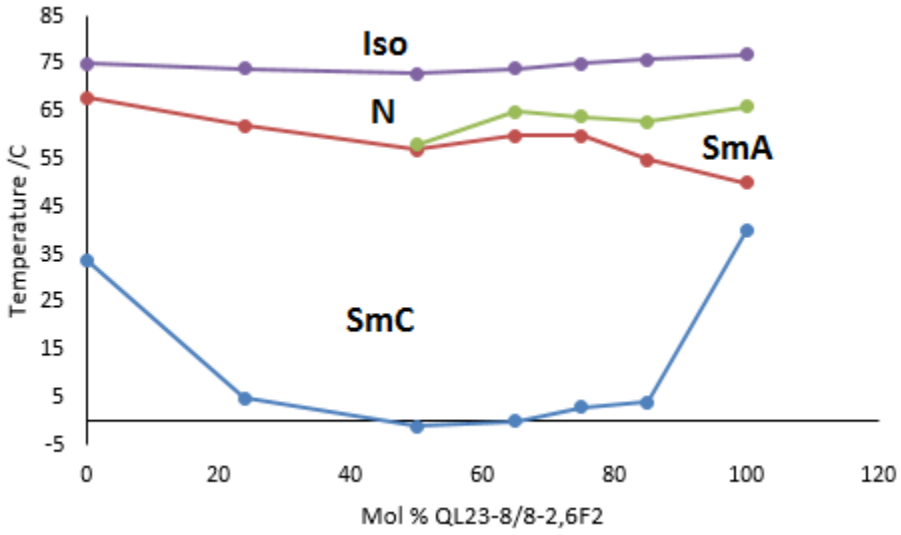

Figure 6-4: Phase diagram of **QL22-8/8-2,6F2** and **QL23-8/8-2,6F2** mixtures

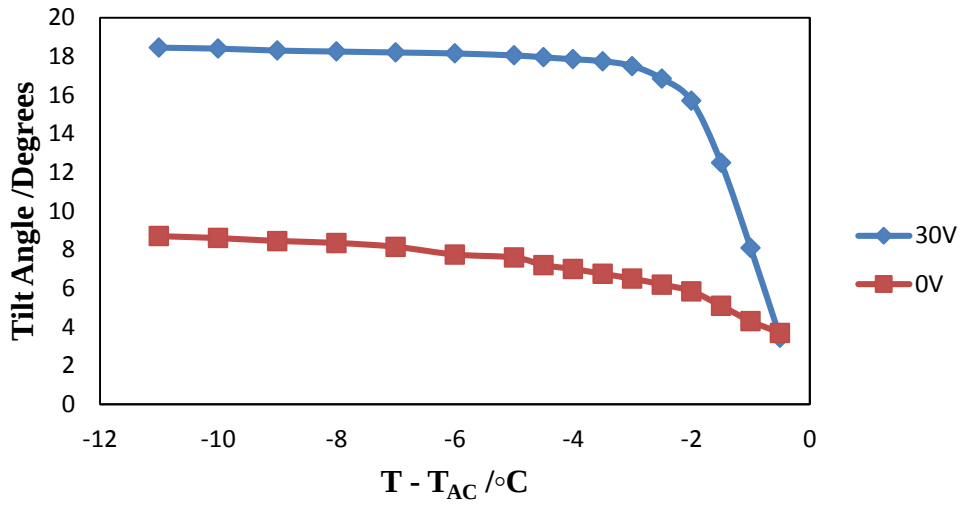

Figure 6-5: Optical Tilt angle measurements θ_{opt} (T) and θ_{opt}(E_{max}) for 50% mixture of **QL22-8/8-2,6F$_2$ / QL23-8/8-2,6F$_2$**.

The tilt angle measurements show, for the neat system, that the tilt angle is very low for a SmC-N mixture. The tilt angle and POM images show the characteristics of a pseudo SmA phase due to low starting tilt and overall tilt angles. On application of an applied field the optical tilt increases to approximately 9.8 degrees at $T - T_{AC}$ = -10. The very low θ_{opt} (T) tilt of these compounds allows for a unique use in applications. The SAXS data showing the maximum layer contraction of these mixtures are shown in Figure 6-6.

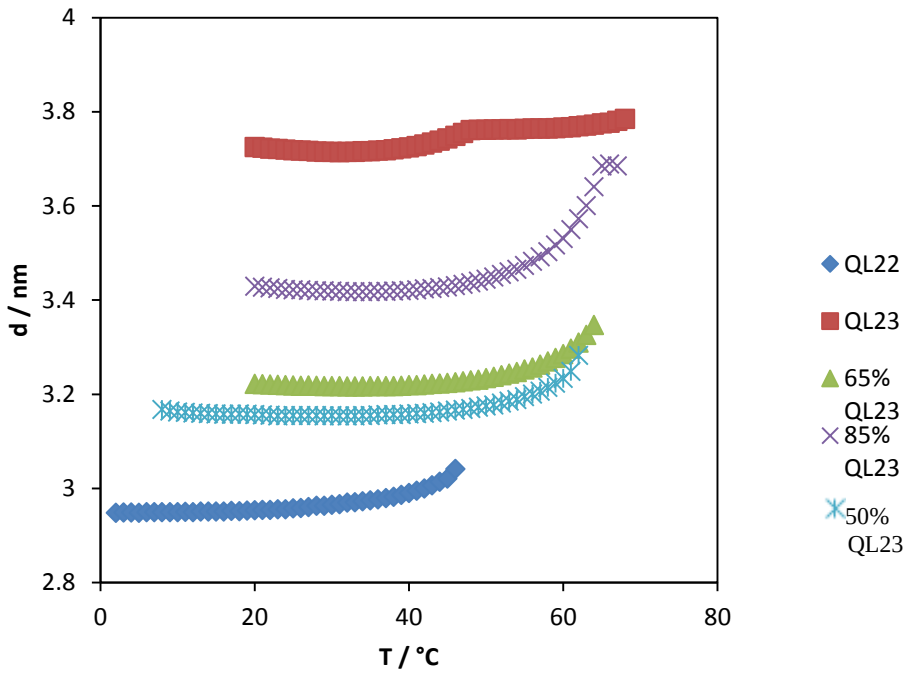

Figure 6-6: Small-angle X-ray scattering experiments showing layer spacing of **QL22-8/8-2,6F2** / **QL23-8/8-2,6F2** mixtures on cooling from isotropic liquid.

The SAXS data shows the change in layer spacing decreases as the mol fraction of **QL22-8/8-2,6F2** is increased. It also shows that the layer contraction of these materials, when fully tilted, is 3%, as shown in Figure 6-6. In the surface stabilized cell, these mesogens should have a decreased layer shrinkage. It is important to remember that the molecules in these compounds will only be completely bistable at low applied fields, near θ_{opt} (E) = θ_{opt} (T) due to an increase in tilt with increasing applied electric field E, when θ_{opt} (T) is equal to or approximately θ_{opt} (E). While pushing the system to the maximum tilt is possible with increased applied field this is not ideal for applications due to the increased power consumption cost and the decreased bistablility.

The mixture was found to align well without the formation of chevrons in a rubbed poly(imide) cell. When a large electric field is applied the mixture switches between light and dark states. Alignment and switching of this mixture is shown in Figure 6-7.

a) 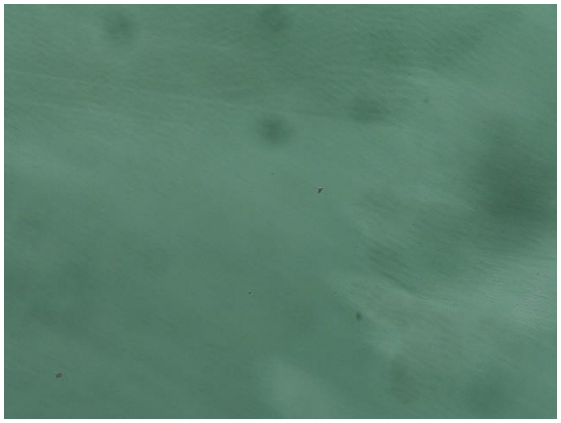 b) 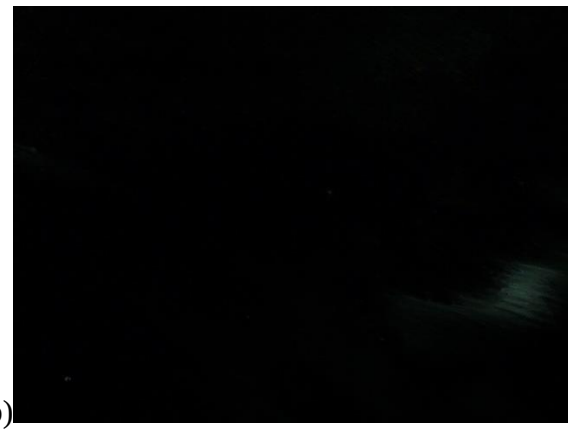

Figure 6-7: POM pictures of 1:1 mixture of **QL22-8/8-2,6F$_2$** / **QL23-8/8-2,6F$_2$** in (a) bright state and (b) dark state

Chapter 7: Experimental:

7.1 General Experimental:

^{1}H and ^{13}C NMR spectra were recorded using Bruker Avance 300 and 400 spectrometers; chemical shifts (δ) are reported in parts per million (ppm) relative to TMS. 1-Bromo-n-phenoxyalkanes were obtained by reaction of phenol with 1,n-dibromoalkanes under basic conditions, and n-phenoxyalkan-1-ols were obtained via Mitsunobu reactions of phenol with 1,n-alkanediols using triphenylphosphine and diisopropylcarbodiimide. All solvents and reagents were obtained from commercial sources and used without further purification unless otherwise noted. Anhydrous THF, hexane, ether, DMF and toluene were obtained from a Solv-Tek, Inc. solvent purification system or bought from commercial source. Mass spectra were recorded using Waters/Micromass GC-TOF (low- and high-resolution) and Applied Biosystems/MDS Sciex QSTAR XL QTOF (low-resolution) instruments in electron ionization (EI) mode. Differential scanning calorimetry (DSC) analyses were performed using a TA Instruments Q2000 instrument with a scanning rate of 5 K min^{-1} . Texture analyses were performed using a Nikon Eclipse E600 POL polarized microscope fitted with a Linkam LTS 350 hot stage and TMS 93 temperature controller. Optical tilt angles were measured as a function of temperature by polarized microscopy as half the rotation between the two extinction positions corresponding to opposite signs of an applied electric field using mixtures of liquid crystal and the chiral dopant (R,R)-2-(4-n-octylphenyl)-5-(2,3-difluorooctyloxy)pyrimidine (MDW797, 2-5 mol%). The mixtures were introduced into ITO glass cells with a low pretilt polyimide alignment substrate (< 1°, parallel rubbing, 4 μm spacing, E.H.C. Co,, Japan), and aligned by slow cooling from the isotropic phase to the chiral SmC* phase. Small-angle X-ray scattering experiments were performed on a SAXSess system from Anton Paar

GmbH. Unaligned samples (filled into Hilgenberg Mark capillary tubes of 0.7 mm diameter) were mounted in a temperature controlled sample holder unit (TSC 120). The X-ray beam from a ceramic tube generator was focused by a bent multilayer mirror and shaped by a line collimation block. The X-ray scattering was recorded with a CCD detector (Princeton Instruments SCX-TE-4300K/2) and processed and analysed using the SAXSquant 3.5 software. The monodomain 2D X-ray scattering analyses were performed on a Bruker Nanostar X-ray diffractometer (CuKα radiation, beam diameter 100 μm, HiStar 2D-detector). The samples were filled into Hilgenberg Mark capillary tubes of 0.7 mm in diameter and placed in a temperature-controlled sample holder. After gently cooling the sample from the isotropic to the smectic phase, several large smectic monodomains with different directions of **z** grew inside the capillary. Using the motorized x,y position control of the sample holder, the sample was screened until the X-ray beam probed a scattering volume containing either a single monodomain or several monodomains having the same directions of **z** and **n**.

7.2 Synthesis and Characterization

General procedure for the synthesis of 1-bromo-*n*-phenoxyalkanes (3-*n*). Under a N_2 atmosphere, phenol (1.0 g, 10.6 mmol) was combined with cesium carbonate (5.2 g, 15.9 mmol) in dry acetonitrile (100 mL). After stirring for 5 min, the appropriate dibromoalkane (15.9 mmol) was added to the mixture, which was heated to reflux overnight. The mixture was concentrated, dissolved in ethyl acetate (40 mL), poured onto 10% aq HCl (50 mL) and extracted with EtOAc (2 x 40 mL). The combined organic extracts were washed with sat aq $NaHCO_3$, water, brine, then dried ($MgSO_4$) and concentrated. Purification by flash chromatography on silica gel (0%-15% EtOAc/Hexane) afforded the phenoxy-terminated 1-bromoalkane.

1-Bromo-4-phenoxybutane (3-4). White crystals, 26% yield: ^{1}H NMR (400MHz, $CDCl_3$) δ 7.39-7.24 (m, 2H), 7.02-6.87 (m, 3 H), 4.03 (t, J = 6.1 Hz, 2H), 3.52 (t, J = 6.6 Hz, 2H), 2.16-2.06 (m, 2H), 2.04-1.93 (m, 2H); ^{13}C NMR (100 MHz, $CDCl_3$) δ 158.9, 129.5, 120.8, 114.5, 66.7, 33.5, 29.5, 28.0; MS (EI) *m/z* 230 (M+2, 19), 228 (M+, 19), 137 (70), 134 (71), 107 (11), 94 (100), 77 (26), 65 (31), 55 (50), 51(14); HRMS (EI) *m/z* calcd for $C_{10}H_{13}O^{79}Br$ 228.0150, found 228.0143.

1-Bromo-5-phenoxypentane (3-5). Colorless oil, 15% yield: ^{1}H NMR (400 MHz, $CDCl_3$) δ 7.43-7.23 (m, 2H), 7.05-6.89 (m, 3H), 4.02 (t, J = 6.7 Hz, 2H), 3.47 (t, J = 6.7 Hz, 2H), 2.03-1.93 (m, 2H), 1.89-1.82 (m, 2H), 1.72-1.63 (m, 2H); ^{13}C NMR (100 MHz, $CDCl_3$) δ 158.9, 129.4, 120.5, 114.8, 66.9, 33.6, 32.4, 28.4, 24.8; MS (EI) *m/z* 244 (M+2, 18), 242 (M+, 13), 149 (22), 107 (9), 94 (100), 77 (18), 69 (30), 65 (17); HRMS (EI) *m/z* calcd for $C_{11}H_{15}O^{79}Br$ 242.0306, 244.0287 found 242.0316, 244.0283.

1-Bromo-6-phenoxyhexane (3-6). Colorless oil, 25% yield: ^{1}H NMR (400 MHz, $CDCl_3$) δ 7.48-7.28 (m, 2H), 7.10-6.90 (m, 3H), 4.02 (t, J = 6.4 Hz, 2H), 3.48 (t, J = 6.7 Hz, 2H), 2.07-1.93 (m, 2H), 1.93-1.80 (m, 2H), 1.64-1.50 (m, 4H); ^{13}C NMR (100 MHz, $CDCl_3$) δ 159.1, 129.5, 120.6, 114.6, 67.7, 67.7, 32.8, 29.2, 28.0, 25.4; MS (EI) *m/z* 258 (M+2, 16), 256 (M+, 17), 165 (7), 107 (9), 94 (100), 77 (15), 65 (15); HRMS (EI) *m/z* calcd for $C_{12}H_{17}O^{79}Br$ 256.0463, 258.0443 found 256.0473, 258.0435.

General procedure for the synthesis of *n*-phenoxy-1-alkanols (4-*n*). Under a N_2 atmosphere, phenol (1.0 g, 10.6 mmol) was combined with the appropriate alkanediol (15.9 mmol) and triphenylphosphine (4.17 g, 15.9 mmol) in dry THF (100 mL). After stirring for 5 min, DIAD (3.21 g, 3.1 mL, 15.9 mmol) was added dropwise over 5 min. The mixture was stirred at room temperature overnight, then concentrated and purified by flash chromatography on silica gel **(0%-**

15% EtOAc/Hexane) to give the phenoxy-terminated alkan-1-ol as a yellow solid. The product was recrystallized from acetonitrile and then from hexanes to give a white solid.

7-Phenoxy-1-heptanol (4-7). White crystals, 45.5% yield: ^{1}H NMR (400 MHz, $CDCl_3$) δ7.31-7.23 (m, 2H), 6.97-6.82 (m, 3H), 3.95 (t, *J* = 6.52 Hz, 2H), 3.64 (t, *J* = 6.6 Hz, 2H), 1.83-1.72 (m, 2H), 1.63-1.53 (m, 2H), 1.53-1.43 (m, 2 H) 1.43-1.34 (m, 4H);^{13}C NMR (100 MHz, $CDCl_3$) δ 159.1, 129.4, 120.5, 114.5, 67.8, 53.0, 32.7, 29.23, 29.18, 26.0, 25.7. MS (EI) *m/z* 208 (M+, 24), 94 (100), 77 (13), 55 (24); HRMS (EI) *m/z* calcd for $C_{13}H_{20}O_2$ 208.1463, found 208.1473.

8-Phenoxy-1-octanol (4-8). White crystals, 53% yield: ^{1}H NMR (400 MHz, $CDCl_3$) δ, 7.28-7.12 (m, 2H), 6.92-6.79 (m, 3H), 3.88 (t, *J* = 6.6 Hz, 2H), 3.56 (t, *J* = 6.6 Hz, 2H), 1.79-1.65 (m, 2H), 1.56-1.25 (m, 10H); ^{13}C NMR (100 MHz, $CDCl_3$) δ 159.1, 129.4, 120.5, 114.5, 67.9, 63.0, 32.8, 29.2, 29.1, 25.8, 25.5; MS (EI) *m/z* (222 ([M+H]+, 222(21), 103(11), 94(100), 86(39), 84(58), 76(14), 69(15), 55(15), 51(27) HRMS (EI) m/z calcd for $C_{14}H_{22}O_2$, 222.1620 found 222.1611

9-Phenoxy-1-nonanol (4-9). White crystals, 44% yield: ^{1}H NMR (400MHz, $CDCl_3$) δ 7.29-7.13 (m, 2H), 6.93-6.77 (m, 3H), 3.88 (t, *J* = 6.6 Hz, 2H), 3.57 (t, *J* = 6.6 Hz, 2H), 1.82-1.63 (m, 2H), 1.61-1.08 (m, 12H); ^{13}C NMR (100 MHz, $CDCl_3$) δ 159.1, 129.4, 120.5, 114.5, 67.9, 63.1, 32.8, 29.5, 29.35, 29.32, 29.29, 26.1, 25.8; MS (EI) m/z (236 ([M+H]+, 236(23), 94(100), 69(11), 55(16) HRMS (EI) m/z calcd for C15H24O2, 236.1776 found 236.1765.

10-Phenoxy-1-decanol (4-10). White crystals, 29% yield: ^{1}H NMR (400MHz, $CDCl_3$) δ7.30–7.16(m, 2H), 6.92-6.79 (m, 3H), 3.87 (t, *J* = 6.6 Hz, 2H), 3.57 (t, *J* = 6.6 Hz, 2H), 1.76-1.64 (m, 2H), 1.54-1.43 (m, 2H), 1.42-1.16 (m, 12H); ^{13}C NMR (100 MHz, $CDCl_3$) δ159.1, 129.4, 120.5, 114.5, 67.9, 63.1, 32.8, 29.53, 29.50, 59.41, 29.40, 29.38, 29.30, 26.1, 25.7; MS (EI) *m/z* 250 (M+, 24), 94 (100), 55 (18); HRMS (EI) *m/z* calcd for $C_{16}H_{26}O_2$ 250.1933, found 250.1926.

10-Phenoxy-1-undecanol (4-11). White crystals, 41% yield: ^{1}H NMR (400 MHz, $CDCl_3$) δ 7.35-7.21 (m, 2H), 7.03-6.85 (m, 3H), 3.98 (t, J = 6.6 Hz, 2H), 3.66 (t, J = 6.6 Hz, 2H), 1.84-1.73 (m, 2H), 1.68-1.51 (m, 2H), 1.50-1.23 (m, 14H); ^{13}C NMR (100 MHz, $CDCl_3$) δ 159.2, 129.4, 120.5, 114.5, 67.9, 63.1, 32.8, 29.59, 29.55, 29.51, 29.43, 29.40, 29.3, 26.1, 25.8; MS (EI) *m/z* 264 (M+, 26), 94 (100), 55 (20); HRMS (EI) *m/z* calcd for $C_{17}H_{28}O_2$ 264.2089, found 264.2095.

12-Phenoxy-1-dodecanol (4-12). White crystals, 18% yield: ^{1}H NMR (400 MHz, $CDCl_3$) δ 7.30-7.14 (m, 2H), 6.92-6.74 (m, 3H), 3.88 (t, J = 6.6 Hz, 2H), 3.57 (t, J = 6.6 Hz, 2H), 1.80-1.63 (m, 2H), 1.58-1.34 (m, 4H), 1.29-1.16 (m, 14H); ^{13}C NMR (100 MHz, $CDCl_3$) δ **xxx ?**, 129.4, 120.5, 114.5, 67.9, 63.1, 32.8, 29.60, 29.56, 29.45, 29.40, 29.3, 26.1, 25.8; MS (EI) *m/z* 278 (M+, 27), 94 (100), 55 (18); HRMS (EI) *m/z* calcd for $C_{18}H_{30}O_2$ 278.2246, found 278.2236.

General procedure for the synthesis of 2-(4-hydroxyphenyl)-5-(*n*-phenoxy-1-alkyloxy)-pyrimidine (5-*n*). Method A. Under a N_2 atmosphere, 2-(4-hydroxyphenyl)pyrimidin-5-ol (0.187 g, 1.0 mmol) was combined with **4-*n*** (0.9 mmol) and triphenylphosphine (0.235 g, 0.9 mmol) in dry THF (40 mL). After stirring the solution for 5 min, DIAD (0.181 g, 0.18 mL 0.91 mmol) were added dropwise over 5 min. The mixture was stirred at room temperature overnight, and then concentrated and purified by flash chromatography on silica gel **(0%-20% EtOAc/Hexane)** to give **5-*n*** as a yellow solid. The product was recrystallized from acetonitrile and then from hexanes to give a white solid.

2-(4-Hydroxyphenyl)-5-(7-phenoxy-1-heptyloxy)pyrimidine (5-7). White solid, 44% yield: ^{1}H NMR (400 MHz, $CDCl_3$) δ 8.37 (s, 2H), 8.20 (d, J = 8.8 Hz, 2H), 7.23-7.20 (m, 2H), 6.89-6.85 (m, 3H), 6.83 (d, J = 8.8 Hz, 2H), 4.02 (t, J = 6.4 Hz, 2H), 3.90 (t, J = 6.4 Hz, 2H), 1.82-1.66 (m, 2H), 1.65-1.32 (m, 4H), 1.32-1.14 (m, 4H); ^{13}C NMR (100 MHz, $CDCl_3$) δ 159.1, 157.7,

157.6, 151.2 143.9, 130.0, 129.43, 129.40 120.6, 115.56, 114.5, 68.9, 67.7, 29.2, 29.07, 29.06, 29.04, 26.0, 25.8; MS (EI) *m/z* 378 (M+, 33), 188 (100), 119 (15), 94 (72), 84 (36), 77 (17), 73 (15), 69 (20), 67 (10), 55 (49) 50 (20); HRMS (EI) *m/z* calcd for $C_{23}H_{26}N_2O_3$ 378.1943, found 378.1929.

2-(4-Hydroxyphenyl)-5-(8-phenoxy-1-octyloxy)pyrimidine (5-8). White solid, 38% yield: ^{1}H NMR (400 MHz, $CDCl_3$) δ 8.34 (s, 2H), 8.09 (d, J = 8.8 Hz, 2H), 7.23-7.17 (m, 2H), 6.88-6.74 (m, 5H), 3.98 (t, J = 6.4 Hz, 2H), 3.88 (t, J = 6.4 Hz, 2H), 1.80-1.66 (m, 4H), 1.40 (m, 4H), 1.36-1.29 (m, 4H);^{13}C NMR (100 MHz, $CDCl_3$) δ 160.0, 159.1, 157.6, 154.4, 151.2, 143.9, 129.38, 129.37, 120.5, 115.6, 114.5, 69.0, 67.8, 29.29, 29.27, 29.26, 29.24, 26.0, 25.8 MS (EI) *m/z* 392 (M+, 49), 188 (100), 132 (11), 119 (14), 94 (47), 77 (14), 69 (18), 55 (18); HRMS (EI) *m/z* calcd for $C_{24}H_{28}N_2O_3$ 392.2100, found 392.2087.

2-(4-Hydroxyphenyl)-5-(9-phenoxy-1-nonyloxy)pyrimidine (5-9). White solid, 74% yield: ^{1}H NMR (400 MHz, $CDCl_3$) δ 8.44 (s, 2H), 8.23 (d, J = 8.8 Hz, 2H), 7.34-7.23 (m, 2H), 6.98-6.87 (m, 5H), 4.10 (t, J = 6.4 Hz, 2H), 3.98 (t, J = 6.6 Hz, 2H), 1.96-1.74 (m, 4H), 1.57-1.34 (m, 10H); ^{13}C NMR (100 MHz, $CDCl_3$) δ 151.1,143.9, 129.4, 129.3, 115.5, 114.5, 69.1, 67.8, 29.4, 29.31, 29.30, 29.29, 29.1 26.0, 25.8 MS (EI) m/z (406 ([M+H]+, 406(71), 313(16), 300(19), 257(15), 243(12), 201(18), 188(100), 94(19), 69(11), 55(11) HRMS (EI) m/z calcd for C25H30O3N2, 406.2256 found 406.2239.

2-(4-hydroxyphenyl)-5-(10-phenoxy-1-decyloxy)pyrimidine (5-10). White solid, 75% yield: ^{1}H NMR (400 MHz ,$CDCl_3$) δ 8.35 (s, 2H), 8.16 (d, J = 8.8 Hz, 2H), 7.24-7.17 (m, 3H), 6.86-6.76 (m, 5H), 4.01 (t, J = 6.4 Hz, 2H), 3.88 (t, J = 6.6 Hz, 2H), 1.84-1.62 (m, 4H), 1.47-1.15 (m, 12H); ^{13}C NMR (100 MHz, $CDCl_3$) δ 159.1,151.2, 143.8,129.4, 120.5, 115.6, 114.5, 69.1, 67.9, 29.47, 29.44, 29.40, 29.3, 29.29, 29.1, 26.1, 25.9; MS (EI) *m/z* 420 (M+, 35), 327 (13), 314

(15), 201 (28), 188 (100), 132 (12), 119 (16), 94 (57), 77 (14), 55 (24); HRMS (EI) *m/z* calcd for $C_{26}H_{32}O_3N_2$ 420.2413; found 420.2398.

2-(4-Hydroxyphenyl)-5-(11-phenoxy-1-undecyloxy)pyrimidine (5-11). White solid, 50% yield: ^{1}H NMR (400 MHz, $CDCl_3$) δ 8.36 (s, 2H), 8.19 (d, J = 8.6 Hz, 2H), 7.24-7.18 (m, 2H), 6.89-6.80 (m, 5H), 4.01 (t, J = 6.4 Hz, 2H), 3.88 (t, J = 6.6 Hz, 2H), 1.81-1.66 (m, 4H), 1.40-1.16 (m, 14H); ^{13}C NMR (100 MHz, $CDCl_3$) δ159.1,151.1,143.9, 129.4, 129.0, 120.4, 115.5, 114.5, 67.9, 67.9, 29.56, 29.55, 29.54, 29.513, 29.507, 29.49, 29.40, 29.39, 29.1, 26.1, 26.0, 25.9; MS (EI) *m/z* 434 (M+, 31), 341 (12), 328 (12), 201 (20), 188 (100), 119 (13), 94 (45), 55(18); HRMS (EI) *m/z* calcd for $C_{27}H_{34}O_3N_2$ 434.2570, found 434.2558 .

2-(4-Hydroxyphenyl)-5-(12-phenoxy-1-dodecyloxy)pyrimidine (5-12). White solid, 57% yield: ^{1}H NMR (400 MHz, $CDCl_3$) δ 8.35 (s, 2H), 8.16 (d, J = 8.6 Hz, 2H), 7.26-7.16 (m, 3H), 6.88-6.79 (m, 5H), 4.01 (t, J = 6.6 Hz, 2H), 3.88 (t, J = 6.6 Hz, 2H), 1.79-1.65 (m, 4H), 1.43-1.15 (m, 16H); ^{13}C NMR (100 MHz, $CDCl_3$) δ 159.1,157.5, 151.2, 143.9, 129.4, 129.3, 120.5, 115.5, 114.5, 69.0, 67.9, 29.6, 29.54, 29.51, 29.4, 29.3, 29.1, 26.1, 25.9; MS (EI) *m/z* 448 (M+, 20), 355 (15), 342 (16), 201 (16), 188 (100), 199 (11), 94 (43), 55 (18); HRMS (EI) *m/z* calcd for $C_{28}H_{36}O_3N_2$ 448.2726, found 448.2713.

Method B. Under a N_2 atmosphere, 2-(4-hydroxyphenyl)pyrimidin-5-ol (0.187 g, 1.0 mmol) was combined with cesium carbonate (0.293 g, 0.9 mmol) in dry DMF (40 mL). After stirring for 5 min, **3-*n*** (0.9 mmol) was added to the mixture, which was stirred at room temperature overnight. The mixture was then concentrated, dissolved in EtOAc (40 mL), poured onto 10% aq HCl (50 mL) and extracted with EtOAc (2 x 40 mL). The combined organic extracts were washed with sat aq $NaHCO_3$, water, and brine, then dried ($MgSO_4$) and concentrated. Purification by flash

chromatography on silica gel **(0%-20% EtOAc/Hexane)** gave **5-*n*** as a yellow solid. The product was recrystallized from acetonitrile and then from hexanes to give a white solid.

2-(4-Hydroxyphenyl)-5-(4-phenoxy-1-butyloxy)pyrimidine (5-4). White solid, 54% yield: ^{1}H NMR (400 MHz, $CDCl_3$) δ 8.35 (s, 2H), 8.18 (d, J = 8.6 Hz, 2H), 7.26-7.16 (m, 2H), 6.92-6.79 (m, 5H), 4.11 (t, J = 5.8 Hz, 2H), 3.99 (t, J = 5.7 Hz, 2H), 2.03-1.86 (m, 4H); ^{13}C NMR (100 MHz, 1:1 DMSO-d_6:C_6D_6) δ 159.8, 158.9, 150.9, 143.9, 129.4, 129.0, 120.4, 115.5, 114.5, 68.2, 66.9, 25.5, 25.4; MS (EI) *m/z* 336 (M+, 69),188 (38), 159 (13), 149 (88), 132 (23), 119 (17), 107 (100), 94 (53), 77 (39), 65 (15), 55 (30); HRMS (EI) *m/z* calcd for $C_{20}H_{20}N_2O_3$ 336.1474, found 336.1459

2-(4-Hydroxyphenyl)-5-(5-phenoxy-1-pentyloxy)pyrimidine (5-5). White solid, 31% yield: ^{1}H NMR (300 MHz, $CDCl_3$) δ 8.44 (s, 2H), 8.18 (d, J = 9 Hz, 2H), 7.34-7.25 (m, 2H), 7.00-6.84 (m, 5H), 4.10 (t, J = 6 Hz, 2H), 4.01 (t, J = 6 Hz, 2H), 1.98-1.82 (m, 4H) 1.75-1.62 (m, 2H).

2-(4-Hydroxyphenyl)-5-(6-phenoxy-1-hexyloxy)pyrimidine (5-6). White solid, 29% yield: ^{1}H NMR (300 MHz, $CDCl_3$) δ 8.56 (s, 2H), 8.43 (d, 2H), 7.33 (m, 2H), 7.02-6.85 (m, 5H), 4.16 (t, 2H), 4.01 (t, 2H), 2.10-1.90 (m, 4H), 1.54-1.90 (m, 4H).

General procedure for the synthesis of 5-(1-alkyloxy)-2-(4-hydroxyphenyl)pyrimidine (6-*n*). The procedure described for the synthesis of **5-*n*** according to Method A was repeated with 2-(4-hydroxyphenyl)pyrimidin-5-ol and the appropriate alkan-1-ol to give **6-*m*** (n = 4, 5, 6, 7, 8, 9, 12); the procedure described for the synthesis of **5-*n*** according to Method B was repeated with 2-(4-hydroxyphenyl)pyrimidin-5-ol and the appropriate 1-bromoalkane to give **6-*m*** (n = 10, 11).

5-(1-Butyloxy)-2-(4-hydroxyphenyl)pyrimidine (6-4). White solid, 48% yield: ^{1}H NMR (400 MHz, $CDCl_3$) δ 8.35 (s, 2H), 8.17 (d, J = 8.8 Hz, 2H), 6.87-6.81 (d, J = 8.8 Hz, 2H), 4.02 (t, J = 6.6 Hz, 2H), 1.81-1.70 (m, 2H), 1.50-1.40 (m, 2H), 0.93 (t, J = Hz, 3H); ^{13}C NMR (100 MHz,

$CDCl_3$) δ 158.1, 151.2, 143.9, 129.3, 115.6, 68.7, 31.1, 22.0, 13.9; MS (EI) *m/z* 244 (M+, 41), 188 (100), 119 (27), 105 (13); HRMS (EI) *m/z* calcd for $C_{14}H_{16}N_2O_2$ 244.1212, found 244.1219.

2-(4-Hydroxyphenyl)-5-(1-pentyloxy)pyrimidine (6-5). White solid, 63% yield: ^{1}H NMR (400 MHz, $CDCl_3$) δ 8.35 (s, 2H), 8.17 (d, *J* = 8.7 Hz, 2H), 6.30 (d, *J* = 8.7 Hz, 2H), 4.01 (t, *J* = 6.6 Hz, 2H), 1.84-1.71 (m, 2H), 1.45-1.28 (m, 4H), 0.87 (t, *J* = 7.1 Hz, 3H); ^{13}C NMR (100 MHz, $CDCl_3$) δ 157.5, 143.9, 129.3, 115.5, 68.3, 28.8, 22.4, 22.0, 13.6; MS (EI) *m/z* 258 (M+, 41), 188 (100),132 (13),119 (20); HRMS (EI) *m/z* calcd for $C_{15}H_{18}N_2O_2$ 258.1368, found 258.1359.

5-(1-Hexyloxy)-2-(4-hydroxyphenyl)pyrimidine (6-6). White solid, 62% yield: ^{1}H NMR (400 MHz, $CDCl_3$) δ 8.35 (s, 2H), 8.17 (d, *J* = 8.7, 2H), 6.77 (d, *J* = 8.7, 2H), 3.99 (t, *J* = 6.6 Hz, 2H), 1.78-1.69 (m, 2H), 1.44-1.35 (m, 2H), 1.29-1.23 (m, 4H), 0.84 (t, *J* = 7.6 Hz, 3H); ^{13}C NMR (100 MHz, $CDCl_3$) δ 158.1, 157.7, 151.2, 143.9, 129.5, 129.4, 115.7, 69.1, 31.5, 29.1, 25.5, 22.6, 14.0; MS (EI) *m/z* 272 (M+, 41),188 (100), 132 (10), 119 (16); HRMS (EI) *m/z* calcd for $C_{16}H_{20}N_2O_2$ 272.1525, found 272.1516.

5-(1-Heptyloxy)-2-(4-hydroxyphenyl)pyrimidine (6-7). White solid, 52% yield: ^{1}H NMR (400 MHz, $CDCl_3$) δ 8.35 (s, 2H), 8.16 (d, *J* = 8.8 Hz, 2H), 6.84 (d, *J* = 8.6 Hz, 2H), 4.01 (t, *J* = 6.4 Hz, 2H), 1.83-1.67 (m, 2H), 1.45-1.36 (m, 2H), 1.36-1.15 (m, 6H), 0.83 (t, *J* = 6.8 Hz, 3H); ^{13}C NMR (100 MHz, $CDCl_3$) δ 157.7, 151.2, 143.9, 129.9, 129.1, 115.7, 69.1, 31.7, 29.1, 25.8, 22.6, 14.1; MS (EI) *m/z* 286 (M+, 42),188 (100), 132 (11), 119 (15), 84 (13), 57 (12); HRMS (EI) *m/z* calcd for $C_{17}H_{22}N_2O_2$ 286.1681, found 286.1673.

2-(4-Hydroxyphenyl)-5-(1-octyloxy)pyrimidine (6-8). White solid, 73% yield: ^{1}H NMR (400 MHz, $CDCl_3$) δ 8.35 (s, 2H), 8.10 (d, *J* = 8.8 Hz, 2H), 6.78 (d, *J* = 8.8 Hz, 2H), 3.99 (t, *J* = 6.6 Hz, 2H), 1.78-1.69 (m, 2 H), 1.33-1.15 (m, 12H), 0.81 (t, *J* = 6.8 Hz, 3H), ^{13}C NMR (100 MHz, $CDCl_3$) δ 157.7, 151.2, 143.9, 129.8, 129.4, 115.6, 69.1, 31.8, 29.27, 29.19, 29.1 25.9, 14.1; MS

(EI) *m/z* 286 (M+, 42), 188 (100), 132 (11), 119 (15), 84 (13), 57 (12); MS (EI) m/z (392 ([M+H]+, 392(49),188(100), 132(11), 119(14), 94(47), 77(14), 69(18), 55(18) HRMS (EI) m/z calcd for C24H28N2O3, 392.2100 found 392.2087 .

2-(4-Hydroxyphenyl)-5-(1-nonyloxy)pyrimidine (6-9). White solid, 85% yield: ^{1}H NMR (400 MHz, $CDCl_3$) δ 8.35 (s, 2H), 8.13 (d, J = 8.3 Hz, 2H), 6.82 (d, J = 8.3 Hz, 2H), 4.00 (t, J = 6.6 Hz, 2H), 1.69-1.81 (m, 2H), 1.34-1.44 (m, 2H), 1.16-1.32 (m, 12H), 0.81 (t, J = 6.8 Hz, 3H); ^{13}C NMR (100 MHz, $CDCl_3$) δ 157.1, 151.2, 143.9, 129.4, 115.6, 69.1, 31.9, 29.5, 29.34, 29.31, 29.1, 25.9, 22.7, 14.1; MS (EI) *m/z* 314 (M+, 45), 188 (100), 132 (11), 119 (13). HRMS (EI) *m/z* calcd for $C_{19}H_{26}N_2O_2$ 314.1994, found 314.1986 .

5-(1-Decyloxy)-2-(4-Hydroxyphenyl)pyrimidine (6-10). White solid, 63% yield: ^{1}H NMR (300 MHz, $CDCl_3$) δ 9.01 (br s, 1H), 8.43 (s, 2H), 8.12 (d, J = 9 Hz, 2H), 6.84 (d, J = 9 Hz, 2H), 4.04 (t, J = 6 Hz, 2H), 1.89-1.73 (m, 2H), 1.51-1.21 (m, 14H), 0.89 (t, J = 6 Hz, 3H).

2-(4-Hydroxyphenyl)-5-(1-undecyloxy)pyrimidine (6-11). White solid, 52**%** yield: ^{1}H NMR (400 MHz, $CDCl_3$) δ 8.91 (br s, 1H), 8.31 (s, 2H), 8.02 (d, J = 9 Hz, 2H), 6.73 (d, J = 9 Hz, 2H), 3.92 (t, J = 6 Hz, 2H), 1.75-1.64 (m, 2H), 1.41-1.12 (m, 16H), 0.78 (t, J = 7 Hz, 3H).

5-(1-Dodecyloxy)-2-(4-Hydroxyphenyl)pyrimidine (6-12). White solid, 27**%** yield: ^{1}H NMR (400 MHz, $CDCl_3$) δ 8.36 (s, 2H), 8.17 (d, J = 8.8 Hz, 2H), 6.84 (d, J = 8.8 Hz, 2H), 4.01 (t, J = 6.44 Hz, 2H), 1.84-1.66 (m, 2H), 1.52-1.34 (m, 2H), 1.36-1.16 (m, 16H), 0.81 (t, J = 6.8 Hz, 3H); ^{13}C NMR (100 MHz, $CDCl_3$) δ 157.8, 157.6, 151.2, 143.9, 129.9, 129.4, 115.6, 69.0, 31.9, 29.65, 29.63, 29.62, 29.58, 29.53, 29.34, 29.32, 29.1, 25.9, 22.7, 14.1; MS (EI) *m/z* 356 (M+, 65), 188 (100), 159 (10), 119 (9), 57 (11); HRMS (EI) *m/z* calcd for $C_{22}H_{32}N_2O_2$ 356.2464, found 356.2453.

General procedure for the synthesis of 2-(4-(1-alkyloxy)phenyl)-5-(*n*-phenoxy-1-alkyloxy)pyrimidine (QL11-*m/n*). The procedure described for the synthesis of **5-*n*** according to Method A was repeated with **5-*n*** and the appropriate alkan-1-ol to give **QL11-*m/n*** (*m/n* = 12/4, 9/7-4/12); the procedure described for the synthesis of **5-*n*** according to Method B was repeated with **5-*n*** and the appropriate 1-bromoalkane to give **QL11-*m/n*** (*m/n* = 11/5, 10/6).

2-(4-(1-Dodecyloxy)phenyl)-5-(4-phenoxy-1-butyloxy)pyrimidine (QL11-4/12). White solid, 46% yield: ^{1}H NMR (400 MHz, C_6D_6) δ 8.93 (d, J = 8.6 Hz, 2H), 8.26 (s, 2H), 7.20-7.18 (m, 2H), 7.05 (d, J = 8.84 Hz, 2H), 6.90-6.83 (m, 3H), 3.67 (t, J = 6.44 Hz, 2H), 3.56 (t, J = 5.68 Hz, 2H), 3.31 (t, J = 5.5 Hz, 2H), 1.68-1.58 (m, 2H), 1.57-1.49 (m, 4H), 1.41-1.23 (m, 18H), 0.92 (t, J = 6.7 Hz, 3H); MS (EI) *m/z* 504 (M+, 100), 188 (14), 149 (89), 107 (52) , 94 (16), 55 (17); HRMS (EI) *m/z* calcd for $C_{32}H_{44}N_2O_3$ 504.3352, found 504.3376.

5-(5-Phenoxy-1-pentyloxy)-2-(4-(1-undecyloxy)phenyl)pyrimidine (QL11-5/11). White solid, 20**%** yield: ^{1}H NMR (400 MHz, $CDCl_3$) δ 8.35 (s, 2H), 8.20 (d, J = 8.8 Hz, 2H), 7.25-7.17 (m, 2H), 6.89 (d, J = 8.8 Hz, 2H), 6.87-6.82 (m, 3H), 4.04 (m, 4 H)**,** 3.94 (t, J = 6.4 Hz, 2H), 1.89-1.77 (m, 4H), 1.77-1.69 (m, 2H), 1.67-1.57 (m, 2H), 1.47-1.32 (m, 2H), 1.32-1.13 (m, 16H), 0.82 (t, J = 6.6, Hz, 3H); ^{13}C NMR (100 MHz, $CDCl_3$) δ 143.8, 129.5, 129.0, 120.7, 114.51, 114.47, 68.8, 68.1, 67.5, 31.9, 29.60, 29.57, 29.53, 29.3, 29.1, 29.0, 25.9, 22.71, 22.68, 14.1. MS (EI) *m/z* 504 (M+, 100), 258 (48), 188 (65), 94 (51); HRMS (EI) *m/z* calcd for $C_{32}H_{44}N_2O_3$ 504.3352, found 504.3369.

2-(4-(1-Decyloxy)phenyl)-5-(6-phenoxy-1-hexyloxy)pyrimidine (QL11-6/10). White solid, 37**%** yield: ^{1}H NMR (300 MHz, $CDCl_3$) δ 8.42 (s, 2H), 8.30 (d, J = 8.8 Hz, 2H), 7.32-7.23 (m, 2 H), 6.98 (d, J = 8.8 Hz, 2 H), 6.95-6.88 (m, 3H), 4.11 (t, J = 6.4 Hz, 2H), 4.04 (t, J = 6.4 Hz, 2H), 4.00 (t, J = 6.4 Hz, 2H), 1.76-1.95 (m, 6H), 1.30-1.64 (m, 18H), 0.91 (t, J = 6.6 Hz, 3H); ^{13}C

NMR (75 MHz, $CDCl_3$) δ 143.8, 129.4, 129.0, 120.6, 114.5, 68.8, 68.1, 67.6, 31.9, 29.60, 29.56, 29.4, 29.304 29.28, 29.1, 26.1, 25.9, 25.7, 22.7, 14.1; MS (EI) *m/z* 504 (M+, 100), 411 (15), 398 (15), 355 (10), 327 (14), 285 (37), 272 (35), 201 (14), 188 (96), 94 (42), 55 (20); HRMS (EI) *m/z* calcd for $C_{32}H_{44}N_2O_3$ 504.3352, found 504.3366.

2-(4-(1-Nonyloxy)phenyl)-5-(7-phenoxy-1-heptyloxy)pyrimidine (QL11-9/7). White solid, 28% yield: ^{1}H NMR (400 MHz, $CDCl_3$) δ 8.42 (s, 2H), 8.27 (d, *J* = 8.8 Hz, 2H), 7.32-7.27 (m, 2H), 6.98 (d, *J* = 8.8 Hz, 2H), 6.96-6.88 (m, 3H), 4.09 (t, *J* = 6.4 Hz, 2H), 4.03 (t, *J* = 6.6 Hz, 2H), 3.96 (t, *J* = 6.6 Hz, 2H), 1.89-1.75 (m, 6H), 1.54-1.43 (m, 6H), 1.43-1.30 (m, 12H), 0.90 (t, *J* = 7.1 Hz, 3H); ^{13}C NMR (100 MHz, $CDCl_3$) δ 160.8, 159.0, 157.9, 151.8, 143.9, 130.1,129.4, 129.0, 121.0, 114.5, 114.4 68.9, 68.2, 67.9, 31.8, 29.6, 29.4, 29.3, 29.2, 29.09, 29.07, 26.1, 25.9, 22.7, 14.1; MS (EI) *m/z* 504 (M+, 100), 188 (48), 94 (43), 55 (11); HRMS (EI) *m/z* calcd for $C_{32}H_{44}N_2O_3$ 504.3352, found 504.3329.

2-(4-(1-Octyloxy)phenyl)-5-(8-phenoxy-1-octyloxy)pyrimidine (QL11-8/8). White solid, 71% yield: ^{1}H NMR (400 MHz, $CDCl_3$) δ8.42 (s, 2H), 8.29 (d, *J* = 9.1 Hz, 2H), 7.32-7.26 (m, 2H), 7.01 (d, *J* = 9.1 Hz, 2H), 6.92 (m, 3H), 4.12 (t, *J* = 6.4 Hz, 2H), 4.04 (t, *J* = 6.6 Hz, 2H), 3.98 (t, *J* = 6.7 Hz, 2H), 1.90-1.77 (m, 6H), 1.55-1.27 (m, 18H)**,** 0.90 (t, *J* = 6.4, 3H); ^{13}C NMR (100 MHz, $CDCl_3$) δ 160.8, 159.2, 157.9, 151.1, 143.9, 130.2, 129.4, 129.0, 120.5, 114.5, 114.4, 68.9, 68.1, 67.8, 31.9, 29.4, 29.28, 29.26, 29.1, 26.1, 25.8 , 14.1; MS (EI) *m/z* 504 (M+, 100), 300 (11), 188 (55), 94 (29), 59 (10), 55 (9); HRMS (EI) *m/z* calcd for $C_{32}H_{44}N_2O_3$ 504.3352, found 504.3368.

2-(4-(1-Heptyloxy)phenyl)-5-(9-phenoxy-1-nonyloxy)pyrimidine (QL11-7/9). White solid, 86**%** yield: ^{1}H NMR (400 MHz, $CDCl_3$) δ 8.42 (s, 2H), 8.27 (d, *J* = 8.8 Hz, 2H), 7.32-7.28 (m, 2H), 6.98 (d, *J* = 8.8 Hz, 2H), 6.96-6.88 (m, 3H), 4.09 (t, *J* = 6.4 Hz, 2H), 4.03 (t, *J* = 6.6 Hz, 2H), 3.98 (t, *J* = 6.4 Hz, 2H), 1.93-1.77 (m, 6H), 1.58-1.43 (m, 6H), 1.43-1.25 (m, 12H), 0.90 (t, *J*

= Hz, 3H); ^{13}C NMR (100 MHz, $CDCl_3$) δ 143.8, 129.4, 129.0, 120.5, 114.5, 114.4, 68.9, 68.1, 67.7, 31.9, 29.29, 29.28, 29.0, 26.1, 26.0, 25.9, 22.7, 14.1; MS (EI) *m/z* 504 (M+, 100), 188 (45), 94 (30), 55 (11); HRMS (EI) *m/z* calcd for $C_{32}H_{44}N_2O_3$ 504.3352, found 504.3374.

2-(4-(1-Hexyloxy)phenyl)-5-(10-phenoxy-1-decyloxy)pyrimidine (QL11-6/10). White solid, 52**%** yield: ^{1}H NMR (400 MHz, $CDCl_3$)δ8.42 (s, 2H), 8.27 (d, *J* = 9.1 Hz, 2H), 7.31-7.28 (m, 2H), 6.98 (d, J = 9.1 Hz, 2H), 6.95-6.89 (m, 3H), 4.09 (t, *J* = 6.6 Hz, 2H), 4.03 (t, *J* = 6.6 Hz, 2H), 3.96 (t, *J* = 6.6 Hz, 2H), 1.89-1.74 (m, 6H), 1.55-1.44 (m, 6H), 1.42-1.33 (m, 12H), 0.92 (t, *J* = Hz, 3H); ^{13}C NMR (100MHz, $CDCl_3$) δ 160.8, 159.2, 157.6, 151.3, 143.9,, 130.2, 129.4, 129.0, 120.5, 114.5, 114.4, 68.9, 68.1, 67.9, 31.6, 29.47, 29.45, 29.37, 29.30, 29.2, 29.1,;MS (EI) *m/z* 504 (M+, 100), 188 (41), 94 (22), 55 (15); HRMS (EI) *m/z* calcd for $C_{32}H_{44}N_2O_3$ 504.3352, found 504.3371.

2-(4-(1-Pentyloxy)phenyl)-5-(11-phenoxy-1-undecyloxy)pyrimidine (QL11-5/11). White solid, 42**%** yield: ^{1}H NMR (400 MHz, $CDCl_3$) δ 8.42 (s, 2H), 8.28 (d, *J* = 8.8 Hz, 2H), 7.24-7.32 (m, 2H), 6.98 (d, *J* = 9.0 Hz, 2H), 6.95-6.88 (m, 3H), 4.09 (t, *J* = 6.4 Hz, 2H), 4.03 (t, *J* = 6.7 Hz, 2H), 3.96 (t, *J* = 6.6 Hz, 2H), 1.93-1.74 (m, 6H), 1.54-1.42 (m, 6H), 1.42-1.29 (m, 12H), 0.95 (t, *J* = Hz, 3H); ^{13}C NMR (100 MHz, $CDCl_3$) δ 160.8, 159.2, 151.3,143.9, 130.4, 129.4, 129.0, 120.5, 114.5, 114.4, 69.0, 68.1, 67.9, 29.53, 29.50, 29.48, 29.4, 29.3, 29.1, 29.0, 28.2, 26.1, 25.9, 22.5, 14.0; MS (EI) *m/z* 504 (M+, 100), 350 (5), 188 (65), 163 (22), 107 (12), 94 (15): HRMS (EI) *m/z* calcd for $C_{32}H_{44}N_2O_3$ 504.3352, found 504.3364.

2-(4-(1-Butyloxy)phenyl)-5-(12-phenoxy-1-dodecyloxy)pyrimidine (QL11-4/12). White solid, 58**%** yield: ^{1}H NMR (400 MHz, $CDCl_3$) δ 8.42 (s, 2H), 8.27 (d, *J* = 9.0 Hz 2H), 7.32-7.28 (m, 2H), 6.97 (d, *J* = 9.0 Hz, 2H), 6.95-6.89 (m, 3H), 4.08 (t, *J* = 6.4 Hz, 2H), 4.04 (t, *J* = 6.6 Hz, 2H), 3.96 (t, *J* = 6.6 Hz, 2H), 1.88-1.74 (m, 6H), 1.56-1.43 (m, 6H), 1.42-1.29 (m, 12H), 1.01 (t, *J*

= Hz, 3H); ^{13}C NMR (100 MHz, $CDCl_3$) δ 160.7, 159.2, 157.7, 151.1, 143.9, 130.1, 129.4, 129.0, 120.5, 114.5, 114.4, 69.0, 67.9, 67.8, 31.4, 29.56, 29.55, 29.52, 29.4, 29.3, 29.1, 26.1, 25.9, 19.3, 13.9 MS (EI) *m/z* 504 (M+, 100), 411 (15), 398 (15), 355 (10), 244 (36), 188 (62), 94 (47), 55 (15); HRMS (EI) *m/z* calcd for $C_{32}H_{44}N_2O_3$ 504.3352, found 504.3366.

General procedure for the synthesis of 5-(1-alkyloxy)-2-(4-(*n*-phenoxy-1-alkyloxy)-phenyl)pyrimidine (QL12-*m/n*). The procedure described for the synthesis of **5-*n*** according to Method A was repeated with **6-*m*** and the appropriate alkan-1-ol to give **QL12-*m/n*** (*m/n* = 12/4, 9/7-7/9, 5/11, 4/12); the procedure described for the synthesis of **6-*m*** according to Method B was repeated with **5-*n*** and the appropriate 1-bromoalkane to give **QL12-*m/n*** (*m/n* = 11/5, 10/6, 6/10).

5-(1-Dodecyloxy)-2-(4-(4-phenoxy-1-butyloxy)phenyl)pyrimidine (QL12-12/4). White solid, 78.0% yield: ^{1}H NMR (400 MHz, C_6D_6) δ 8.92 (d, *J* = 8.6 Hz, 2H), 8.31 (s, 2H), 7.19-7.13 (m, 2H), 6.99 (d, *J* = 8.8 Hz, 2H), 6.89-6.84 (m, 3H), 3.63-3.57 (m, 4H), 3.38 (t, *J* = 6.4 Hz, 2H), 1.74-1.60 (m, 4H), 1.50-1.42 (m, 2H), 1.42-1.26 (m, 12H), 1.26-1.19 (m, 6H), 0.93 (t, *J* = 6.0 Hz, 3H): MS (EI) *m/z* 504 (M+, 26), 188 (12), 149 (100), 107 (41); HRMS (EI) *m/z* calcd for $C_{32}H_{44}N_2O_3$ 504.3352, found 504.3371.

2-(4-(5-Phenoxy-1-pentyloxy)-5-(1-undecyloxy)phenyl)pyrimidine (QL12-11/5). White solid, 50% yield: ^{1}H NMR (400 MHz, $CDCl_3$) δ 8.42 (s, 2H), 8.27 (d, *J* = 9.1 Hz, 2H), 7.31-7.27 (m, 2H), 6.98 (d, *J* = 9.1 Hz, 2H), 6.96-6.88 (m, 3H), 4.09 (t, *J* = 6.4 Hz, 2H), 4.03 (t, *J* = 6.6 Hz, 2H), 3.96 (t, *J* = 6.6 Hz, 2H), 1.89-1.75 (m, 6H), 1.54-1.42 (m, 6H), 1.42-1.30 (m, 12H), 0.95 (t, *J* = Hz, 3H); ^{13}C NMR (100 MHz, $CDCl_3$) δ 160.6, 159.0, 157.6, 151.1, 143.8, 130.2, 129.4 129.0, 120.7, 114.51, 114.43, 68.8, 68.1, 67.5, 31.9, 29.61, 29.59, 29.54, 29.3, 29.12, 29.08, 29.04, 26.1, 22.71, 22.68, 14.1; MS (EI) *m/z* 504 (M+, 100), 188 (40), 163 (70), 107 (22), 94 (20), 69 (35), 55 (8); HRMS (EI) *m/z* calcd for $C_{32}H_{44}N_2O_3$ 504.3352, found 504.3372.

5-(1-Decyloxy)-2-(4-(6-phenoxy-1-hexyloxy)phenyl)pyrimidine (QL12-10/6). White solid, 13% yield: ^{1}H NMR (400 MHz, $CDCl_3$) δ 8.42 (s, 2H), 8.27 (d, J = 8.8 Hz, 2H), 7.31-7.28 (m, 2H), 6.98 (d, J = 8.8 Hz, 2H), 6.95-6.88 (m, 3H), 4.09 (t, J = 6.6 Hz, 2H), 4.03 (t, J = 6.6 Hz, 2H), 3.96 (t, J = 6.6 Hz, 2H), 1.88-1.75 (m, 6H), 1.54-1.43 (m, 6H), 1.42-1.34 (m, 12H), 0.93 (t, J = 6.6 Hz, 3H); ^{13}C NMR (75 MHz, $CDCl_3$) δ 160.6, 159.1, 157.7, 151.1, 143.9, 130.1, 129.4, 128.9, 120.5, 114.5, 114.4, 69.5, 68.8, 31.9, 30.9, 29.5, 29.33, 29.31, 29.26, 29.23, 29.1, 26.6, 26.4, 23.4, 14.8; MS (EI) *m/z* 504 (M+, 100), 328 (12), 188 (50), 94 (22); HRMS (EI) *m/z* calcd for $C_{32}H_{44}N_2O_3$ 504.3352, found 504.3374.

5-(1-Nonyloxy)-2-(4-(7-phenoxy-1-heptyloxy)phenyl)pyrimidine (QL12-9/7). White solid, 18% yield: ^{1}H NMR (400 MHz, $CDCl_3$) δ 8.42 (s, 2H), 8.27 (d, J = 9.1 Hz 2H), 7.31-7.28 (m, 2H), 6.98 (d, J = 9.1 Hz, 2H), 6.96-6.89 (m, 3H), 4.09 (t, J = 6.6 Hz, 2H), 4.04 (t, J = 6.6 Hz, 2H), 3.98 (t, J = 6.6 Hz, 2H), 1.89-1.78 (m, 6H), 1.54-1.44 (m, 6H), 1.41-1.25 (m, 12H), 0.90 (t, J = Hz, 3H); ^{13}C NMR (100 MHz ,$CDCl_3$) δ 160.6, 151.3, 143.9, 130.2 129.4, 129.0, 120.5, 114.5, 114.4, 69.0, 68.0, 67.8, 31.9, 29.49, 29.3, 29.24, 29.23, 29.15, 26.0, 22.7, 14.1; MS (EI) *m/z* 504 (M+, 100), 314 (22), 188 (47),94 (34), 55 (14); HRMS (EI) *m/z* calcd for $C_{32}H_{44}N_2O_3$ 504.3352, found 504.3335.

5-(1-Octyloxy)-2-(4-(8-phenoxy-1-octyloxy)phenyl)pyrimidine (QL12-8/8). White solid, 80% yield: ^{1}H NMR (400 MHz, $CDCl_3$) δ 8.34 (s, 2H), 8.20 (d, J = 9.1 Hz, 2H), 7.23-7.17 (m, 2H), 6.89 (d, J = 8.8 Hz, 2H), 6.88-6.80 (m, 3H), 4.00 (t, J = 6.6 Hz, 2H), 3.95 (t, J = 6.6 Hz, 2H), 3.88 (t, J = 6.6 Hz, 2H), 1.82-1.66 (m, 6H), 1.47-1.37 (m, 6H), 1.37-1.30 (m, 6H), 1.30-1.19 (m, 6H), 0.82 (t, J = 6.8 Hz, 3H); ^{13}C NMR (100 MHz, $CDCl_3$) δ 160.7, 159.1, 157.6, 151.1, 143.9, 130.1, 129.4, 129.0, 120.5, 114.5, 114.4, 69.0, 68.0, 67.8, 31.8, 29.33, 29.30, 29.26, 29.21, 29.1,

26.0, 25.9, 14.1; MS (EI) *m/z* 504 (M+, 100), 368 (11), 300 (35), 188 (79), 94 (35); HRMS (EI) *m/z* calcd for $C_{32}H_{44}N_2O_3$ 504.3352, found 504.3367.

5-(1-Heptyloxy)-2-(4-(9-phenoxy-1-nonyloxy)phenyl)pyrimidine (QL12-7/9). White solid, 39.0% yield: ^{1}H NMR (400 MHz, $CDCl_3$) δ 8.44 (s, 2H), 8.28 (d, *J* = 8.8 Hz, 2H), 7.32-7.29 (m, 2H), 6.98 (d, *J* = 8.8 Hz, 2H), 6.95-6.90 (m, 3H), 4.10 (t, *J* = 6.6 Hz, 2H), 4.04 (t, *J* = 6.6 Hz, 2H), 3.98 (t, *J* = 6.6 Hz, 2H), 1.92-1.75 (m, 6H), 1.56-1.44 (m, 6H), 1.44-1.25 (m, 12H), 0.92 (m, 3H); ^{13}C NMR (100 MHz, $CDCl_3$) δ 159.1,143.9, 129.4, 129.0, 114.5, 114.4, 69.0, 68.1, 67.9, 31.8, 29.5, 29.33, 29.30, 29.26, 29.1, 29.0, 14.1; MS (EI) *m/z* 504 (M+, 82), 398 (15), 355 (14), 299 (18), 286 (41), 188 (100), 159 (12), 94 (70), 69 (11), 55 (22); HRMS (EI) *m/z* calcd for $C_{32}H_{44}N_2O_3$ 504.3352, found 504.3368.

5-(1-Hexyloxy)-2-(4-(10-phenoxy-1-decyloxy)phenyl)pyrimidine (QL12-6/10). White solid, 30.6% yield: ^{1}H NMR (400 MHz, $CDCl_3$) δ 8.42 (s, 2H), 8.28 (d, *J* = 8.8 Hz, 2H), 7.31-7.28 (m, 2H), 6.98 (d, *J* = 8.8 Hz, 2H), 6.95-6.88 (m, 3H), 4.09 (t, *J* = 6.6 Hz, 2H), 4.03 (t, *J* = 6.6 Hz, 2H), 3.96 (t, *J* = 6.6 Hz, 2H), 1.88-1.74 (m, 6H), 1.54-1.43 (m, 6H), 1.42-1.30 (m, 12H), 0.93 (t, *J* = Hz, 3H); ^{13}C NMR (100 MHz, $CDCl_3$) δ 160.7, 159.2, 157.7, 151.1, 143.9, 130.1, 129.4, 129.0, 120.5, 114.5, 114.4, 69.0, 68.0, 67.9, 31.5, 29.5, 29.4, 29.31, 29.26, 29.1, 25.8, 21.6, 14.0; MS (EI) *m/z* 504 (M+, 44), 285 (18), 272 (21), 188 (50), 159 (11), 94 (100), 77 (15), 55 (25); HRMS (EI) *m/z* calcd for $C_{32}H_{44}N_2O_3$ 504.3352, found 504.3371.

5-(1-Pentyloxy)-2-(4-(11-phenoxy-1-undecyloxy)phenyl)pyrimidine (QL12-5/11). White solid, 52.9% yield: ^{1}H NMR (400 MHz, $CDCl_3$) δ 8.42 (s, 2H), 8.27 (d, *J* = 9.1 Hz, 2H), 7.30-7.27 (m, 2H), 6.98 (d, *J* = 9.1 Hz, 2H), 6.94-6.86 (m, 3H), 4.09 (t, *J* = 6.6 Hz, 2H), 4.03 (t, *J* = 6.6 Hz, 2H), 3.96 (t, *J* = 6.6 Hz, 2H), 1.88-1.75 (m, 6H), 1.53-1.40 (m, 6H), 1.40-1.30 (m, 12H), 0.96 (t, *J* = Hz, 3H); ^{13}C NMR (100 MHz, $CDCl_3$) δ 143.9, 129.4, 129.0, 120.5, 114.5, 114.4, 69.0, 68.1,

67.9, 29.55, 29.54, 29.51, 29.394, 29.387, 29.31, 29.27, 26.1, 22.4, 14.0; MS (EI) *m/z* 504 (M+, 100), 398 (11), 271 (22), 258 (56), 188 (79), 94 (76), 55 (14); HRMS (EI) *m/z* calcd for $C_{32}H_{44}N_2O_3$ 504.3352, found 504.3369.

5-(1-Butyloxy)-2-(4-(12-phenoxy-1-dodecyloxy)phenyl)pyrimidine (QL12-4/12). White solid, 20.9% yield: ^{1}H NMR (400 MHz, $CDCl_3$) δ 8.42 (s, 2H), 8.28 (d, J = 9.1 Hz, 2H), 7.31-7.28 (m, 2H), 6.98 (d, J = 9.1 Hz, 2H), 6.94-6.86 (m, 3H), 4.10 (t, J = 6.4 Hz, 2H), 4.03 (t, J = 6.6 Hz, 2H), 3.96 (t, J = 6.6 Hz, 2H), 1.87-1.74 (m, 6H), 1.55-1.42 (m, 6H), 1.42-1.28 (m, 12 H), 1.01 (t, J = 7.5 Hz, 3H); ^{13}C NMR (100 MHz, $CDCl_3$) δ 160.7, 143.9, 129.4, 129.0, 120.5, 114.5, 114.4, 69.0, 68.1, 67.9,29.57, 29.55, 29.4, 29.31, 29.27, 26.1, 22.4, 14.0; MS (EI) *m/z* 504 (M+, 100), 411 (11), 398 (16), 257 (18), 244 (55), 188 (77), 94 (76), 55 (16); HRMS (EI) *m/z* calcd for $C_{32}H_{44}N_2O_3$ 504.3352, found 504.3366.

Procedure for the synthesis of 1-bromo-*n*-(*x*-fluorophenoxy)alkanes (7(*n*-*x*)), 1-bromo-8-(*x*,*y*-difluorophenoxy)octane, and (8(*x*,*y*)), 1-bromo-8-(2,6-dimethylphenoxy)octane (9) and 1-bromo-8-(2,3,4,5,6-pentafluoro-phenoxy)octane (10). Under a N_2 atmosphere, the appropriate fluorinated phenol (10.6 mmol) was combined with cesium carbonate (5.2 g, 15.9 mmol) in dry acetonitrile (100 mL). After stirring for 5 min, the appropriate dibromoalkane (15.9 mmol) was added to the mixture, which was heated to reflux overnight. After cooling, the mixture was concentrated, dissolved in EtOAc (40 mL) and washed with 10% aq HCl (50 mL). The aqueous phase was extracted with EtOAc (2 × 40 mL) and the combined organic extracts were washed with sat aq $NaHCO_3$, water, brine, dried ($MgSO_4$) and concentrated. The crude product was purified by flash chromatography on silica gel (0%-15% EtOAc/Hexane).

1-Bromo-4-(2-fluorophenoxy)butane (7(4-2)). Clear oil, 23% yield: ^{1}H NMR (400MHz , $CDCl_3$) δ 7.01-6.87 (m, 4H), 4.08 (t, J = 6.1 Hz, 2H), 3.51 (t, J = 6.6 Hz, 2H), 2.18-2.06 (m, 2H),

2.04-1.95 (m, 2 H); ^{13}C NMR (100 MHz, $CDCl_3$) δ 152.9 (d, J = 246 Hz), 124.3 (d, J = 5 Hz), 121.2 (d, J = 7 Hz), 116.2 (d, J = 18 Hz), 115.0 (d, J = 2 Hz), 115.1 (d, J = 2 Hz), 68.4, 33.4, 29.3, 27.9; LRMS (EI) *m/z* 248 ((M+2, 9), 246 (M+, 9), 137 (65), 134 (66), 112 (100), 92 (13), 83 (18), 64 (11), 57 (10).

1-Bromo-4-(3-fluorophenoxy)butane (7(4-3)). Clear oil, 47% yield: ^{1}H NMR (400 MHz, $CDCl_3$) δ 7.24 (d, J = 6.8 Hz, 1H), 6.74-6.56 (m, 3H), 4.00 (t, J = 6.1 Hz, 2H), 3.51 (t, J = 6.6 Hz, 2H), 2.15-2.03 (m, 2H), 2.0-1.90 (m, 2H); ^{13}C NMR (100 MHz, $CDCl_3$) δ 163.6 (d, J = 245 Hz), 160.2 (d, J = 11 Hz), 130.1 (d, J = 10 Hz), 110.2 (d, J = 3 Hz), 107.5 (d, J = 21 Hz), 102.1 (d, J = 24 Hz), 67.1, 33.3, 29.4, 27.7; LRMS (EI) *m/z* 248 ((M+2, 16), 246 (M+, 16), 137 (80), 135 (80), 112 (100), 95 (14), 86 (27), 84 (55), 83 (17).

1-Bromo-4-(4-fluorophenoxy)butane (7(4-4)). Clear oil, 36% yield: ^{1}H NMR (400MHz , $CDCl_3$) δ 6.98 (dd, J = 9.3, 8.3 Hz, 2H), 6.87-6.80 (m, 2H), 3.96 (t, J = 6.1 Hz, 2H), 3.50 (t, J = 6.7 Hz, 2H), 2.12-2.02 (m, 2H), 1.99-1.87 (m, 2H); ^{13}C NMR (100 MHz, $CDCl_3$) δ 157.3 (d, J = 238 Hz), 155.1 (d, J = 2 Hz), 115.8 (d, J = 23 Hz), 115.5 (d, J = 8 Hz), 67.5, 33.4, 29.5, 28.0; LRMS (EI) *m/z* 248 (M+2, 14), 246 (M+, 14), 137 (72), 135 (74), 112 (100), 95 (14), 84 (13), 83 (20), 55 (57).

1-Bromo-6-(2-fluorophenoxy)hexane (7(6-2)). Clear oil, 24% yield: ^{1}H NMR (400 MHz, $CDCl_3$) δ 7.13-7.03 (m, 2H), 6.97 (m, 1H), 6.93-6.85 (m, 1H), 4.04 (t, J = 6.4 Hz, 2H), 3.43 (t, J = 6.8 Hz, 2H), 1.93-1.88 (m, 2H), 1.88-1.47 (m, 2H), 1.59-1.47 (m, 4H); ^{13}C NMR (100 MHz, $CDCl_3$) δ 152.7 (d, J = 245 Hz) 147.0 (d, J = 10 Hz) 124.2 (d, J = 4 Hz) 120.8 (d, J = 7 Hz) 116.0 (d, J = 18 Hz) 114.9 (d, J = 2 Hz), 69.1, 33.7, 32.6, 29.0, 27.8, 25.1; LRMS (EI) *m/z* 276 (M+2, 8), 274 (M+, 8), 165 (13), 163 (14), 112 (100), 84 (61), 55(55).

1-Bromo-6-(3-fluorophenoxy)hexane (7(6-3)). Clear oil, 17% yield: ^{1}H NMR (400 MHz, $CDCl_3$) δ 7.23 (d, J = 6.8 Hz, 1H), 6.73-6.59 (m, 3H), 3.96 (t, J = 6.3 Hz, 2H), 3.45 (t, J = 6.8 Hz, 2H), 2.00-1.87 (m, 2H), 1.87-1.78 (m, 2H), 1.59-1.46 (m, 4H); ^{13}C NMR (100 MHz, $CDCl_3$) δ 163.7 (d, J = 245 Hz), 160.5 (d, J = 11 Hz), 130.2 (d, J = 10 Hz), 110.3 (d, J = 3 Hz), 107.3 (d, J = 21 Hz), 102.1 (d, J = 25 Hz), 68.0, 33.8, 32.7, 29.0, 27.9, 25.3; LRMS (EI) *m/z* 276 (M+2, 16), 274 (M+, 16), 112 (100), 95 (11), 83 (37).

1-Bromo-6-(4-fluorophenoxy)hexane (7(6-4)). Clear oil, 35% yield: ^{1}H NMR ($CDCl_3$, 400 MHz) δ 7.03-6.92 (m, 2H), 6.88-6.79 (m, 2H), 3.93 (t, J = 6.3 Hz, 2H), 3.44 (t, J = 6.7 Hz, 2H), 2.02-1.83 (m, 2H), 1.83-1.65 (m, 2H), 1.65-1.46 (m, 4H); ^{13}C NMR (100 MHz, $CDCl_3$) δ 157.2 (d, J = 238 Hz), 155.2 (d, J = 2 Hz), 115.8 (d, J = 23 Hz), 115.4 (d, J = 8 Hz), 68.4, 33.8, 32.7, 29.1, 27.9, 25.3; LRMS (EI) *m/z* 276 ((M+2, 12), 274 (M+, 12), 112 (100), 86 (19), 84 (33).

1-Bromo-8-(2-fluorophenoxy)octane (7(8-2)). Clear oil, 15% yield: ^{1}H NMR (400 MHz, $CDCl_3$) δ 7.11-7.02 (m, 2H), 6.99-6.93 (m, 1H), 6.85-6.92 (m, 1H) 4.03 (t, J = 6.6 Hz, 2H), 3.42 (t, J = 6.9 Hz, 2H), 1.92-1.78 (m, 4H), 1.55-1.30 (m, 8H); ^{13}C NMR (100 MHz, $CDCl_3$) δ 152.7 (d, J = 245 Hz), 147.1 (d, J = 10 Hz), 124.2 (d, J = 4 Hz), 120.8 (d, J = 7 Hz), 116.1 (d, J = 18 Hz), 114.9 (d, J = 2 Hz), 69.3, 33.9, 32.7, 29.2, 29.1, 28.6, 28.1, 25.8; LRMS (EI) *m/z* 304 (M+2, 8), 302 (M+, 8), 112 (100), 86 (30), 84(45), 69 (17), 69 (14).

1-Bromo-8-(3-fluorophenoxy)octane (7(8-3)). Clear oil, 9 % yield: ^{1}H NMR (400 MHz, $CDCl_3$) δ 7.22 (d, J = 6.9 Hz, 1H), 6.72-6.59 (m, 3H), 3.94 (t, J = 6.4 Hz, 2H), 3.43 (t, J = 6.9 Hz, 2H), 1.93-1.83 (m, 2H), 1.83-1.74 (m, 2H), 1.54-1.43 (m, 4H), 1.42-1.33 (m, 4H); ^{13}C NMR (100 MHz, $CDCl_3$) δ 163.6 (d, J = 244 Hz), 160.5 (d, J = 11 Hz), 130.0 (d, J = 10 Hz), 110.3 (d, J = 3 Hz), 106.5 (d, J = 21 Hz), 102.0 (d, J = 25 Hz), 68.1, 33.9, 32.7, 29.1, 29.0, 28.6, 28.0, 25.9; LRMS (EI) *m/z* 304 (M+2, 17), 302 (M+, 17), 193 (17), 191 (17), 151 (12), 149 (12), 137 (42), 135 (43),

112 (41), 111 (75), 109 (14), 107 (14), 95 (10), 86 (28), 84 (44), 83 (14), 69 (100), 67 (12), 57 (42), 56 (12), 55 (94), 51 (20).

1-Bromo-8-(4-fluorophenoxy)octane (7(8-4)). Clear oil, 30% yield: ^{1}H NMR (400 MHz, $CDCl_3$) δ 7.03-6.92 (m, 2H), 6.89-6.78 (m, 2H), 3.92 (t, J = 6.6 Hz, 2H), 3.42 (t, J = 6.9 Hz, 2H), 1.93-1.72 (m, 4H), 1.53-1.29 (m, 8H); ^{13}C NMR (100 MHz, $CDCl_3$) δ 157.1 (d, J = 238 Hz), 155.2 (d, J = 2 Hz), 115.7 (d, J = 23 Hz), 115.4 (d, J = 8 Hz), 68.5, 33.9, 32.7, 29.2, 29.1, 28.6, 28.0, 25.9; LRMS (EI) *m/z* 304 (M+2, 8), 302 (M+, 8), 69 (14).

1-Bromo-8-(2,3-difluorophenoxy)octane (8(2,3)). White solid, 43% yield: mp 27-28 ºC; ^{1}H NMR (400 MHz, $CDCl_3$) δ 6.95 (m, 1H), 6.80-6.69 (m, 2H), 4.04 (t, J = 6.4 Hz, 2H), 3.42 (t, J = 6.8 Hz, 2H), 1.93-1.78 (m, 4H), 1.54-1.42 (m, 4H), 1.42-1.29 (m, 4H); ^{13}C NMR (100 MHz, $CDCl_3$) δ 151.4 (dd, J = 246, 10 Hz), 148.8 (dd, J = 7, 3 Hz), 141.4 (dd, J = 247, 14 Hz), 123.0 (dd, J = 9, 5 Hz), 109.7 (d, J = 2 Hz), 108.8 (d, J = 18 Hz), 69.7, 33.8, 32.7, 29.0, 28.6, 28.0, 25.7; LRMS (EI) *m/z* 322 (M+2, 28), 320 (M+, 29), 190 (37), 150 (24), 147 (20), 137 (25), 135 (24) 130 (100), 111 (49), 84 (13), 69 (55), 57 (20), 55 (11).

1-Bromo-8-(2,4-difluorophenoxy)octane (8(2,4)). Clear oil, 46% yield: ^{1}H NMR (400 MHz, $CDCl_3$) δ 6.90 (ddd, J = 9.1, 7.8, 5.3 Hz, 1H), 6.85 (td, J = 7.6, 4.2 Hz, 1H), 6.77 (td, J = 3.0, 1.8 Hz, 1H), 3.99 (t, J = 6.4 Hz, 2H), 3.41 (t, J = 6.8 Hz, 2H), 1.93-1.84 (m, 2H), 1.83-1.74 (m, 2H), 1.55-1.37 (m, 4H), 1.37-1.25 (m, 4H); ^{13}C NMR (100 MHz, $CDCl_3$) δ 156.3 (dd, J = 241, 10 Hz), 152.5 (dd, J = 249, 12 Hz), 143.6 (dd, J = 11, 4 Hz), 115.6 (dd, J = 10, 3 Hz), 110.1 (dd, J = 22, 4 Hz), 104.7 (dd, J = 26, 22 Hz), 70.1, 33.8, 32.7, 29.1, 29.0, 28.6, 28.0, 25.7; LRMS (EI) *m/z* 322 (M+2, 17), 320 (M+, 19), 130 (100), 69 (22), 55 (15).

1-Bromo-8-(2,5-difluorophenoxy)octane (8(2,5)). Clear oil, 23% yield: ^{1}H NMR (400 MHz, $CDCl_3$) δ 7.03-6.95 (m, 1H), 6.72-6.64 (m, 1H), 6.60-6.51 (m,1H), 3.99 (t, J = 6.6 Hz, 2H),

3.41 (t, *J* = 6.8 Hz, 2H), 1.93-1.75 (m, 4H), 1.55-1.37 (m, 4H), 1.37-1.25 (m, 4H); ^{13}C NMR (100 MHz, $CDCl_3$) δ 158.7 (dd, *J* = 242, 2 Hz), 148.9 (dd, *J* = 241, 3 Hz), 147.8 (dd, *J* = 12, 10 Hz), 116.0 (dd, *J* = 21, 10 Hz), 106.1 (dd, *J* = 24, 7 Hz), 102.5 (dd, *J* = 28, 2 Hz), 69.4, 33.8, 32.7, 29.0, 28.9, 28.6, 28.0, 25.7; LRMS (EI) *m/z* 322 (M+2, 38), 320 (M+, 36), 192 (29), 190 (31), 150 (25), 148 (30), 137 (21), 135 (24), 130 (100), 111 (43), 69 (63), 57 (20), 55 (14).

1-Bromo-8-(2,6-difluorophenoxy)octane (8(2,6)). Clear oil, 30% yield: ^{1}H NMR (400 MHz, $CDCl_3$) δ 6.99-6.83 (m, 3H), 4.12 (t, *J* = 6.4 Hz, 2H), 3.41 (t, *J* = 6.8 Hz, 2H), 1.91-1.81 (m, 2H), 1.80-1.70 (m, 2H), 1.54-1.40 (m, 4H), 1.40-1.28 (m, 4H); ^{13}C NMR (100 MHz, $CDCl_3$) δ 156.3 (dd, *J* = 248, 6 Hz), 135.8 (t, *J* = 14 Hz), 122.4 (t, *J* = 9 Hz), 112.0 (dd, *J* = 17, 7 Hz), 74.6 (t, *J* = 3 Hz), 33.8, 32.7, 29.8, 29.0, 28.6, 28.0, 25.5; LRMS (EI) *m/z* 322 (M+2, 22), 320 (M+, 25), 192 (38), 190 (43), 150 (21), 148 (21), 137 (31), 135 (29), 130 (100), 111 (55), 85 (40), 83 (63), 69 (56), 57 (20), 55 (13), 51 (15).

1-Bromo-8-(3,4-difluorophenoxy)octane (8(3,4)). Clear oil, 25% yield: ^{1}H NMR (400 MHz, $CDCl_3$) δ 7.05 (ddd, *J* = 10, 9.1, 8.7 Hz, 1H), 6.76-6.67 (m, 1H), 6.62-6.55 (m, 1H), 3.89 (t, *J* = 6.4 Hz, 2H), 3.42 (t, *J* = 6.9 Hz, 2H), 1.93-1.82 (m, 2H), 1.81-1.71 (m, 2H), 1.52-1.41 (m, 4H), 1.41-1.32 (m, 4H); ^{13}C NMR (100 MHz, $CDCl_3$) δ 155.4 (dd, *J* = 8, 2 Hz) 150.4 (dd, *J* = 247, 14 Hz), 144.8 (dd, *J* = 239, 12 Hz), 117.1 (dd, *J* = 19, 2 Hz), 109.7 (dd, *J* = 6, 4 Hz), 103.9 (d, *J* = 20 Hz) 68.7, 33.9, 32.7, 29.1, 29.0, 28.6, 28.0, 25.8; LRMS (EI) *m/z* 322 (M+2, 17), 320 (M+, 19), 130 (100), 69 (22), 55 (15).

1-Bromo-8-(3,5-difluorophenoxy)octane (8(3,5)). Clear oil, 20% yield: ^{1}H NMR (400 MHz, $CDCl_3$) δ 6.45-6.35 (m, 3H), 3.91 (t, *J* = 6.6 Hz, 2H), 3.41 (t, *J* = 6.8 Hz, 2H), 1.93-1.82 (m, 2H), 1.81-1.72 (m, 2H), 1.51-1.40 (m, 4H), 1.40-1.31 (m, 4H); ^{13}C NMR (100 MHz, $CDCl_3$) δ 163.6 (dd, *J* = 246, 15 Hz), 161.1 (t, *J* = 14 Hz), 98.2 (dd, *J* = 21, 8 Hz), 96.0 (t, *J* = 26 Hz), 68.5,

32.8, 29.8, 29.0, 28.6, 28.0, 25.4; LRMS (EI) *m/z* 322 (M+2, 34), 320 (M+, 34), 192 (40), 190 (29), 150 (23), 148 (24), 137 (23), 135 (26), 130 (100), 111 (43), 69 (67), 57 (22), 55 (16).

1-Bromo-8-(2,6-dimethylphenoxy)octane (9) Clear oil, 23.7% yield: ^{1}H NMR (400 MHz, $CDCl_3$) δ 7.03 (d, *J* = 7.6 Hz, 2H), 6.93 (dd, *J* = 8.1, 6.8 Hz, 1H), 3.78 (d, *J* = 6.6 Hz, 2H), 3.45 (d, *J* = 6.6 Hz, 2H), 1.93 - 1.85 (m, 4H), 1.55 - 1.31 (m, 8H); ^{13}C NMR (100 MHz, $CDCl_3$) 156.1, 130.9, 128.8, 123.6, 72.2, 34.0, 32.8, 30.4, 29.4, 28.8, 28.2, 26.1, 16.3; HRMS (EI) *m/z* calcd for $C_{16}H_{25}OBr$ 314.1063, found 314.1070

1-Bromo-8-(2,3,4,5,6-pentafluorophenoxy)octane (10(2,3,4,5,6)) Clear oil, 64% yield ^{1}H NMR (400 MHz, $CDCl_3$) δ 4.16 (t, *J*=6.4 Hz, 2H), 3.42 (t, *J*=7.0 Hz, 2H), 1.95 – 1.84 (m, 2H), 1.82 - 1.73 (m, 2H), 1.54 - 1.30 (m, 8H); ^{13}C NMR (100 MHz, $CDCl_3$) δ 75.7 (t, *J*=2.93 Hz), 33.8, 32.8, 29.8, 29.0, 28.6, 28.0, 25.4; LRMS (EI) *m/z* 376 (M+2, 6), 374 (M+, 5), 193 (33), 192 (30), 191 (35), 190 (28), 184 (10), 151 (16), 150 (18), 149 (16), 148 (18), 148 (18), 137 (19), 135 (20), 111 (70), 71 (15), 69 (100), 57, (50), 55 (28);

General procedure for the synthesis of 5-(*n*-(*x*-fluorophenoxy)-1-alkyloxy)-2-(4-hydroxyphenyl)pyrimidine (11(*n*-*x*)). Under a N_2 atmosphere, 2-(4-hydroxyphenyl)pyrimidin-5-ol (0.187 g, 1.0 mmol) was combined with cesium carbonate (0.293 g, 0.9 mmol) in dry acetonitrile (40 mL). After stirring for 5 min, **7(*n*-*x*)** (0.9 mmol) was added to the mixture, which was heated to reflux overnight. After cooling, the mixture was concentrated, dissolved in EtOAc (40 mL) and washed with 10% aq HCl (50 mL). The aqueous phase was extracted with EtOAc (2 × 40 mL) and the combined organic extracts were washed with sat aq $NaHCO_3$, water, brine, then dried ($MgSO_4$) and concentrated. Purification by flash chromatography on silica gel (0%-20% EtOAc/Hexane) gave the product, which was recrystallized from acetonitrile and then from hexanes to give a white solid.

5-(4-(2-Fluorophenoxy)-1-butyloxy)-2-(4-hydroxyphenyl)pyrimidine (11(4-2)). White solid, 46% yield: mp 147-148 ˚C; ^{1}H NMR (400 MHz, $CDCl_3$) δ 8.43 (s, 2H), 8.25 (d, J = 8.8 Hz, 2H), 7.12-7.03 (m, 2H), 7.01-6.95 (m, 1H), 6.93-6.88 (m, 3H), 4.20 (t, J = 5.9 Hz, 2H), 4.14 (t, J = 5.7 Hz, 2H), 2.12-1.90 (m, 4H); ^{13}C NMR (100 MHz, DMSO-d_6) δ 157.6 (d, J = 252 Hz), 150.7, 146.4 (d, J = 10 Hz), 143.9, 143.9, 128.6, 128.2, 124.7 (d, J = 4 Hz), 120.9 (d, J = 7 Hz), 115.9 (d, J = 18 Hz) 115.3, 115.0 (d, J = 2 Hz), 68.2, 68.1, 25.2, 25.1; LRMS (EI) *m/z* 354 (M+, 31), 236 (10), 188 (68), 167 (75), 125 (100), 69 (38), 55 (84).

5-(4-(3-Fluorophenoxy)-1-butyloxy)-2-(4-hydroxyphenyl)pyrimidine (11(4-3)). White solid, 54% yield: mp 148-150 ˚C; ^{1}H NMR (400 MHz, $CDCl_3$) δ 8.44 (s, 2H), 8.26 (d, J = 8.6 Hz, 2H), 7.24 (td, J = 8.3, 7.0 Hz, 1H), 6.93 (d, J = 8.3 Hz, 2H), 6.74-6.59 (m, 3H), 4.19 (t, J = 5.9 Hz, 2H), 4.06 (t, J = 5.7 Hz, 2H), 2.12-1.97 (m, 4H); ^{13}C NMR (100 MHz, DMSO-d_6) δ 163.0 (d, J = 244 Hz), 160.1 (d, J = 11 Hz) 159.1, 156.6, 150.7, 144.0, 130.6 (d, J = 10 Hz), 128.7, 128.2, 115.3, 110.8 (d, J = 3 Hz), 107.0 (d, J = 21 Hz), 101.9◦ (d, J = 25 Hz), 68.1, 67.4, 25.2, 25.0; LRMS (EI) *m/z* 354 (M+, 37), 188 (54), 167, (88), 125 (100), 55 (52).

5-(4-(4-Fluorophenoxy)-1-butyloxy)-2-(4-hydroxyphenyl)pyrimidine (11(4-4)). White solid, 56% yield: mp 159-161 ˚C; ^{1}H NMR (400 MHz, $CDCl_3$) δ8.44 (s, 2H), 8.25 (d, J = 8.6 Hz, 2H), 7.01-6.94 (m, 2H), 6.92 (d, J = 8.8 Hz, 2H), 6.88-6.82 (m, 2H), 4.18 (t, J = 5.9 Hz, 2H), 4.02 (t, J = 5.8 Hz, 2H), 2.09-1.96 (m, 4H); ^{13}C NMR (100 MHz, DMSO-d_6) δ 159.1, 156.6, 154.9 (d, J = 2 Hz) 156.4 (d, J = 235 Hz), 150.7, 144.0, 128.6, 128.2, 115.7 (d, J = 23 Hz), 115.6 (d, J = 7 Hz), 115.3, 68.2, 67.6, 25.2, 25.0; LRMS (EI) *m/z* 354 (M+, 57), 188 (53), 167, (71), 125 (100), 69 (17), 55 (61).

5-(6-(2-Fluorophenoxy)-1-hexyloxy)-2-(4-hydroxyphenyl)pyrimidine (11(6-2)). White solid, 18% yield: 126-129 ˚C; ^{1}H NMR (400 MHz, $CDCl_3$) δ 8.42 (s, 2H), 8.25 (d, J = 8.8 Hz, 2H),

7.11-7.02 (m, 2H), 7.00-6.86 (m, 4H), 4.11 (t, *J* = 6.4 Hz, 2H), 4.06 (t, *J* = 6.3 Hz, 2H), 1.92-1.85 (m, 4H), 1.65-1.55 ppm (m, 4H); ^{13}C NMR (100 MHz, 1:1 $CDCl_3$/DMSO-d_6) δ 157.9, 157.6, 152.7 (d, *J* = 245 Hz), 151.1, 147.1 (d, *J* = 11 Hz), 143.8, 129.8, 129.2, 124.2 (d, *J* = 4 Hz), 120.8 (d, *J* = 7 Hz), 116.3, 116.0 (d, *J* = 18 Hz), 114.9 (d, *J* = 2 Hz), 69.3, 68.8, 29.2, 29.0, 25.8, 25.7; LRMS (EI) *m/z* 382 (M+, 42), 270 (19), 188 (100), 132 (10), 119 (16), 112 (15), 83 (17).

5-(6-(3-Fluorophenoxy)-1-hexyloxy)-2-(4-hydroxyphenyl)pyrimidine (11(6-3)). White solid, 52% yield: mp 124-127 ˚C; ^{1}H NMR (400 MHz, 1:1 $CDCl_3$/DMSO-d_6) δ 8.41 (s, 2H), 8.20 (d, *J* = 8.8 Hz, 2H), 7.14-7.04 (m, 1H), 6.84 (d, *J* = 8.6 Hz, 2H), 6.58-6.52 (m, 1H), 6.51-6.45 (m, 2H), 4.02 (t, *J* = 6.3 Hz, 2H), 3.84 (t, *J* = 6.3 Hz, 2H), 1.81-1.74 (m, 2H), 1.73-1.66 (m, 2H), 1.44-1.30 (m, 4H); ^{13}C NMR (100 MHz, $CDCl_3$) δ 163.0 (d, *J* = 244 Hz), 159.9 (d, *J* = 11 Hz), 158.6, 157.2, 150.3, 143.2, 129.6 (d, *J* = 10 Hz), 128.5, 128.4, 115.0, 109.8 (d, *J* = 3 Hz) 106.6 (d, *J* = 21 Hz), 101.5 (d, *J* = 25 Hz), 68.1, 67.4, 28.4, 28.4, 25.2, 25.0; LRMS (EI) *m/z* 382 (M+, 89), 188 (100), 125 (12), 119 (15), 112 (14), 83 (20), 55 (32). ˚

5-(6-(4-Fluorophenoxy)-1-hexyloxy)-2-(4-hydroxyphenyl)pyrimidine (11(6-4)). White solid, 45% yield: mp 108-110 ˚C; ^{1}H NMR (400 MHz, $CDCl_3$) δ 8.93 (s, 1H), 8.32 (s, 2H), 8.12 (d, *J* = 8.6 Hz, 2H), 6.94-6.83 (m, 4H), 6.81-6.70 (m, 2H), 4.01 (t, *J* = 6.1 Hz, 2H), 3.85 (t, *J* = 6.1 Hz, 2H), 1.88-1.75 (m, 4H), 1.66-1.22 (m, 4H); ^{13}C NMR (100 MHz, $CDCl_3$) δ 157.6, 157.5, 157.1 (d, *J* = 238 Hz), 155.1 (d, *J* = 2 Hz), 151.1, 143.8, 130.2, 129.3, 115.7 (d, *J* = 23 Hz), 115.5, 115.4 (d, *J* = 8 Hz), 68.8, 68.4, 29.2, 29.0, 25.8, 25.7; LRMS (EI) *m/z* 382 (M+, 100), 188 (97), 125 (13), 112 (13), 83 (27).

5-(8-(2-Fluorophenoxy)-1-octyloxy)-2-(4-hydroxyphenyl)pyrimidine (11(8-2)). White solid, 51% yield: mp 126-129 ˚C; ^{1}H NMR (400 MHz, $CDCl_3$) δ 8.42 (s, 2H), 8.22 (d, *J* = 8.6 Hz, 2H), 7.11-7.01 (m, 1H), 7.00-6.93 (m, 3H), 6.93-6.85 (m, 2H), 4.08 (t, *J* = 6.4 Hz, 2H), 4.04 (t, *J*

= 6.6 Hz, 2H), 1.88-1.78 (m, 4H), 1.56-1.37 (m, 8H); ^{13}C NMR (100 MHz, 1:1 $CDCl_3$/DMSO-d_6) δ 157.59, 157.57, 152.8 (d, J = 246 Hz), 151.2, 147.1 (d, J = 10 Hz), 143.9, 130.1, 129.3, 124.2 (d, J = 4 Hz), 120.9, 116.1 (d, J = 18 Hz), 115.5, 114.97 (d, J = 2.20 Hz) , 69.4, 68.9, 29.7, 29.2, 29.2, 29.1, 25.9, 25.8; LRMS (EI) *m/z* 410 (M+, 56), 188 (100), 119 (10), 112 (15), 69 (20), 55 (17).

5-(8-(3-Fluorophenoxy)-1-octyloxy)-2-(4-hydroxyphenyl)pyrimidine (11(8-3)). White solid, 60% yield: mp 106-108 ˚C; ^{1}H NMR (400 MHz, 1:1 $CDCl_3$/DMSO-d_6) δ8.97 (s, 1H), 8.31 (s, 2H), 8.10 (d, J = 8.8 Hz, 2H), 7.17-7.06 (td, J = 8.3, 7.1 Hz, 1H), 6.83 (d, J = 8.8 Hz, 2H), 6.62-6.47 (m, 3H), 3.99 (t, J = 6.4 Hz, 2H), 3.85 (t, J = 6.4 Hz, 2H), 1.79-1.64 (m, 4H), 1.46-1.36 (m, 4H), 1.35-1.27 ppm (m, 4H); ^{13}C NMR (100 MHz, 1:1 $CDCl_3$/DMSO-d_6) δ 163.3 (d, J = 244 Hz), 160.2 (d, J = 3 Hz), 158.8, 157.5, 150.6, 143.5, 129.9 (d, J = 10 Hz), 128.8, 128.7, 115.3, 110.0 (d, J = 3 Hz), 106.9 (d, J = 21 Hz), 101.8 (d, J = 26 Hz), 68.6, 67.9, 28.9, 28.8, 25.6, 25.5; LRMS (EI) *m/z* 410 (M+, 50), 188 (100), 119 (11), 112 (12), 69 (15).

5-(8-(4-Fluorophenoxy)-1-octyloxy)-2-(4-hydroxyphenyl)pyrimidine (11(8-4)). White solid, 46% yield: mp 127-129 ˚C; ^{1}H NMR (400 MHz, $CDCl_3$) δ 8.43 (s, 2H) 8.22 (d, J = 8.8 Hz, 2H) 7.01-6.93 (m, 2H) 6.89 (d, J = 8.8 Hz, 2H) 6.86-6.80 (m, 2H), 4.08 (t, J = 6.4 Hz, 2H), 3.92 (t, J = 6.4 Hz, 2H), 1.88-1.74 (m, 6H) 1.55-1.37 (m, 6H); ^{13}C NMR (100 MHz, $CDCl_3$) δ 157.7, 157.6, 157.1 (d, J = 238 Hz), 155.2 (d, J = 2 Hz), 151.2, 143.9, 129.3, 129.0, 115.5, 115.4 (d, J = 7 Hz), 115.7 (d, J = 23 Hz), 68.9, 68.6, 29.2, 29.2, 29.1, 25.9, 25.8; LRMS (EI) *m/z* 410 (M+, 60), 300 (12), 188 (100), 112 (13), 69 (18).

General procedure for the synthesis of 5-(8-(*x*,*y*-difluorophenoxy)-1-octyloxy)-2-(4-hydroxyphenyl)pyrimidine (12(*x*,*y*)), 5-(8-(2,6-Dimethylphenoxy)-1-octyloxy)-2-(4-hydroxyphenyl)pyrimidine (13), and 5-(8-(2,3,4,5,6-Pentafluorophenoxy)-1-octyloxy)-2-(4-

hydroxyphenyl)pyrimidine (14). The general procedure described for the synthesis of **8(*n*-*x*)** was repeated with 2-(4-hydroxyphenyl)pyrimidin-5-ol (0.187 g, 1.0 mmol), cesium carbonate (0.293 g, 0.9 mmol) and **8(*x*,*y*)** (0.290 g, 0.9 mmol) to give the product as a white solid.

5-(8-(2,3-Difluorophenoxy)-1-octyloxy)-2-(4-hydroxyphenyl)pyrimidine (12(2,3)). White solid, 35% yield: mp 90-92 °C; ^{1}H NMR (400 MHz, 1:1 $CDCl_3$/DMSO-d_6) δ (s, 1H), 8.33 (s, 2H), 8.11 (d, J = 8.8 Hz, 2H), 6.96-6.87 (m, 1H), 6.84 (d, J = 8.8 Hz, 2H), 6.71-6.62 (m, 2H), 4.01 (t, J = 6.4 Hz, 2H), 3.97 (t, J = 6.6 Hz, 2H), 1.82-1.71 (m, 4H), 1.49-1.39 (m, 4H), 1.38-1.31 (m, 4H); ^{13}C NMR (100 MHz, 1:1 $CDCl_3$/DMSO-d_6) δ 158.8, 157.6, 150.7, 151.1 (dd, J = 246, 10 Hz), 148.5 (dd, J = 8, 3 Hz), 143.5, 141.1 (dd, J = 247, 15 Hz), 128.8, 122.9 (dd, J = 9, 5 Hz), 115.4, 109.6 (d, J = 3 Hz), 108.6 (d, J = 18 Hz) 69.5, 68.6, 28.9, 28.9, 28.8, 28.8, 25.51, 25.49; LRMS (EI) *m/z* 428 (M+, 68), 188 (100), 130 (13), 119 (10), 69 (14), 55 (12).

5-(8-(2,4-Difluorophenoxy)-1-octyloxy)-2-(4-hydroxyphenyl)pyrimidine (12(2,4)). White solid, 40% yield: mp 111-112 °C; ^{1}H NMR (400 MHz, $CDCl_3$) δ 8.42 (s, 2 H), 8.25 (d, J=8.8 Hz, 2 H), 6.95-6.89 (m, 2 H), 6.89-6.82 (m, 1 H), 6.81–6.74 (m, 1 H), 4.09 (t, J=6.6 Hz, 2 H), 4.00 (t, J=6.6 Hz, 2 H), 1.91 - 1.76 (m, 4 H), 1.55 - 1.38 (m, 4H), 1.33 - 1.24 (m, 4 H) ^{13}C NMR (100 MHz, DMSO-d_6) ^{13}C NMR (101 MHz, DMSO-d_6) δ ppm 159.1, 156.6, 155.4 (dd, J=239, 11 Hz), 150.8, 151.4 (dd, J=245, 11 Hz), 143.9, 143.3 (dd, J=11, 3 Hz), 128.6, 128.2, 115.6 (dd, J=10, 3 Hz,), 115.3, 110.7 (dd, J=22, 4 Hz), 104.7 (dd, J=27, 22 Hz), 69.2, 68.47,, 28.6,, 28.54, 28.50, 25.3, 25.2; LRMS (EI) *m/z* 428 (M+, 77), 188 (100), 69 (13), 55 (10).

5-(8-(2,5-Difluorophenoxy)-1-octyloxy)-2-(4-hydroxyphenyl)pyrimidine (12(2,5)). White solid, 39% yield: mp 95-98 °C; ^{1}H NMR (400 MHz, $CDCl_3$) δ 8.16 (s, 2H), 7.89 (d, J = 8.8 Hz, 2H), 6.73 (ddd, J = 10.7, 9.0, 5.6 Hz, 1H), 6.59 (d, J = 8.8 Hz, 2H), 6.41 (ddd, J = 9.9, 6.9, 2.9 Hz, 1H), 6.32-6.25 (m, 1H), 3.80 (t, J = 6.4 Hz, 2H), 3.72 (t, J = 6.4 Hz, 2H), 1.60-1.50 (m, 6H), 1.27-

1.08 (m, 6H); ^{13}C NMR (100 MHz, $CDCl_3$) δ 158.3, 157.7, 158.8 (dd, J = 242, 3 Hz), 151.2, 149.0 (dd, J = 242, 3 Hz), 147.8 (dd, J = 12, 11 Hz), 143.9, 129.4, 129.4, 116.1 (dd, J = 20, 10 Hz), 115.7, 106.3 (dd, J = 24, 7 Hz), 102.6 (dd, J = 28, 2 Hz), 69.5, 69.0, 29.2, 29.05, 28.97, 25.80, 25.75, 21.9; LRMS (EI) *m/z* 428 (M+, 80), 188 (100), 130 (21), 91 (31), 69(37), 55(31).

5-(8-(2,6-Difluorophenoxy)-1-octyloxy)-2-(4-hydroxyphenyl)pyrimidine (12(2,6)). White solid, 52% yield: mp 125-127 ˚C; ^{1}H NMR (400 MHz, $CDCl_3$) δ 8.45 (s, 2H), 8.19 (d, J = 8.8 Hz, 2H), 7.05-6.85 (m, 5H), 4.15 (t, J = 6.3 Hz, 2H), 4.09 (t, J = 6.8 Hz, 2H), 1.90-1.70 (m, 4H), 1.65-1.55 (m, 4H), 1.53-1.35 (m, 4H); ^{13}C NMR (100 MHz, $CDCl_3$) δ157.9, 157.6, 155.9 (dd, J = 248, 5 Hz), 151.2, 143.9, 135.8 (t, J = 14 Hz), 129.7, 129.3, 122.5 (t, J = 9 Hz), 115.6, 112.1 (dd, J = 17, 7 Hz), 74.7 (t, J = 3 Hz), 69.0, 29.9, 29.2, 29.1, 29.0, 25.7, 25.5; MS (EI) *m/z* 428 (M+, 78), 188 (100), 130 (14), 119 (11), 69(19), 55(16).

5-(8-(3,4-Difluorophenoxy)-1-octyloxy)-2-(4-hydroxyphenyl)pyrimidine (12(3,4)). White solid, 51% yield: mp 105-108 ˚C; ^{1}H NMR (400 MHz, 1:1 $CDCl_3$/DMSO-d_6) δ8.87 (s, 1H), 8.33 (s, 2H), 8.11 (d, J = 8.8 Hz, 2H), 6.98 (ddd, J = 10.1, 9.1, 8.7 Hz, 1H), 6.85 (d, J = 8.8 Hz, 2H), 6.63 (ddd, J = 12.2, 6.6, 2.9 Hz, 1H), 6.54-6.48 (m, 1H), 4.01 (t, J = 6.4 Hz, 2H), 3.83 (t, J = 6.8 Hz, 2H), 1.82-1.65 (m, 4H), 1.50-1.30 (m, 8H); ^{13}C NMR (100 MHz, 1:1 $CDCl_3$/DMSO-d_6) δ159.1, 156.6, 155.3 (dd, J = 9, 2 Hz), 150.8, 149.6 (dd, J = 244, 14 Hz), 143.9, 143.8 (dd, J = 238, 12 Hz), 128.6, 128.2, 117.4 (dd, J = 17, 2 Hz), 115.3, 110.6, (dd, J = 6, 3 Hz) 103.9 (d, J = 20 Hz), 68.5, 68.4, 28.6, 28.5, 28.4, 25.3, 25.2; LRMS (EI) *m/z* 428 (M+, 69), 188 (100), 69 (14).

5-(8-(3,5-Difluorophenoxy)-1-octyloxy)-2-(4-hydroxyphenyl)pyrimidine (12(3,5)). White solid, 46% yield: mp 110-112 ˚C; ^{1}H NMR (400 MHz, 1:1 $CDCl_3$/DMSO-d_6) δ 8.92 (s, 1H), 8.31 (s, 2H), 8.09 (d, J = 8.8 Hz, 2H), 6.82 (d, J =8.8 Hz, 2H), 6.38-6.27 (m, 3H), 3.99 (t, J = 6.4 Hz, 2H), 3.83 (t, J = 6.4 Hz, 2 H), 1.80-1.68 (m, 4H), 1.50-1.35 (m, 4H), 1.35-1.27 (m, 4H); ^{13}C NMR

(100 MHz, 1:1$CDCl_3$/DMSO-d_6) δ 163.5 (dd, J = 244, 16 Hz), 161.1 (t, J = 12 Hz), 159.1, 157.8, 150.8, 143.7, 129.8.79, 128.76, 115.6, 98.2 (dd, J = 21, 8 Hz), 95.9 (t, J = 26 Hz), 68.8, 68.5, 29.1, 29.1, 29.0, 28.8, 25.8, 25.7; LRMS (EI) *m/z* 410 (M+, 74), 188 (100), 69 (16), 55 (11).

5-(8-(2,6-Dimethylphenoxy)-1-octyloxy)-2-(4-hydroxyphenyl)pyrimidine (13). White solid, 195 mg, 59% yield: ^{1}H NMR (400 MHz, $CDCl_3$) δ 8.44 (s, 2H), 8.25 (d, J = 8.8 Hz, 2H), 7.02 (d, J = 7.3 Hz, 2H), 6.98 - 6.90 (m, 3 H), 4.09 (t, J = 6.6 Hz, 2H), 3.77 (t, J = 6.8 Hz, 2H), 2.30 (s, 6H), 1.90 - 1.80 (m, 4 H), 1.53 - 1.45 (m, 8 H); ^{13}C NMR (100 MHz, $CDCl_3$) δ 157.6, 157.4, 156.0, 151.2, 143.9, 130.9, 130.3, 129.3, 128.8, 123.6, 115.5, 72.2, 68.9, 30.4, 29.5, 29.3, 29.1, 26.1, 25.8, 22.0;

5-(8-(2,3,4,5,6-Pentafluorophenoxy)-1-octyloxy)-2-(4-hydroxyphenyl)pyrimidine (14). The general procedure described for the preparation of **4(*n*-*x*)** was repeated with 2-(4-hydroxyphenyl)pyrimidin-5-ol (0.290 g, 1.54 mmol), cesium carbonate (0.510 g, 0.94 mmol) and **3** (0.353 g, 1.08 mmol) to give **6** (0.30 g, 66% yield) as a white solid: mp 85-87 °C; ^{1}H NMR (400 MHz, $CDCl_3$) δ8.41 (s, 2H) 8.15 (d, J = 8.8 Hz, 2H), 6.87 (d, J = 8.8 Hz, 2H), 4.14 (t, J = 6.4 Hz, 2H), 4.06 (t, J = 6.8 Hz, 2H), 1.90-1.70 (m, 4H), 1.55-1.40 (m, 4H), 1.40-1.30 (m, 4H); ^{13}C NMR (100 MHz, $CDCl_3$) δ 158.3, 157.6, 151.0, 143.8, 129.2, 115.5, 114.4, 75.8 (t, J = 3 Hz), 69.0, 29.8, 29.1, 29.0, 25.8, 25.5; LRMS (EI) *m/z* 482 (M+, 76), 188 (100), 69 (33), 55 (26).

General procedure for the synthesis of 2-(4-(1-alkyloxy)phenyl)-5-(*n*-(*x*-fluoro-phenoxy)-1-alkyloxy)pyrimidine (QL20-*m*/*n*-*x*F). Under a N_2 atmosphere, **11(*n*-*x*)** (0.192 mmol) was combined with cesium carbonate (94 mg, 0.29 mmol) in dry acetonitrile (40 mL). After stirring for 5 min, the appropriate 1-bromoalkane (0.29 mmol) was added to the mixture, which was heated to reflux overnight. After cooling, the mixture was concentrated, dissolved in EtOAc (40 mL) and washed with 10% aq HCl (50 mL). The aqueous layer was extracted with

EtOAc (2 × 40 mL) and the combined organic extracts were washed with sat aq $NaHCO_3$, water, brine, dried ($MgSO_4$) and concentrated. Purification by flash chromatography on silica gel (0%-20% EtOAc/Hexane) gave the product, which was recrystallized from acetonitrile and then from hexanes to give a white solid.

5-(8-(2-Fluorophenoxy)-1-octyloxy)-2-(4-(1-octyloxy)phenyl)pyrimidine (QL20-8/8-2F). White solid, 95% yield: ^{1}H NMR (400 MHz, $CDCl_3$) δ8.42 (s, 2H), 8.28 (d, J = 8.8 Hz, 2H), 7.12-7.02 (m, 2H), 7.00-6.94 (m, 3H), 6.91-6.84 (m, 1H), 4.08 (t, J = 6.4 Hz, 2H), 4.03 (m, 4H), 1.90-1.75 (m, 6H), 1.58-1.22 (m, 18H), 0.90 (t, J = 7.1 Hz, 3H); ^{13}C NMR (100 MHz, $CDCl_3$) δ160.7, 157.7, 152.8 (d, J = 246 Hz), 151.0, 147.1 (d, J = 12 Hz), 143.8, 130.0, 128.9, 124.2 (d, J = 4 Hz), 120.8 (d, J = 7 Hz), 116.1 (d, J = 18 Hz), 114.9 (d, J = 2 Hz), 114.4, 69.3, 68.9, 68.1, 31.8, 29.4, 29.3, 29.23, 29.21, 29.18, 29.1, 26.0, 25.9, 25.8, 22.7, 14.1; LRMS (EI) *m/z* 522 (M+, 100), 188 (46), 69 (18); HRMS (EI) *m/z* calcd for $C_{32}H_{43}FN_2O_3$ 522.3257, found 522.3271.

Anal. calcd for $C_{32}H_{43}FN_2O_3$: C, 73.53; H, 8.29; N, 5.36. Found: C, 73.52; H, 8.21; N, 5.25.

5-(8-(3-Fluorophenoxy)-1-octyloxy)-2-(4-(1-octyloxy)phenyl)pyrimidine (QL20-8/8-3F). White solid, 90% yield: ^{1}H NMR (400 MHz, $CDCl_3$) δ 8.42 (s, 2H), 8.28 (d, J = 9.1 Hz, 2H), 7.21 (td, J = 8.2, 7.1 Hz, 1H), 6.98 (d, J = 9.1 Hz, 2H), 6.72-6.57 (m, 3H), 4.09 (t, J = 6.4 Hz, 2H), 4.02 (t, J = 6.7 Hz, 2H), 3.95 (t, J = 6.6 Hz, 2H), 1.92-1.73 (m, 6H), 1.57-1.24 (m, 18H), 0.90 (t, J = 7.1 Hz, 3H); ^{13}C NMR (100 MHz, $CDCl_3$) δ 163.7 (d, J = 246 Hz), 160.7, 160.5 (d, J = 11 Hz), 157.7, 151.0, 143.8, 130.1 (d, J = 10 Hz), 130.1, 129.0, 114.4, 110.3 (d, J = 3 Hz), 107.2 (d, J = 22 Hz), 102.1 (d, J = 25 Hz), 68.9, 68.2, 68.1, 31.8, 29.4, 29.26, 29.23, 29.1, 26.04, 25.94, 25.8, 22.7, 14.1; LRMS (EI) *m/z* 522 (M+, 100), 410 (11), 188 (50); HRMS (EI) *m/z* calcd for $C_{32}H_{43}FN_2O_3$ 522.3257, found 522.3245. Anal. calcd for $C_{32}H_{43}FN_2O_3$: C, 73.53; H, 8.29; N, 5.36. Found: C, 73.24; H, 8.22; N, 5.31.

5-(8-(4-Fluorophenoxy)-1-octyloxy)-2-(4-(1-octyloxy)phenyl)pyrimidine (QL20-8/8-4F). White solid, 73% yield: ^{1}H NMR (400 MHz, $CDCl_3$) δ 8.42 (s, 2H), 8.28 (d, J = 8.8 Hz, 2H), 7.01-6.93 (m, 4H), 6.88-6.78 (m, 2H), 4.09 (t, J = 6.6 Hz, 2H), 4.02 (t, J = 6.6 Hz, 2H), 3.92 (t, J = 6.6 Hz, 2H), 1.90-1.72 (m, 6H), 1.56-1.21 (m, 18H), 0.90 (t, J = 7.1 Hz, 3H); ^{13}C NMR (100 MHz, $CDCl_3$) δ 161.4, 157.8 (d, J = 237.9 Hz), 158.4, 155.9 (d, J = 2.2 Hz), 151.7, 144.5, 130.7, 129.6, 115.7 (d, J = 23.4 Hz), 115.4 (d, J = 7.3 Hz), 115.1, 69.5, 69.2, 68.8, 32.5, 30.0, 29.93, 29.91, 29.8, 26.7, 26.6, 26.5, 23.3, 14.8; LRMS (EI) *m/z* 522 (M+, 100), 188 (50), 112 (12), 69 (12); HRMS (EI) *m/z* calcd for $C_{32}H_{43}FN_2O_3$ 522.3257, found 522.3243. Anal. calcd for $C_{32}H_{43}FN_2O_3$: C, 73.53; H, 8.29; N, 5.36. Found: C, 73.31; H, 8.31; N, 4.98.

2-(4-(1-Decyloxy)phenyl)-5-(6-(2-fluorophenoxy)-1-hexyloxy)pyrimidine (QL20-10/6-2F). White solid, 56% yield: ^{1}H NMR (400 MHz, $CDCl_3$) δ8.42 (s, 2H), 8.28 (d, J = 9.1 Hz, 2H), 7.11-7.03 (m, 2H), 7.00-6.94 (m, 3H), 6.92-6.85 (m, 1H), 4.10 (t, J = 6.4 Hz, 2H), 4.06 (t, J = 6.4 Hz, 2H), 4.02 (t, J = 6.7 Hz, 2H), 1.93-1.76 (m, 6H), 1.62-1.24 (m, 18H), 0.89 (t, J = 6.6 Hz, 3H); ^{13}C NMR (100 MHz, $CDCl_3$) δ 160.7, 157.7, 152.8 (d, J = 239 Hz), 151.0, 147.1 (d, J = 11 Hz), 143.8, 130.1, 128.9, 124.2 (d, J = 4 Hz), 121.0 (d, J = 7 Hz), 116.2 (d, J = 18 Hz), 115.0 (d, J = 2 Hz), 114.4, 69.2, 68.7, 68.1, 31.9, 29.6, 29.5,, 29.4, 29.3, 29.3, 29.1, 29.0, 26.0, 25.7, 25.6, 22.7, 14.1; LRMS (EI) *m/z* 522 (M+, 100), 382 (13), 188 (48), 112 (10), 83 (18); HRMS (EI) *m/z* calcd for $C_{32}H_{43}FN_2O_3$ 522.3257, found 522.3257. Anal. calcd for $C_{32}H_{43}FN_2O_3$: C, 73.53; H, 8.29; N, 5.36. Found: C, 73.77; H, 8.33; N, 4.95.

2-(4-(1-Decyloxy)phenyl)-5-(6-(3-fluorophenoxy)-1-hexyloxy)pyrimidine (QL20-10/6-3F). White solid, 39% yield: ^{1}H NMR (400 MHz, $CDCl_3$) δ8.42 (s, 2H), 8.28 (d, J = 9.1 Hz, 2H), 7.22 (td, J = 8.2, 7.2 Hz, 1H), 6.98 (d, J = 9.1 Hz, 2H), 6.74-6.58 (m, 3H), 4.10 (t, J = 6.3 Hz, 2H), 4.02 (t, J = 6.6 Hz, 2H), 3.97 (t, J = 6.4 Hz, 2H), 1.93-1.76 (m, 2H), 1.62-1.53 (m, 4H), 1.53-1.20

(m, 18H), 0.89 (t, *J* = 6.6 Hz, 3H); ^{13}C NMR (100 MHz, $CDCl_3$) δ 164.9, 161.4 (d, *J* = 208 Hz), 160.6 (d, *J* = 22 Hz), 157.7, 151.0, 143.8, 130.1 (d, *J* = 10 Hz), 130.0, 129.0, 114.4, 110.3 (d, *J* = 3 Hz), 107.3 (d, *J* = 21 Hz), 102.1 (d, *J* = 26 Hz), 68.7, 68.1, 68.0, 31.9, 29.6, 29.5, 29.4, 29.3, 29.25, 29.1, 29.0, 26.0, 25.8, 25.7, 22.7, 14.1; LRMS (EI) *m/z* 522 (M+, 100), 382 (33), 188 (80), 83 (23), 55 (26); HRMS (EI) *m/z* calcd for $C_{32}H_{43}FN_2O_3$ 522.3258, found 522.3244. Anal. calcd for $C_{32}H_{43}FN_2O_3$: C, 73.53; H, 8.29; N, 5.36. Found: C, 73.30; H, 8.33; N, 5.24

2-(4-(1-Decyloxy)phenyl)-5-(6-(4-fluorophenoxy)-1-hexyloxy)pyrimidine (QL20-10/6-4F). White solid, 71% yield: ^{1}H NMR (400 MHz, $CDCl_3$) δ8.42 (s, 2H), 8.28 (d, *J* = 8.8 Hz, 2H), 7.02-6.92 (m, 4H), 6.88-6.78 (m, 2H), 4.10 (t, *J* = 6.3 Hz, 2H), 4.03 (t, *J* = 6.6 Hz, 2H), 3.94 (t, *J* = 6.3 Hz, 2H), 1.95-1.75 (m, 6H), 1.59-1.22 (m, 18H), 0.89 (t, *J* = 6.8 Hz, 3H); ^{13}C NMR (100 MHz, $CDCl_3$) δ 160.7, 157.1 (d, *J* = 239 Hz), 157.8, 155.2 (d, *J* = 2 Hz), 151.0, 143.8, 130.0, 129.0, 115.7 (d, *J* = 23 Hz), 115.4 (d, *J* = 7 Hz), 114.4, 68.7, 68.4, 68.1, 31.9, 29.6, 29.5, 29.4, 29.3, 29.25, 29.2, 29.1, 26.0, 25.8, 25.7, 22.7, 14.1; LRMS (EI) *m/z* 522 (M+, 100), 382 (17), 188 (50), 112 (10), 83 (16), 55 (19); HRMS (EI) *m/z* calcd for $C_{32}H_{43}FN_2O_3$ 522.3257, found 522.3243. Anal. calcd for $C_{32}H_{43}FN_2O_3$: C, 73.53; H, 8.29; N, 5.36. Found: C, 73.93; H, 8.33; N, 4.99.

2-(4-(1-Dodecyloxy)phenyl)-5-(4-(2-fluorophenoxy)-1-butyloxy)pyrimidine (QL20-12/4-2F). White solid, 58% yield: ^{1}H NMR (400 MHz, $CDCl_3$) δ8.43 (s, 2H), 8.28 (d, *J* = 8.8 Hz, 2H), 7.12-7.03 (m, 2H), 7.01-6.95 (m, 3H), 6.94-6.88 (m, 1H), 4.20 (t, *J* = 5.8 Hz, 2H), 4.14 (t, *J* = 5.8 Hz, 2H), 4.03 (t, *J* = 6.6 Hz, 2H), 2.13-2.01 (m, 4H), 1.86-1.77 (m, 2H), 1.53-1.42 (m, 2H), 1.42-1.10 (m, 16H), 0.89 ppm (t, *J* = 6.8 Hz, 3H); ^{13}C NMR (100 MHz, $CDCl_3$) δ160.7, 157.8, 152.8 (d, *J* = 245 Hz), 150.9, 146.9 (d, *J* = 10 Hz), 143.8, 130.0, 129.0, 124.3 (d, *J* = 4 Hz), 121.2 (d, *J* = 7 Hz), 116.2 (d, *J* = 18 Hz), 115.0 (d, *J* = 2 Hz), 114.4, 68.8, 68.4, 68.1, 31.9, 29.7, 29.6, 29.6, 29.56, 29.4, 29.33, 29.25, 26.0, 25.8, 22.7, 14.1; LRMS (EI) *m/z* 522 (M+, 100), 188 (28), 167

(80), 125 (48); HRMS (EI) *m/z* calcd for $C_{32}H_{43}FN_2O_3$, 522.3257, found 522.3257. Anal. calcd for $C_{32}H_{43}FN_2O_3$: C, 73.53; H, 8.29; N, 5.36. Found: C, 73.81; H, 8.38; N, 5.05.

2-(4-(1-Dodecyloxy)phenyl)-5-(4-(3-fluorophenoxy)-1-butyloxy)pyrimidine (QL20-12/4-3F). White solid, 38% yield: ^{1}H NMR (400 MHz, $CDCl_3$) δ8.43 (s, 2H), 8.28 (d, *J* = 8.8 Hz, 2H), 7.23 (td, *J* = 8.3, 7.0 Hz, 1H), 6.98 (d, *J* = 8.8 Hz, 2H), 6.73-6.57 (m, 3H), 4.18 (t, *J* = 5.8 Hz, 2H), 4.07-3.99 (m, 4H), 2.10-1.96 (m, 6H), 1.88-1.74 (m, 6H), 1.53-1.19 (m, 12H), 0.89 (t, *J* = 7.1 Hz, 3H); ^{13}C NMR (100 MHz, $CDCl_3$) δ 163.7 (d, *J* = 245 Hz), 160.8, 160.3 (d, *J* = 11 Hz), 157.9, 150.9, 143.8, 130.2 (d, *J* = 10 Hz), 130.0, 129.0, 114.5, 110.3 (d, *J* = 3 Hz), 107.6 (d, *J* = 22 Hz), 102.2 (d, *J* = 25 Hz), 68.4, 68.1, 67.6, 31.9, 29.7, 29.63, 29.60, 29.57, 29.4, 29.3, 29.3, 26.04 (s), 25.99, 25.7, 22.7, 14.1; LRMS (EI) *m/z* 522 (M+, 100), 188 (16), 167 (80), 125 (43); HRMS (EI) *m/z* calcd for $C_{32}H_{43}FN_2O_3$, 522.3257, found 522.3271. Anal. calcd for $C_{32}H_{43}FN_2O_3$: C, 73.53; H, 8.29; N, 5.36. Found: C, 73.28; H, 7.98; N, 5.30.

2-(4-(1-Dodecyloxy)phenyl)-5-(4-(4-fluorophenoxy)-1-butyloxy)pyrimidine (QL20-12/4-4F). White solid, 82% yield: ^{1}H NMR (400 MHz, $CDCl_3$) δ8.43 (s, 2H), 8.28 (d, *J* = 8.8 Hz, 2H), 7.01-6.95 (m, 4H), 6.87-6.81 (m, 2H), 4.18 (t, *J* = 5.9 Hz, 2H), 4.05-4.00 (m, 4H), 2.10-1.95 (m, 4H), 1.86-1.76 (m, 2H), 1.54-1.24 (m, 18H), 0.89 (t, *J* = 6.8 Hz, 3H); ^{13}C NMR (100 MHz, $CDCl_3$) δ 160.8, 157.9, 157.3 (d, *J* = 238 Hz), 155.0 (d, *J* = 2 Hz), 150.9, 143.8, 130.0, 129.0, 115.8 (d, *J* = 23 Hz), 115.4 (d, *J* = 7 Hz), 114.5, 68.5, 68.1, 67.9, 31.9, 29.7, 29.63, 29.60, 29.57, 29.41, 29.34, 29.27, 26.04, 26.02, 25.8, 22.7, 14.1; LRMS (EI) *m/z* 522 (M+, 100), 188 (20), 167 (94), 125 (53); HRMS (EI) *m/z* calcd for $C_{32}H_{43}FN_2O_3$ 522.3257, found 522.3243. Anal. calcd for $C_{32}H_{43}FN_2O_3$: C, 73.53; H, 8.29; N, 5.36. Found: C, 73.73; H, 7.97; N, 5.21.

General procedure for the synthesis of 5-(8-(*x*,*y*-difluorophenoxy)-1-octyloxy)-2-(4-(1-octyloxy)phenyl)pyrimidine (QL22-8/8-*x*,*y*F$_2$). The general procedure described for the

synthesis of **QL20-*m/n-x*F** was repeated with **12(*x,y*)** (82 mg, 0.192 mmol), cesium carbonate (94 mg, 0.29 mmol) and 1-bromooctane (56 mg, 0.29 mmol) to give the product as a white solid.

5-(8-(2,3-Difluorophenoxy)-1-octyloxy)-2-(4-(1-octyloxy)phenyl)pyrimidine (QL22-8/8-2,3F$_2$). White solid, 58% yield: ^{1}H NMR (400 MHz, $CDCl_3$) δ 8.43 (s, 2H), 8.29 (d, J = 8.8 Hz, 2H), 6.97-6.94, (m, 3H), 6.81-6.71 (m, 2H), 4.10 (t, J = 6.4 Hz, 2H), 4.07-4.01 (m, 4H), 1.91-1.78 (m, 6H), 1.58-1.47 (m, 6H), 1.46-1.26 (m , 12H), 0.91 (t, J = 7.1 Hz, 3H); ^{13}C NMR (100 MHz, $CDCl_3$) δ 160.7, 157.7, 151.1, 151.5 (dd, J = 247, 10 Hz), 148.9 (dd, J = 8, 3 Hz), 143.8, 141.5 (dd, J = 247, 14 Hz), 130.1, 129.0, 123.1 (dd, J = 9, 5 Hz), 114.4, 109.9 (d, J = 3 Hz), 109.0 (d, J = 18 Hz), 69.8, 68.9, 68.1, 31.8, 29.4, 29.28, 29.25, 29.2, 29.13, 29.11, 26.06, 25.84, 25.81, 22.7, 14.1; LRMS (EI) *m/z* 540 (M+, 100), 428 (13), 188 (31), 69 (12); HRMS (EI) *m/z* calcd for $C_{32}H_{42}F_2N_2O_3$ 540.3164, found, 540.3160. Anal. calcd for $C_{32}H_{42}F_2N_2O_3$: C, 71.08; H, 7.83; N, 5.18. Found: C, 71.03; H, 7.81; N, 5.08.

5-(8-(2,4-Difluorophenoxy)-1-octyloxy)-2-(4-(1-octyloxy)phenyl)pyrimidine (QL22-8/8-2,4F$_2$). White solid, 60% yield: ^{1}H NMR (400 MHz, $CDCl_3$) δ 8.42 (s, 2H), 8.28 (d, J = 8.8 Hz, 2H), 6.98 (d, J = 8.8 Hz, 2H), 6.94-6.82 (m, 2H), 6.80-6.74 (m, 1H), 4.08 (t, J = 6.4 Hz, 2H), 4.03 (t, J = 6.8 Hz, 2H), 4.00 (t, J = 6.8 Hz, 2H), 1.91-1.75 (m, 6H), 1.57-1.24 (m, 18H), 0.93 (t, J = 7.1 Hz, 3H); ^{13}C NMR (100 MHz, $CDCl_3$) δ160.7, 157.7, 156.4 (dd, J = 242, 10 Hz), 152.6 (dd, J = 250, 12 Hz), 151.0, 143.8, 143.7 (dd, J = 11, 4 Hz), 130.1, 129.0, 115.8 (dd, J = 10, 4 Hz), 114.4, 110.2 (dd, J = 23, 4 Hz), 104.8 (dd, J = 27, 23 Hz), 70.3, 68.9, 68.1, 31.8, 29.4, 29.3, 29.22, 29.20, 29.1, 26.0, 25.83, 25.78, 22.6, 14.1; LRMS (EI) *m/z* 540 (M+, 100), 428 (13), 188 (58), 130 (51), 69 (33), 55 (30); HRMS (EI) *m/z* calcd for $C_{32}H_{42}F_2N_2O_3$ 540.3164, found 540.3173. Anal. calcd for $C_{32}H_{42}F_2N_2O_3$: C, 71.08; H, 7.83; N, 5.18. Found: C, 71.20; H, 7.91; N, 5.07.

5-(8-(2,5-Difluorophenoxy)-1-octyloxy)-2-(4-(1-octyloxy)phenyl)pyrimidine (QL22-8/8-2,5F$_2$). White solid, 78% yield: ^{1}H NMR (400 MHz, $CDCl_3$) δ 8.42 (s, 2H), 8.27 (d, J = 8.8 Hz, 2H), 7.05-6.95 (m, 3H), 6.69 (ddd, J = 9.9, 6.8, 3.0 Hz, 1H), 6.52-6.61 (m, 1H), 4.09 (t, J = 6.4 Hz, 2H), 4.03 (t, J = 6.8 Hz, 2H), 4.00 (t, J = 6.6 Hz, 2H), 1.89-1.77 (m, 6H), 1.55-1.25 (m, 18H), 0.90 (t, J = 7.1 Hz, 3H); ^{13}C NMR (100 MHz, $CDCl_3$) δ 160.7, 158.8 (dd, J = 242, 2 Hz), 157.7, 151.1, 149.0 (dd, J = 242, 3 Hz), 147.8 (dd, J = 12, 10 Hz), 143.8, 130.1, 129.0, 116.0 (dd, J = 20, 10 Hz), 114.4, 106.2 (dd, J = 24, 7 Hz), 102.6 (dd, J = 27, 2 Hz), 69.5, 68.9, 68.0, 31.8, 29.3, 29.24, 29.20, 29.17, 29.10, 29.0, 26.0, 25.9, 25.8, 22.6, 14.1; LRMS (EI) *m/z* 540 (M+, 100), 428 (13), 188 (58), 130 (51), 69 (33), 55 (30); HRMS (EI) *m/z* calcd for $C_{32}H_{42}F_2N_2O_3$ 540.3164, found 540.3173. Anal. calcd for $C_{32}H_{42}F_2N_2O_3$: C, 71.08; H, 7.83; N, 5.18. Found: C, 70.90; H, 8.00; N, 5.22.

5-(8-(2,6-Difluorophenoxy)-1-octyloxy)-2-(4-(1-heptyloxy)phenyl)pyrimidine (QL22-7/8-2,6F$_2$). White solid, 79% yield: ^{1}H NMR (400 MHz, $CDCl_3$) δ 8.44 (s, 2 H), 8.29 (d, J=8.8 Hz, 2H), 6.99 (d, J=8.8 Hz, 2H), 6.99 - 6.85 (m, 3 H), 4.15 (t, J=6.6 Hz, 4H), 4.10 (t, J=6.4 Hz, 2H), 4.04 (t, J=6.6 Hz, 2H), 1.90-1.75 (m, 6H), 1.59-1.49 (m, 6 H), 1.49-1.39 (m, 6 H), 1.39-1.29 (m, 4 H), 0.92 (t, J=6.8 Hz, 3H); ^{13}C NMR (100 MHz, $CDCl_3$) δ 160.7, 157.7, 156.4 (dd, J=246, 6 Hz), 151.1, 143.9, 130.1, 129.0, 128.2 (d, J=12 Hz), 122.5 (d, J=14 Hz), 114.5, 112.1 (dd, J=15, 6 Hz), 74.7 (t, J=2 Hz), 68.9, 68.1, 31.8, 29.9, 29.3, 29.21, 29.17, 29.10, 29.09, 26.0, 25.8, 25.6, 22.6, 14.0; LRMS (EI) *m/z* 526 (M+, 100), 428 (17), 188 (84), 130 (21), 69 (21), 55 (17); HRMS (EI) *m/z* calcd for $C_{31}H_{40}N_2O_3F_2$ 526.3007, found 526.3015

5-(8-(2,6-Difluorophenoxy)-1-octyloxy)-2-(4-(1-octyloxy)phenyl)pyrimidine (QL22-8/8-2,6F$_2$). White solid, 70% yield: ^{1}H NMR (400 MHz, $CDCl_3$) δ 8.43 (s, 2H), 8.29 (d, J = 8.8 Hz, 2H), 6.99 (d, J = 8.8 Hz, 2H), 6.96-6.85 (m, 3H), 4.15 (t, J = 6.6 Hz, 2H), 4.10 (t, J = 6.6 Hz, 2H),

4.04 (t, *J* = 6.6 Hz, 2H), 1.91-1.74 (m, 6H), 1.60-1.26 (m, 18H), 0.91 (t, *J* = 7.1 Hz, 3H); ^{13}C NMR (100 MHz, $CDCl_3$) δ 160.7, 157.7, 156.4 (dd, *J* = 248, 5 Hz) 151.1, 143.8, 135.8 (t, *J* = 14 Hz), 130.1, 129.0, 122.5 (t, *J* = 10 Hz), 114.4, 112.1 (dd, *J* = 17, 7 Hz), 74.7 (t, *J* = 3 Hz), 68.9, 68.1, 31.8, 29.9, 29.4, 29.3, 29.24, 29.21, 29.16, 29.10, 26.1, 25.8, 25.6, 22.7, 14.1; LRMS (EI) *m/z* 540 (M+, 100), 428 (10), 188 (50), 69 (11); HRMS (EI) *m/z* calcd for $C_{32}H_{42}F_2N_2O_3$ 540.3163, found 540.3169.

5-(8-(2,6-Difluorophenoxy)-1-octyloxy)-2-(4-(1-nonyloxy)phenyl)pyrimidine (QL22-9/8-2,6F$_2$). White solid, 92% yield: ^{1}H NMR (400 MHz, $CDCl_3$) δ ppm 8.34 (s, 2H), 8.20 (d, *J*=8.8 Hz, 2H), 6.90 (d, *J*=8.8 Hz, 2H), 6.99 - 6.85 (m, 3H), 4.06 (t, *J*=6.6 Hz, 2H), 4.01 (t, *J*=6.4 Hz, 2H), 3.95 (t, *J*=6.6 Hz, 2H), 1.80 - 1.70 (m, 6H), 1.52 – 1.42 (m, 6H), 1.42-1.26 (m, 6H), 1.26 - 1.17 (m, 8H), 0.82 (t, *J*=6.8 Hz, 3H); ^{13}C NMR (100 MHz, $CDCl_3$) δ 160.7, 157.7, 156.4 (dd, *J*=245, 7 Hz), 151.1, 143.9, 130.1, 129.0, 128.4 (d, *J* = 2 Hz), 122.6 (t, *J* = 10 Hz), 114.5, 112.1 (dd, *J*=16, 7 Hz); LRMS (EI) *m/z* 554 (M+, 100), 188 (41); HRMS (EI) *m/z* calcd for $C_{33}H_{44}N_2O_3F_2$ 554.3329, found 554.3320

2-(4-(1-Decyloxy)phenyl)-5-(8-(2,6-difluorophenoxy)-1-octyloxy)pyrimidine (QL22-10/8-2,6F$_2$). White solid, 87% yield: ^{1}H NMR (400 MHz, $CDCl_3$) δ 8.33 (s, 2H), 8.19 (d, *J*=8.8 Hz, 2H), 6.89 (d, *J*=8.8 Hz, 2H), 6.89 - 6.75 (m, 3H), 4.05 (t, *J* = 6.4 Hz, 2H), 3.99 (t, *J* = 6.4 Hz, 2H), 3.93 (t, *J* = 6.6 Hz, 2H), 1.80 - 1.60 (m, 6 H), 1.50 – 1.37 (m, 6H), 1.37 – 1.25 (m, 6H), 1.25 – 1.15 (m, 10H), 0.81 (dd, *J*=7.07, 6.32 Hz); ^{13}C NMR (100 MHz, $CDCl_3$) δ 160.7, 157.7, 156.4 (dd, *J* = 248, 6 Hz), 151.1, 143.8, 130.1, 129.0, 128.3 (d, *J* = 2 Hz), 122.6 (t, *J* = 10 Hz), 114.4, 112.1 (dd, *J* = 16.1, 6.6 Hz), 74.7 (t, *J* = 3 Hz), 68.9, 68.1, 31.9, 29.9, 29.59, 29.57, 29.4, 29.3, 29.3, 29.22, 29.17, 29.10, 26.06, 25.8, 25.6, 22.7, 14.1; LRMS (EI) *m/z* 568 (M+, 100), 428 (9),

188 (48); HRMS (EI) *m/z* calcd for $C_{34}H_{46}N_2O_3F_2$ 568.3472, found 568.3477 Anal. calcd for $C_{32}H_{42}F_2N_2O_3$ 71.08; H, 7.83; N, 5.18. Found: C, 71.33; H, 7.65; N, 5.21.

5-(8-(3,4-Difluorophenoxy)-1-octyloxy)-2-(4-(1-octyloxy)phenyl)pyrimidine (QL22-8/8-3,4F$_2$). White solid, 70% yield: ^{1}H NMR (400 MHz, $CDCl_3$) δ 8.42 (s, 2H), 8.28 (d, *J*=8.8 Hz, 2H), 7.05 (ddd, *J*=10.1, 9.1, 8.7 Hz, 1H), 6.98 (d, *J*=8.8 Hz, 2H), 6.75 - 6.65 (m, 1H), 6.63 - 6.54 (m, 1H), 4.09 (t, *J*=6.4 Hz, 2H), 4.03 (t, *J*=6.7 Hz, 2 H), 3.90 (t, *J*=6.4 Hz, 1H), 1.91 - 1.70 (m, 8H), 1.55 - 1.27 (m, 18H), 0.90 (t, *J*=6.82 Hz, 3H); ^{13}C NMR (100 MHz, $CDCl_3$) δ 160.7, 157.7, 155.4 (dd, *J* = 8, 3 Hz), 151.0, 150.5 (dd, *J* = 245, 14 Hz), 143.8, 144.9 (dd, *J* = 239, 16 Hz), 130.1, 129.0, 117.1 (dd, *J* = 18, 2 Hz) 114.4, 109.8 (dd, *J* = 5, 4 Hz), 104.0 (d, *J* = 20 Hz), 68.9, 68.7, 68.1, 31.8, 30.9, 29.4, 29.3, 29.2, 29.1, 26.0, 25.9, 25.8, 22.6, 14.1; LRMS (EI) *m/z* 540 (M+, 100), 428 (14), 188 (55), 130 (18), 69 (15), 55 (14); HRMS (EI) *m/z* calcd for $C_{32}H_{42}F_2N_2O_3$ 540.3163, found 540.3173. Anal. calcd for $C_{32}H_{42}F_2N_2O_3$: C, 71.08; H, 7.83; N, 5.18. Found: C, 71.13; H, 7.88; N, 4.84.

5-(8-(3,5-Difluorophenoxy)-1-octyloxy)-2-(4-(1-octyloxy)phenyl)pyrimidine (QL22-8/8-3,5F$_2$). White solid, 66% yield: ^{1}H NMR (400 MHz, $CDCl_3$) δ 8.42 (s, 2H), 8.28 (d, *J* = 8.8 Hz, 2H), 6.98 (d, *J* = 8.8 Hz, 2H), 6.42 (d, *J* = 9.6 Hz, 3H), 4.09 (t, *J* = 6.4 Hz, 2H), 4.03 (t, *J* = 6.6 Hz, 2H), 3.93 (t, *J* = 6.6 Hz, 2H), 1.92-1.72 (m, 6H), 1.55-1.45 (m, 6H), 1.45-1.39 (m, 6H), 1.38-1.27 (m, 6H), 0.90 (t, *J* = 6.8 Hz, 3H); ^{13}C NMR (100 MHz, $CDCl_3$) δ 163.7 (dd, *J* = 246, 15 Hz), 161.1 (t, *J* = 14 Hz), 160.7, 157.7, 151.0, 143.8, 130.1, 129.0, 114.4, 98.2 (dd, *J* = 19, 7 Hz), 96.0 (t, *J* = 26 Hz), 68.9, 68.6, 68.1, 31.8, 29.4, 29.3, 29.22, 29.19, 29.1, 28.9, 26.0, 25.9, 25.8, 22.6, 14.1; LRMS (EI) *m/z* 540 (M+, 100), 188 (50), 130 (20), 69 (21), 55 (14); HRMS (EI) *m/z* calcd for $C_{32}H_{42}F_2N_2O_3$ 540.3163, found 540.3157. Anal. calcd for $C_{32}H_{42}F_2N_2O_3$: C, 71.08; H, 7.83; N, 5.18. Found: C, 71.44; H, 8.26; N, 5.01.

2-(4-(8-(2,6-Dimethylphenoxy)-1octyloxy)phenyl)-5-(1-octyloxy)pyrimidine (QL30-8/8-2,6Me$_2$) White solid, 60% yield: ^{1}H NMR (400 MHz, $CDCl_3$) δ 8.44 (s, 2H), 8.30 (d, *J* = 8.8 Hz, 2H), 7.02 (d, *J* = 7.3 Hz, 2H), 7.00 (d, *J* = 9.1 Hz, 2H), 6.93 (dd, *J* = 7.8, 6.8 Hz, 1H), 4.10 (t, *J* = 6.4 Hz, 2H), 4.05 (t, *J* = 6.6 Hz, 2H), 3.79 (t, *J* = 6.6 Hz, 2H), 2.30 (s, 6H), 1.90-1.77 (m, 6 H), 1.56-1.37 (m, 6H), 1.37-1.26 (s, 6H), 0.92 (t, *J*=7.1 Hz, 3 H); ^{13}C NMR (100 MHz, $CDCl_3$) δ = 160.7, 157.7, 156.1, 151.1, 143.9, 130.9, 130.1, 129.0, 128.8, 123.6, 114.5, 72.3, 69.0, 68.0, 31.8, 30.5, 29.5, 29.4, 29.3, 29.3, 29.2, 29.1, 26.1, 26.0, 25.9, 22.7, 16.3, 14.1; LRMS (EI) *m/z* 532 (M+, 100), 427 (11), 411 (61), 398 (12), 368 (11), 325 (11), 300 (58), 188 (87), 122 (35), 105 (11), 69 (21), 55(22); HRMS (EI) *m/z* calcd for $C_{34}H_{48}N_2O_3$ 532.3665, found 532.3642

5-(8-(2,3,4,5,6-Pentafluorophenoxy)-1-octyloxy)-2-(4-(1-octyloxy)phenyl)pyrimidine (QL27-8/8). The general procedure described for the synthesis of **QL20-*m/n-x*F** was repeated with **14** (95 mg, 0.20 mmol), cesium carbonate (96 mg, 0.30 mmol) and 1-bromooctane (84 mg, 0.30 mmol) to give **QL27-8/8** as a white solid(108 mg, 92% yield): ^{1}H NMR (400 MHz, $CDCl_3$) *δ* 8.43 (s, 2H), 8.28 (d, *J* = 8.6 Hz, 2H), 6.99 (d, *J* = 9.1 Hz, 2H), 4.17 (t, *J* = 6.4 Hz, 2H), 4.10 (t, *J* = 6.4 Hz, 2H), 4.04 (t, *J* = 6.6 Hz, 2H), 1.94-1.74 (m, 6H), 1.59-1.25 (m, 18H), 0.92 (t, *J* = 7.1 Hz, 3H); ^{13}C NMR (100 MHz, $CDCl_3$) *δ* 160.7, 157.7, 151.1, 143.8, 130.1, 129.0, 114.5, 75.82 (t, *J* = 2.9), 68.9, 68.1, 31.8, 29.8, 29.4, 29.28, 29.25, 29.21, 29.14, 29.10, 26.1, 25.8, 25.5, 22.7, 14.1; LRMS (EI) *m/z* 594 (M+, 100), 482 (38), 188 (97), 149 (17), 97 (16), 85 (12), 83 (14), 81 (12), 71 (18), 69 (32), 57 (35), 55 (32); HRMS (EI) *m/z* calcd for $C_{32}H_{39}F_5N_2O_3$ 594.2888, found 594.2881. Anal. calcd for $C_{32}H_{39}F_5N_2O_3$: C, 64.63; H, 6.61; N, 4.71. Found: C, 64.39; H, 6.78; N, 4.78.

General procedure for the synthesis of 5-(1-alkyloxy)-2-(4-(8-*x*-fluorophenoxy-1-alkyloxy)-phenyl)pyrimidine (QL21-*m/n-x*F). Under a N_2 atmosphere, **(6-8)** (0.187 g, 1.0 mmol) was combined with cesium carbonate (0.293 g, 0.9 mmol) in dry DMF (40 mL). After

stirring for 5 min, **7-*n*** (0.9 mmol) was added to the mixture, which was stirred at room temperature overnight. The mixture was then concentrated, dissolved in EtOAc (40 mL), poured onto 10% aq HCl (50 mL) and extracted with EtOAc (2 x 40 mL). The combined organic extracts were washed with sat aq $NaHCO_3$, water, and brine, then dried ($MgSO_4$) and concentrated. Purification by flash chromatography on silica gel **(0%-20% EtOAc/Hexane)**. The product was recrystallized from acetonitrile and then from hexanes to give a white solid.

2-(4-(4-(2-Fluorophenoxy)-1-octyloxy)phenyl)-5-(1-octyloxy)pyrimidine (QL21-8/8-2F) White solid, 59% yield: ^{1}H NMR (400 MHz, $CDCl_3$) δ 8.42 (s, 2H), 8.28 (d, *J* = 9.1 Hz, 2H), 7.14 - 7.01 (m, 2H), 6.98 (d, *J* = 9.1 Hz, 2H), 6.98 (m, 1 H), 6.88 (m, 1H), 4.08 (t, *J* = 6.4 Hz, 2H), 4.03 (t, *J* = 6.6 Hz, 2H), 4.03 (t, *J* = 6.5 Hz, 2H), 1.89 - 1.79 (m, 6H), 1.55 - 1.44 (m, 6H), 1.44-1.39 (m, 6 H), 1.38 - 1.28 (m, 6 H), 0.91 (t, *J* = 7.3 Hz, 3H); ^{13}C NMR (100 MHz, $CDCl_3$) δ 157.6, 157.6, 152.7 (d, *J* = 246 Hz), 151.1, 147.2 (d, *J* = 10 Hz), 143.8, 130.1, 128.9, 124.2 (d, *J* = 4 Hz), 120.8 (d, J = 7 Hz), 116.1 (d, *J* = 18 Hz), 114.9 (d, *J* = 2 Hz), 114.4, 69.4, 68.9, 68.0, 31.8, 29.3, 29.3, 29.2, 29.19, 29.1, 26.0, 25.9, 22.6, 14.1; LRMS (EI) *m/z* 522 (M+, 100), 300 (35), 188 (77), 112 (11), 69 (11); HRMS (EI) *m/z* calcd for $C_{32}H_{43}N_2O_3F$ 522.3257, found 522.3243.

2-(4-(8-(3-Fluorophenoxy)-1-octyloxy)phenyl)-5-(1-octyloxy)pyrimidine (QL21-8/8-3F) White solid, 57% yield: ^{1}H NMR (400 MHz, $CDCl_3$) δ8.42 (s, 2H), 8.28 (d, *J* = 8.8 Hz, 2H), 7.21 (td, *J* = 8.8, 6.8 Hz, 1 H), 6.98 (d, *J* = 8.8 Hz, 2H), 6.71 - 6.58 (m, 3H), 4.08 (t, *J* = 6.4 Hz, 2H), 4.03 (t, *J* = 6.6 Hz, 2H), 3.94 (t, *J* = 6.4 Hz, 2H), 1.89 - 1.74 (m, 6 H), 1.55 - 1.25 (m, 18 H), 0.90 (t, *J* = 6.6 Hz, 3H); ^{13}C NMR (100 MHz, $CDCl_3$) δ 163.7 (d, *J*=244 Hz), 160.7, 160.5 (d, *J* = 11 Hz), 157.7, 151.1, 143.8, 130.1 (d, *J* = 10 Hz), 129.0, 114.4, 110.3 (d, *J* = 3 Hz), 107.2 (d, *J* = 21 Hz), 102.1 (d, *J* = 25 Hz), 69.0, 68.2, 68.0, 31.8, 29.3, 29.3, 29.2, 29.1, 26.0, 26.0, 25.9, 22.6,

14.1; LRMS (EI) *m/z* 522 (M+, 100), 300 (25), 188 (72), 112 (10), 69 (9), 55(9); HRMS (EI) *m/z* calcd for $C_{32}H_{43}N_2O_3F$ 522.3257, found 522.3239.

2-(4-(8-(4-Fluorophenoxy)-1octyloxy)phenyl)-5-(1-octyloxy)pyrimidine (QL21-8/8-4F) White solid, 60% yield: ^{1}H NMR (400 MHz, $CDCl_3$) δ 8.42 (s, 2H), 8.28 (d, *J* = 8.8 Hz, 2H), 7.04 – 6.91 (m, 2H), 6.98 (d, 8.8 Hz, 2H), 6.86-6.78 (m, 2H), 4.08 (t, *J* = 6.4 Hz, 2H), 4.03 (t, *J* = 6.6 Hz, 2H), 3.92 (t, *J* = 6.4 Hz, 2H), 1.89 - 1.73 (m, 6H), 1.56 - 1.26 (m, 18H), 0.90 (t, *J*=6.8 Hz, 3 H); ^{13}C NMR (100 MHz, $CDCl_3$) δ 160.6, 158.3, 156.4 (d, *J* = 243 Hz), 155.3 (d, *J* = 2 Hz), 151.1, 143.8, 130.1, 129.0, 115.7 (d, *J* = 23 Hz), 115.4 (d, *J* = 8 Hz), 114.4, 69.0, 68.6, 68.0, 31.8, 29.3, 29.2, 29.1, 26.0, 25.9, 22.6, 14.1; LRMS (EI) *m/z* 522 (M+, 100), 300 (31), 188 (75), 112 (10), 69 (12), 55(10); HRMS (EI) *m/z* calcd for $C_{32}H_{43}N_2O_3F$ 522.3257, found 522.3244

2-(4-(8-(2,6-Difluorophenoxy)-1octyloxy)phenyl)-5-(1-octyloxy)pyrimidine (QL23-8/8-2,6F$_2$) Under a N_2 atmosphere, (**6-8)** (0.192 mmol) was combined with cesium carbonate (94 mg, 0.29 mmol) in dry acetonitrile (40 mL). After stirring for 5 min, the appropriate 1-bromoalkane (0.29 mmol) was added to the mixture, which was heated to reflux overnight. After cooling, the mixture was concentrated, dissolved in EtOAc (40 mL) and washed with 10% aq HCl (50 mL). The aqueous layer was extracted with EtOAc (2 × 40 mL) and the combined organic extracts were washed with sat aq $NaHCO_3$, water, brine, dried ($MgSO_4$) and concentrated. Purification by flash chromatography on silica gel (0%-20% EtOAc/Hexane) gave the product, which was recrystallized from acetonitrile and then from hexanes to give a white solid, 94% yield: ^{1}H NMR (400 MHz, $CDCl_3$) δ 8.43 (s, 2H), 8.29 (d, *J* = 8.8 Hz, 2H), 6.99 (d, *J* = 9.1 Hz, 2H), 6.90 (d, *J* = 7.8 Hz, 3H), 4.15 (t, *J* = 6.8 Hz, 2H), 4.09 (t, *J* = 6.6 Hz, 2H), 4.04 (t, *J* = 6.6 Hz, 2H), 1.89 - 1.73 (m, 6H), 1.56-1.46 (m, 6H), 1.46-1.38 (m Hz, 6H), 1.38 - 1.30 (m, 6H), 0.91 (t, *J* = 6.6 Hz, 3H); ^{13}C NMR (100 MHz, $CDCl_3$) δ 160.7, 157.7, 156.4 (dd, *J*=257, 5 Hz), 151.1, 143.9, 135.9

(t, J = 7 Hz), 130.1, 129.0, 122.5 (t, *J* = 9 Hz), 114.4, 112.1 (dd, *J* = 16, 7 Hz), 74.7 (t, *J* = 4 Hz), 69.0, 68.1, 31.8, 29.9, 29.3, 29.24, 29.21, 29.19, 29.1, 26.0, 25.9, 25.6, 22.6, 14.1; LRMS (EI) *m/z* 540 (M+, 100), (11), 300 (12), 188 (48); HRMS (EI) *m/z* calcd for $C_{32}H_{42}N_2O_3F_2$ 540.3160, found 540.3163

5-(8-(2,6-Dimethylphenoxy)-1-octyloxy)-2-(4-(1-octyloxy)phenyl)pyrimidine (QL31-8/8-2,6Me$_2$) The general procedure for **QL23-8/8-2,6F$_2$** was followed with **9** to afford a white solid, 39% yield:^{1}H NMR (400 MHz, $CDCl_3$) δ 8.44 (s, 2H), 8.30 (d, *J* = 9.1 Hz, 2H), 7.03 (m, 2H), 7.00 (d, *J* = 9.1 Hz, 2H), 6.93 (dd, *J* = 7.8, 6.8 Hz, 1H), 4.10 (t, *J* = 6.4 Hz, 3H), 4.04 (t, *J* = 6.6 Hz, 3H), 3.79 (t, *J* = 6.6 Hz, 3H), 2.30 (s, 6H), 1.90-1.77 (m, 6 H), 1.57-1.39 (m, 6 H), 1.39-1.29 (m, 6H), 0.92 (t, *J* = 6.8 Hz, 3H); ^{13}C NMR (100 MHz, $CDCl_3$) δ 160.7, 157.7, 156.1, 151.1, 143.8, 130.9, 130.1, 129.0, 128.8, 123.6, 114.5, 72.2, 68.9, 68.1, 31.8, 30.4, 29.5, 29.4, 29.3, 29.3, 29.3, 29.1, 26.1, 26.1, 25.9, 22.7, 16.3, 14.1; LRMS (EI) *m/z* 532 (M+, 100), 411 (69), 368 (22), 300 (70), 188 (83), 122 (29), 69 (22), 55(18); HRMS (EI) *m/z* calcd for $C_{34}H_{48}N_2O_3$ 532.3665, found 532.3652

2,7-Hydroxy-7-(tetrahydro-2H-pyran-2-yloxy)-9-fluorenone. (15) 2,7-dihydroxy-9-fluorenone (1.070g, 5.04mmol) was dissolved in THF (25mL). p-toluenesulfonic acid (0.011g, 0.06mmol) was then added along with 3,4-dihydro-2H-pyran (1.00mL). The reaction was left overnight to stir at room temperature. The mixture was dissolved in ethyl acetate (40mL) and washed with sodium bicarbonate (30mL). The aqueous layer was extracted with ethyl acetate (2 x 20mL) and the combined organic extracts were washed with brine (1 x 30mL). The mixture was then dried ($MgSO_4$) and concentrated. Purification was performed using flash chromatography on silica gel (1% methanol in dichloromethane) to give 2,7-hydroxy-7-(tetrahydro-2H-pyran-2-yloxy)-9-fluorenone (0.361g, 24.2%, 147.8-148.5°C), a redish-orange solid. ^{1}H NMR (400MHz,

$CDCl_3$) δ 7.26 (d, *J* = 2.3 Hz, 1 H), 7.21 (d, *J* = 8.1 Hz, 1 H), 7.17 (d, *J* = 8.1 Hz, 1 H), 7.07 (d, *J* = 2.5 Hz, 1 H), 7.05 (d, *J* = 2.3 Hz, 1 H), 6.84 (dd, *J* = 2.5, 8.1 Hz, 1 H), 6.21-6.67 (br. s, 1 H), 5.43 (t, *J* = 3.2 Hz, 1 H), 3.93 (ddd, *J* = 3.0, 9.0, 11.5 Hz, 1 H), 3.61-3.71 (m, 1 H), 1.94-2.07 (m, 1 H), 1.83-1.94 (m, 2 H), 1.58-1.77 (m, 3 H); ^{13}C NMR (100MHz , $CDCl_3$) δ 194.0, 157.1, 156.4, 138.5, 137.1, 136.1, 135.7, 122.7, 121.1, 120.8, 120.3, 113.1, 112.0, 96.8, 62.4, 30.2, 25.1, 18.7.

General Procedure for the synthesis of 2-(Alkoxy)-7-(tetrahydro-2*H*-pyran-2-yloxy)-9-fluorenone. (16-*n*) 2,7-Hydroxy-7-(tetrahydro-2H-pyran-2-yloxy)-9-fluorenone **(15)** (0.334g, 1.13mmol) was dissolved in acetone (20mL). Potassium carbonate was added (1.200g, 8.68mmol) along with 1-bromoalkane. The reaction was left overnight at reflux. The mixture was dissolved in ethyl acetate (50mL) and HCl was added (20mL). The aqueous layer was washed with ethyl acetate (2 x 20mL). The combined organic extracts were then washed with brine (1 x 20mL) and then dried ($MgSO_4$). Purification was performed using flash chromatography on silica gel (7:1 hexanes to ethyl acetate).

2-(Heptyloxy)-7-(tetrahydro-2*H*-pyran-2-yloxy)-9-fluorenone. (16-7) The general procedure was used with 7-hydroxy-7-(tetrahydro-2H-pyran-2-yloxy)-9-fluorenone (0.390g, 1.32mmol), 1-bromoheptane (0.815g, 4.55mmol) and potassium carbonate (1.293g, 9.36mmol) to yield 2-(heptyloxy)-7-(tetrahydro-2*H*-pyran-2-yloxy)-9-fluorenone (0.388g, 74.7%, 88.4-89.5°C), a bright orange solid. ^{1}H NMR (400 MHz, $CDCl_3$) *δ* 7.31 (dd, *J* = 2.40, 8.21 Hz, 2H), 7.28 (d, *J* = 2.53 Hz, 1H), 7.16 (d, *J* = 2.27 Hz, 1H), 7.08 (dd, *J* = 2.40, 8.21 Hz, 1H), 6.94 (dd, *J* = 2.53, 8.08 Hz, 1H), 5.42 (t, *J* = 3.16 Hz, 1H), 3.99 (t, *J* = 6.69 Hz, 2H), 3.86-3.94 (m, 1H), 3.60-3.67 (m, 1H), 1.94-2.08 (m, 1H), 1.84-1.94 (m, 2H), 1.73-1.84 (m, 2H), 1.61-1.73 (m, 3H), 1.41-1.51 (m, 2H), 1.29-1.41 (m, 6H), 0.91 (t, *J* = 6.57 Hz, 3H); ^{13}C NMR (100 MHz, $CDCl_3$) *δ* 193.7, 159.6, 157.3,

138.3, 137.2, 136.0, 135.9, 122.4, 120.9, 120.6, 120.3, 113.0, 110.1, 96.7, 68.6, 62.2, 31.8, 30.2, 29.2, 29.0, 25.9, 25.1, 22.6, 18.8, 14.1.

2-(Octyloxy)-7-(tetrahydro-2*H*-pyran-2-yloxy)-9-fluorenone. (16-8) The general procedure was used with 7-hydroxy-7-(tetrahydro-2H-pyran-2-yloxy)-9-fluorenone (0.355g, 1.20mmol), 1-bromooctane (0.821g, 4.25mmol) and potassium carbonate (1.360g, 9.84mmol) to give 2-(octyloxy)-7-(tetrahydro-2*H*-pyran-2-yloxy)-9-fluorenone (0.358g, 73.1%, 61.6-63.7°C), a bright orange solid. ^{1}H NMR (400 MHz, $CDCl_3$) δ 7.30 (dd, *J*=9.98, 2.40 Hz, 2 H) 7.27 (d, *J*=2.53 Hz, 1 H) 7.15 (d, *J*=2.53 Hz, 1 H) 7.08 (dd, *J*=8.08, 2.53 Hz, 1 H) 6.93 (dd, *J*=8.08, 2.53 Hz, 1 H) 5.42 (t, *J*=3.16 Hz, 1 H) 3.98 (t, *J*=6.57 Hz, 2 H) 3.85-3.94 (m, 1 H) 3.59-3.67 (m, 1 H) 1.94-2.07 (m, 1 H) 1.83-1.93 (m, 2 H) 1.74-1.83 (m, 2 H) 1.65-1.73 (m, 2 H) 1.41-1.50 (m, 2 H) 1.24-1.40 (m, 9 H) 0.90 (t, *J*=6.82 Hz, 3 H);^{13}C NMR (100 MHz,$CDCl_3$) δ 194.0, 159.9, 157.6, 138.6, 137.5, 136.3, 136.2, 122.7, 121.1, 120.9, 120.6, 113.3, 110.4, 97.0, 68.9, 62.5, 32.1, 30.5, 29.6, 29.5, 29.5, 26.3, 25.4, 22.9, 19.1, 14.4.

2-(Nonyloxy)-7-(tetrahydro-2*H*-pyran-2-yloxy)-9-fluorenone. (16-9) The general procedure was used 7-hydroxy-7-(tetrahydro-2H-pyran-2-yloxy)-9-fluorenone (0.346g, 1.17mmol), 1-bromononane (0.944g, 4.56mmol) and potassium carbonate (1.162g, 8.41mmol) to yield 2-(nonyloxy)-7-(tetrahydro-2*H*-pyran-2-yloxy)-9-fluorenone (0.399g, 80.8%, 82.4-83.7°C), a bright orange solid. ^{1}H NMR (400 MHz, $CDCl_3$) δ 7.30 (dd, *J* = 2.27, 9.60 Hz, 2H), 7.27 (d, *J* = 1.77 Hz, 1H), 7.15 (d, *J* = 2.27 Hz, 1H), 7.08 (dd, *J* = 2.27, 8.08 Hz, 1H), 6.93 (dd, *J* = 2.40, 8.21 Hz, 1H), 5.42 (t, *J* = 3.16 Hz, 1H), 3.98 (t, *J* = 6.57 Hz, 2H), 3.85-3.94 (m, 1H), 3.59-3.67 (m, 1H), 1.94-2.06 (m, 1H), 1.83-1.94 (m, 2H), 1.74-1.83 (m, 2H), 1.62-1.73 (m, 3H), 1.41-1.50 (m, 2H), 1.22-1.40 (m, 10H), 0.89 (t, *J* = 7.07 Hz, 3H); ^{13}C NMR (100 MHz, $CDCl_3$)δ193.7, 159.6, 157.3,

138.3, 137.2, 136.0, 135.9, 122.4, 120.8, 120.5, 120.3, 113.0, 110.1, 96.7, 68.6, 62.2, 31.9, 30.2, 29.5, 29.4, 29.2, 29.2, 26.0, 25.1, 22.6, 18.7, 14.1.

2-(Decyloxy)-7-(tetrahydro-2*H*-pyran-2-yloxy)-9-fluorenone. (16-10) The general procedure was used 2,7-Hydroxy-7-(tetrahydro-2H-pyran-2-yloxy)-9-fluorenone (0.334g, 1.13mmol) was dissolved in acetone (20mL). Potassium carbonate was added (1.200g, 8.68mmol) along with 1-bromodecane (0.843g, 3.81mmol) to give 2-(decyloxy)-7-(tetrahydro-2*H*-pyran-2-yloxy)-9-fluorenone (0.372g, 75.6%, 72.6-74.4°C), a bright orange solid.^{1}H NMR (400MHz , $CDCl_3$) δ 7.30 (dd, *J* = 2.3, 9.1 Hz, 2 H), 7.27 (d, *J* = 1.8 Hz, 1 H), 7.15 (d, *J* = 2.5 Hz, 1 H), 7.08 (dd, *J* = 2.3, 8.1 Hz, 1 H), 6.93 (dd, *J* = 2.3, 8.1 Hz, 1 H), 5.42 (t, *J* = 3.2 Hz, 1 H), 3.98 (t, *J* = 6.6 Hz, 2 H), 3.90 (ddd, *J* = 3.0, 9.2, 11.6 Hz, 1 H), 3.59-3.68 (m, 1 H), 1.93-2.08 (m, 1 H), 1.84-1.93 (m, 2 H), 1.74-1.83 (m, 2 H), 1.65-1.73 (m, 2 H), 1.41-1.50 (m, 2 H), 1.23-1.41(m, 13 H), 0.89 (t, *J* = 6.7 Hz, 3 H);^{13}C NMR (100 MHz, $CDCl_3$) δ 194.0, 159.9, 157.6, 138.6, 137.5, 136.3, 136.2, 122.7, 121.2, 120.9, 120.6, 113.3, 110.4, 97.0, 68.9, 62.5, 32.2, 30.5, 29.9, 29.8, 29.7, 29.6, 29.5, 26.3, 25.4, 23.0, 19.1, 14.4.

General Procedure for the synthesis of 2-(Alkoxy)-7-hydroxy-9-fluorenone. (17-*n*) 2-(Decyloxy)-7-(tetrahydro-2*H*-pyran-2-yloxy)-9-fluorenone (0.346g, 0.79mmol) was dissolved in THF (10mL) with ethanol (10mL). p-toluenesulfonic acid was added (0.011g, 0.06mmol). The reaction was allowed to heat overnight at about 65°C. The reaction mixture was concentrated and then purified using flash chromatography (5:1 hexanes to ethyl acetate) yielding product.

2-(Heptyloxy)-7-hydroxy-9-fluorenone. (17-7) The general procedure was used with 2-(heptyloxy)-7-(tetrahydro-2*H*-pyran-2-yloxy)-9-fluorenone (0.378g, 0.96mmol) and p-toluenesulfonic acid (0.014g, 0.07mmol) to give 2-(heptyloxy)-7-hydroxy-9-fluorenone (0.298g, 99.9%, 109.0-110.6°C), a red solid. ^{1}H NMR (400 MHz, CD_3OD) *δ* 7.25 (dd, *J* = 8.08, 10.11 Hz,

2H), 6.99 (d, *J* = 2.27 Hz, 1H), 6.87 - 6.94 (m, 2H), 6.83 (dd, *J* = 2.27, 8.08 Hz, 1H), 4.87 (br. s., 1H), 3.93 (t, *J* = 6.44 Hz, 2H), 1.74 (quin, *J* = 6.60 Hz, 2H), 1.40-1.50 (m, 2H), 1.28-1.39 (m, 6H), 0.90 (t, *J* = 6.57 Hz, 3H); ^{13}C NMR (100 MHz, CD_3OD) *δ* 195.7, 160.9, 159.3, 139.1, 137.8, 137.3, 137.0, 122.2, 122.0, 121.7, 121.6, 112.5, 111.4, 69.7, 33.1, 30.5, 30.4, 27.3, 23.8, 14.6.

2-Hydroxy-7-(octyloxy)-9-fluorenone. (17-8) The general procedure was used with 2-(octyloxy)-7-(tetrahydro-2*H*-pyran-2-yloxy)-9-fluorenone (0.320g, 0.78mmol) and p-toluenesulfonic acid (0.01g, 0.05mmol) to give 2-hydroxy-7-(octyloxy)-9-fluorenone (0.222g, 87.4%, 116.5-118.9°C), a red solid. ^{1}H NMR (400 MHz, CD_3OD) δ 7.24-7.28 (d, 1H), 7.20-7.24 (d, 1H), 7.03 (d, *J* = 2.27 Hz, 1H), 6.95 (d, *J* = 2.27 Hz, 1H), 6.90 (dd, *J* = 2.40, 8.21 Hz, 1H), 6.83 (dd, *J* = 2.53, 8.08 Hz, 1H), 4.78 (br. s., 1H), 3.95 (t, *J* = 6.44 Hz, 2H), 1.75 (quin, *J* = 6.80 Hz, 2H), 1.39-1.50 (m, 2H), 1.23-1.37 (m, 8H), 0.88 (t, *J* = 7.07 Hz, 3H);^{13}C NMR (100 MHz, CD_3OD) δ195.8, 160.4, 158.8, 138.8, 137.5, 136.9, 136.7, 122.0, 121.7, 121.5, 121.3, 112.4, 111.3, 69.4, 32.8, 30.3, 30.2, 30.1, 26.9, 23.5, 14.5.

2-Hydroxy-7-(nonyloxy)-9-fluorenone. (17-9) The general procedure was used with 2-(nonyloxy)-7-(tetrahydro-2*H*-pyran-2-yloxy)-9-fluorenone (0.352g, 0.83mmol) and p-toluenesulfonic acid (0.011g, 0.06mmol) to give 2-hydroxy-7-(nonyloxy)-9-fluorenone (0.287g, 101.7%, 111.2-113.3°C), a deep red solid. ^{1}H NMR (400 MHz, CD_3OD) δ 7.26 (d, *J* = 8.34 Hz, 1H), 7.23 (d, *J* = 8.08 Hz, 1H), 7.03 (d, *J* = 2.53 Hz, 1H), 6.95 (d, *J* = 2.02 Hz, 1H), 6.91 (dd, *J* = 2.40, 8.21 Hz, 1H), 6.83 (dd, *J* = 2.27, 8.08 Hz, 1H), 4.81 (br, s, 1H), 3.95 (t, *J* = 6.44 Hz, 2H), 1.75 (quin, *J* = 6.60 Hz, 2H), 1.40-1.49 (m, 2H), 1.22-1.39 (m, 10H), 0.87 (t, *J* = 6.82 Hz, 3H); ^{13}C NMR (100MHz, CD_3OD) δ195.8, 160.5, 158.9, 138.9, 137.5, 137.0, 136.7, 122.1, 121.7, 121.6, 121.4, 112.5, 111.3, 69.5, 32.9, 30.5, 30.4, 30.2, 30.2, 27.0, 23.6, 14.5 LRMS (EI) *m/z* 338 (30), 212 (100).

2-(Decyloxy)-7-hydroxy-9-fluorenone. (17-10) The general procedure was used with 2-(Decyloxy)-7-(tetrahydro-2*H*-pyran-2-yloxy)-9-fluorenone (0.346g, 0.79mmol) was dissolved in THF (10mL) with ethanol (10mL). p-toluenesulfonic acid was added (0.011g, 0.06mmol), which yielded 2-(decyloxy)-7-hydroxy-9-fluorenone (0.275g, 98.4%, 104.3-107.0°C), a deep red solid. ^{1}H NMR (400 MHz, CD_3OD) δ 7.24 (d, *J* = 8.08 Hz, 1H), 7.18-7.22 (d, 1H), 7.03 (d, *J* = 2.27 Hz, 1H), 6.96 (d, *J* = 2.27 Hz, 1H), 6.89 (dd, *J* = 2.53, 8.34 Hz, 1H), 6.83 (dd, *J* = 2.40, 7.96 Hz, 1H), 4.74 (br. s., 1H), 3.94 (t, *J* = 6.44 Hz, 2H), 1.74 (quin, *J* = 6.60 Hz, 2H), 1.38-1.49 (m, 2H), 1.21-1.37 (m, 12H), 0.86 (t, *J* = 7.33 Hz, 3H); ^{13}C NMR (100 MHz, CD_3OD) δ 195.5, 160.1, 158.4, 138.5, 137.2, 136.6, 136.4, 121.7, 121.4, 121.3, 121.0, 112.2, 111.0, 69.2, 32.5, 30.2, 30.2, 30.0, 29.9, 29.8, 26.6, 23.3, 14.3.

General procedure for the synthesis of 2-(8-(2,6-Difluorophenoxy)-1-octyloxy)-7-(alkoxy)-9-fluorenone (QL29-7/8-2,6F$_2$). Under a N_2 atmosphere, (**17-n)** (0.192 mmol) was combined with cesium carbonate (94 mg, 0.29 mmol) in dry acetonitrile (40 mL). After stirring for 5 min, the appropriate 1-bromoalkane (0.29 mmol) was added to the mixture, which was heated to reflux overnight. After cooling, the mixture was concentrated, dissolved in EtOAc (40 mL) and washed with 10% aq HCl (50 mL). The aqueous layer was extracted with EtOAc (2 × 40 mL) and the combined organic extracts were washed with sat aq $NaHCO_3$, water, brine, dried ($MgSO_4$) and concentrated. Purification by flash chromatography on silica gel (0%-20% EtOAc/Hexane) gave the product, which was recrystallized from acetonitrile, methanol and then from hexanes to give a red-orange solid.

2-(8-(2,6-Difluorophenoxy)-1-octyloxy)-7-(heptyloxy)-9-fluorenone (QL29-7/8-2,6F$_2$) Red-orange solid, 98% yield: ^{1}H NMR (400 MHz, $CDCl_3$) δ 7.28 (s, 1H), 7.26 (s, 1H), 7.16 (d, *J*=2.5 Hz, 2 H), 6.95 (d, *J*=2.3 Hz, 2 H), 6.99 - 6.85 (m, *3* H), 4.15 (t, *J*=6.6 Hz, 5 H), 4.00 (t, *J*=6.4

Hz, 9 H), 1.80 (td, *J*=8.5, 4.0 Hz, 14 H), 1.40 (m, 40 H), 0.92 (t, *J*=6.3 Hz, 7 H); ^{13}C NMR (100 MHz, $CDCl_3$) δ 193.9, 159.50, 159.49, 156.3 (dd, *J* = 248, 7 Hz), 137.4 (d, *J* = 1.5 Hz), 136.0, 120.9, 120.4, 112.1 (dd, J = 16, 7 Hz), 110.2 (d, *J* = 2 Hz), 74.7 (t, *J* = 3 Hz), 68.6, 68.5, 31.8, 29.9, 29.3, 29.21, 29.18, 29.1, 29.0, 26.96, 25.91, 25.6, 22.7, 22.6, 14.1; LRMS (EI) *m/z* 550 (M+, 100), 212 (93), 130 (22), 69 (12), 55 (9); HRMS (EI) *m/z* calcd for $C_{34}H_{40}F_2O_4$ 550.2888, found 550.2895

2-(8-(2,6-Difluorophenoxy)-1-octyloxy)-7-(octyloxy)-9-fluorenone (QL29-8/8-2,6F$_2$)

Red-orange solid, 97% yield: ^{1}H NMR (400 MHz, $CDCl_3$) δ 7.28 (s, 1 H), 7.26 (s, 1 H), 7.15 (d, *J* = 2.5 Hz, 2 H),), 6.94 (d, J = 2.8 Hz), 6.99 - 6.80 (m, 3H), 4.34 (t, *J* = 6.6 Hz, 2 H), 4.19 (m, 4 H), 1.99 (m, 6 H), 1.61 (m, 20 H), 1.11 (m, 3 H); ^{13}C NMR (100 MHz, $CDCl_3$) δ 193.1, 159.51, 159.50, 156.3 (dd, *J*=248, 6 Hz), 137.4, 136.0, 135.9, 122.5 (t, *J*=9.1 Hz), 120.8, 120.4, 112.1 (dd, *J*=17, 7 Hz), 110.2 (d, *J* = 2 Hz), 74.7 (t, *J* = 3 Hz), 68.6, 68.5, 31.8, 29.9, 29.3, 29.21, 29.18, 29.15, 26.00, 25.91, 25.6, 22.7, 14.1; LRMS (EI) *m/z* 564 (M+, 78), 212 (100), 130 (21), 69 (15), 55 (13); HRMS (EI) *m/z* calcd for $C_{35}H_{42}F_2O_4$ 564.3056, found 564.3051

2-(8-(2,6-Difluorophenoxy)-1-octyloxy)- 7-(nonyloxy)-9-fluorenone (QL29-9/8-2,6F$_2$)

Red-orange solid, 97% yield: ^{1}H NMR (400 MHz, $CDCl_3$) δ 7.28 (s 1H), 7.26 (s, 1H), 7.16 (d, *J* = 2.3 Hz, 2H), 6.95 (d, *J* = 2.5 Hz, 2 H), 6.99 - 6.85 (m, 3 H), 4.15 (t, *J* = 6.6 Hz, 2 H), 3.99 (m, 4 H), 1.85-1.75 (m, 6 H), 1.60-1.30 (m, 20H), 0.91 (t, *J* = 6.8 Hz, 3H); ^{13}C NMR (100 MHz, $CDCl_3$) δ 193.9, 159.51, 159.50, 156.3 (m, *J* = 248, 6 Hz), 137.4, 136.0, 122.5, 120.8, 120.4, 112.1 (dd, J = 16, 7 Hz), 110.2 (d, *J* = 2 Hz), 74.7 (t, *J* = 3 Hz), 68.6, 68.5, 31.9, 29.9, 29.5, 29.4, 29.3, 29.3, 29.2, 29.2, 29.1, 26.0, 25.9, 25.6, 22.7, 14.1; LRMS (EI) *m/z* 578 (M+, 100), 338 (12), 212 (87), 130 (26), 69 (14), 55 (13); HRMS (EI) *m/z* calcd for $C_{36}H_{44}F_2O_4$ 578.3201, found 578.3207

2-(Decyloxy)-7-(8-(2,6-Difluorophenoxy)-1-octyloxy)-9-fluorenone (QL29-10/8-2,6F$_2$)

Red-orange solid, 92% yield: ^{1}H NMR (400 MHz, $CDCl_3$) δ 7.28 (s 1H), 7.26 (s, 1H), 7.16 (d, *J* = 2.3 Hz, 2H), 6.95 (d, *J* = 2.3 Hz, 2H), 6.99 - 6.85 (m, 3H), 4.15 (t, *J* = 6.6 Hz, 2H), 4.00 (t, J = 6.6 Hz, 4H), 1.87 - 1.75 (m, 6H), 1.54 - 1.24 (m, 20H), 0.91 (t, *J* = 6.8 Hz, 3H); ^{13}C NMR (100 MHz, $CDCl_3$) δ 193.9, 159.51, 159.50 156.3 (dd, *J* = 248, 6 Hz), 137.4, 136.0, 122.5 (t, *J*=9.1 Hz), 120.9, 120.4, 112.1 (dd, *J*=17, 7 Hz), 110.2 (d, *J* = 2 Hz), 74.7 (t, *J* = 3 Hz), 68.6, 68.5, 31.9, 29.9, 29.57, 29.56, 29.4, 29.3, 29.24, 29.20, 29.18, 29.1, 26.0, 25.9, 25.6, 22.7, 14.1; LRMS (EI) *m/z* 592 (M+, 75), 212 (100), 130 (31), 69 (21), 55 (22); HRMS (EI) *m/z* calcd for $C_{37}H_{46}F_2O_4$ 592.3371, found 592.3364

Chapter 8: Conclusion and Future Work:

The objective of this thesis was to investigate phenoxy-terminated liquid crystals for their ability to nanosegregate and to promote ‘de Vries-like’ properties in liquid crystals.

In the first part of this thesis, two sterically equivalent series of phenoxy-terminated mesogens with 2-phenylpyrimidine cores were synthesized (**QL11**, **QL12**). The results showed that phenoxy-terminated liquid crystals have increased melting points compared to their parent compounds, with suppressed SmC mesomorphism. The work also showed that phenoxy-terminated mesogens nanosegregate at the layer interface, but the reduction factor for some of these compounds showed that they are not ‘de Vries-like’, rather somewhere in between a de Vries and classic rigid rod behaviour. The phenoxy-terminated mesogens should be combined with a carbosilane or siloxane end-group on the opposing alkyl chain to further increase the promotion of the SmC phase and ‘de-Vries-like’ properties.

Next, we investigated the effect of fluoro substituent(s) on mesomorphic properties of phenoxy-terminated mesogens (**QL20**, **QL22**). The results showed that mesomorphic properties could be tuned and the SmC phase could be promoted enantiotropically by varying the position of the fluoro substituent in the phenoxy-terminated mesogens. Furthermore, this research showed that computational calculations can be used to predict liquid crystalline mesomorphic behaviour through geometry optimization and the analysis of energies of association calculations of two phenoxy-terminated alkyl chains. Computational calculations should be expanded to more substituents and compared to experimental mesomorphic behaviors. In this case, the promotion of ‘de Vries-like’ behaviour can be speculated to be caused by intermolecular nanosegregration at the layer interface; adding cyano or nitro substituents to increase interactions at the layer interface might increase ‘de Vries-like’ behavior in phenoxy-terminated mesogens.

The investigation of **QL23-8/8-2,6F2** for ‘de Vries-like’ properties shows that it is an intermediate between rigid rod and ‘de Vries-like’ behaviour, but has a low optical tilt value. Further promotion of the SmC phase may allow for observed ‘de Vries-like’ behaviour. To achieve SmC promotion, a stronger SmC promoting core such as a 2-phenylthiadiazole, as shown below, could be used to increase optical tilt in these compounds.

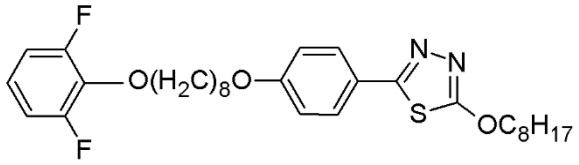

In addition, the investigation of **QL22** showed that a SmC-N liquid crystal with low optical tilt was possible in phenoxy-terminated mesogens. Further investigation revealed that the positive dielectric anisotropy of 2,6-difluorophenoxy-terminated 2-phenylpyrimidine mesogens was problematic for use in SSFLC devices. Synthesis of a series of fluorenone derivatives (**QL29)** showed that these SmC-N mesogens can be tuned to have negative dielectric anisotropy, and can switch between $+\theta$ and $-\theta$ states without the formation of chevrons, however switching times could not be analyzed since the cell used are designed for SmA-SmC aligned mesogens. These mesogens should be examined for their use as SSFLCs in special cells made for SmC-N materials, which can be designed to create a bistable environment and to reduce switching times in these systems. These compounds should also be examined to maximize their spontaneous polarization by doping the mesogens with different chiral dopants with different cores. An example of a chiral dopant with a fluorenone core to be synthesized and examined in the presence of a **QL29** mesogen is shown below.

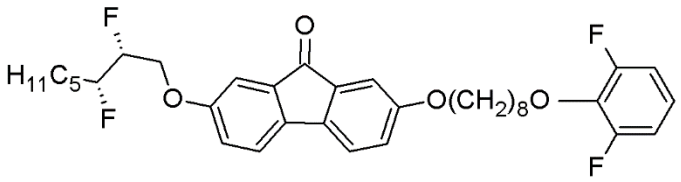

Upon optimization of the chiral dopant, these SmC-N materials (**QL22**, **QL29**) should also be used in mixtures to promote a room temperature SmC liquid crystals phase with negative dielectric anisotropy that can be used for SSFLC applications.

Appendix 1: DSC Profiles of Liquid Crystals

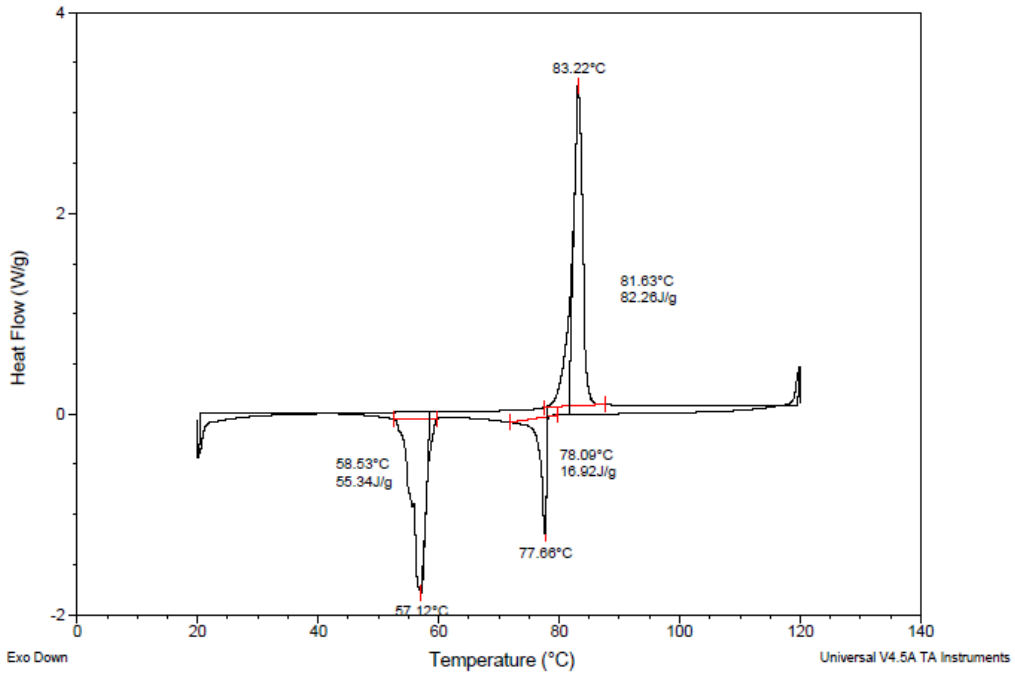

Figure A1-1: DSC profile for compound **QL11-4/12** taken at a scan rate of 5K/min.

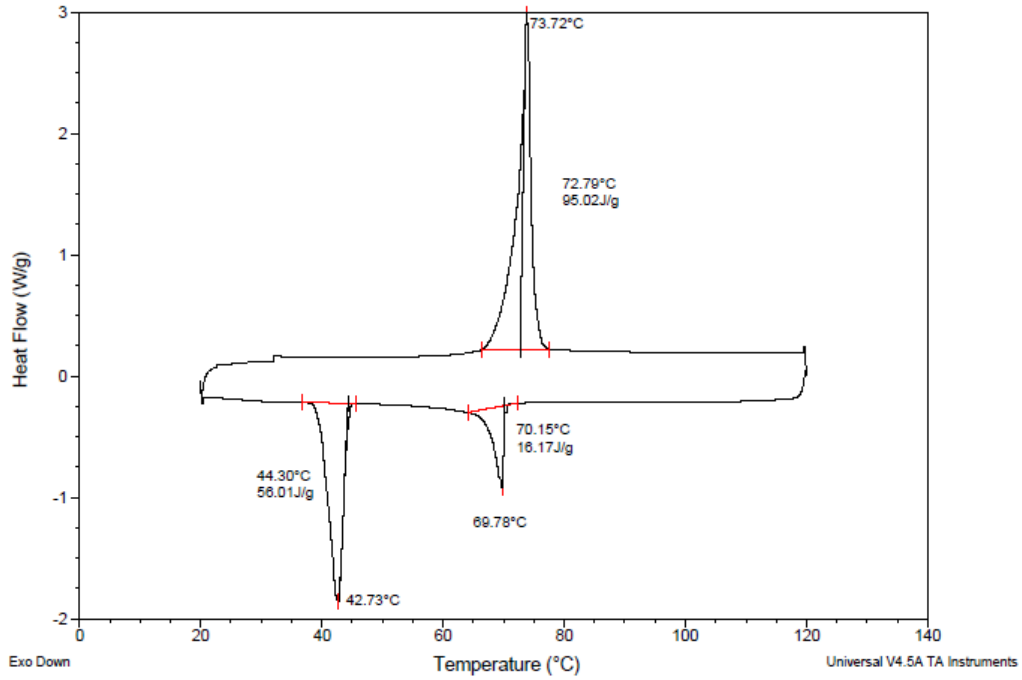

Figure A1-2: DSC profile for compound **QL11-5/11** taken at a scan rate of 5K/min.

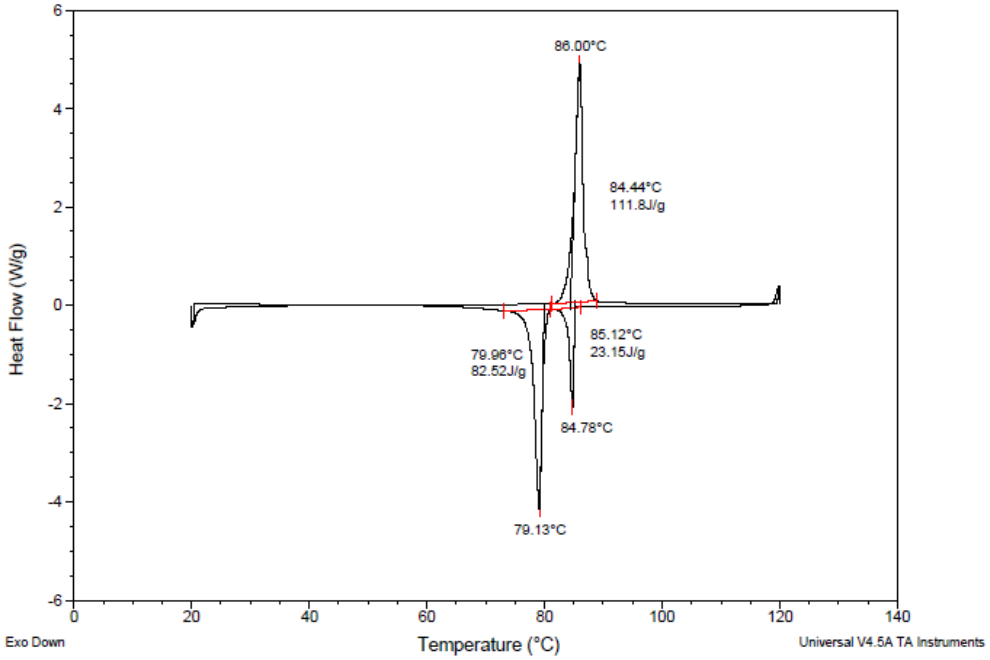

Figure A1-3: DSC profile for compound **QL11-6/10** taken at a scan rate of 5K/min.

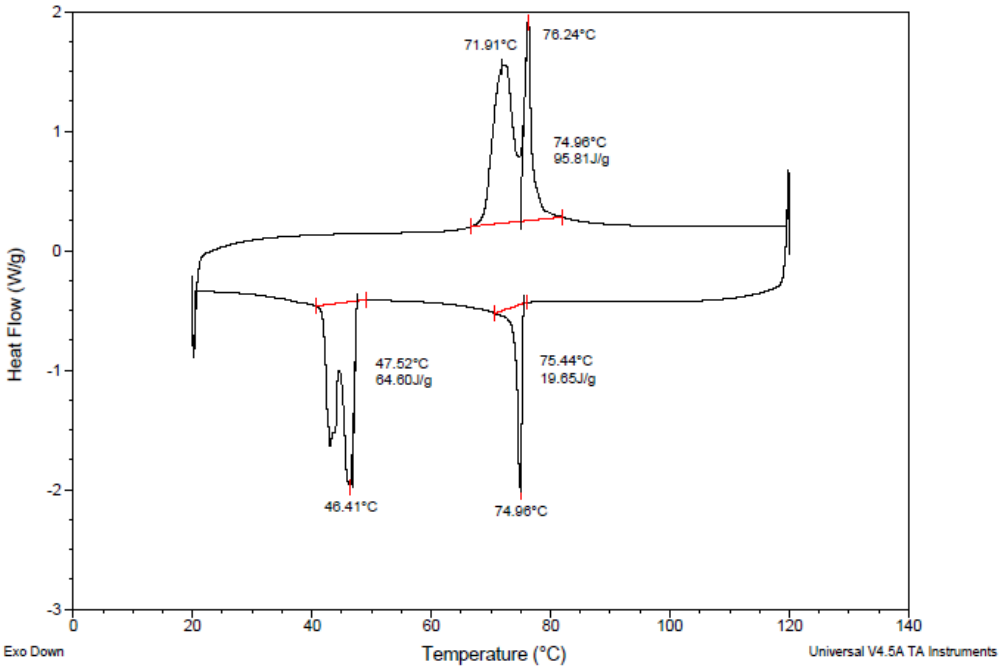

Figure A1-4: DSC profile for compound **QL11-7/9** taken at a scan rate of 5K/min.

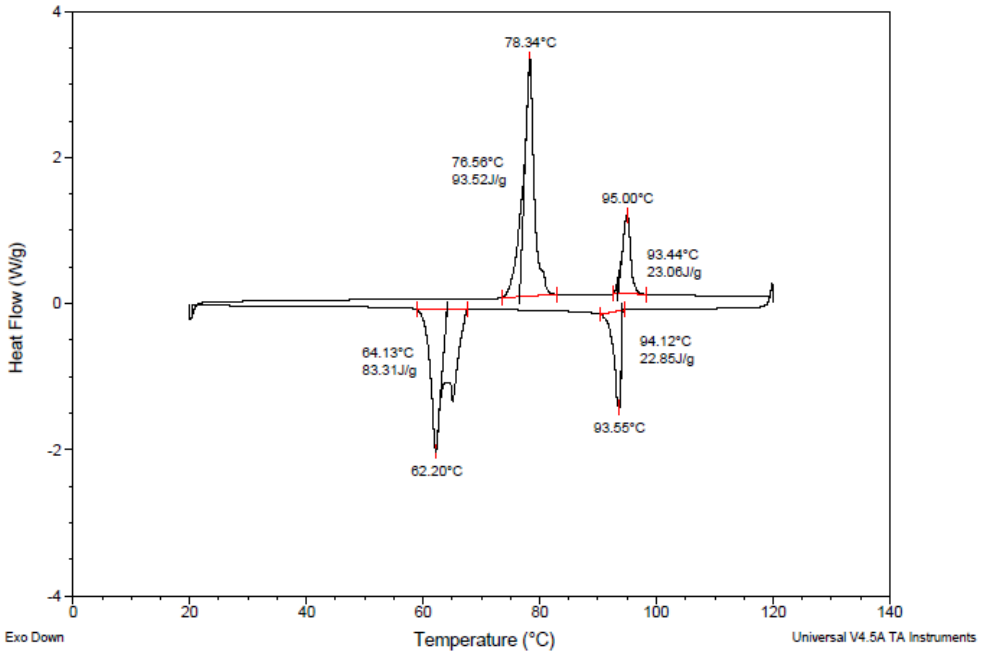

Figure A1-5: DSC profile for compound **QL11-8/8** taken at a scan rate of 5K/min.

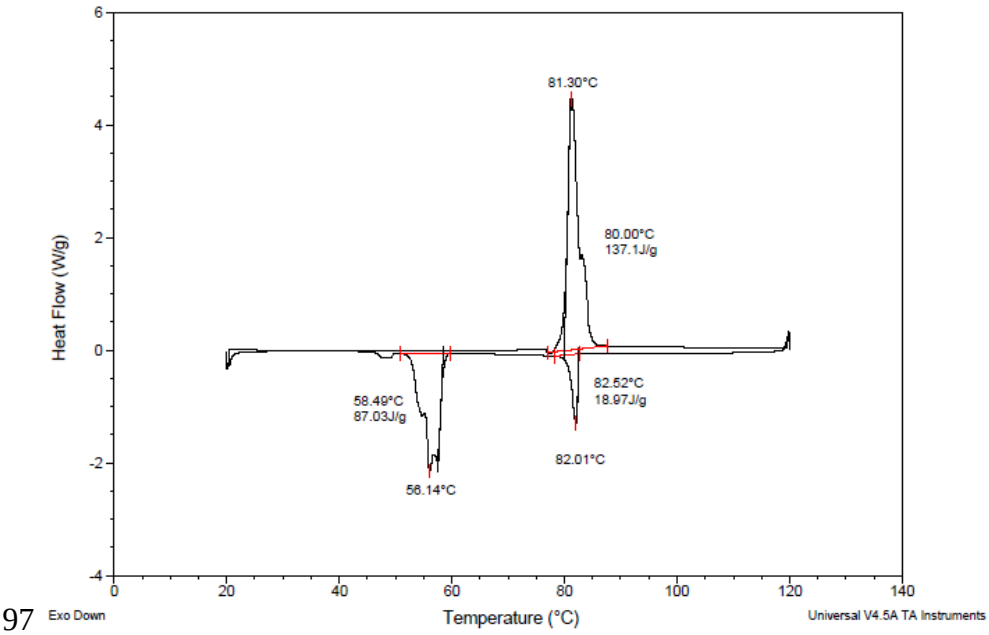

97

Figure A1-6: DSC profile for compound **QL11-9/7** taken at a scan rate of 5K/min.

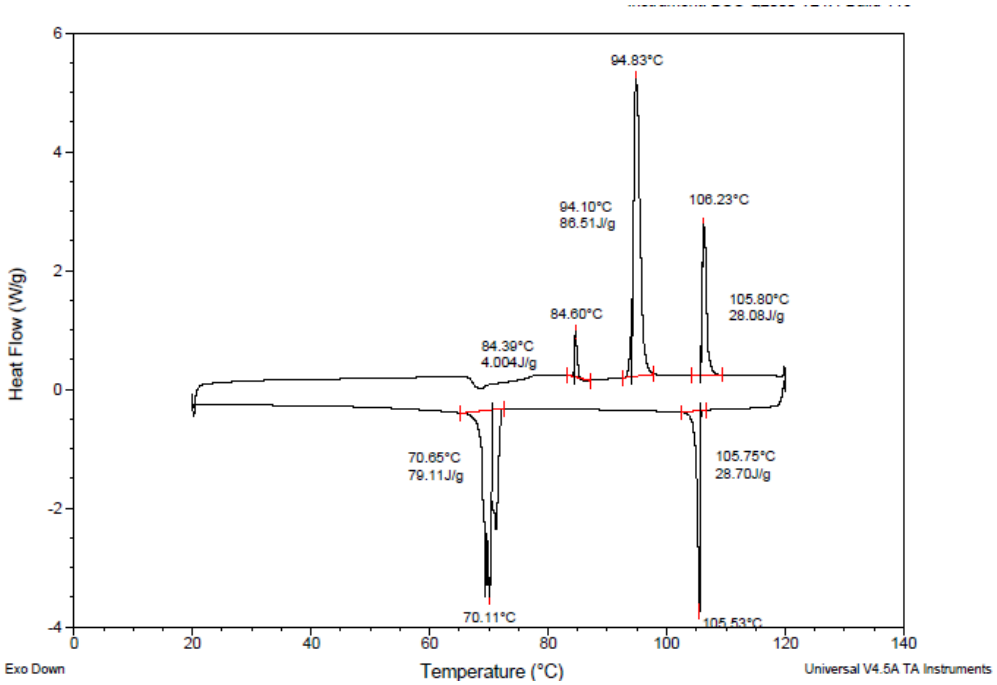

Figure A1-7: DSC profile for compound **QL11-10/6** taken at a scan rate of 5K/min.

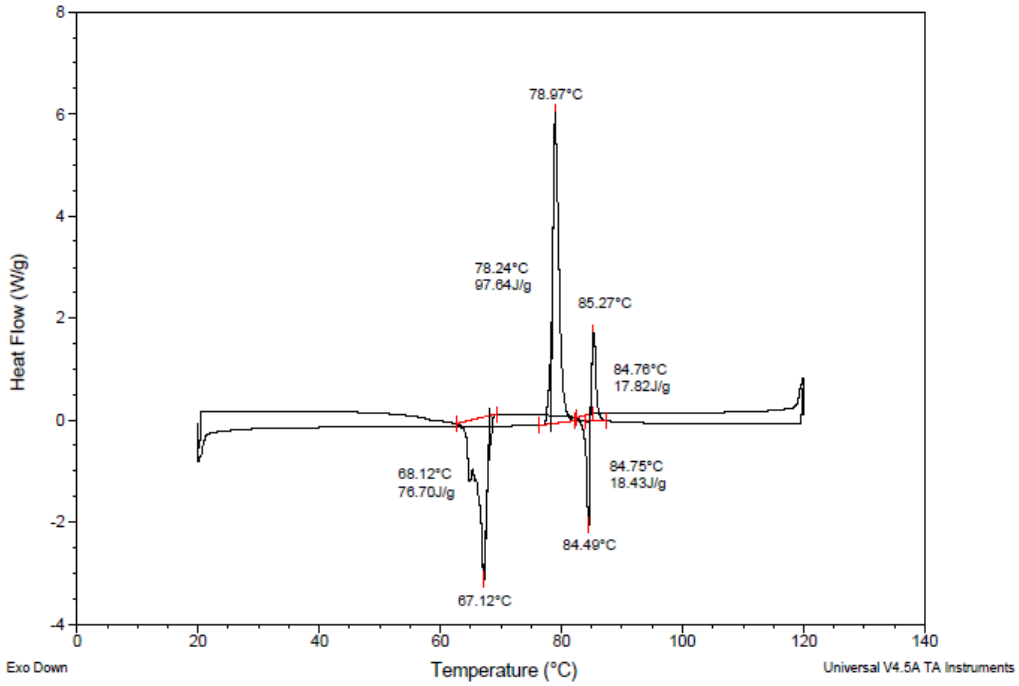

Figure A1-8: DSC profile for compound **QL11-11/5** taken at a scan rate of 5K/min.

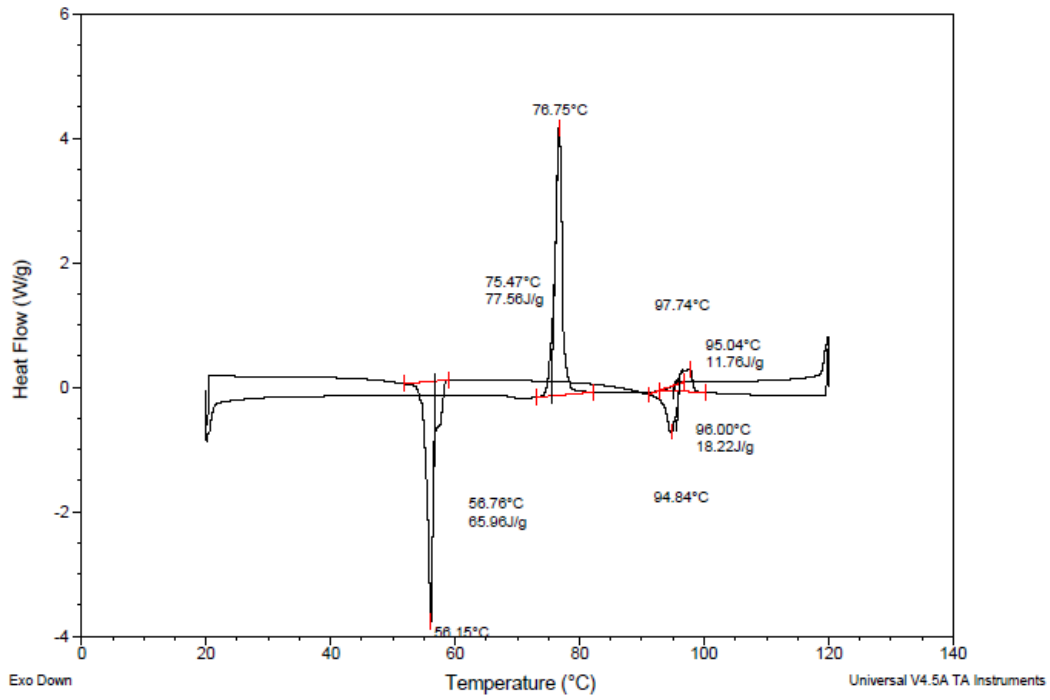

Figure A1-9: DSC profile for compound **QL11-12/4** taken at a scan rate of 5K/min.

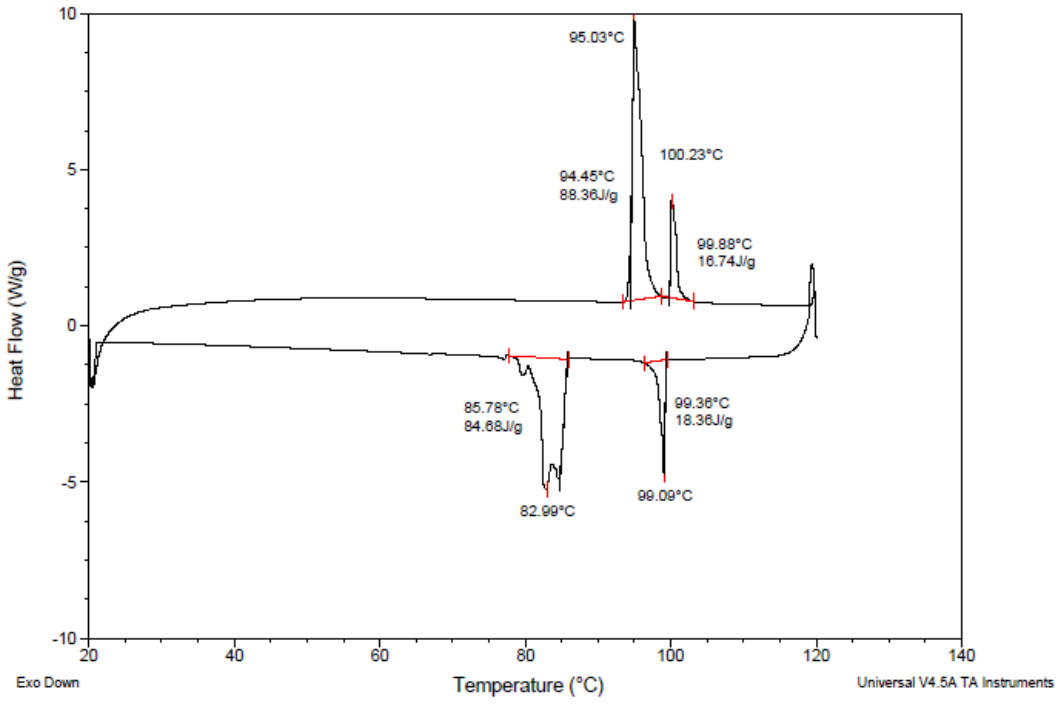

Figure A1-10: DSC profile for compound **QL12-12/4** taken at a scan rate of 5K/min.

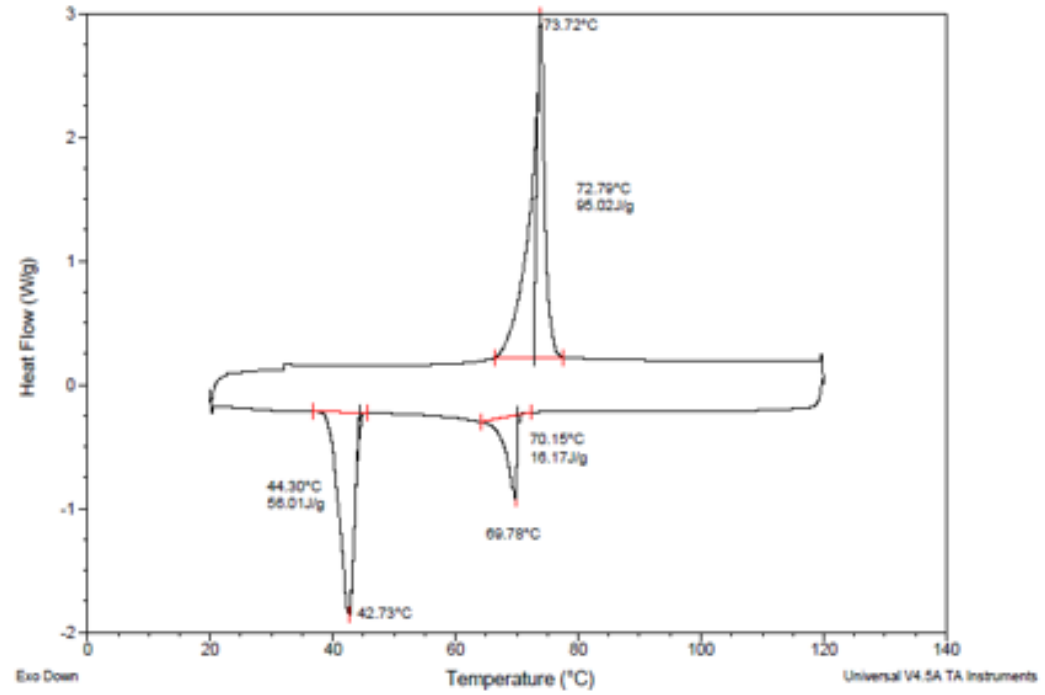

Figure A1-11: DSC profile for compound **QL12-11/5** taken at a scan rate of 5K/min.

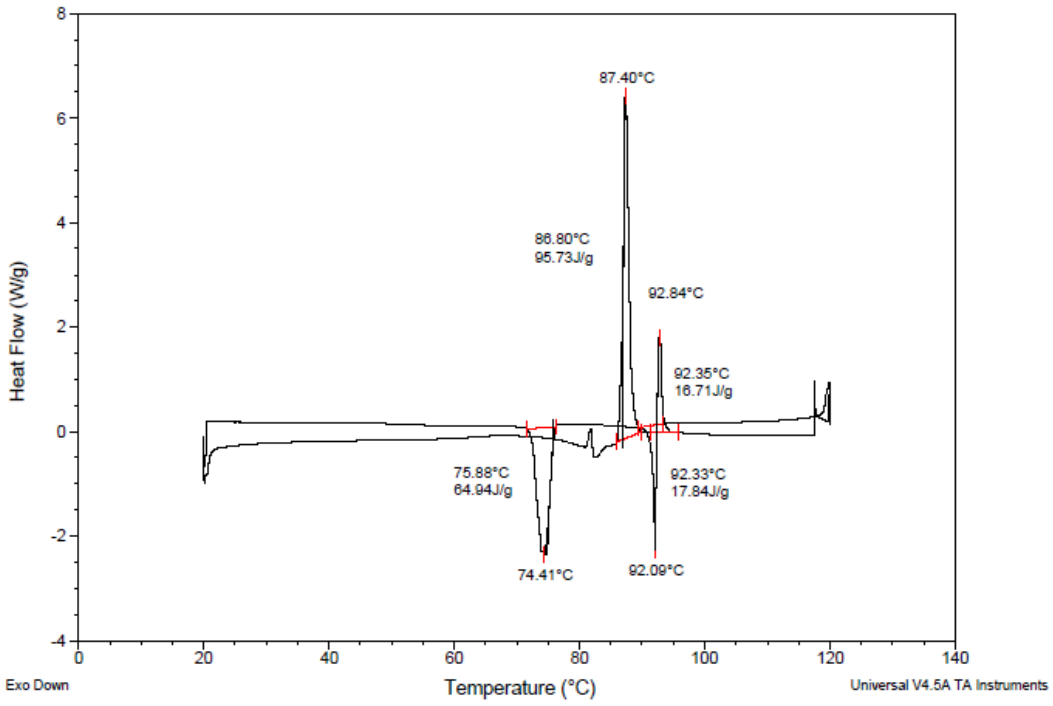

Figure A1-12: DSC profile for compound **QL12-10/6** taken at a scan rate of 5K/min.

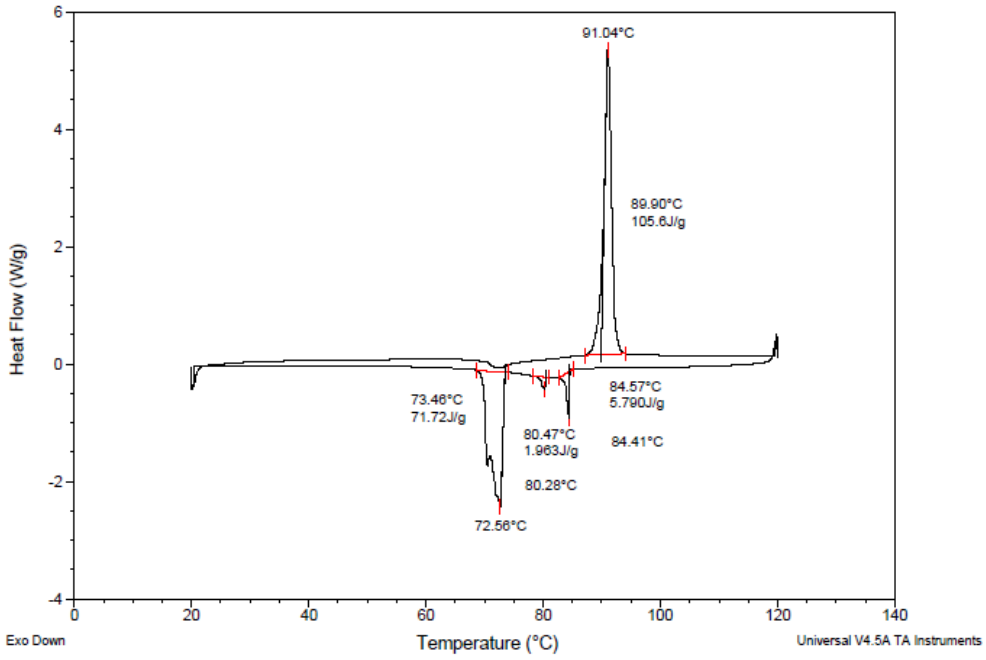

Figure A1-13: DSC profile for compound **QL12-8/8** taken at a scan rate of 5K/min.

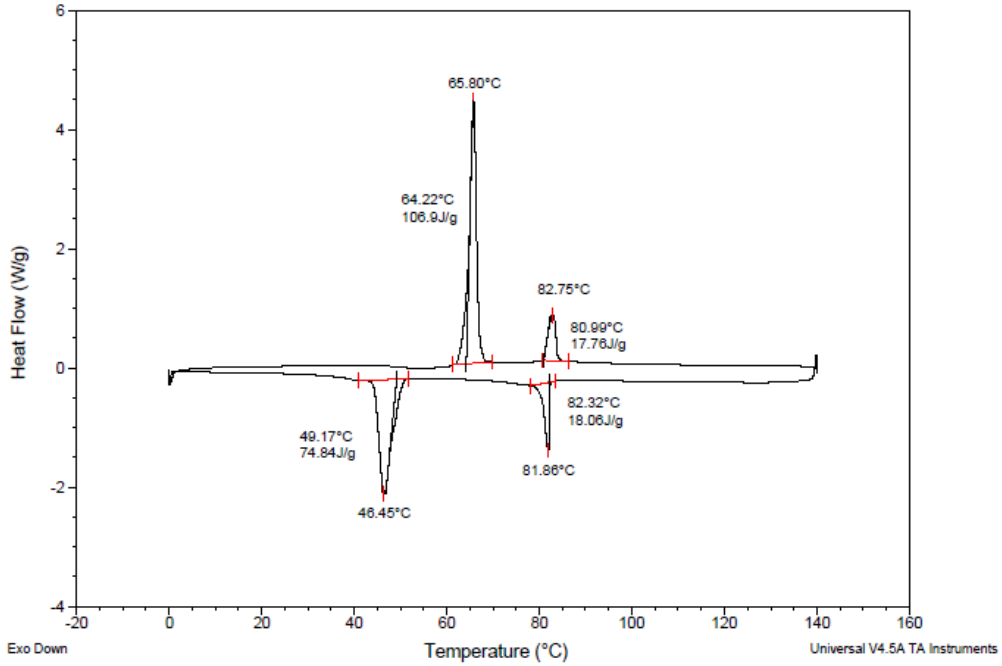

Figure A1-14: DSC profile for compound **QL20-8/8-2F** taken at a scan rate of 5K/min.

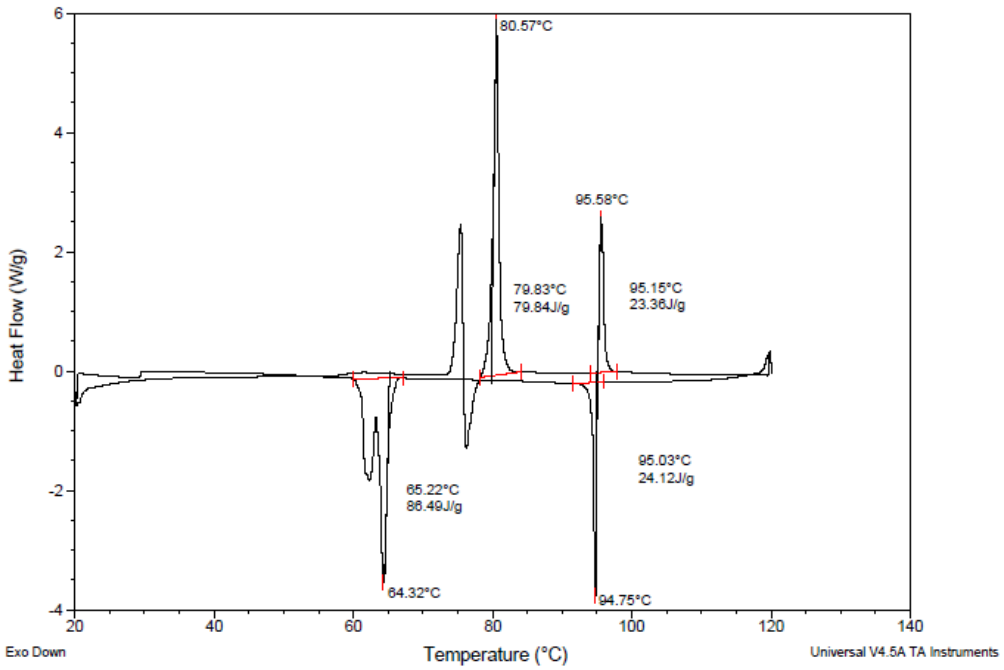

Figure A1-15: DSC profile for compound **QL20-8/8-3F** taken at a scan rate of 5K/min.

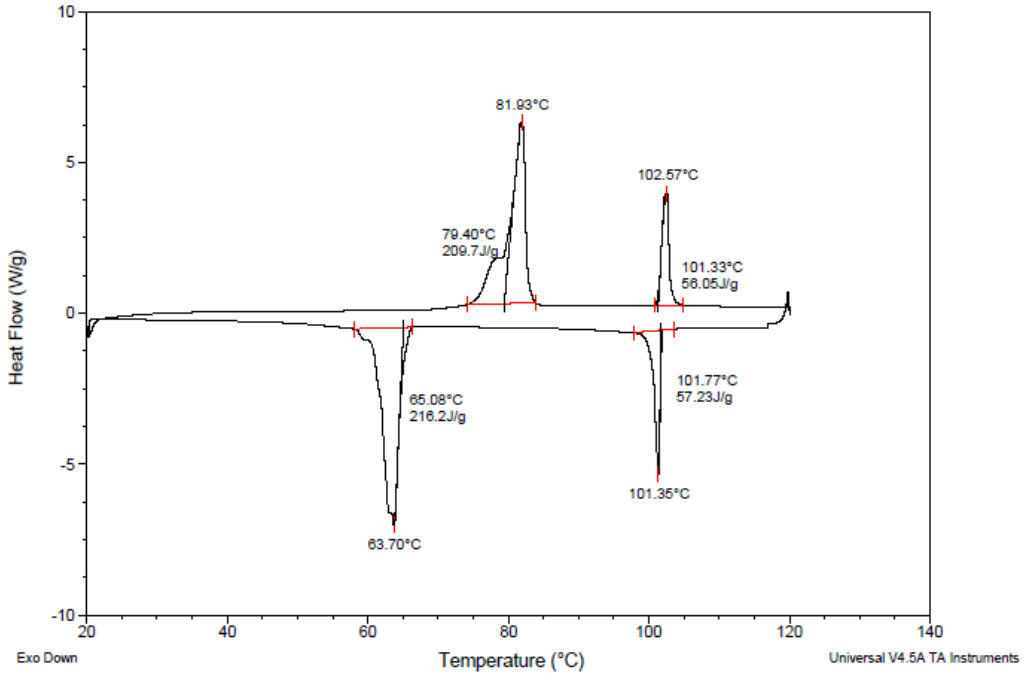

Figure A1-16: DSC profile for compound **QL20-8/8-4F** taken at a scan rate of 5K/min.

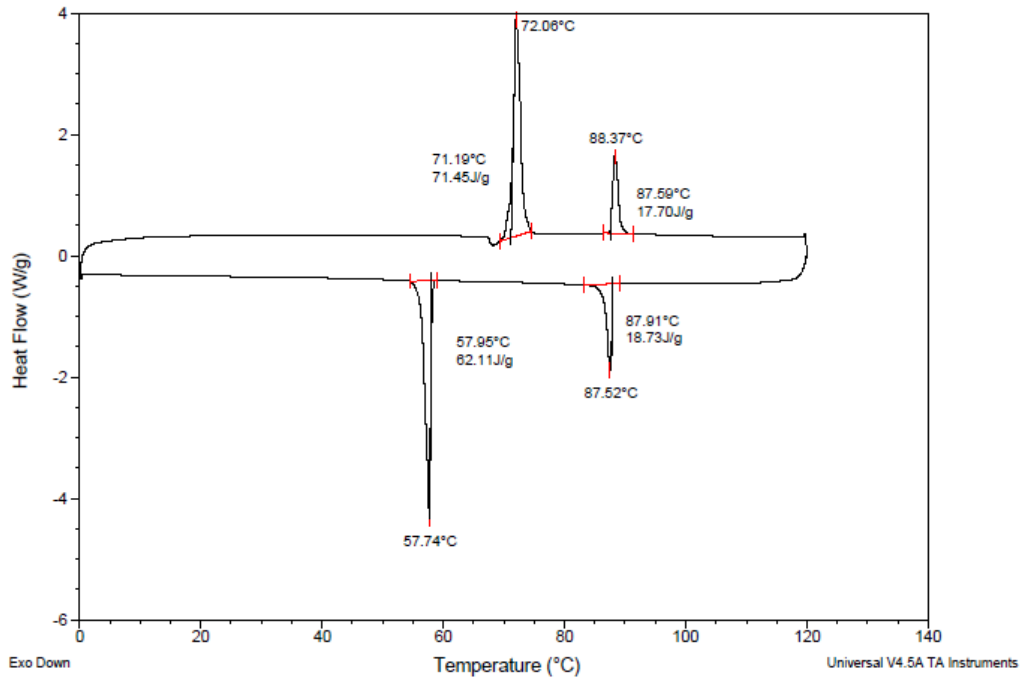

Figure A1-17: DSC profile for compound **QL20-10/6-2F** taken at a scan rate of 5K/min.

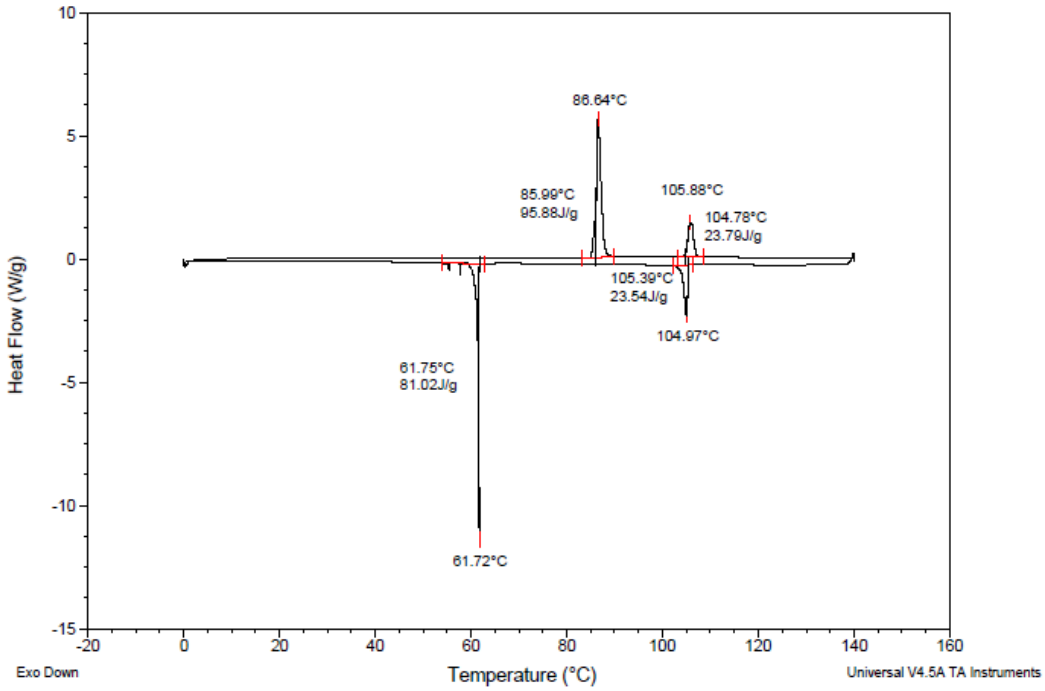

Figure A1-18: DSC profile for compound **QL20-10/6-3F** taken at a scan rate of 5K/min.

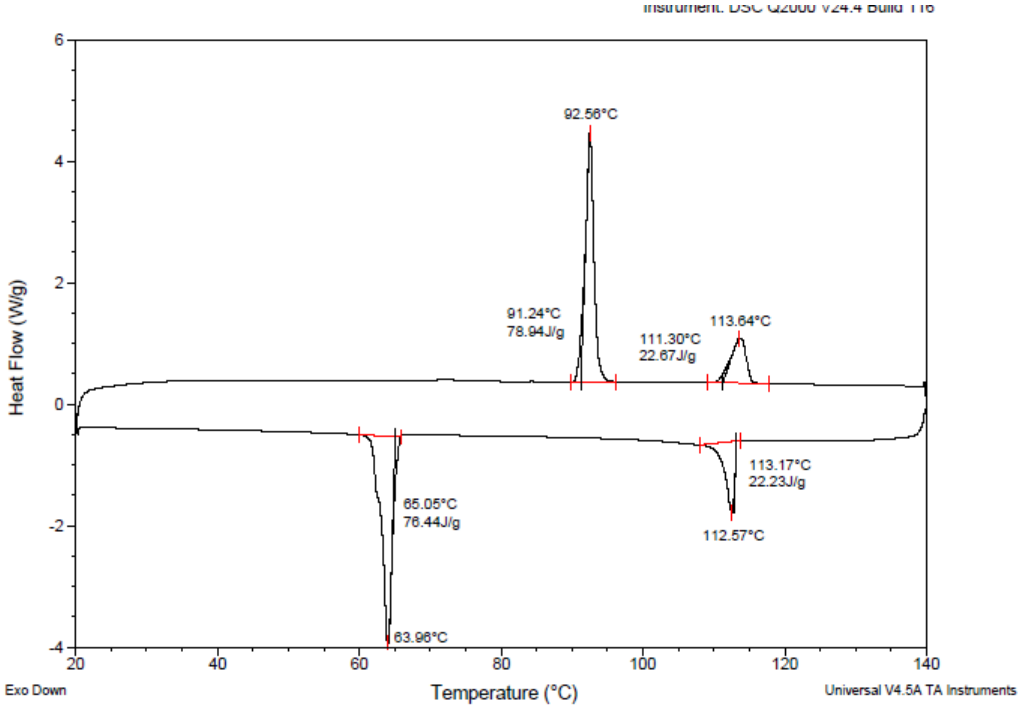

Figure A1-19: DSC profile for compound **QL20-10/6-4F** taken at a scan rate of 5K/min.

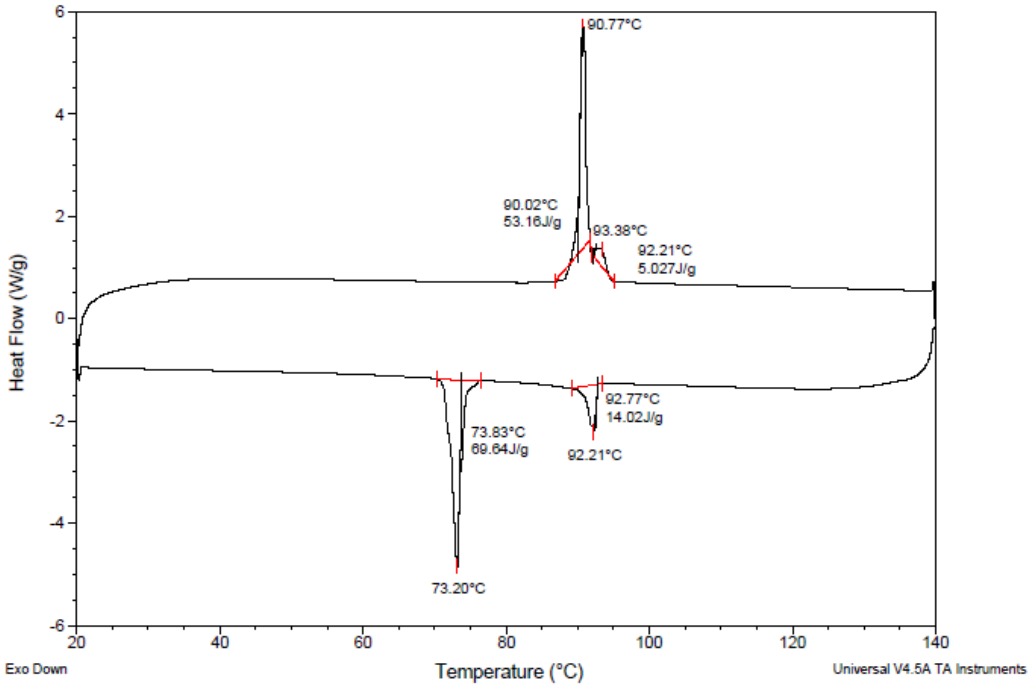

Figure A1-20: DSC profile for compound **QL20-12/4-2F** taken at a scan rate of 5K/min.

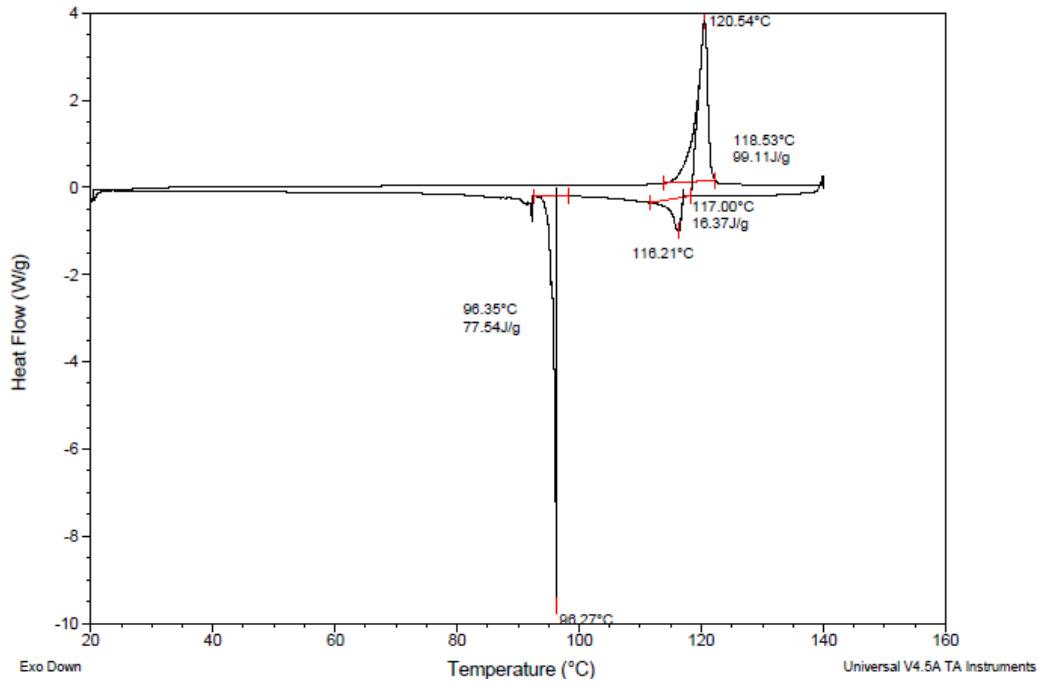

Figure A1-21: DSC profile for compound **QL20-12/4-3F** taken at a scan rate of 5K/min.

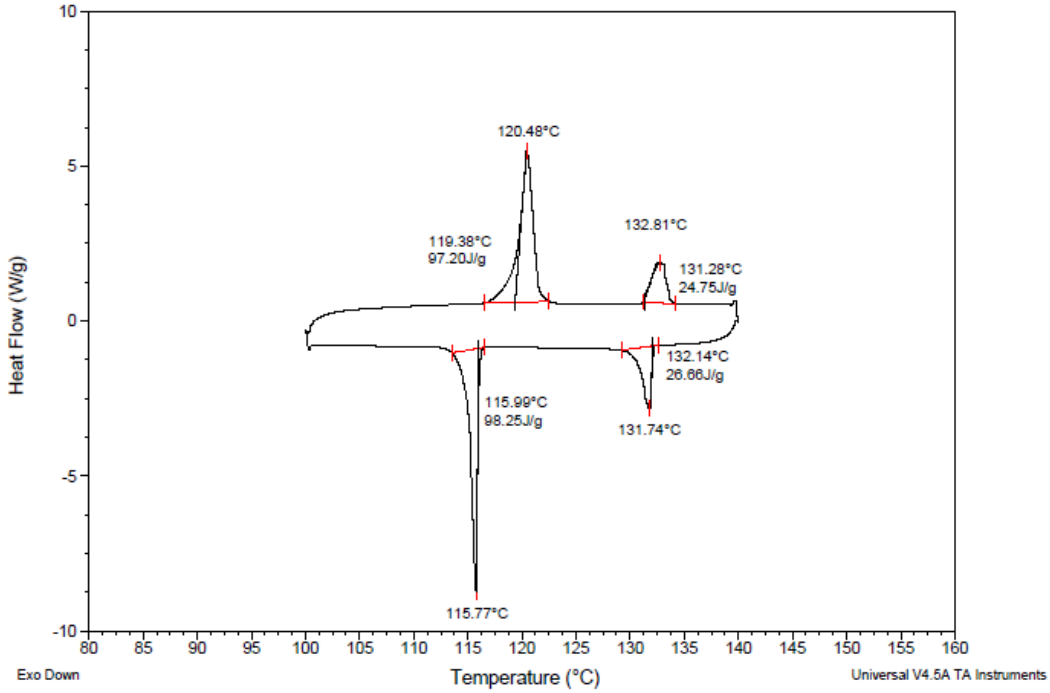

Figure A1-22: DSC profile for compound **QL20-12/4-4F** taken at a scan rate of 5K/min.

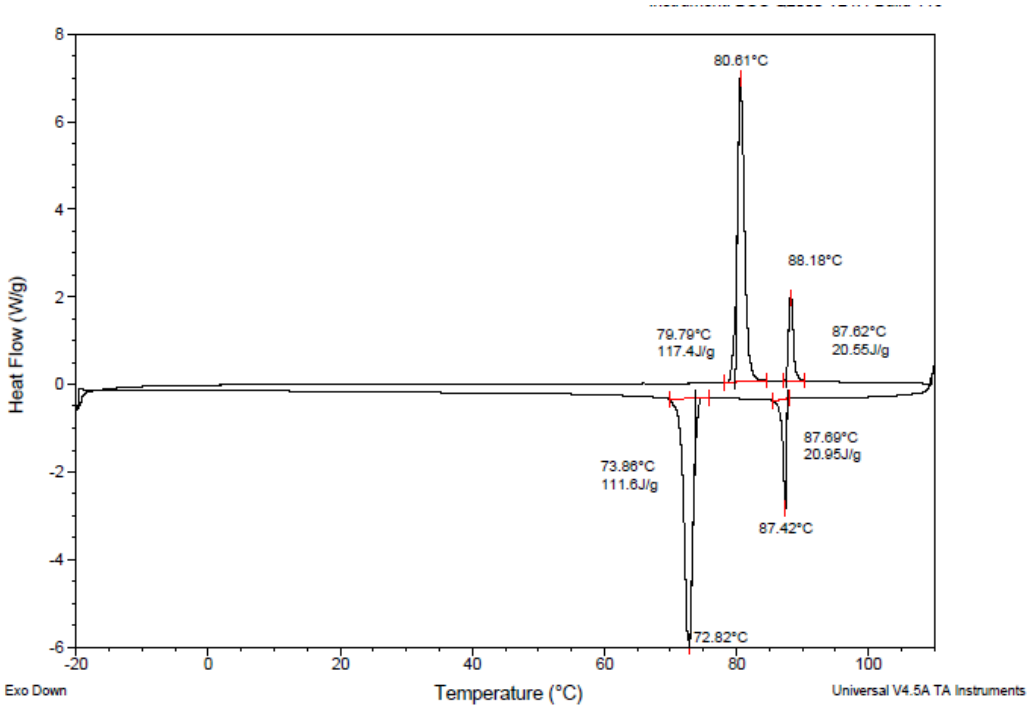

Figure A1-23: DSC profile for compound **QL22-8/8-2,3F$_2$** taken at a scan rate of 5K/min.

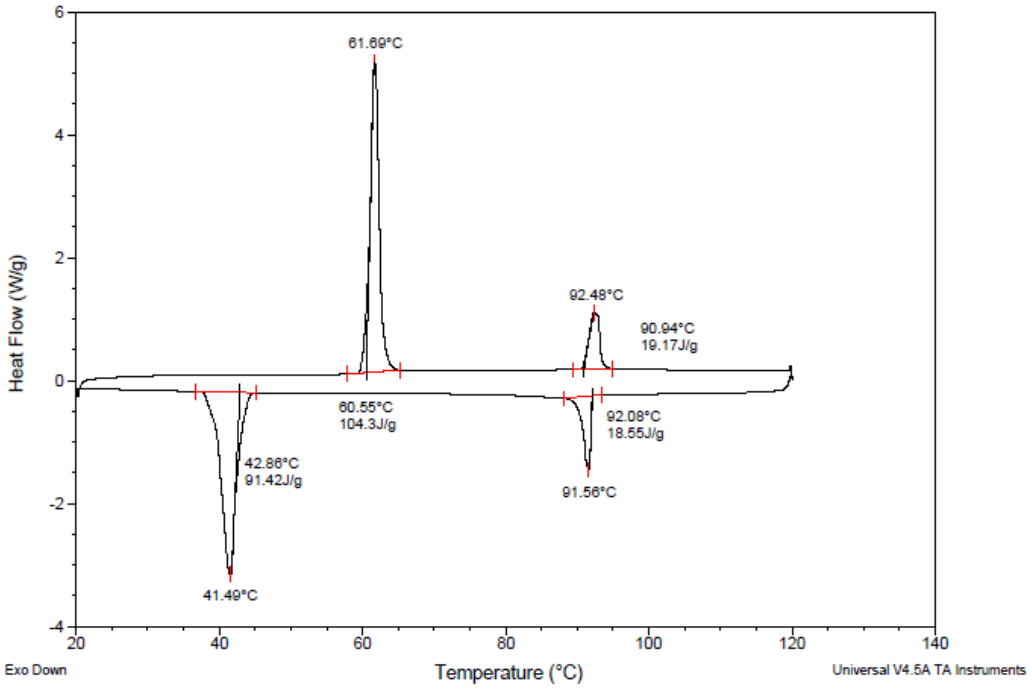

Figure A1-24: DSC profile for compound **QL22-8/8-2,4F$_2$** taken at a scan rate of 5K/min.

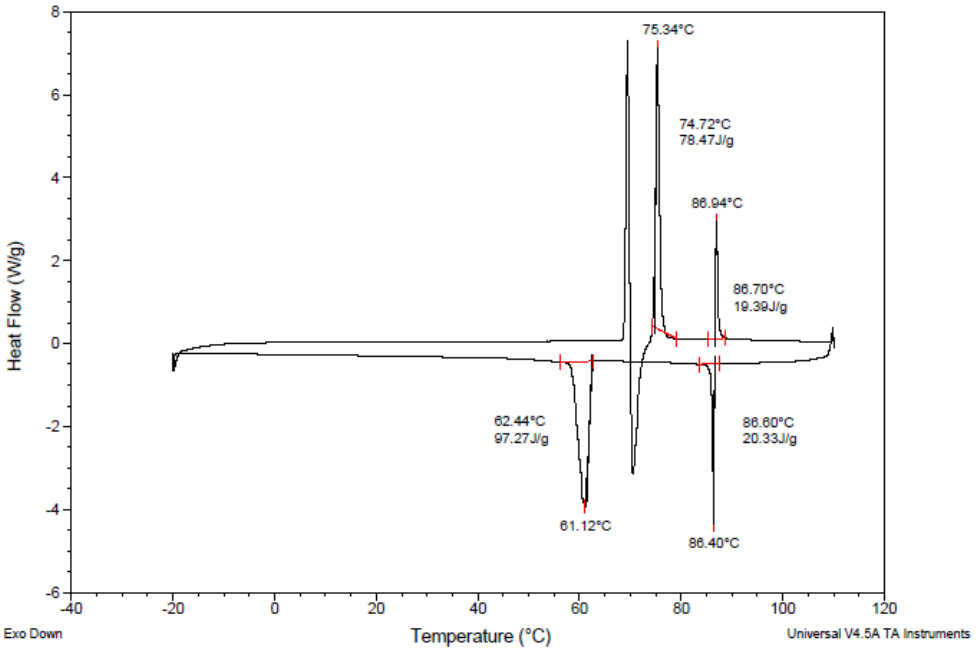

Figure A1-25: DSC profile for compound **QL22-8/8-2,5F$_2$** taken at a scan rate of 5K/min.

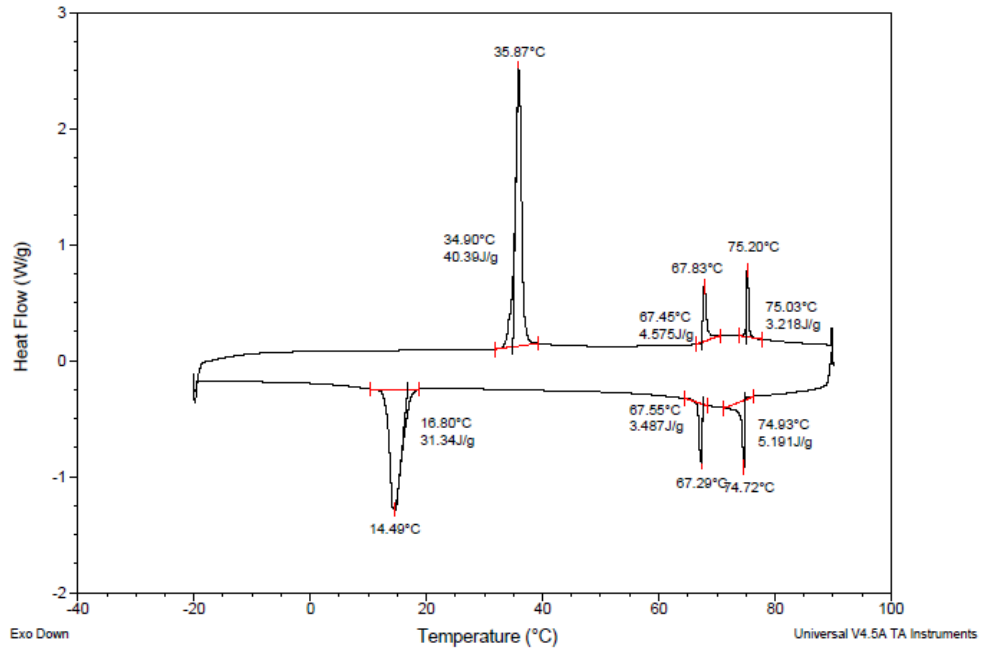

Figure A1-26: DSC profile for compound **QL22-8/8-2,6F$_2$** taken at a scan rate of 5K/min.

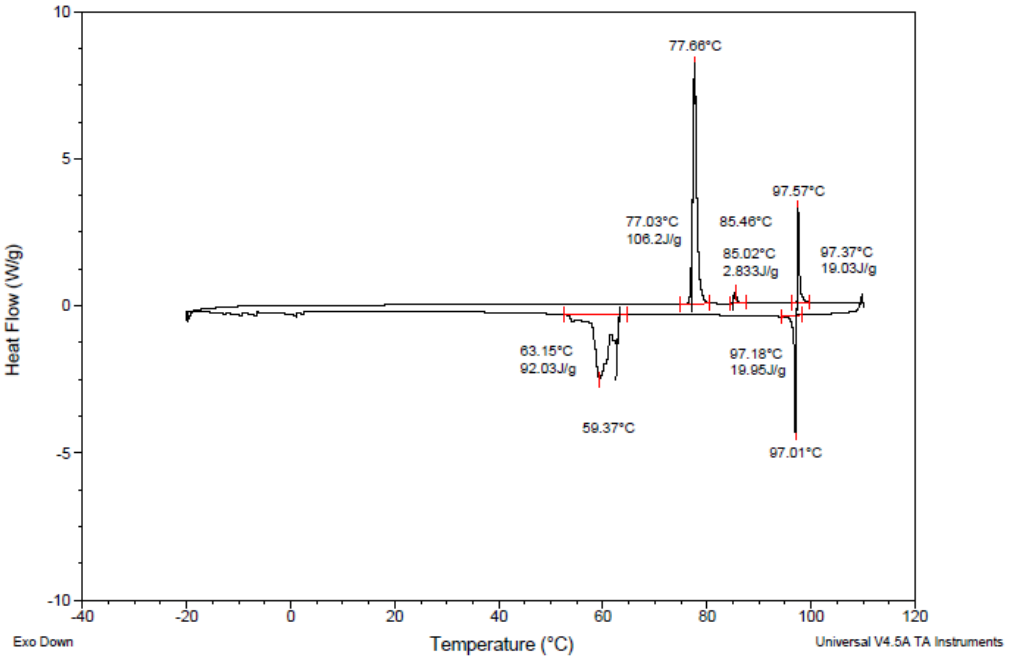

Figure A1-27: DSC profile for compound **QL22-8/8-3,4F$_2$** taken at a scan rate of 5K/min.

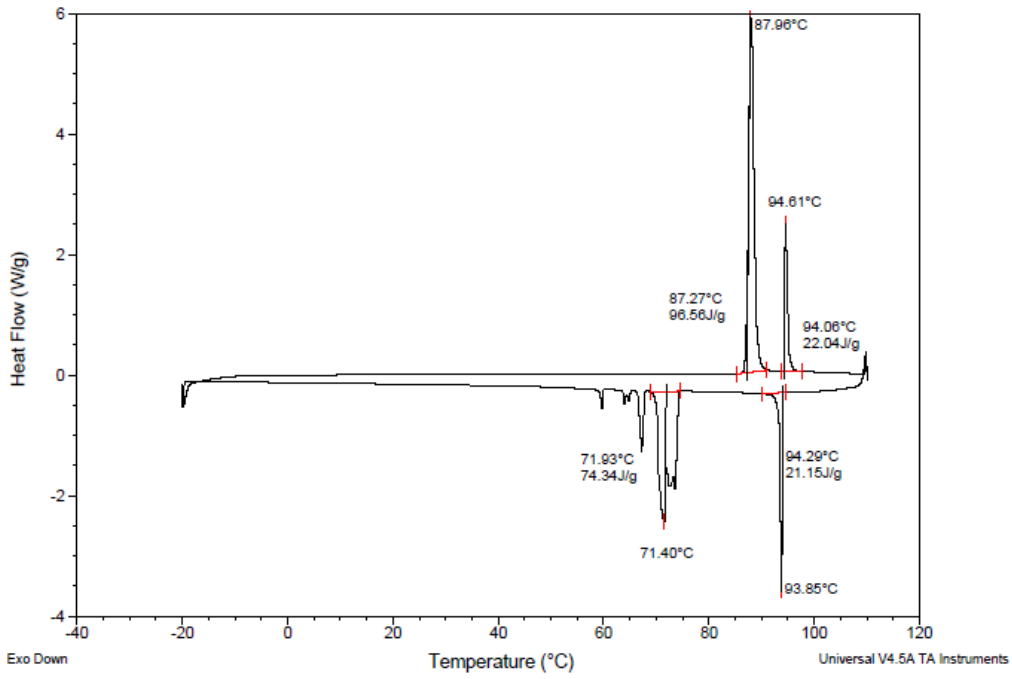

Figure A1-28: DSC profile for compound **QL22-8/8-3,5F$_2$** taken at a scan rate of 5K/min.

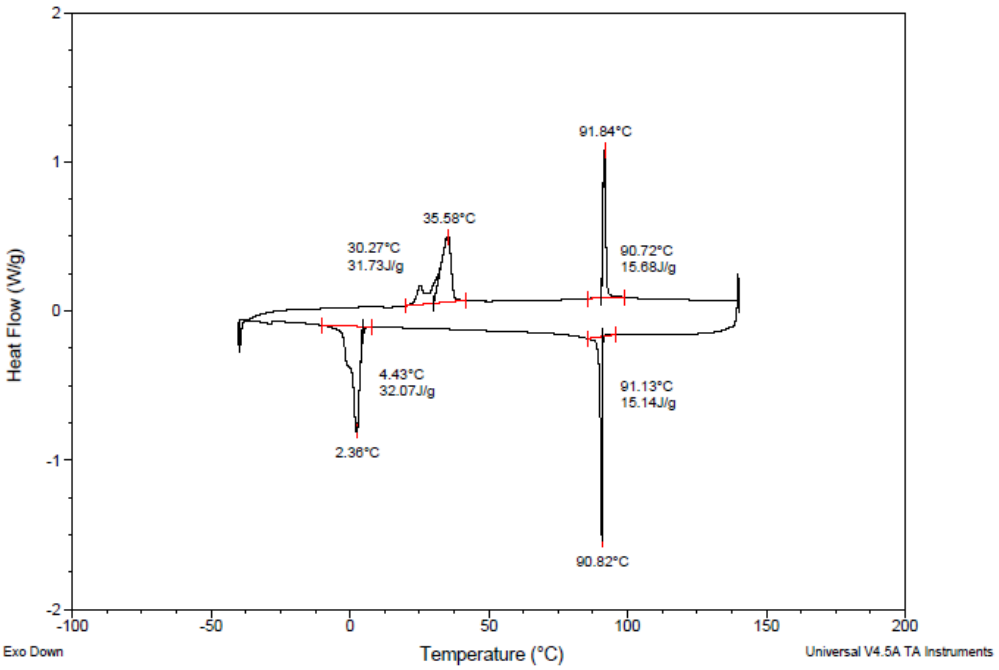

Figure A1-29: DSC profile for compound **QL27-8/8** taken at a scan rate of 5K/min.

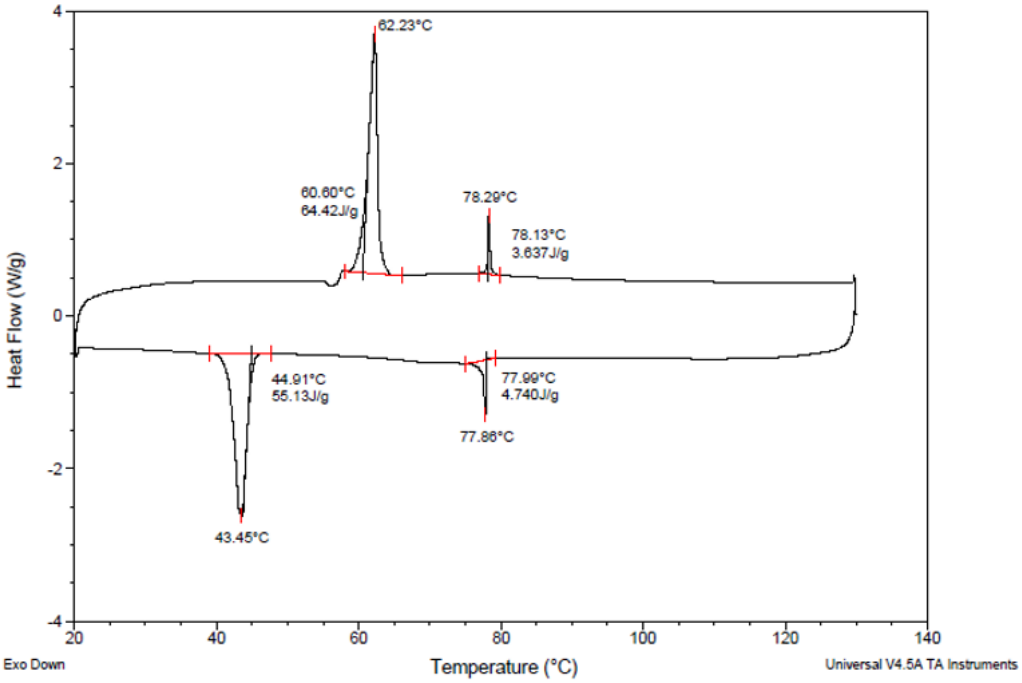

Figure A1-30: DSC profile for compound **QL21-8/8-2F** taken at a scan rate of 5K/min.

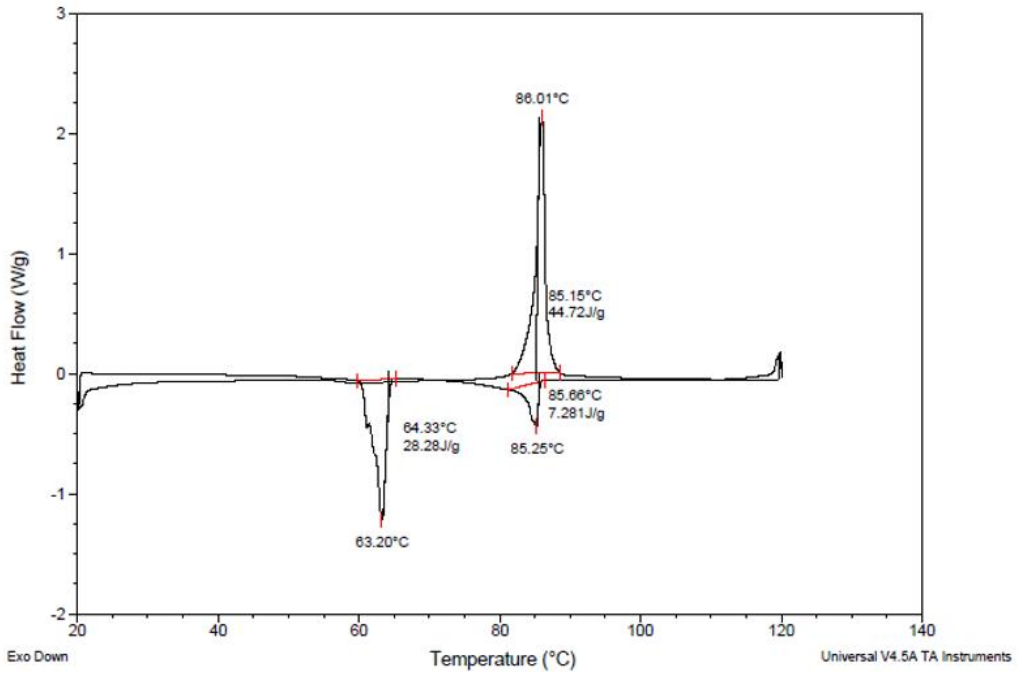

Figure A1-31: DSC profile for compound **QL21-8/8-3F** taken at a scan rate of 5K/min.

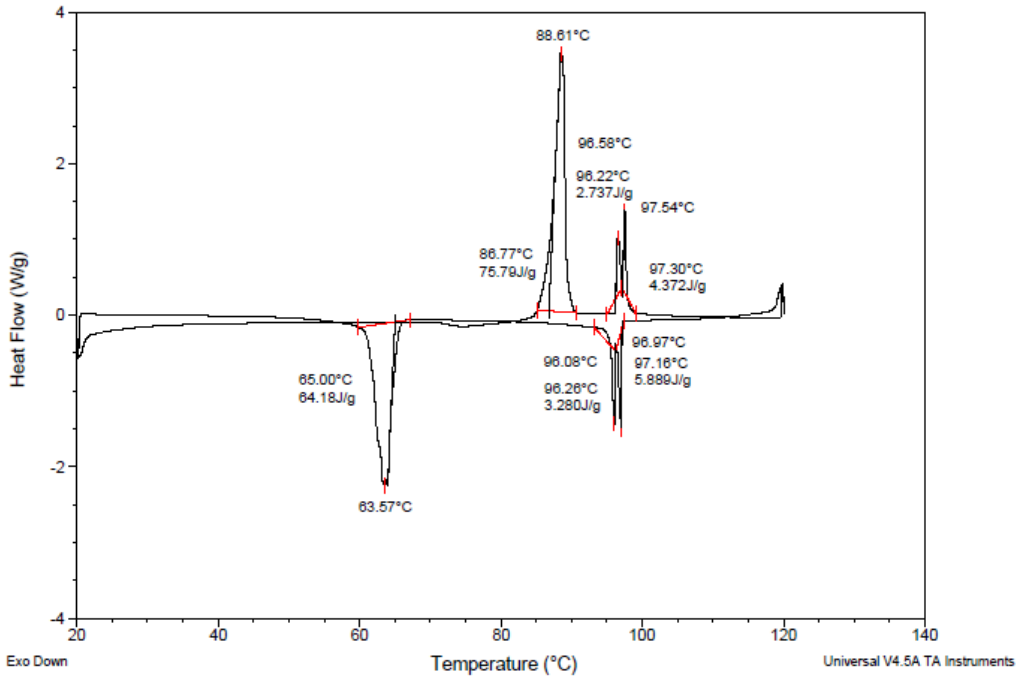

Figure A1-32: DSC profile for compound **QL21-8/8-4F** taken at a scan rate of 5K/min.

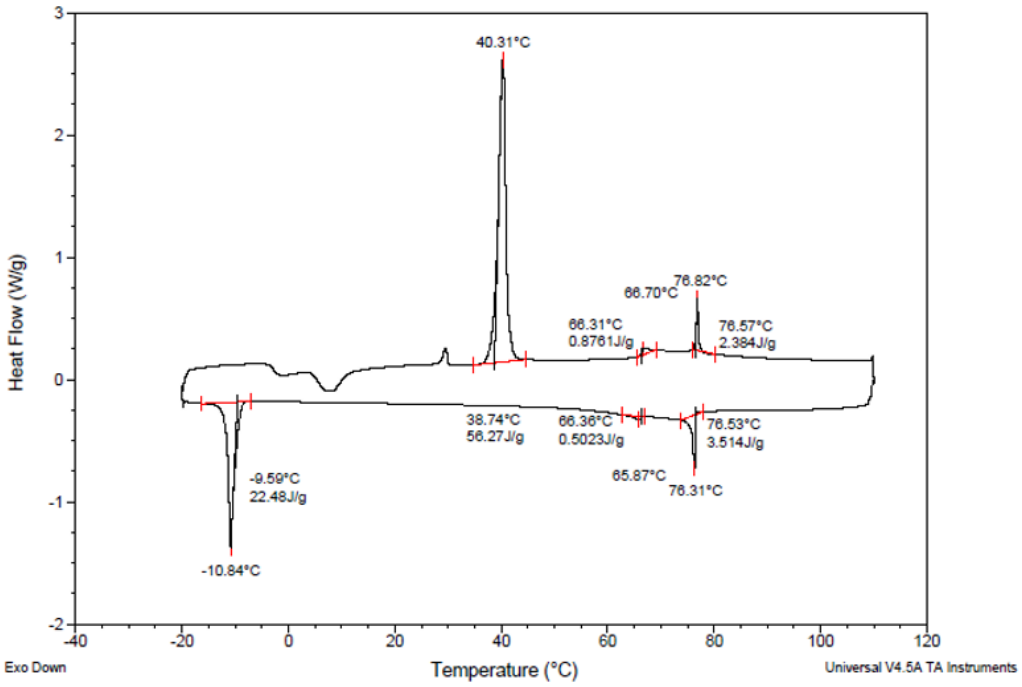

Figure A1-33: DSC profile for compound **QL23-8/8-2,6F$_2$** taken at a scan rate of 5K/min.

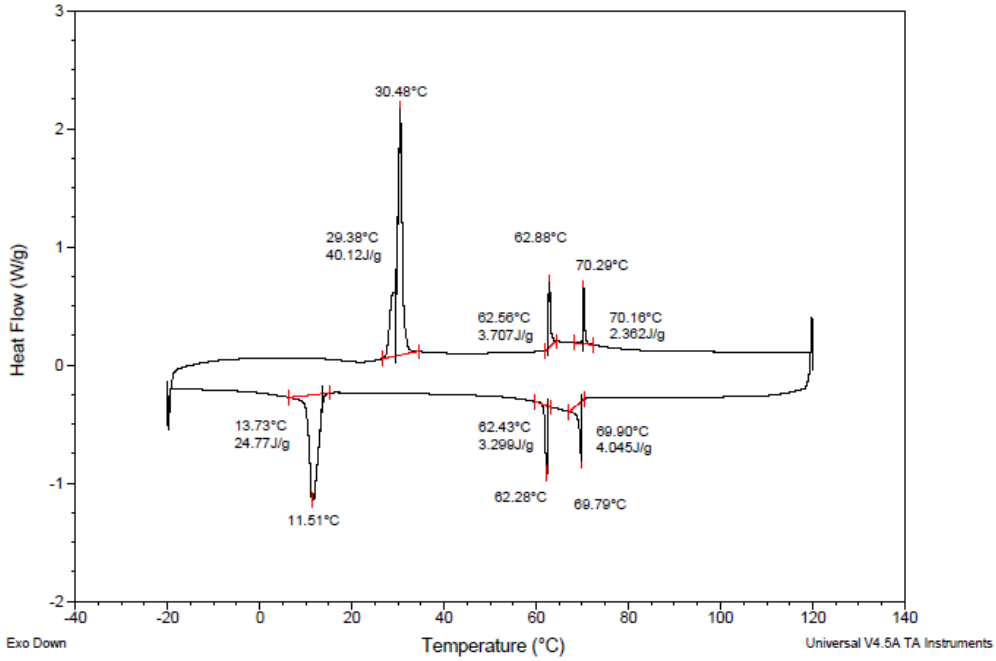

Figure A1-34: DSC profile for compound **QL22-7/8-2,6F$_2$** taken at a scan rate of 5K/min.

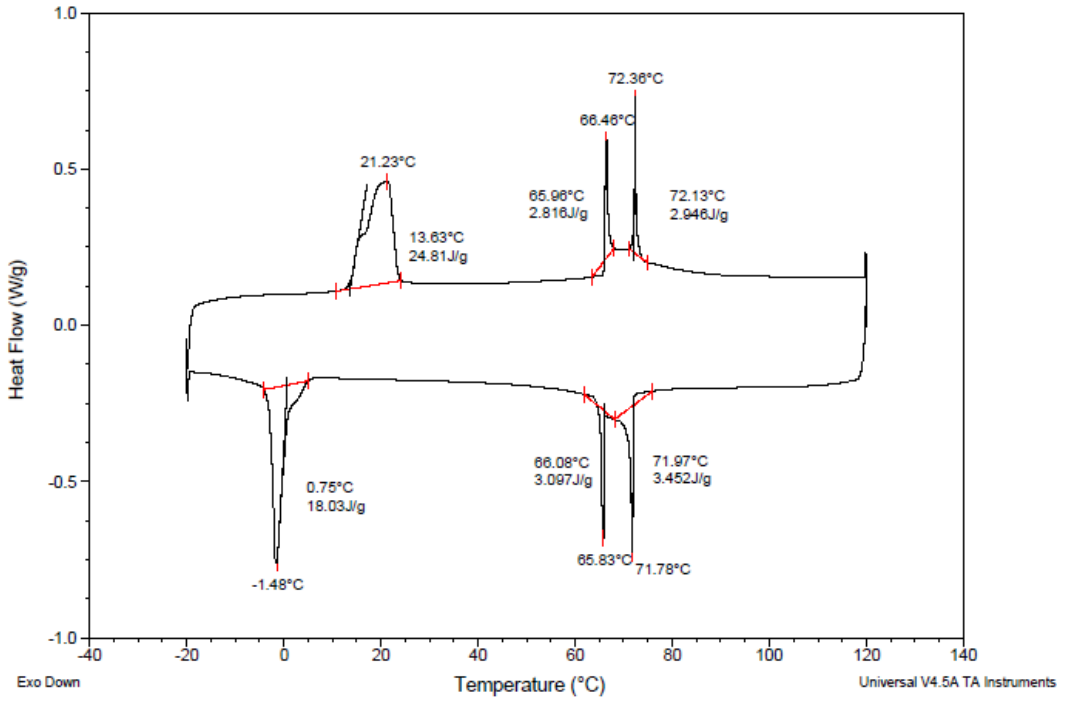

Figure A1- 35: DSC profile for compound **QL22-9/8-2,6F$_2$** taken at a scan rate of 5K/min.

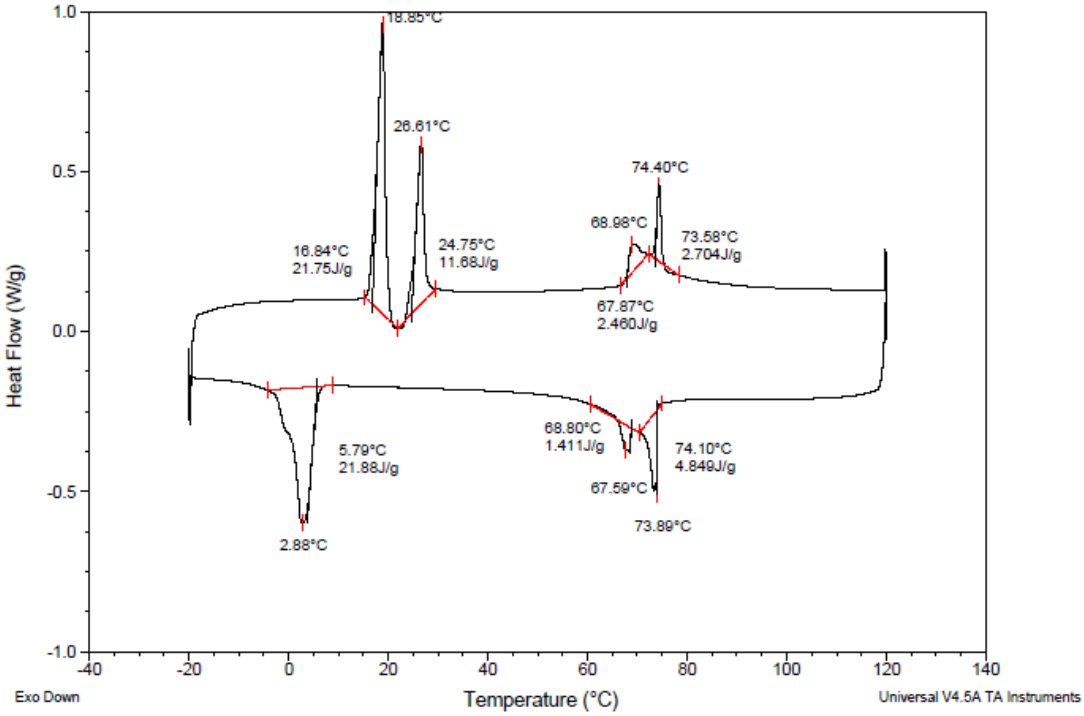

Figure A1-36: DSC profile for compound **QL22-10/8-2,6F$_2$** taken at a scan rate of 5K/min.

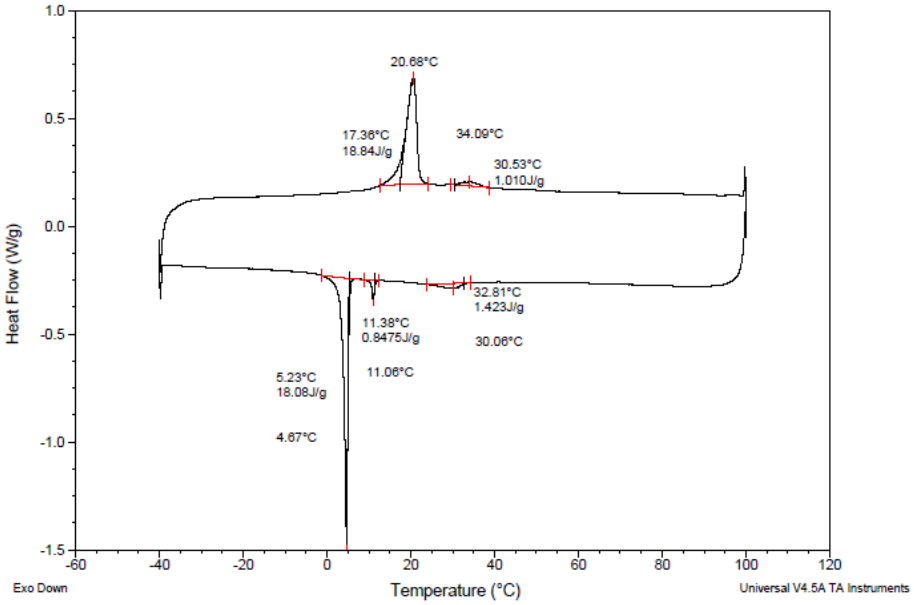

Figure A1-37: DSC profile for compound **QL29-7/8-2,6F$_2$** taken at a scan rate of 5K/min.

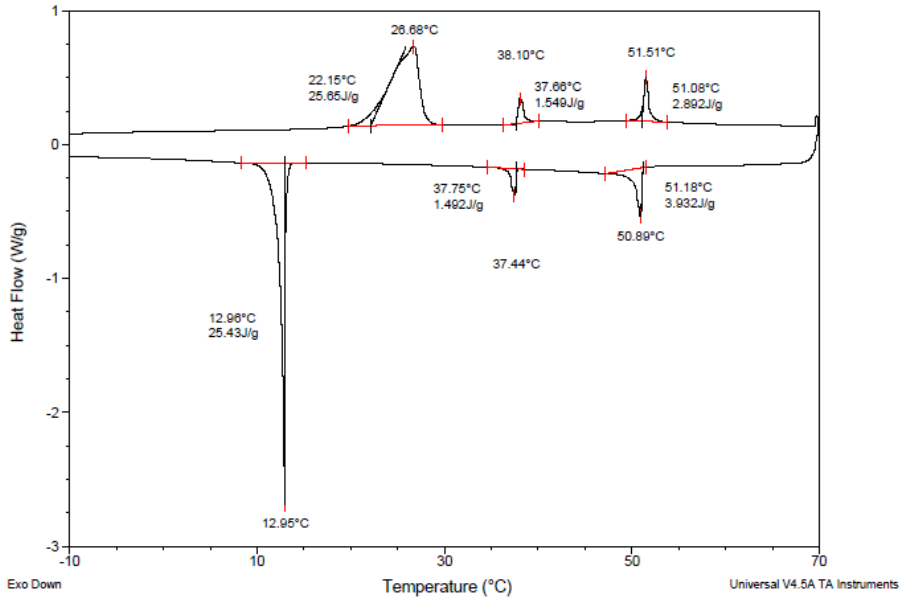

Figure A1-38: DSC profile for compound **QL29-8/8-2,6F$_2$** taken at a scan rate of 5K/min.

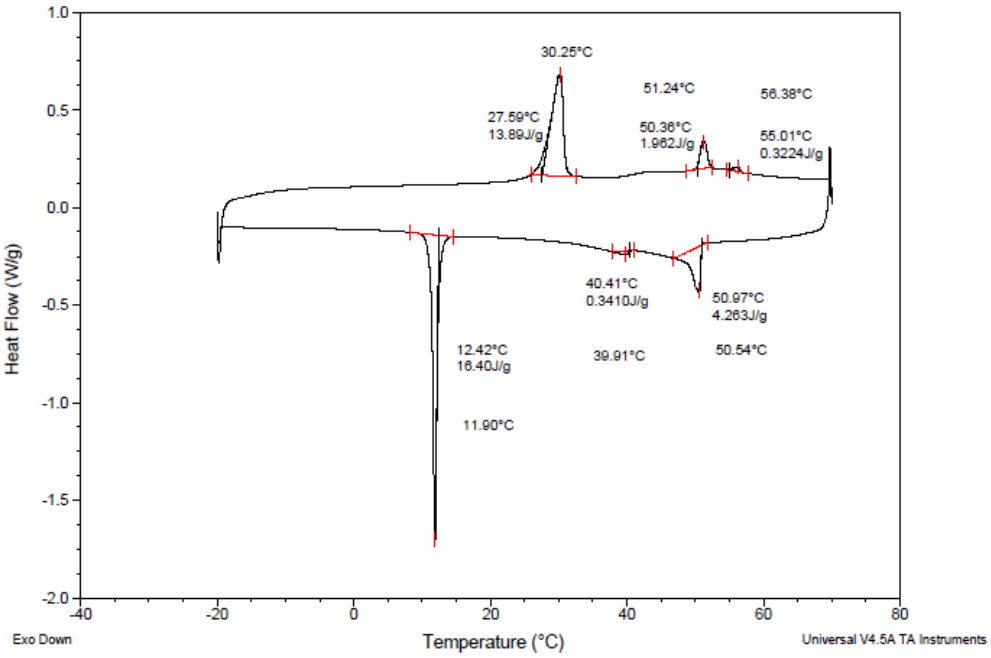

Figure A1-39: DSC profile for compound **QL29-9/8-2,6F$_2$** taken at a scan rate of 5K/min.

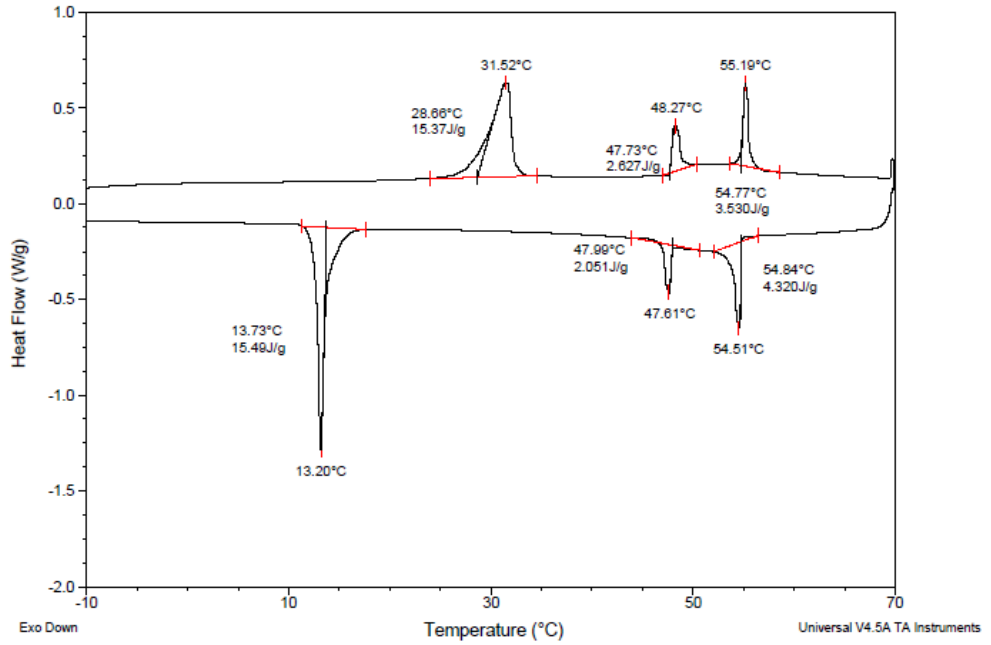

Figure A1-40: DSC profile for compound **QL29-10/8-2,6F$_2$** taken at a scan rate of 5K/min.

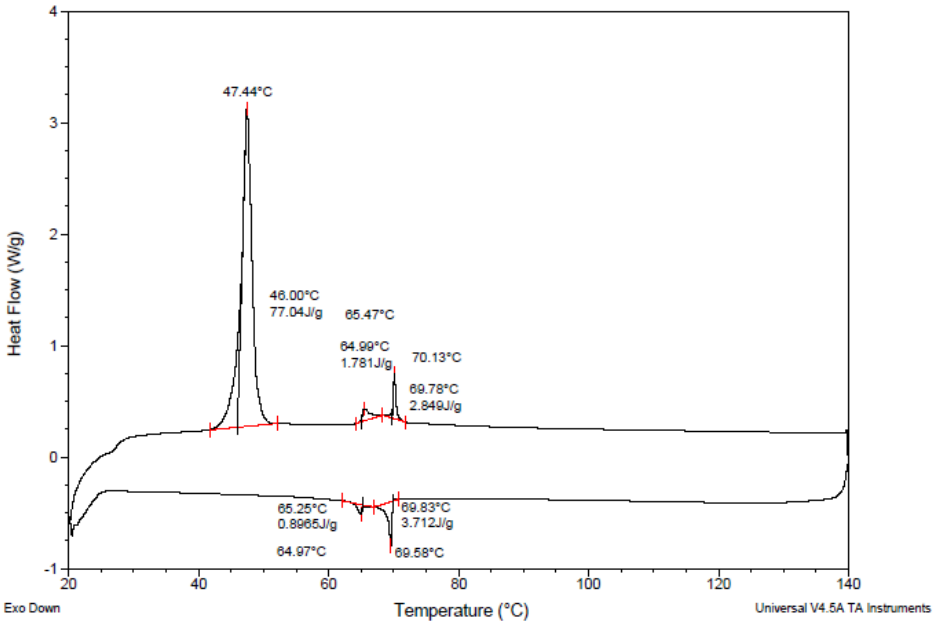

Figure A1-41: DSC profile for compound **QL30-8/8-2,6Me2** taken at a scan rate of 5K/min.

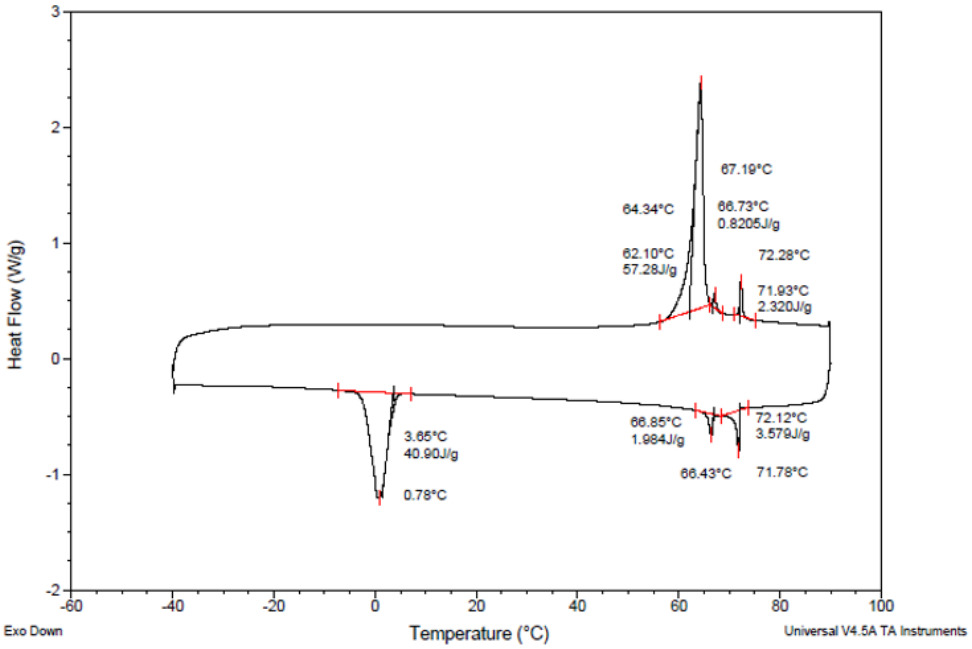

Figure A1-42: DSC profile for compound **QL31-8/8-2,6Me2** taken at a scan rate of 5K/min.

Appendix 2: Textures of Liquid Crystals by Polarized Optical Microscopy

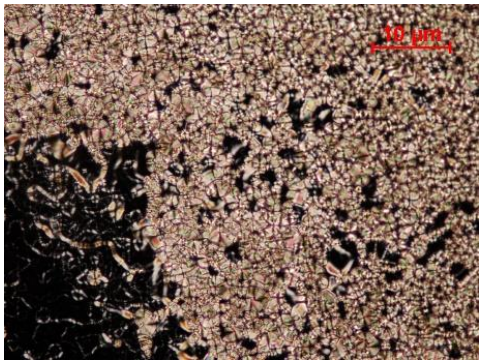

Figure A2-1: Textures of compound **QL11-4/12** observed by polarized microscopy on cooling: in the SmA phase at 62°C (200X Magnification).

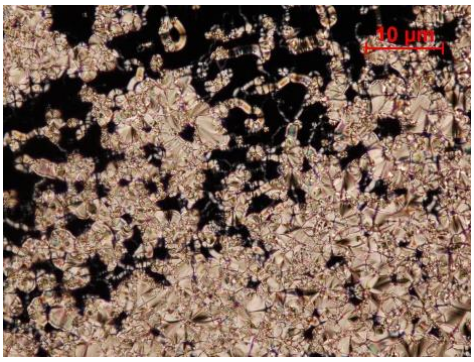

Figure A2-2: Textures of compound **QL11-5/11** observed by polarized microscopy on cooling: in the SmA phase at 63°C (200X Magnification).

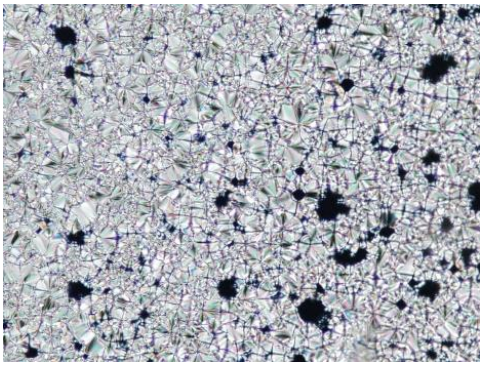

Figure A2-3: Textures of compound **QL11-6/10** observed by polarized microscopy on cooling: in the SmA phase at 85°C (200X Magnification).

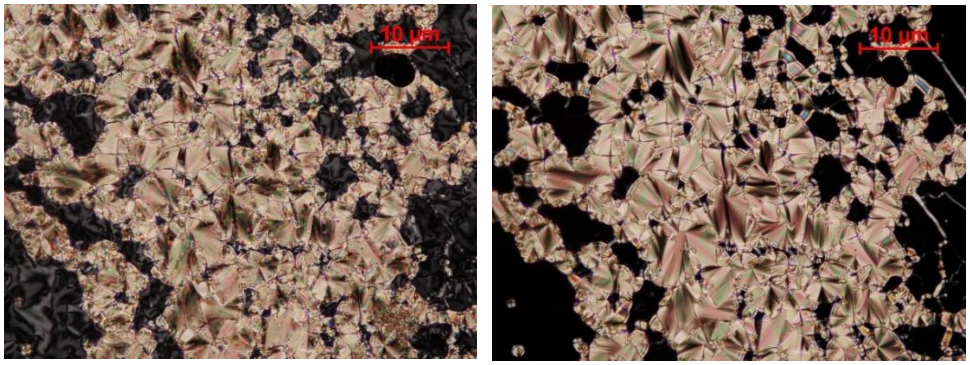

Figure A2-4: Textures of compound **QL11-7/9** observed by polarized microscopy on cooling: in the SmA phase at 74°C (right) and in the SmC phase at 60°C (left) (200X Magnification)

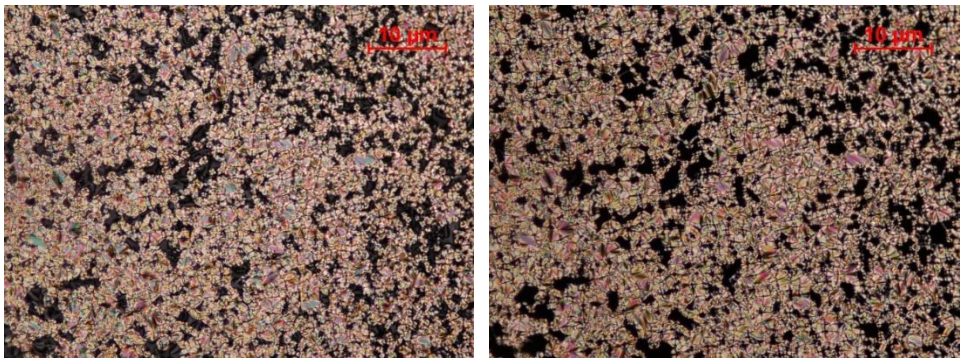

Figure A2-5: Textures of compound **QL11-8/8** observed by polarized microscopy on cooling: in the SmA phase at 95°C (right) and in the SmC phase at 69°C (left) (200X Magnification)

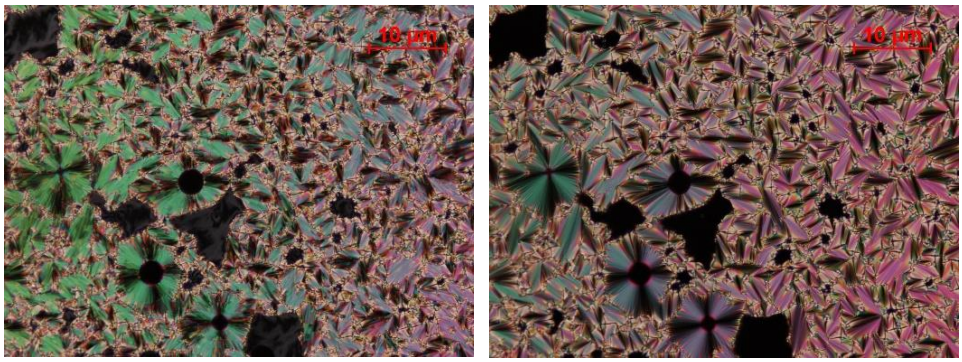

Figure A2-6: Textures of compound **QL11-9/7** observed by polarized microscopy on cooling: in the SmA phase at 80°C (right) and in the SmC phase at 71°C (left) (200X Magnification)

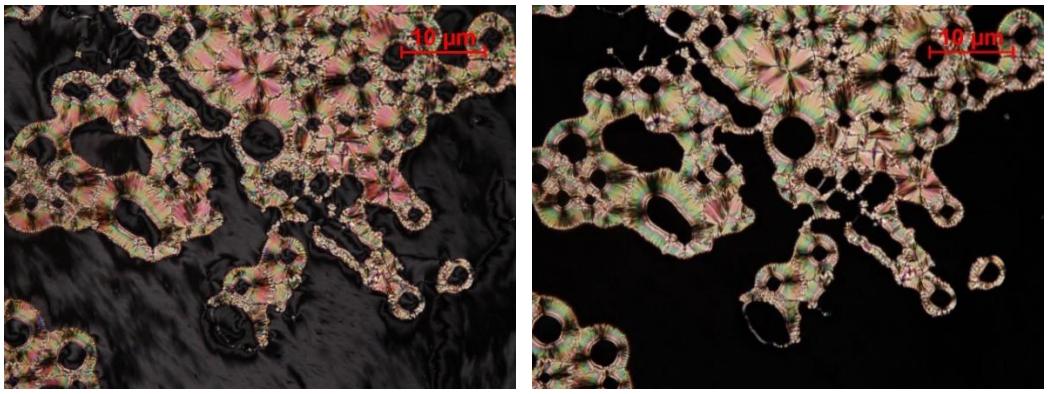

Figure A2-7: Textures of compound **QL11-10/6** observed by polarized microscopy on cooling: in the SmA phase at 95°C (right) and in the SmC phase at 75°C (left) (200X Magnification)

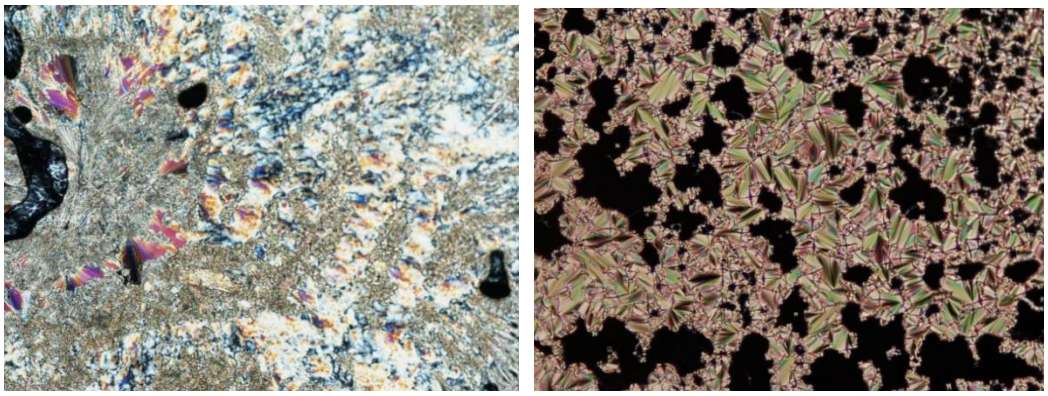

Figure A2-8: Textures of compound **QL11-11/5** observed by polarized microscopy on cooling: in the SmA phase at 82°C (right) and in the SmC phase at 67°C (left) (200X Magnification)

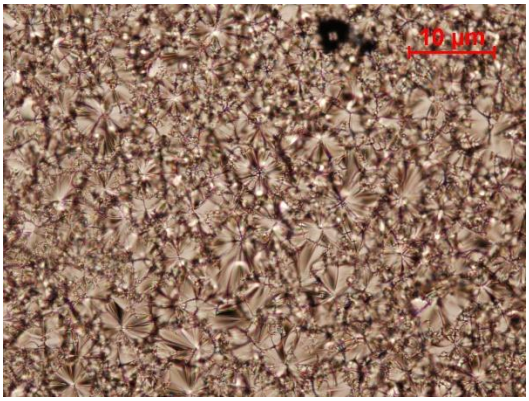

Figure A2-9: Textures of compound **QL11-12/4** observed by polarized microscopy on cooling: in the SmA phase at 113°C (200X Magnification)

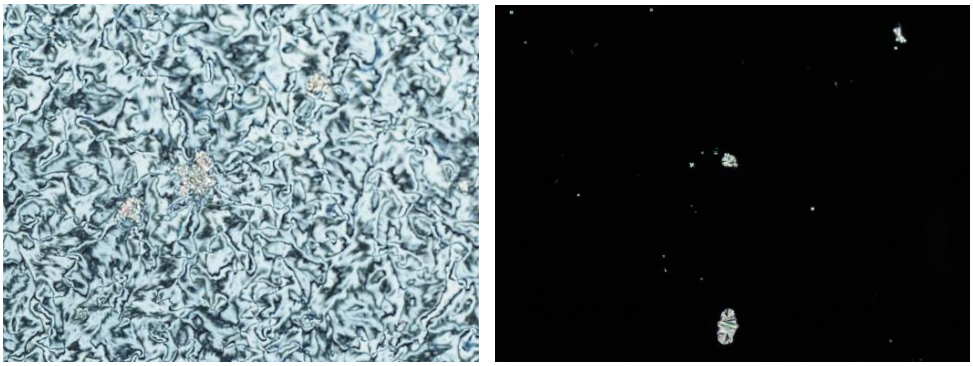

Figure A2-10: Textures of compound **QL12-12/4** observed by polarized microscopy on cooling: in the SmA phase at 101°C (right) and in the SmC phase at 98°C (left) (200X Magnification)

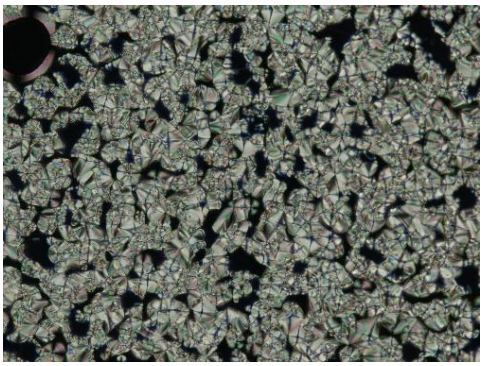

Figure A2-11: Textures of compound **QL12-11/5** observed by polarized microscopy on cooling: in the SmA phase at 79°C (200X Magnification)

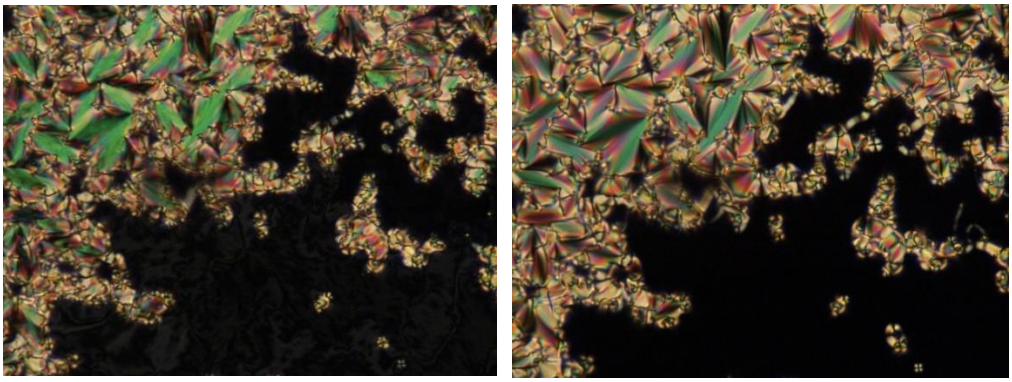

Figure A2-12: Textures of compound **QL12-10/6** observed by polarized microscopy on cooling: in the SmA phase at 93°C (right) and in the SmC phase at 86°C (left) (200X Magnification)

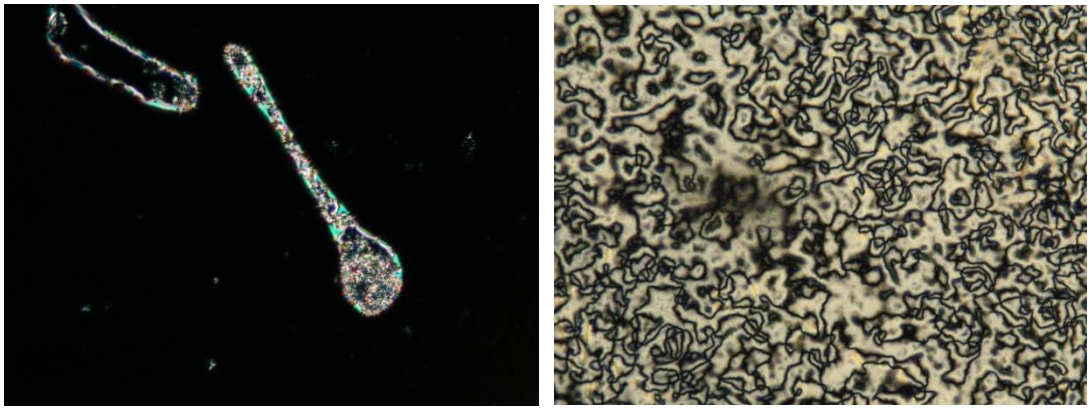

Figure A2-13: Textures of compound **QL12-8/8** observed by polarized microscopy on cooling: in the SmA phase at 81°C (left) and in the N phase at 85°C (right) (200X Magnification)

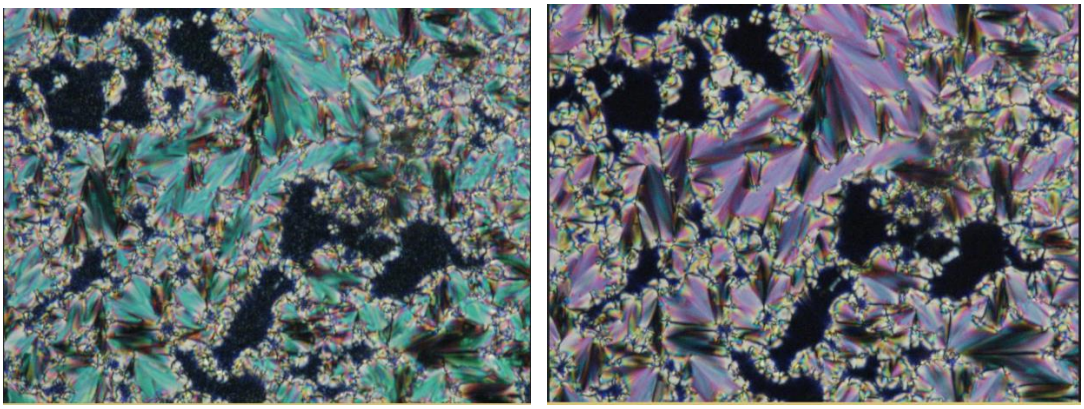

Figure A2-14: Textures of compound **QL20-8/8-2F** observed by polarized microscopy on cooling: in the SmA phase at 82°C (right) and in the SmC phase at 75°C (left) (200X Magnification)

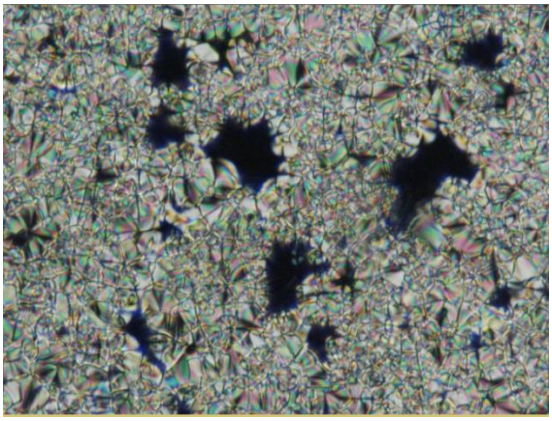

Figure A2-15: Textures of compound **QL20-8/8-3F** observed by polarized microscopy on cooling: in the SmA phase at 81°C (200X Magnification)

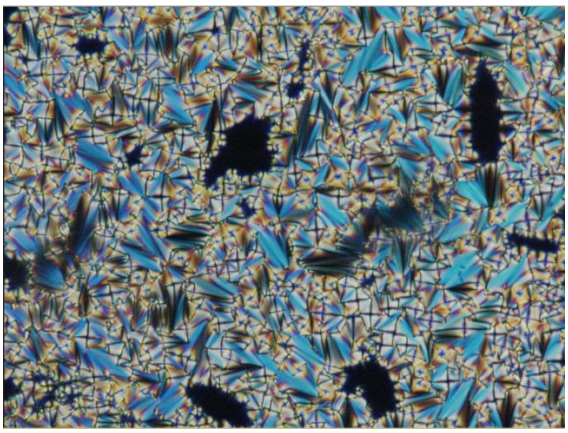

Figure A2-16: Textures of compound **QL20-8/8-4F** observed by polarized microscopy on cooling: in the SmA phase at 94°C (200X Magnification)

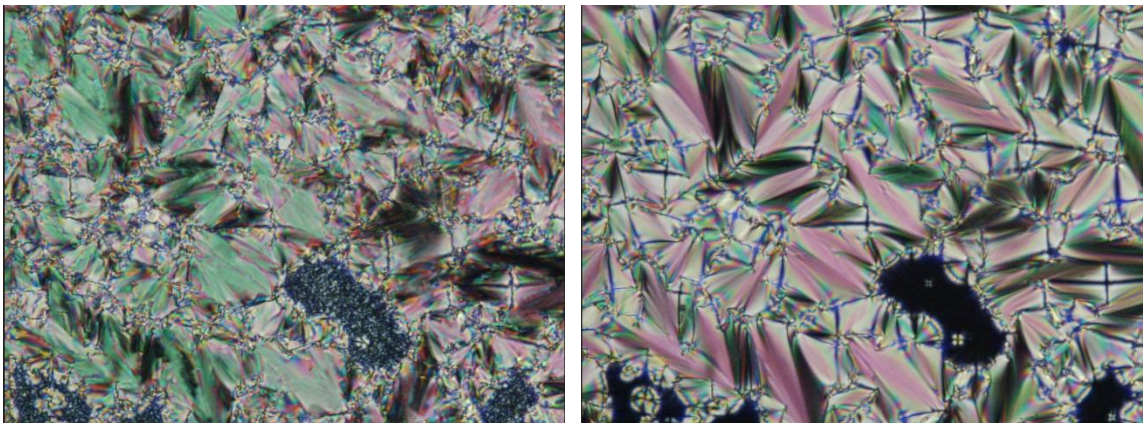

Figure A2-17: Textures of compound **QL20-10/6-2F** observed by polarized microscopy on cooling: in the SmA phase at 89°C (right) and in the SmC phase at 74°C (left) (200X Magnification)

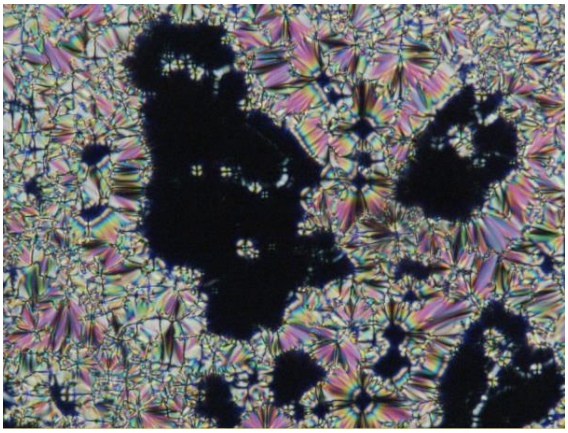

Figure A2-18: Textures of compound **QL20-10/6-3F** observed by polarized microscopy on cooling: in the SmA phase at 94°C (200X Magnification)

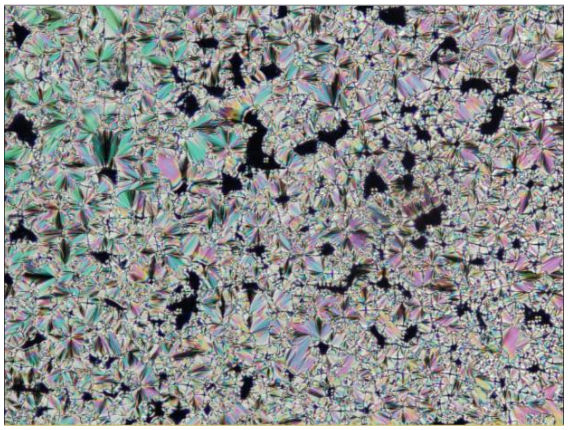

Figure A2-19: Textures of compound **QL20-10/6-4F** observed by polarized microscopy on cooling: in the SmA phase at 90°C (200X Magnification)

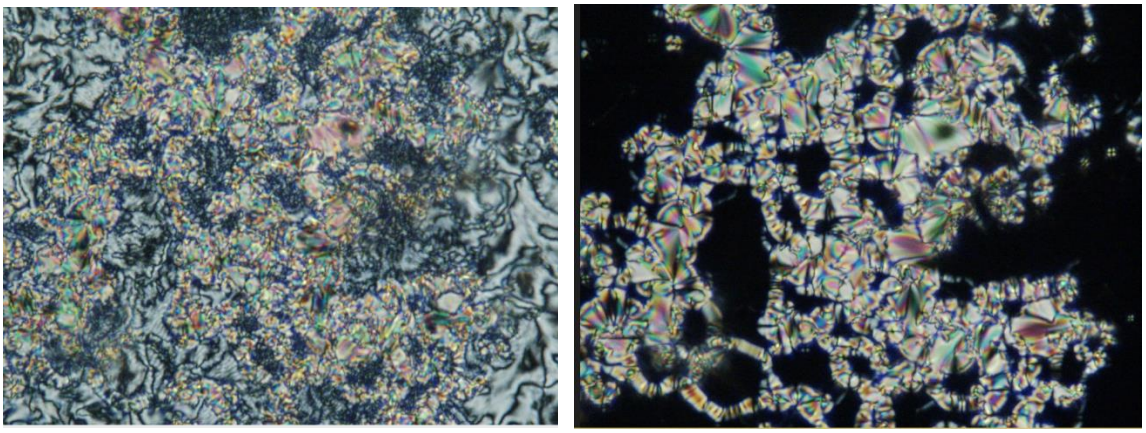

Figure A2-20: Textures of compound **QL20-12/4-2F** observed by polarized microscopy on cooling: in the SmA phase at 95°C (right) and in the SmC phase at 81°C (left) (200X Magnification)

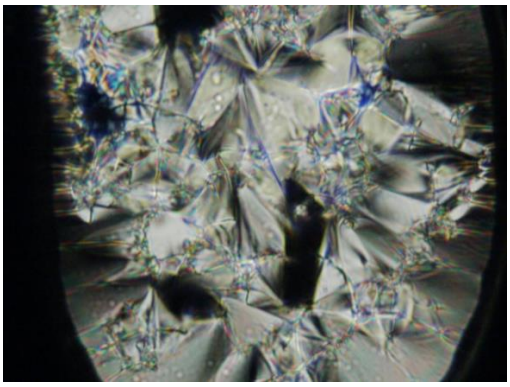

Figure A2-21: Textures of compound **QL20-12/4-3F** observed by polarized microscopy on cooling: in the SmA phase at 111°C (200X Magnification)

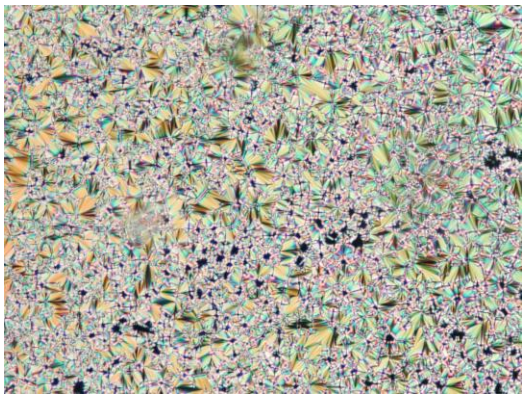

Figure A2-221: Textures of compound **QL20-12/4-4F** observed by polarized microscopy on cooling: in the SmA phase at 124°C (200X Magnification)

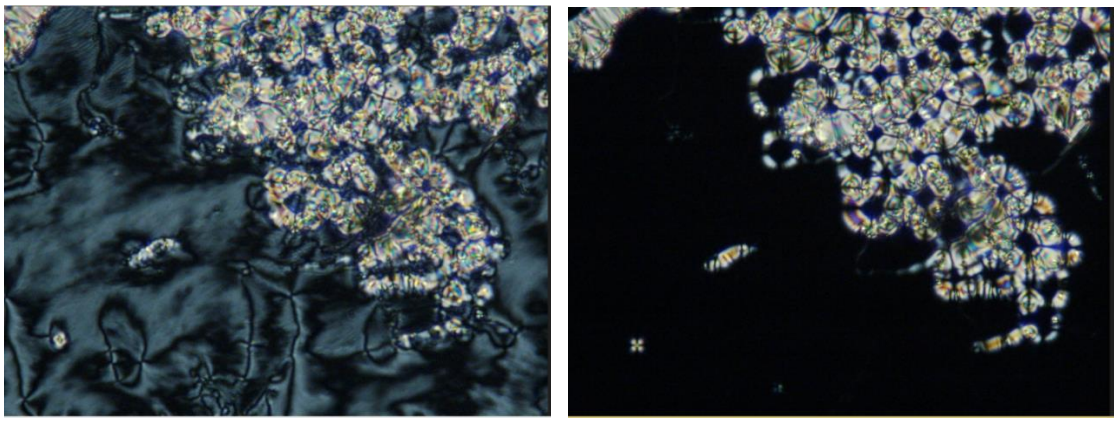

Figure A2-23: Textures of compound **QL22-8/8-2,3F$_2$** observed by polarized microscopy on cooling: in the SmA phase at 86°C (right) and in the SmC phase at 77°C (left) (200X Magnification)

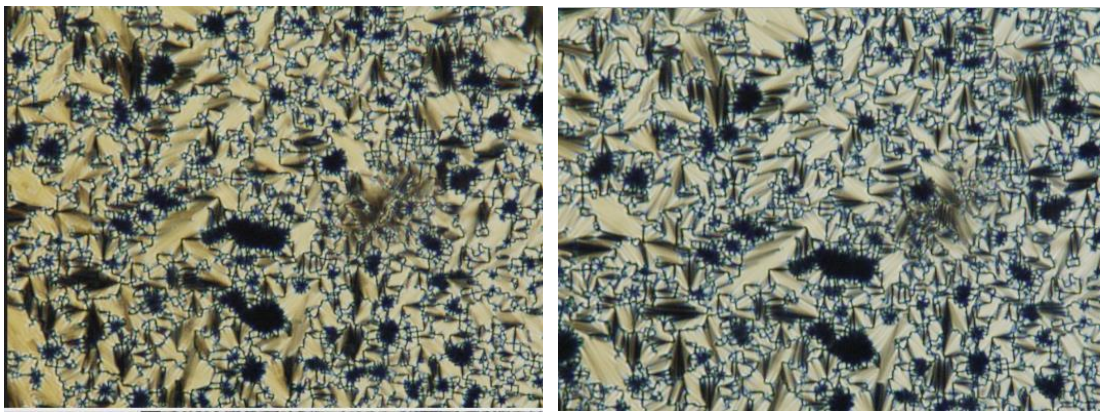

Figure A2-24: Textures of compound **QL22-8/8-2,4F$_2$** observed by polarized microscopy on cooling: in the SmA phase at 85°C (right) and in the SmC phase at 51°C (left) (200X Magnification)

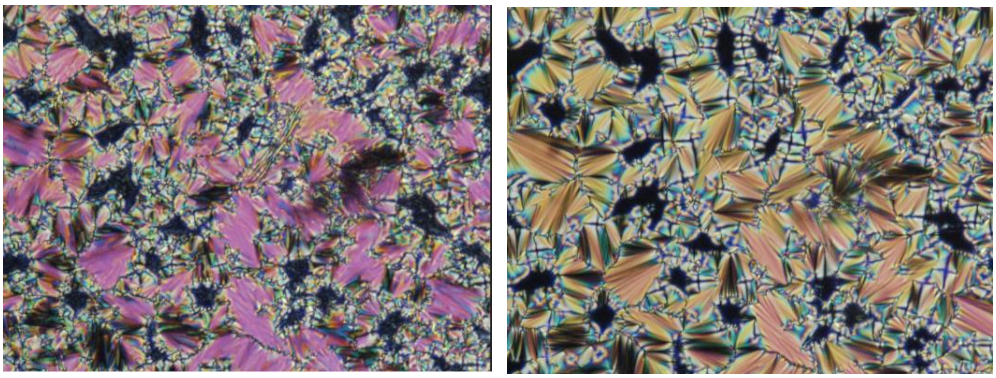

Figure A2-25: Textures of compound **QL22-8/8-2,5F$_2$** observed by polarized microscopy on cooling: in the SmA phase at 86°C (right) and in the SmC phase at 64°C (left) (200X Magnification)

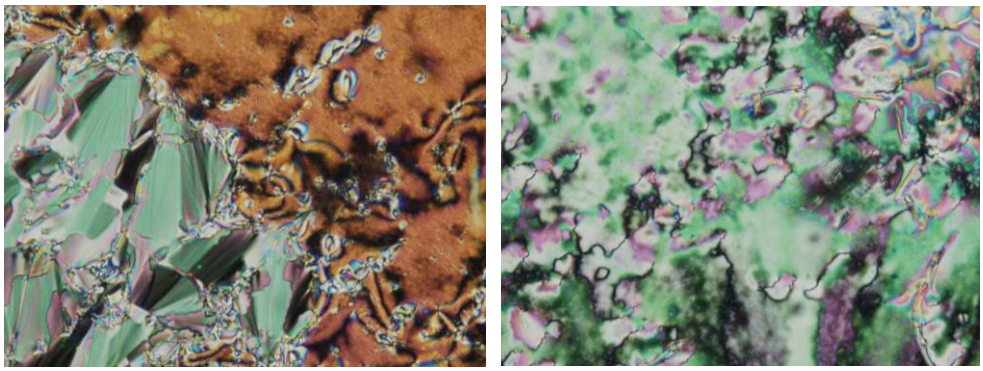

Figure A2-26: Textures of compound **QL22-8/8-2,6F$_2$** observed by polarized microscopy on cooling: in the N phase at 73°C (right) and in the SmC phase at 67°C (left) (200X Magnification)

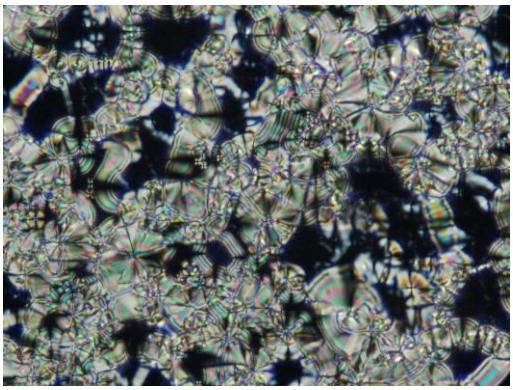

Figure A2-27: Textures of compound **QL22-8/8-3,4F$_2$** observed by polarized microscopy on cooling: in the SmA phase at 75°C (200X Magnification)

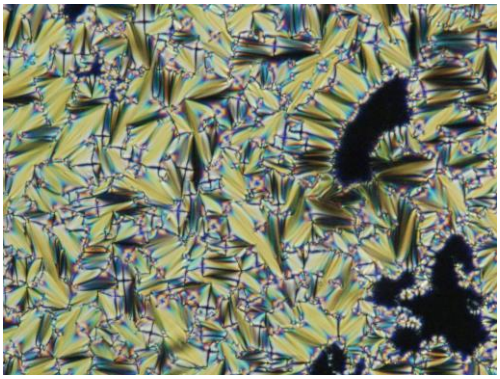

Figure A2-28: Textures of compound **QL22-8/8-3,5F$_2$** observed by polarized microscopy on cooling: in the SmA phase at 93°C (200X Magnification)

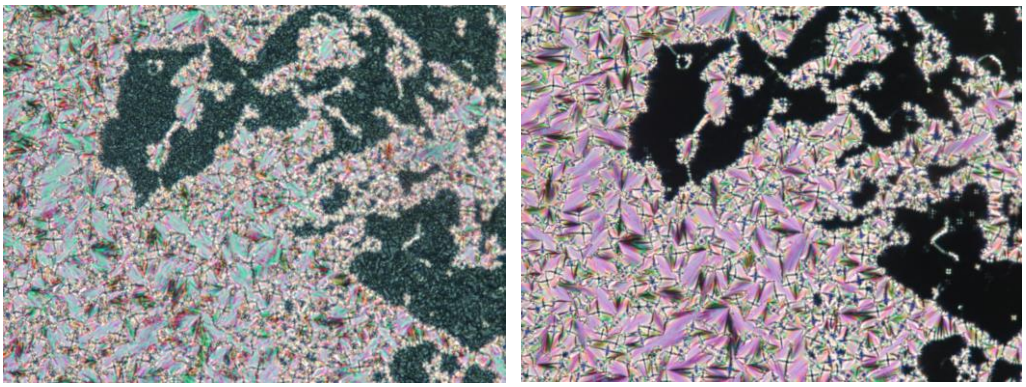

Figure A2-29: Textures of compound **QL27-8/8** observed by polarized microscopy on cooling: in the SmA phase at 70°C (right) and in the SmC phase at 45°C (left) (200X Magnification)

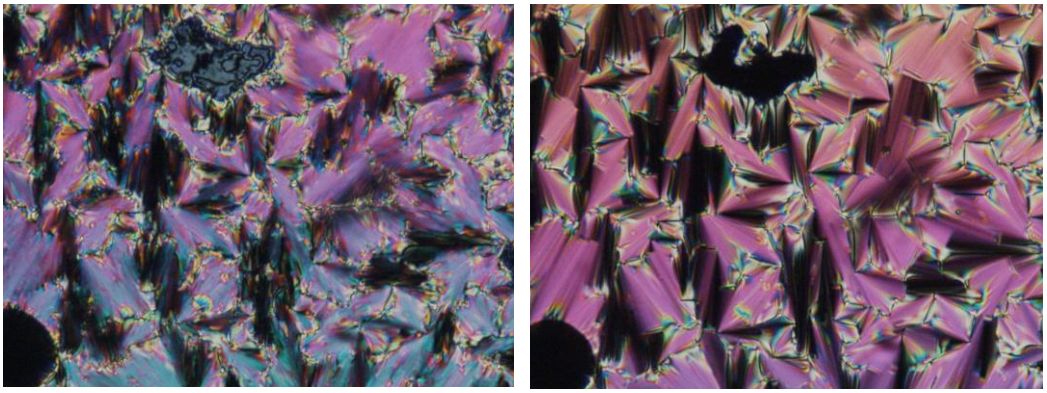

Figure A2-30: Textures of compound **QL21-8/8-2F** observed by polarized microscopy on cooling: in the SmA phase at 67°C (right) and in the SmC phase at 55°C (left) (200X Magnification)

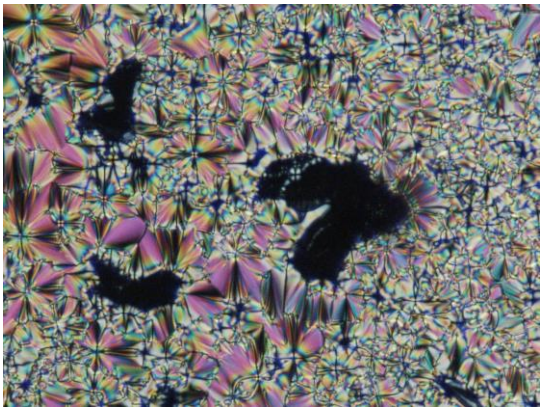

Figure A2-31: Textures of compound **QL21-8/8-3F** observed by polarized microscopy on cooling: in the SmA phase at 85°C (200X Magnification)

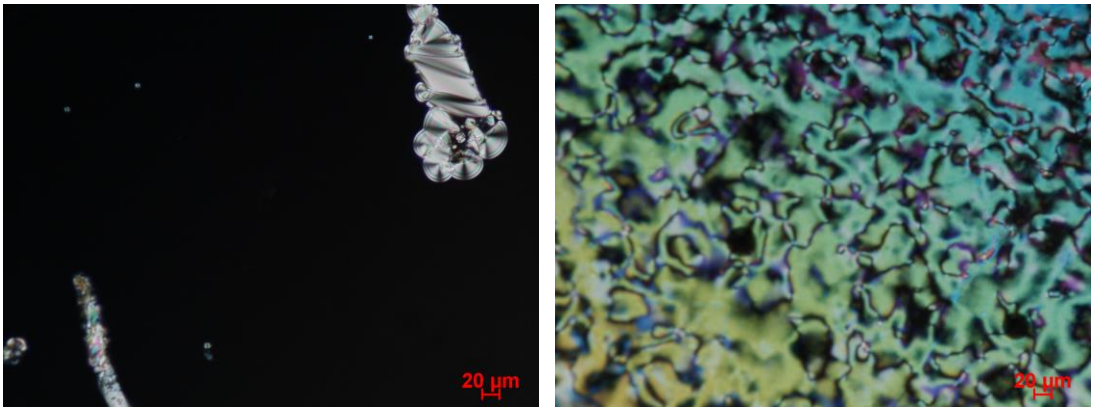

Figure A2-32: Textures of compound **QL21-8/8-4F** observed by polarized microscopy on cooling: in the N phase at 97°C (right) and in the SmA phase at 94°C (left) (200X Magnification)

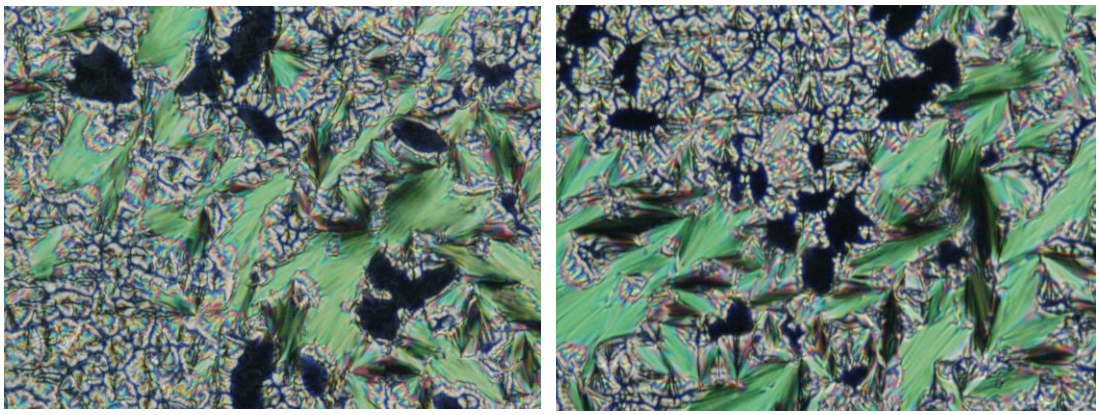

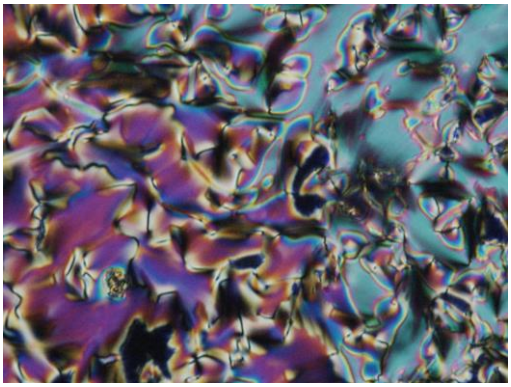

Figure A2-33: Textures of compound **QL23-8/8-2,6F$_2$** observed by polarized microscopy on cooling: in the N phase at 67°C (bottom), in the SmA phase at 64°C (right)and in the SmC phase at 49°C (left) (200X Magnification)

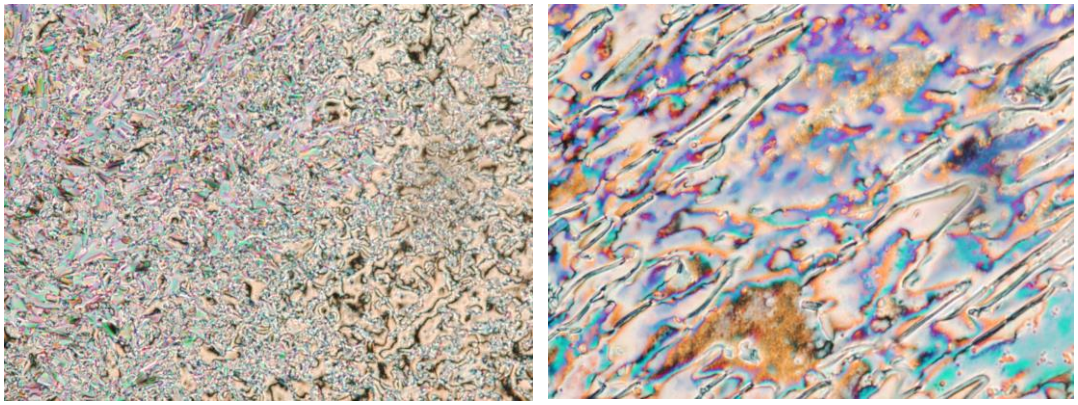

Figure A2-34: Textures of compound **QL22-7/8-2,6F$_2$** observed by polarized microscopy on cooling: in the N phase at 70°C (right), and in the SmC phase at 60°C (left) (200X Magnification)

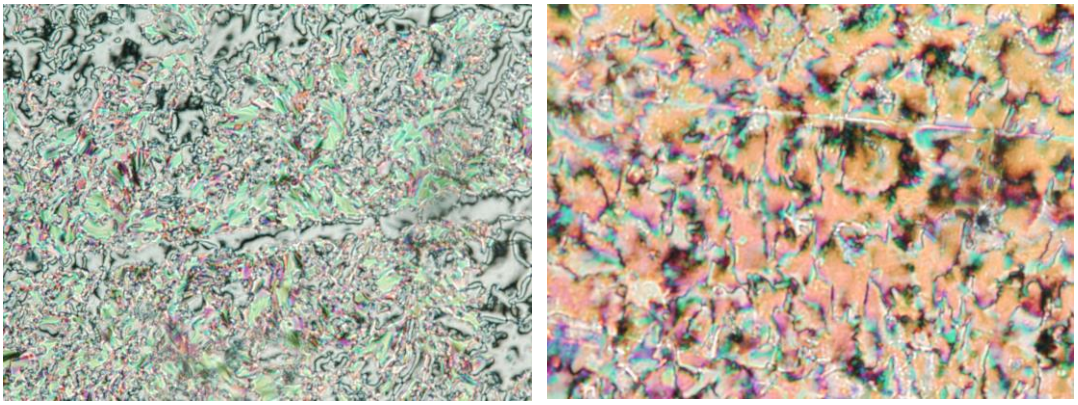

Figure A2-35: Textures of compound **QL22-9/8-2,6F$_2$** observed by polarized microscopy on cooling: in the N phase at 71°C (right), and in the SmC phase at 60°C (left) (200X Magnification)

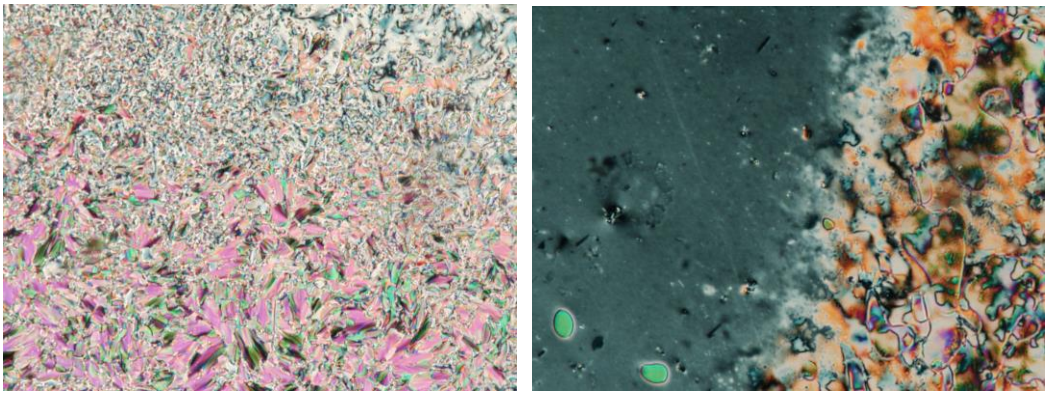

Figure A2-36: Textures of compound **QL22-10/8-2,6F$_2$** observed by polarized microscopy on cooling: in the N phase at 70°C (right), and in the SmC phase at 67°C (left) (200X Magnification)

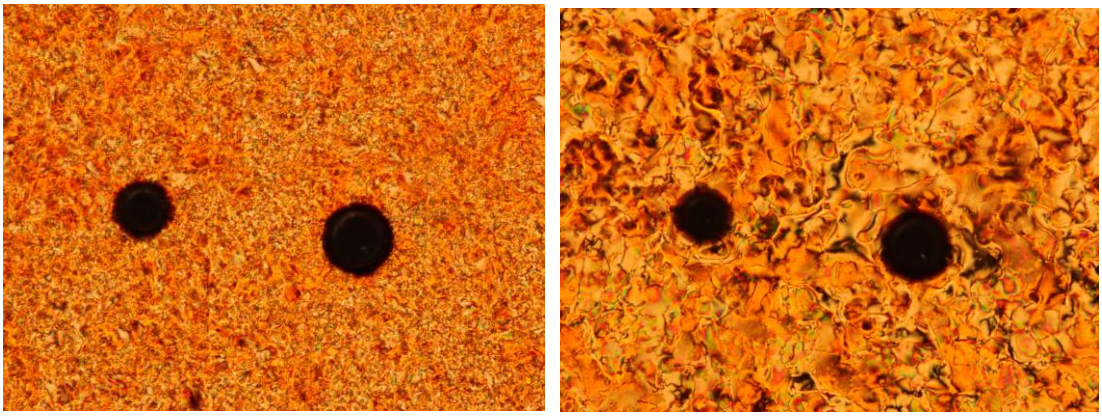

Figure A2-37: Textures of compound **QL29-7/8-2,6F$_2$** observed by polarized microscopy on cooling: in the N phase at 29°C (right), and in the SmC phase at 11°C (left) (200X Magnification)

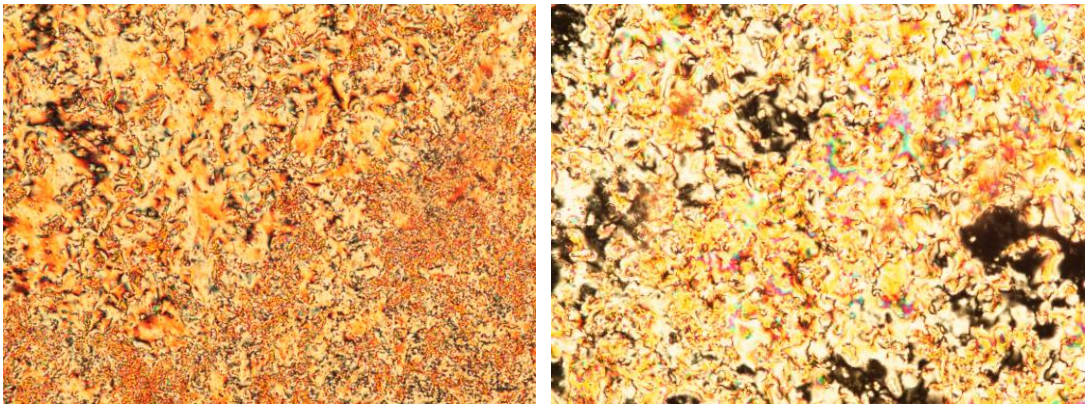

Figure A2-38: Textures of compound **QL29-8/8-2,6F$_2$** observed by polarized microscopy on cooling: in the N phase at 50°C (right), and in the SmC phase at 35°C (left) (200X Magnification)

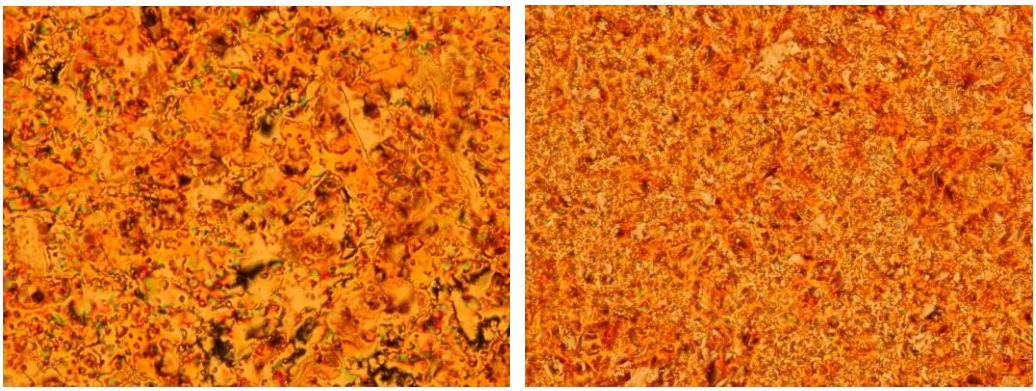

Figure A2-39: Textures of compound **QL29-9/8-2,6F$_2$** observed by polarized microscopy on cooling: in the N phase at 50°C (right), and in the SmC phase at 35°C (left) (200X Magnification)

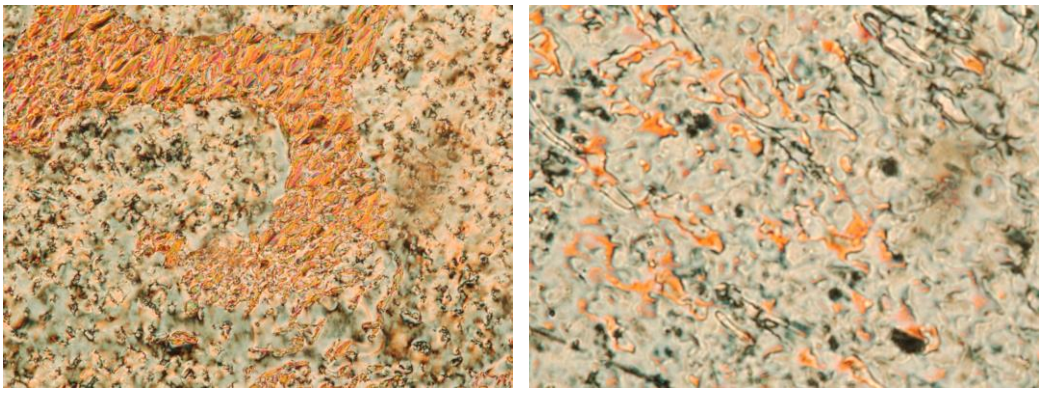

Figure A2-40: Textures of compound **QL29-10/8-2,6F$_2$** observed by polarized microscopy on cooling: in the N phase at 50°C (right), and in the SmC phase at 36°C (left) (200X Magnification)

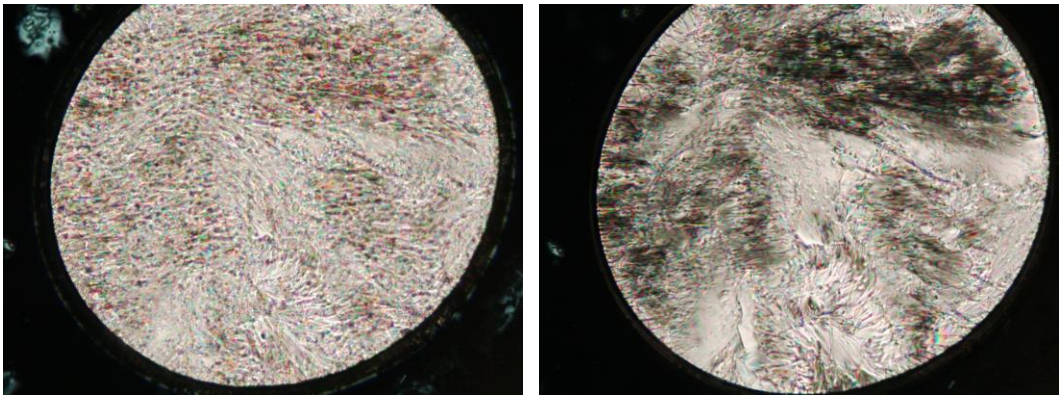

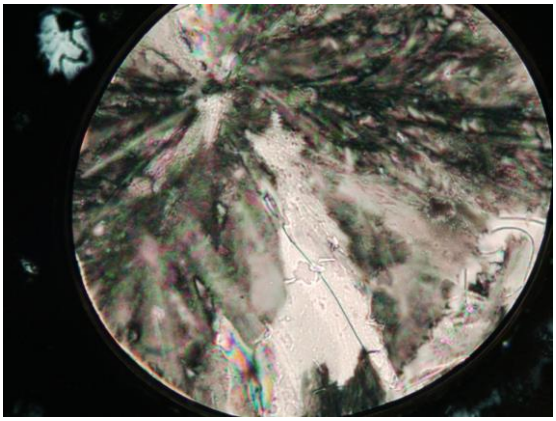

Figure A2-41: Textures of compound **QL30-8/8-2,6Me$_2$** observed by polarized microscopy on cooling: in the N phase at 70°C (bottom), in the SmA phase at 63°C (right) ,and in the SmC phase at 45°C (left) (200X Magnification)

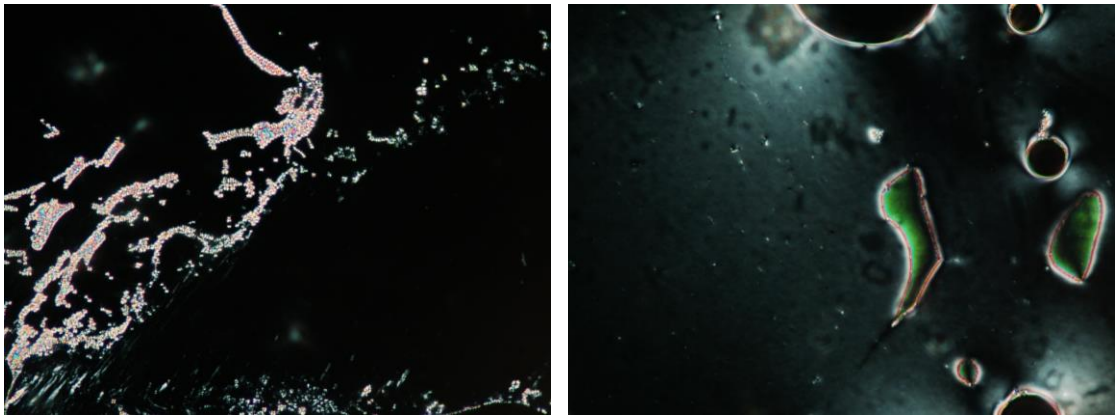

Figure A2-42: Textures of compound **QL31-8/8-2,6Me$_2$** observed by polarized microscopy on cooling: in the N phase at 72°C (right), and in the SmA phase at 60°C (200X Magnification)

Appendix 3: ^{1}H NMR of Novel Liquid Crystals

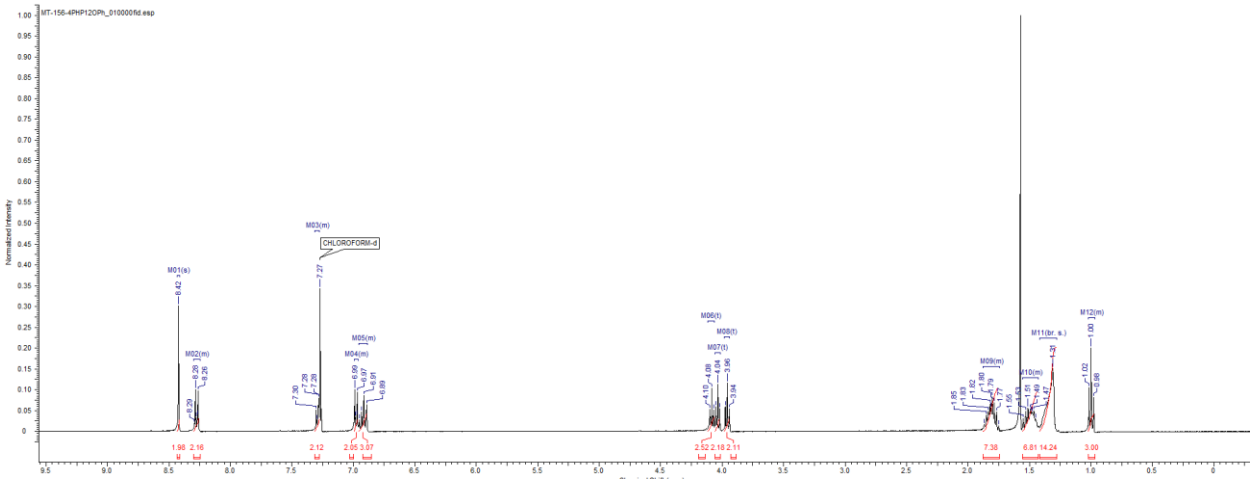

Figure A3-1: 400 MHz ^{1}H NMR spectrum of **QL11-4/12**

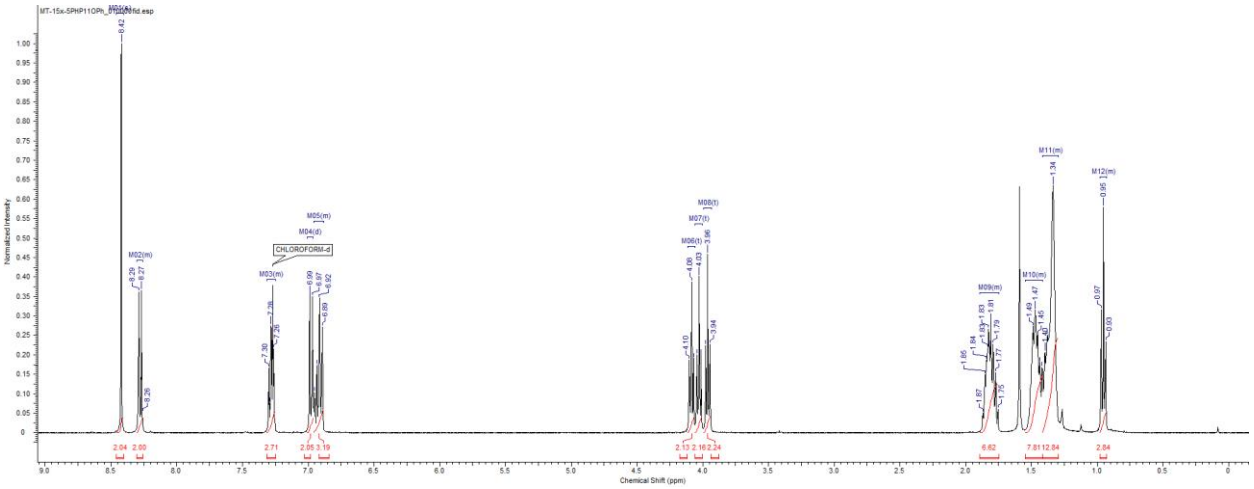

Figure A3-2: 400 MHz ^{1}H NMR spectrum of **QL11-5/11**

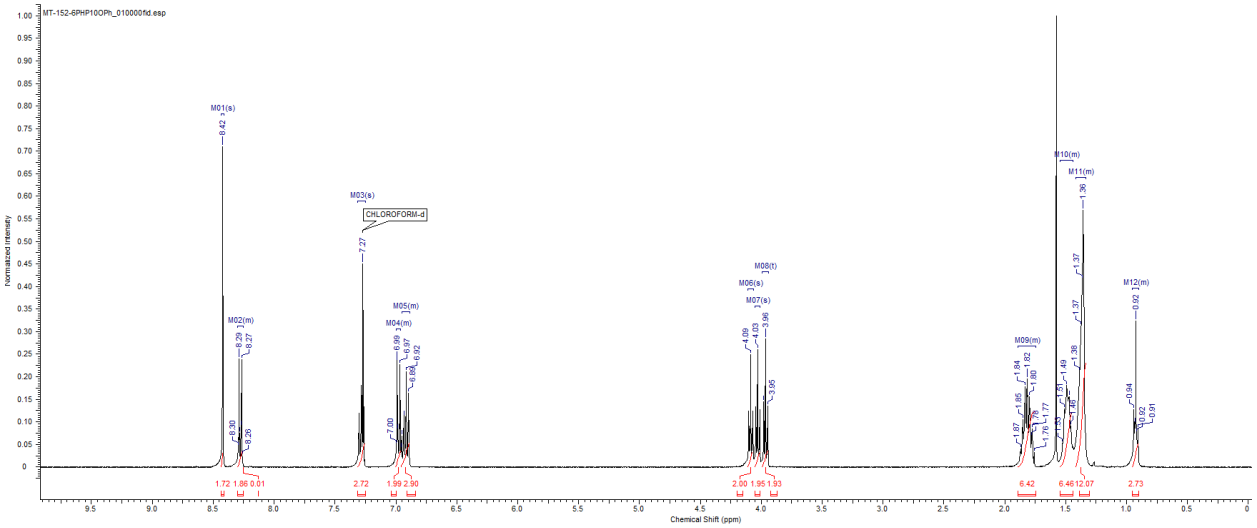

Figure A3-3: 400 MHz ^{1}H NMR spectrum of **QL11-6/10**

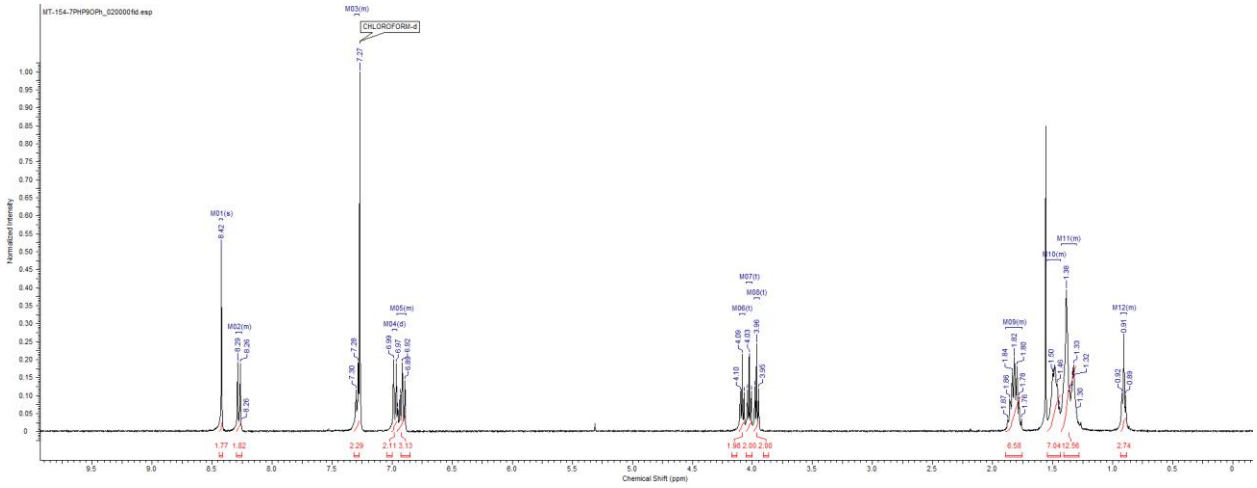

Figure A3-4: 400 MHz ^{1}H NMR spectrum of **QL11-7/9**

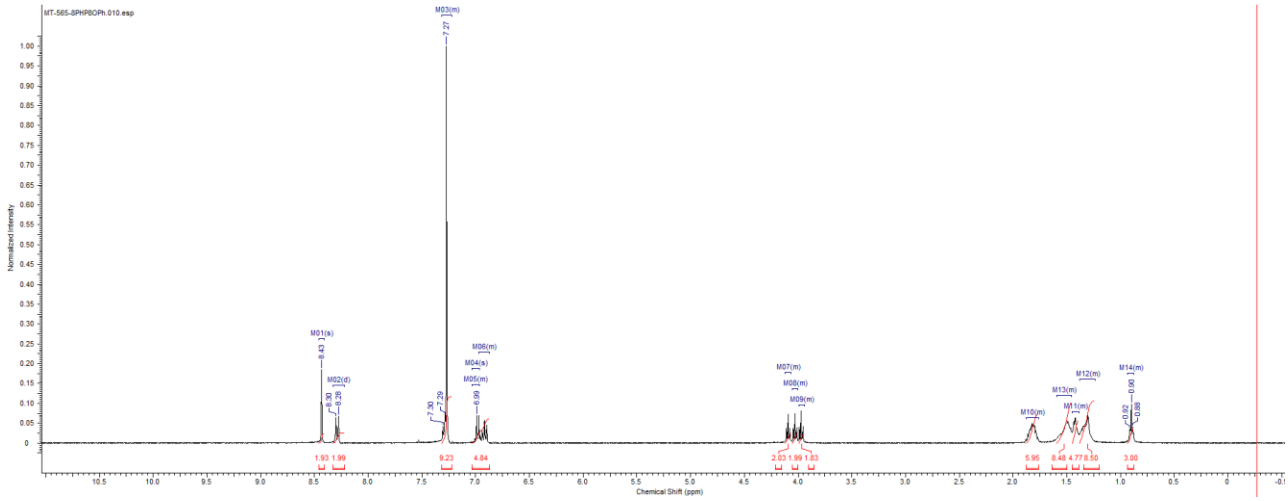

Figure A3-5: 400 MHz ^{1}H NMR spectrum of **QL11-8/8**

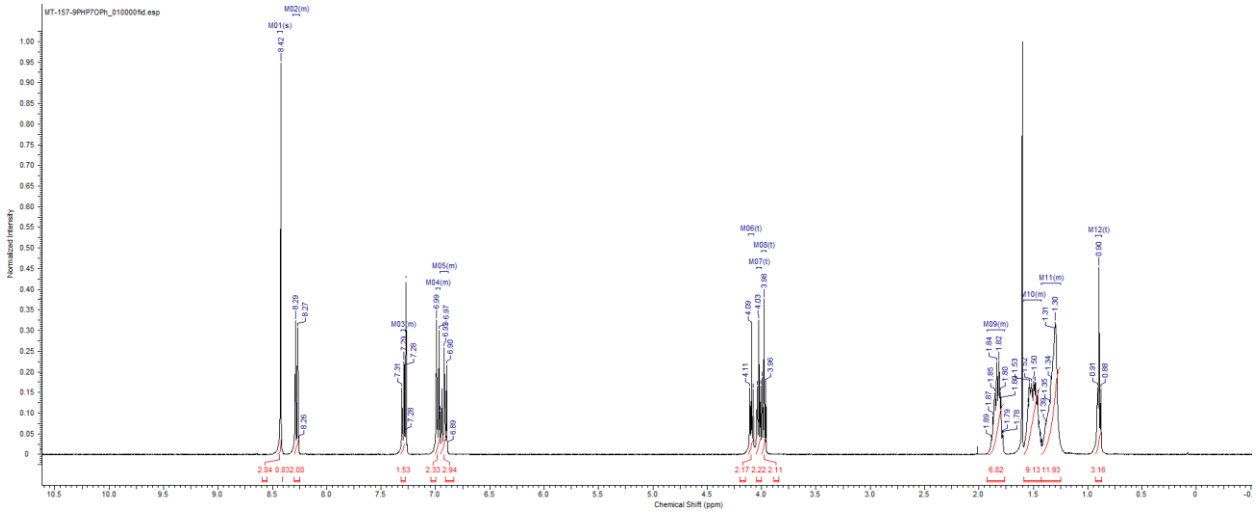

Figure A3-6: 400 MHz ^{1}H NMR spectrum of **QL11-9/7**

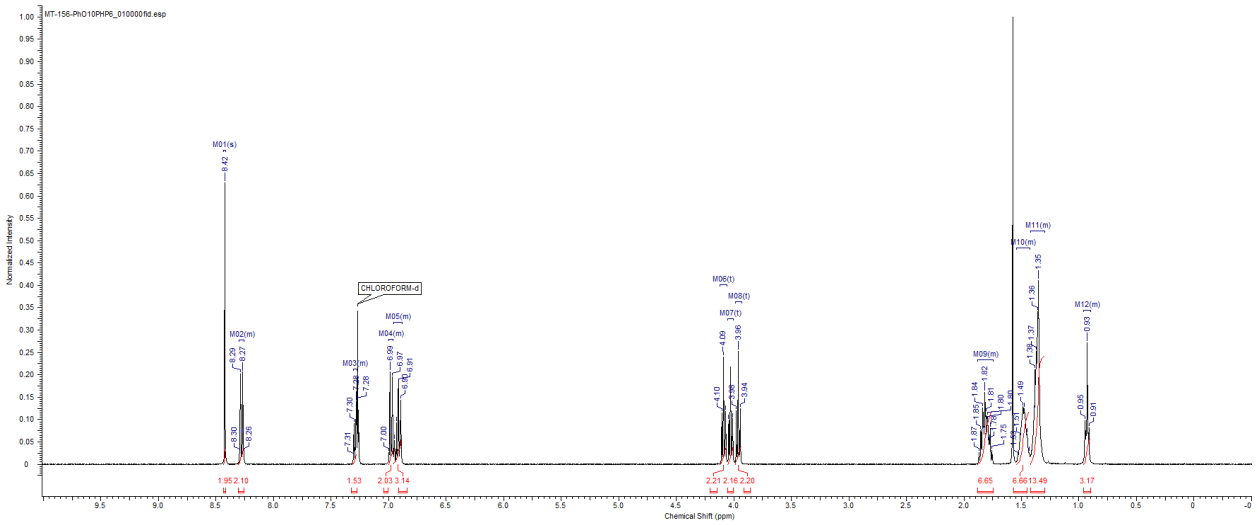

Figure A3-7: 400 MHz ^{1}H NMR spectrum of **QL11-10/6**

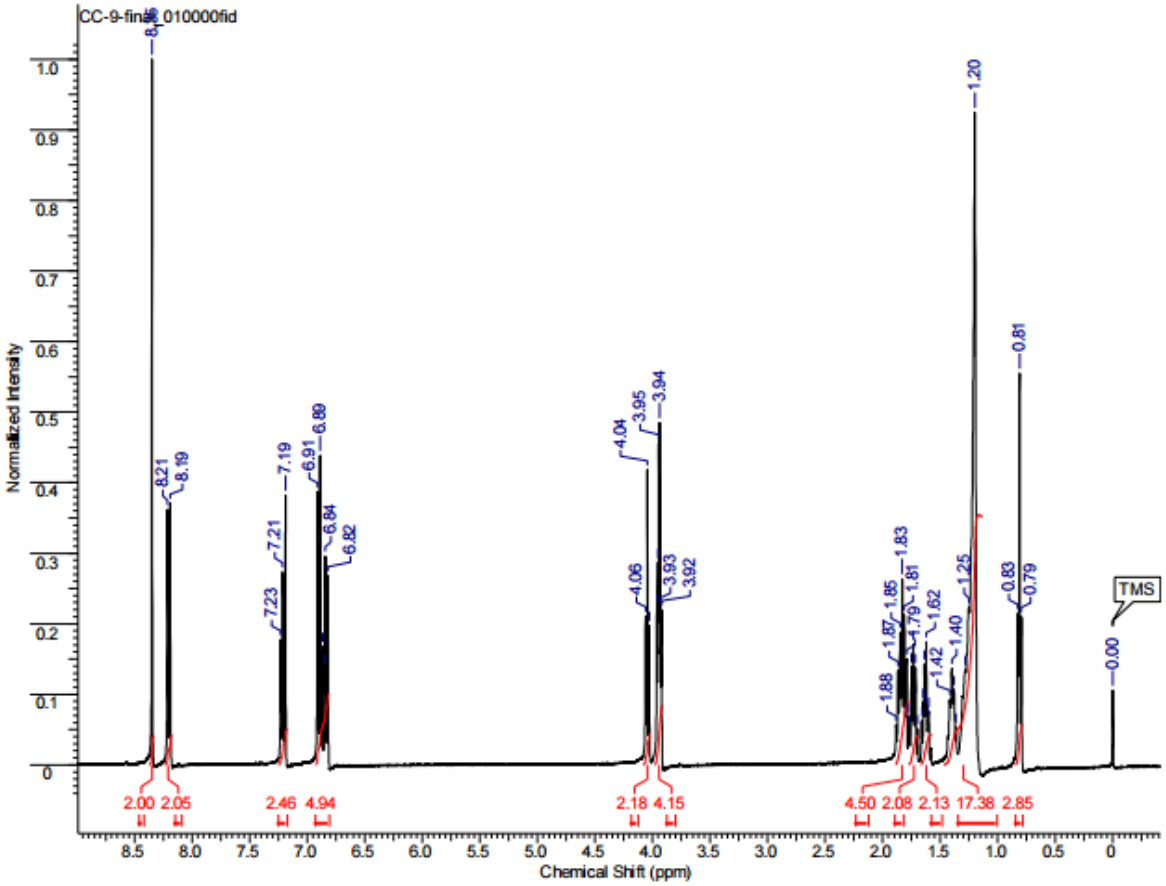

Figure A3-8: 400 MHz ^{1}H NMR spectrum of **QL11-11/5** (By Carolyn Carkner)

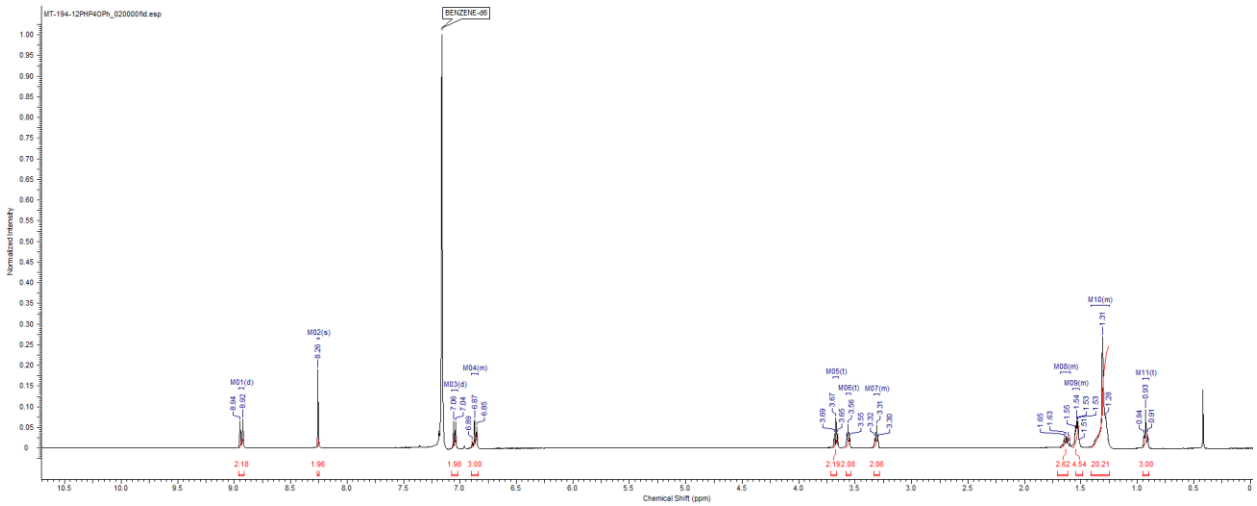

Figure A3-9: 400 MHz ^{1}H NMR spectrum of **QL11-12/4**

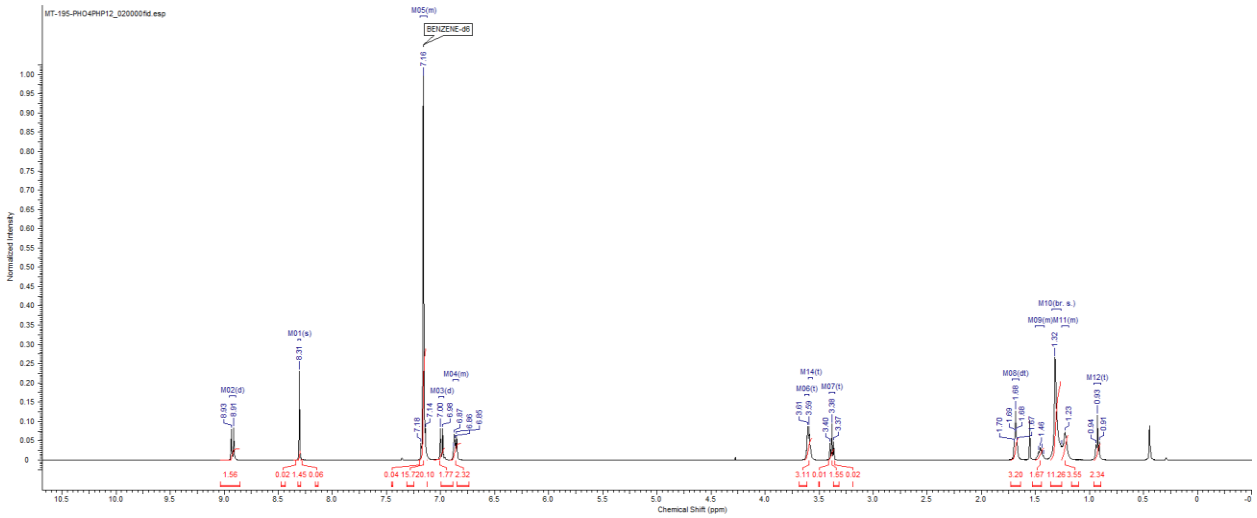

Figure A3-10: 400 MHz ^{1}H NMR spectrum of **QL12-12/4**

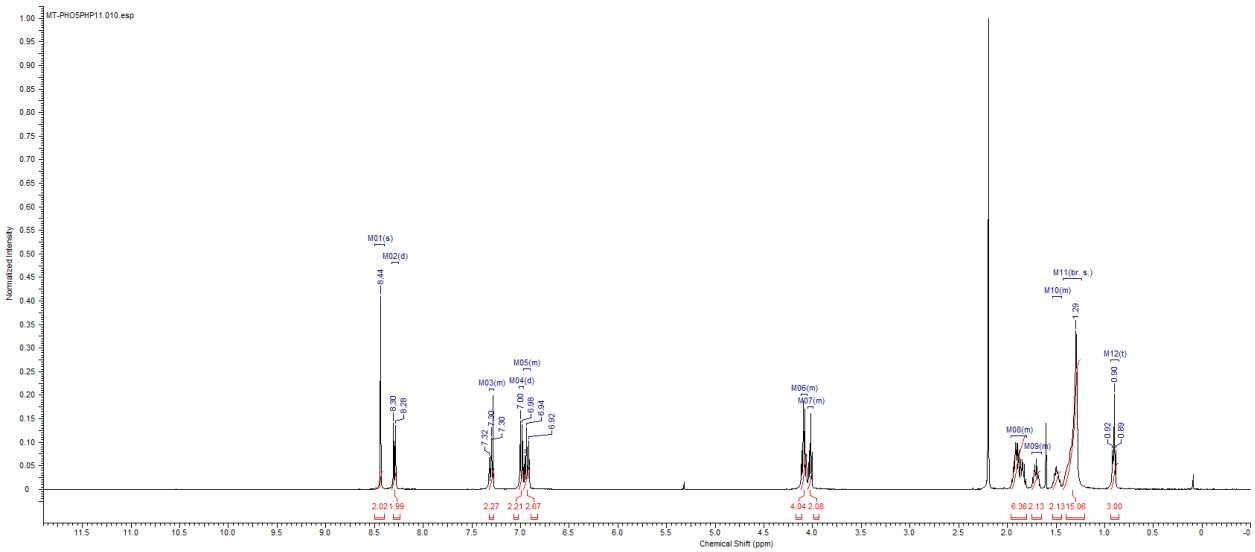

Figure A3-11: 400 MHz ^{1}H NMR spectrum of **QL12-11/5**

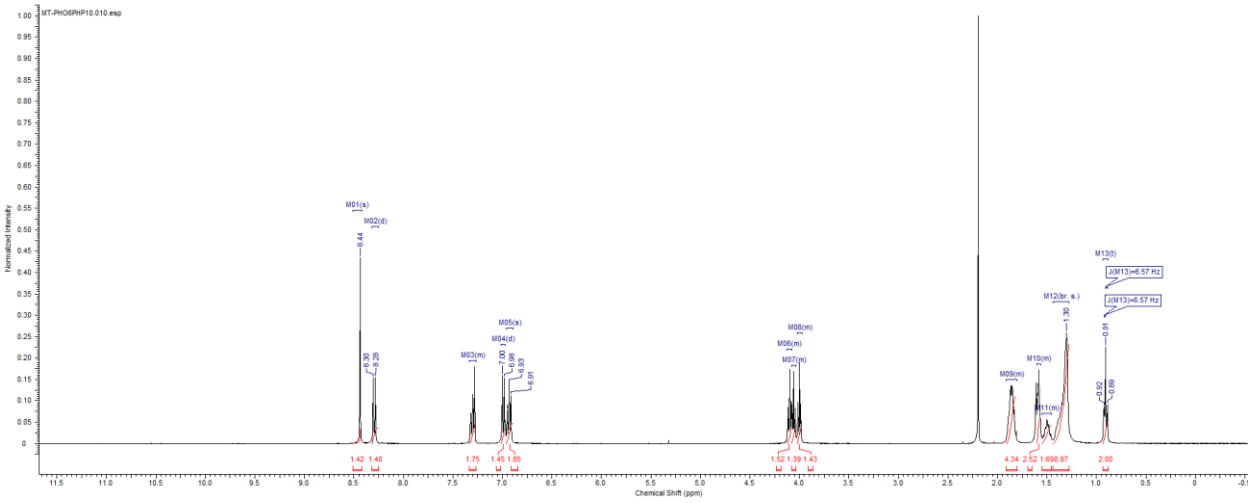

Figure A3-12: 400 MHz ^{1}H NMR spectrum of **QL12-10/6**

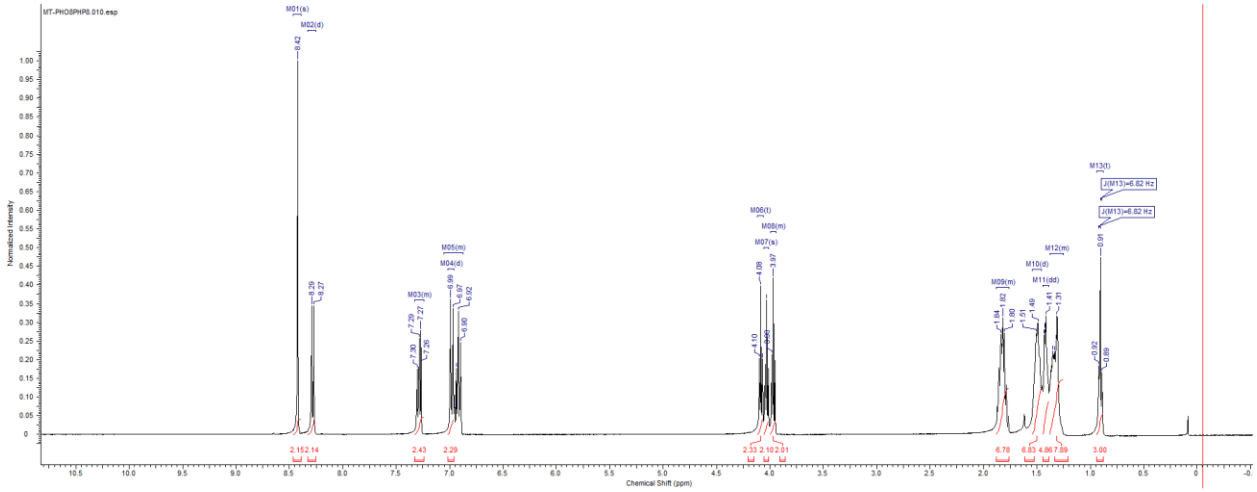

Figure A3-13: 400 MHz ^{1}H NMR spectrum of **QL11-8/8**

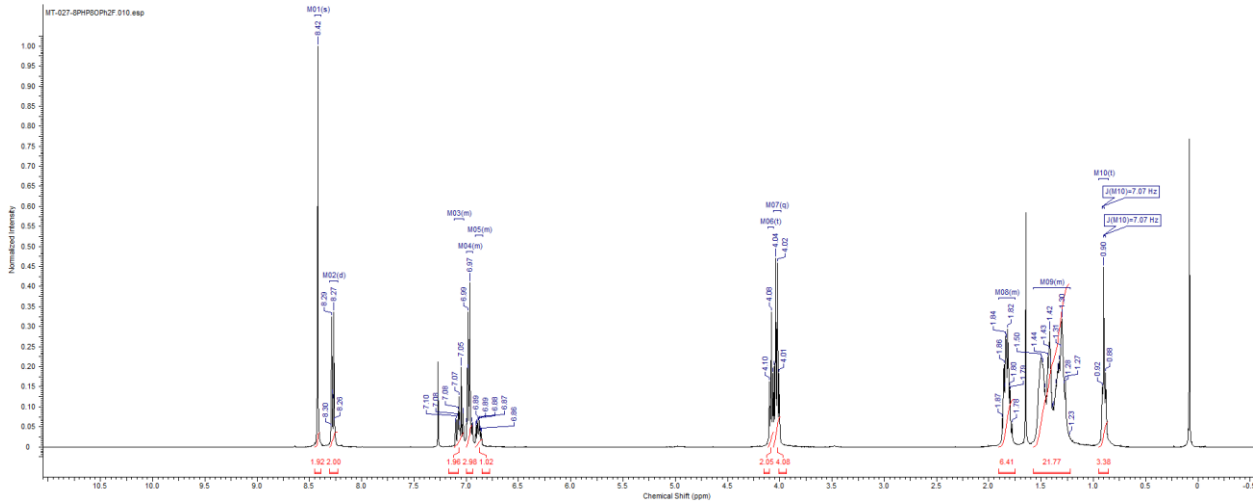

Figure A3-14: 400 MHz ^{1}H NMR spectrum of **QL20-8/8-2F**

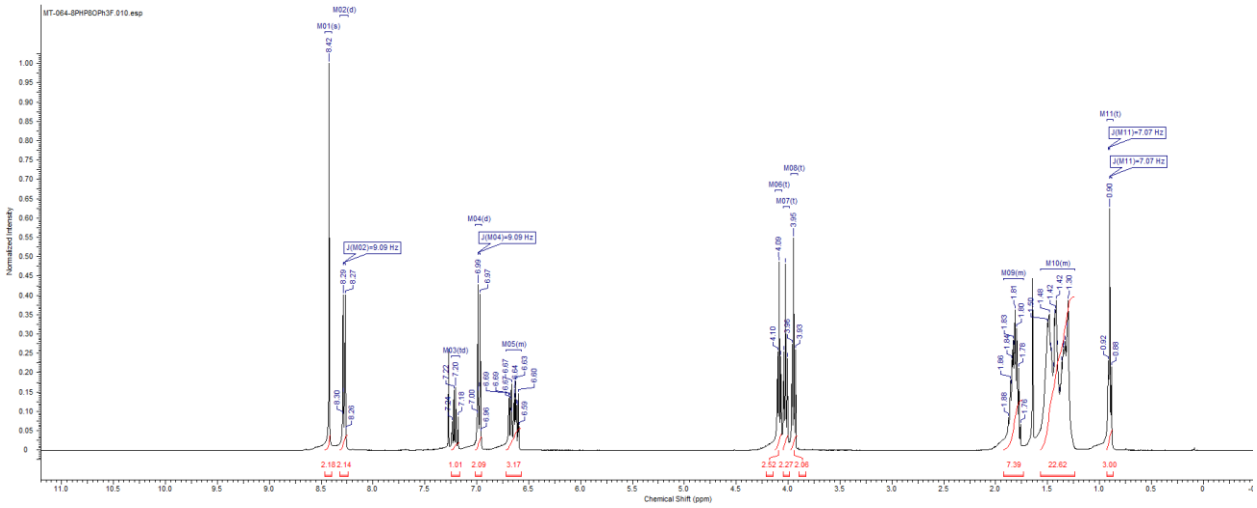

Figure A3-15: 400 MHz ^{1}H NMR spectrum of **QL20-8/8-3F**

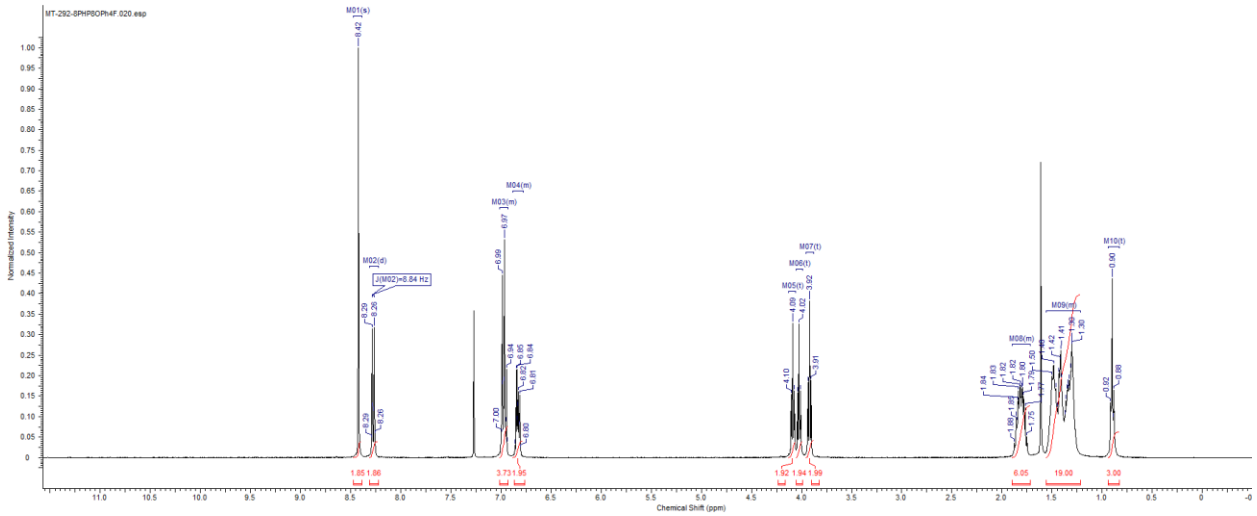

Figure A3-16: 400 MHz ^{1}H NMR spectrum of **QL20-8/8-4F**

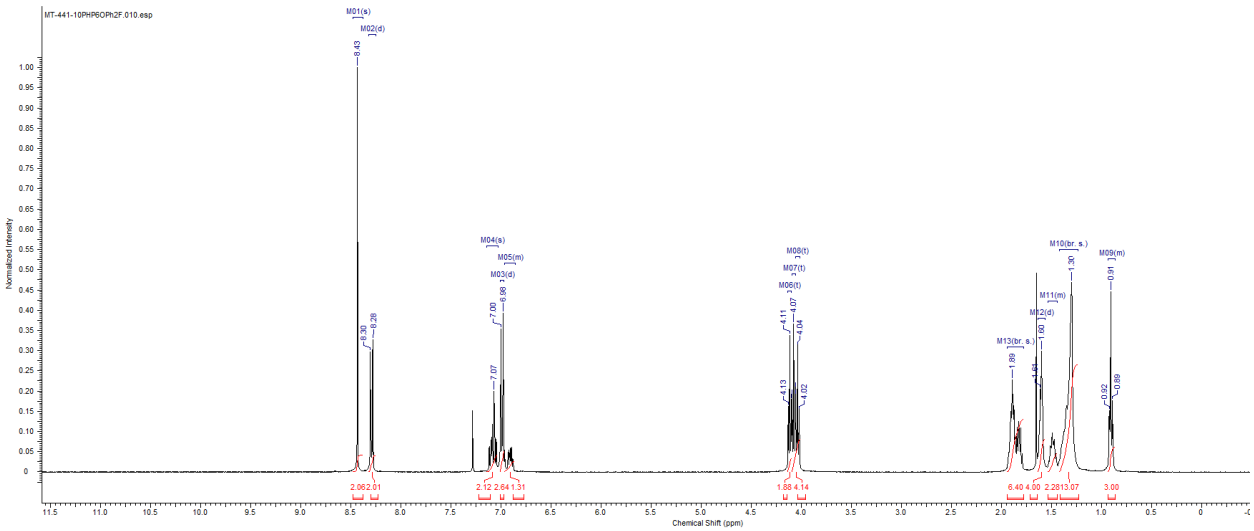

Figure A3-17: 400 MHz ^{1}H NMR spectrum of **QL20-10/6-2F**

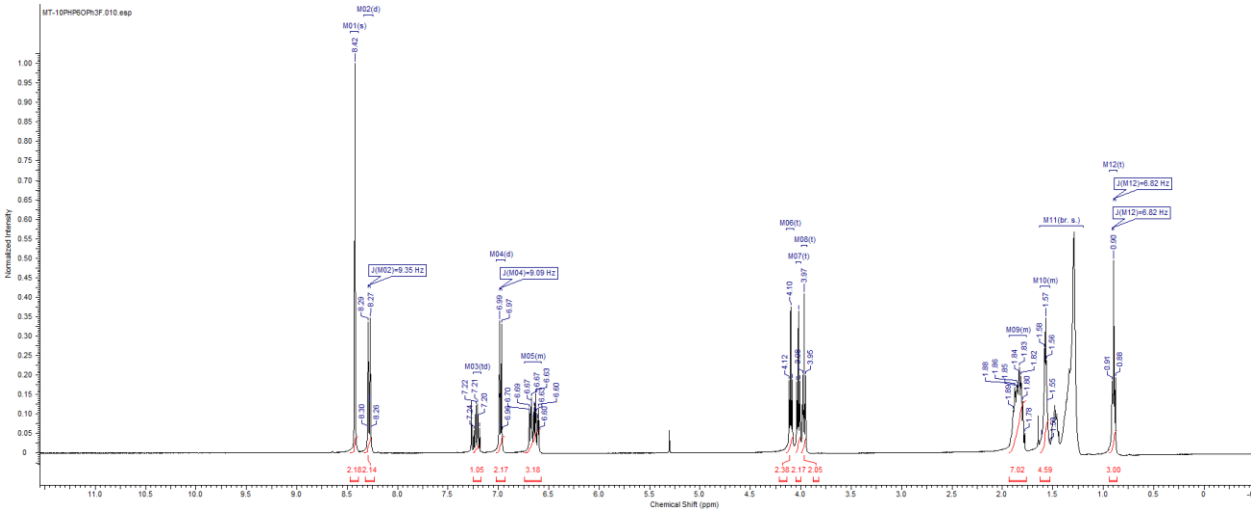

Figure A3-18: 400 MHz ^{1}H NMR spectrum of **QL20-10/6-3F**

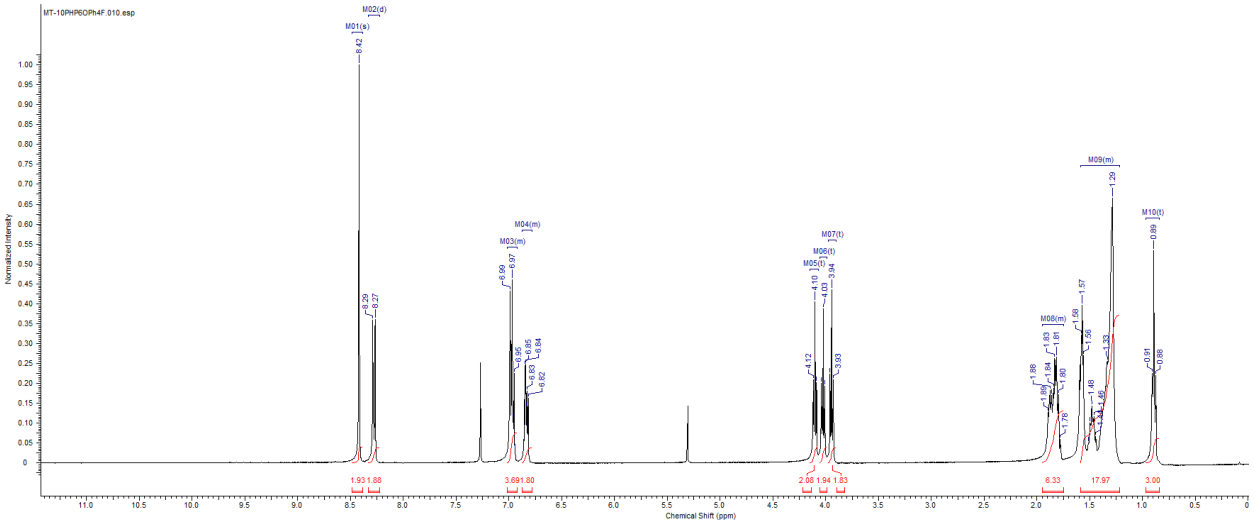

Figure A3-19: 400 MHz ^{1}H NMR spectrum of **QL20-10/6-4F**

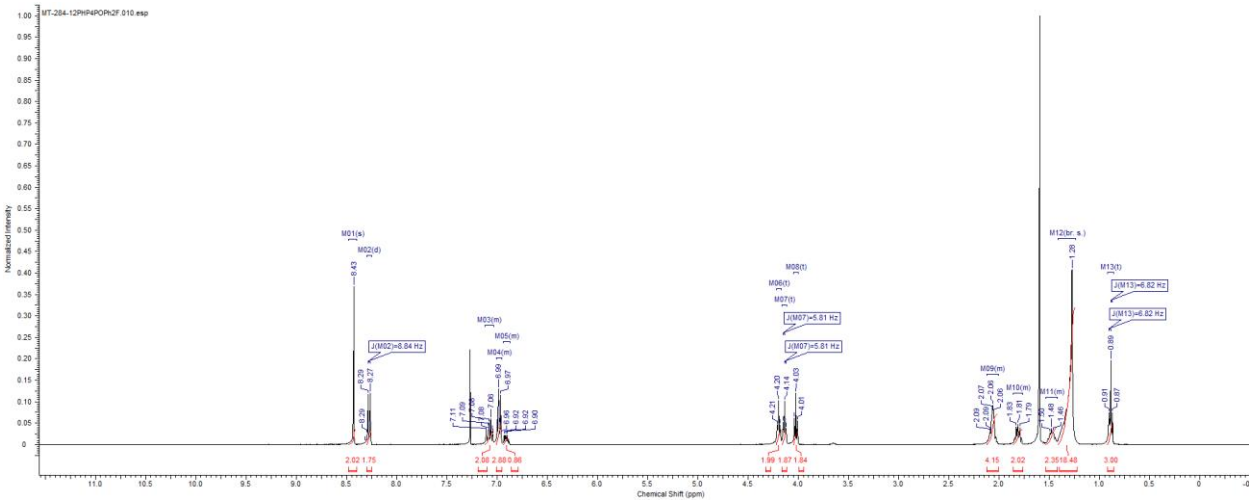

Figure A3-20: 400 MHz ^{1}H NMR spectrum of **QL20-12/4-2F**

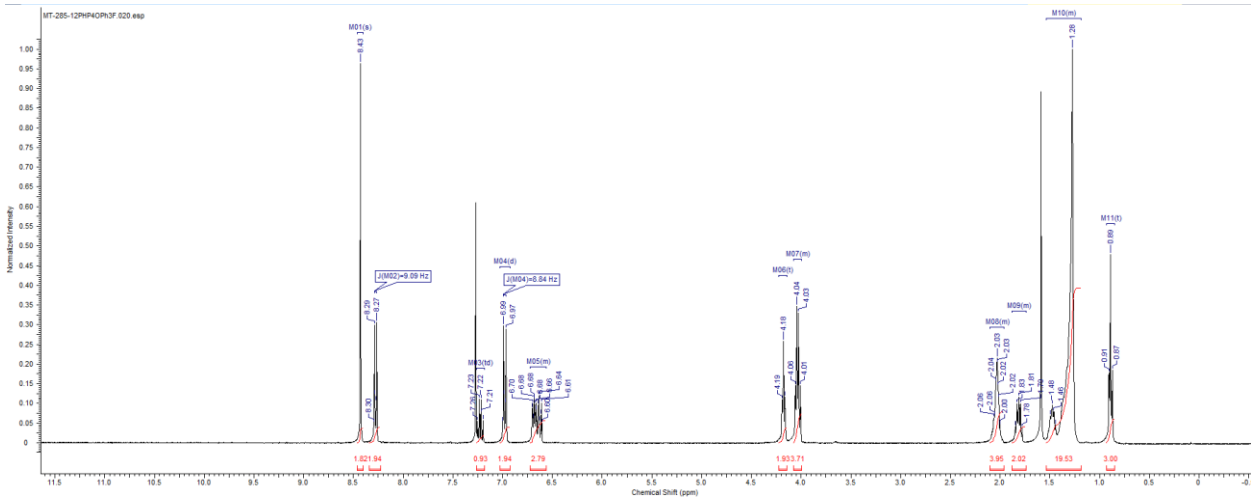

Figure A3-21: 400 MHz ^{1}H NMR spectrum of **QL20-12/4-3F**

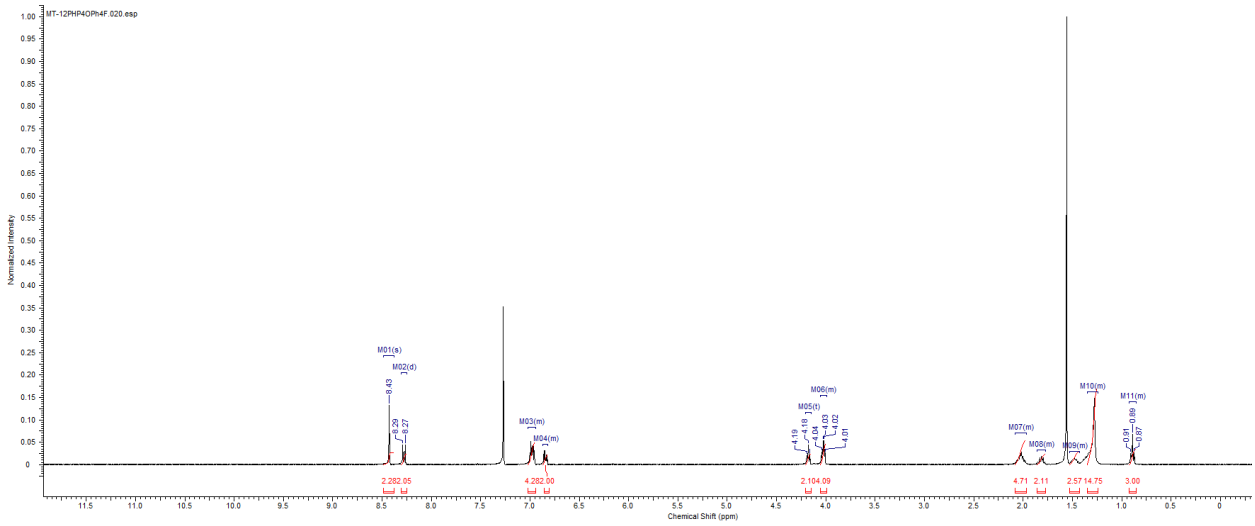

Figure A3-22: 400 MHz ^{1}H NMR spectrum of **QL20-12/4-4F**

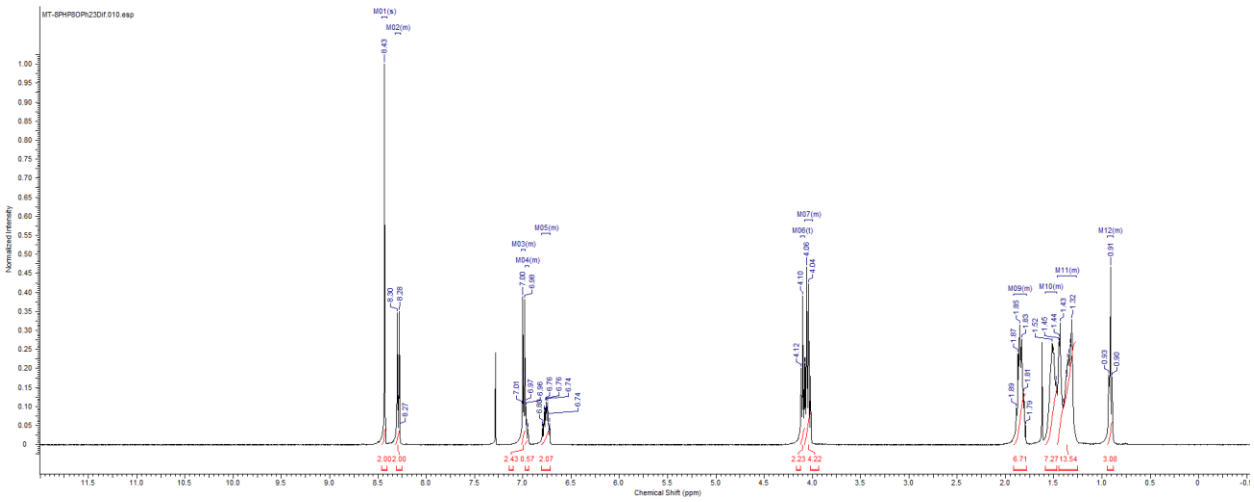

Figure A3-23: 400 MHz ^{1}H NMR spectrum of **QL22-8/8-2,3F$_2$**

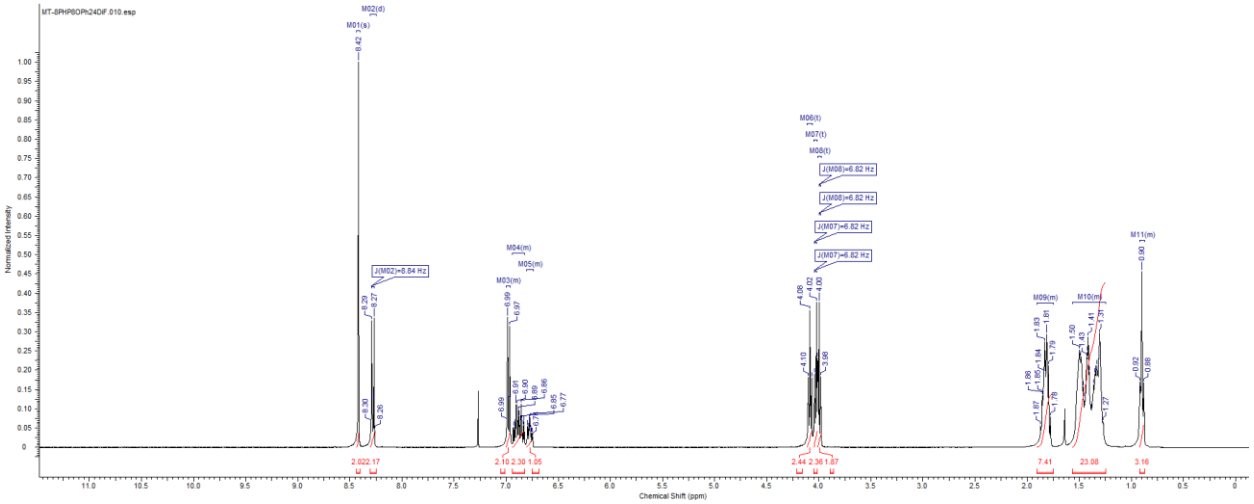

Figure A3-24: 400 MHz ^{1}H NMR spectrum of **QL22-8/8-2,4F$_2$**

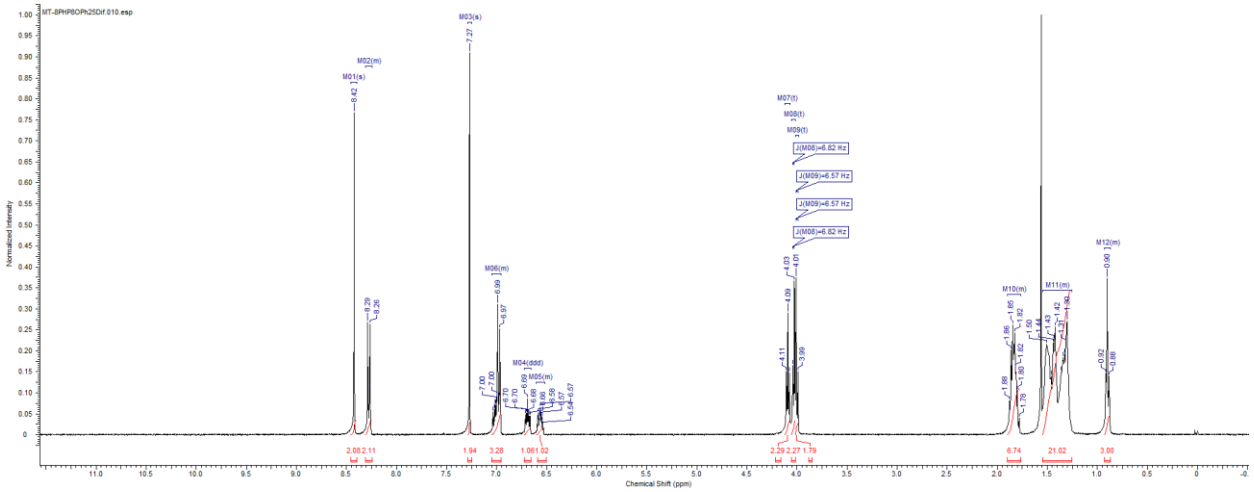

Figure A3-25: 400 MHz ^{1}H NMR spectrum of **QL22-8/8-2,5F$_2$**

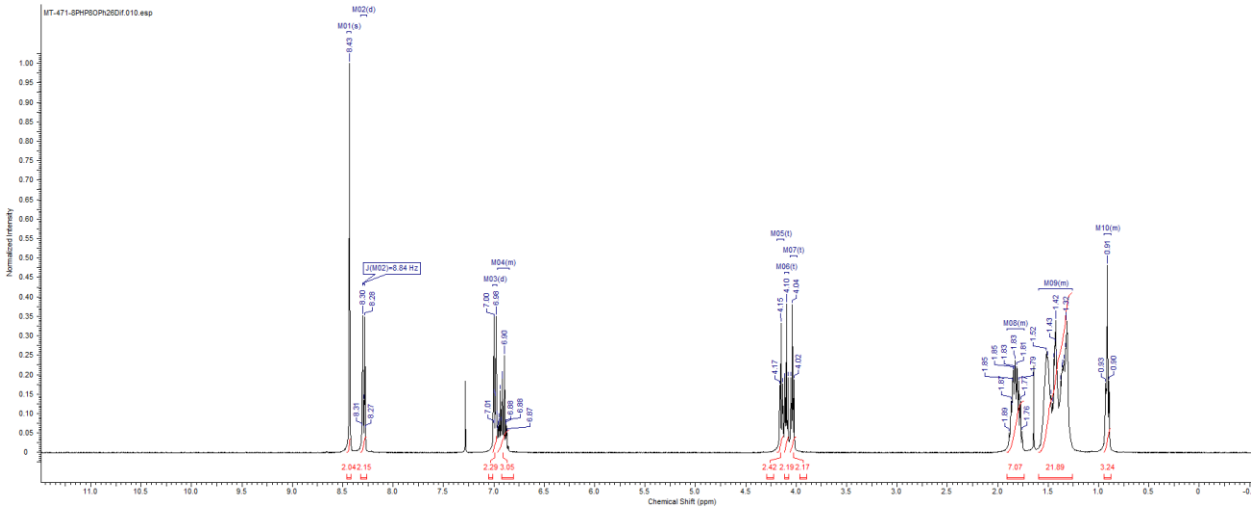

Figure A3-26: 400 MHz ^{1}H NMR spectrum of **QL22-8/8-2,6F$_2$**

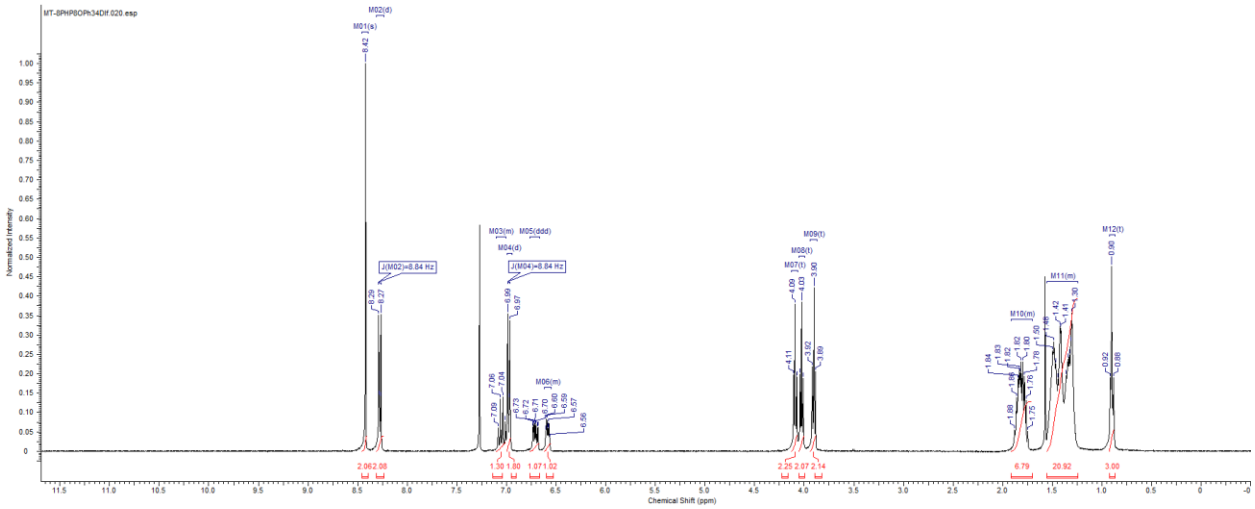

Figure A3-27: 400 MHz ^{1}H NMR spectrum of **QL22-8/8-3,4F$_2$**

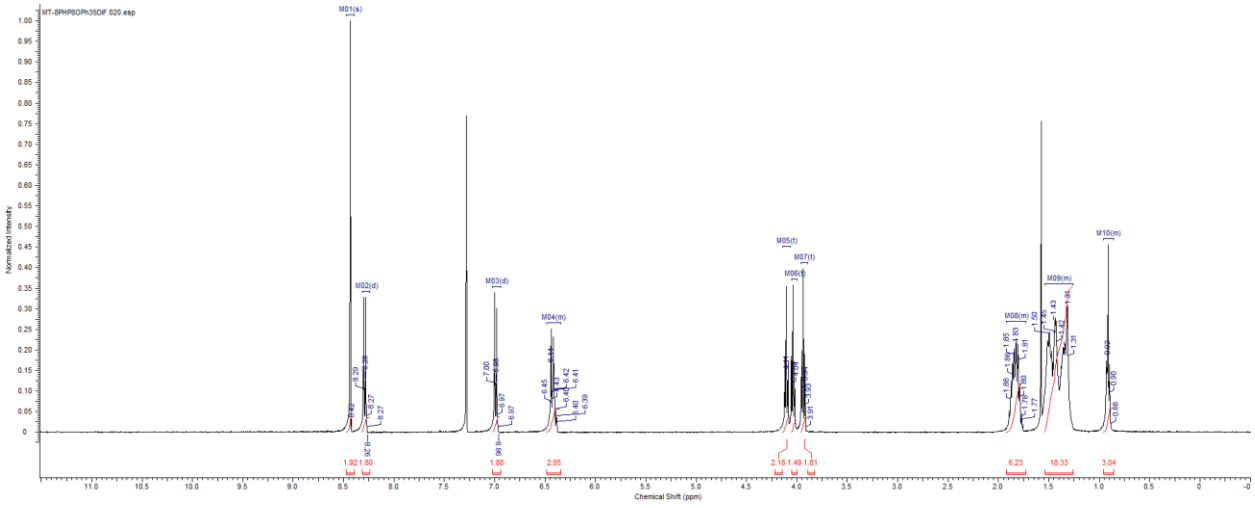

Figure A3-28: 400 MHz ^{1}H NMR spectrum of **QL22-8/8-3,5F$_2$**

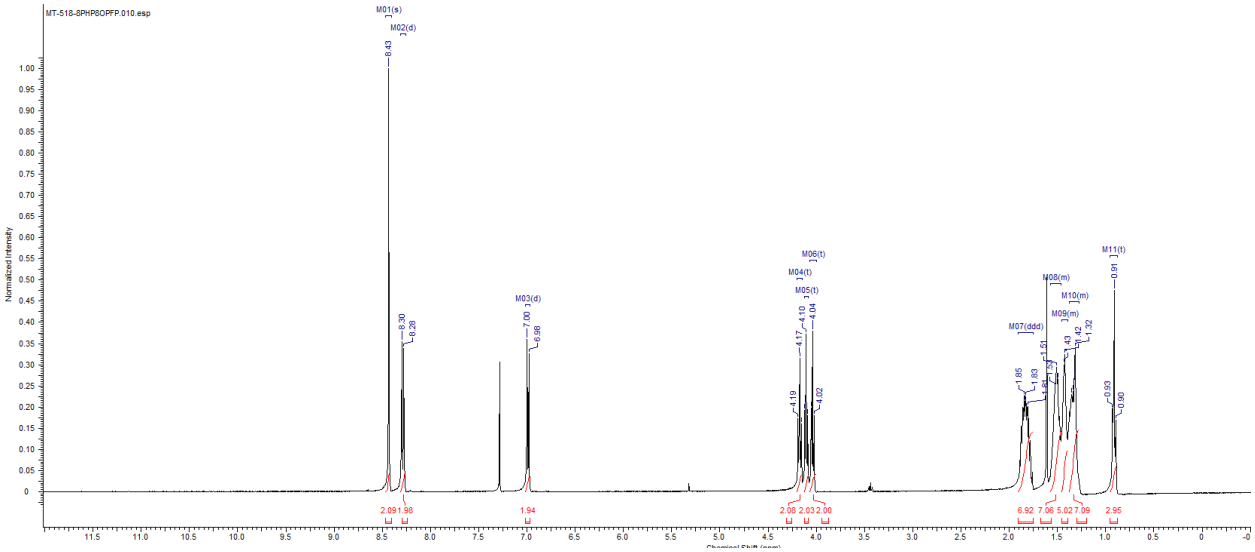

Figure A3-29: 400 MHz ^{1}H NMR spectrum of **QL27-8/8**

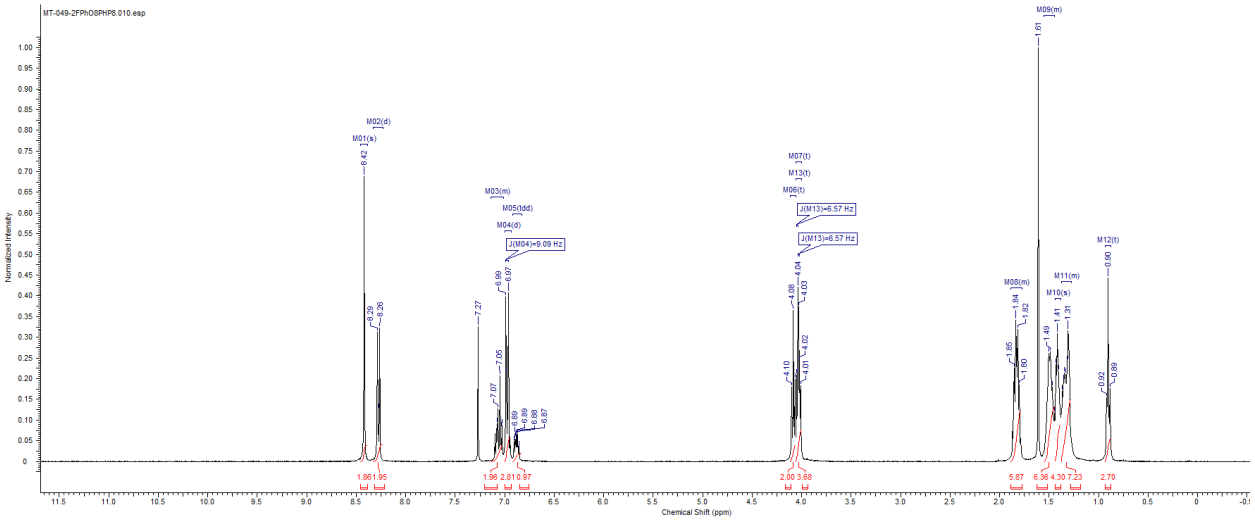

Figure A3-30: 400 MHz ^{1}H NMR spectrum of **QL21-8/8-2F**

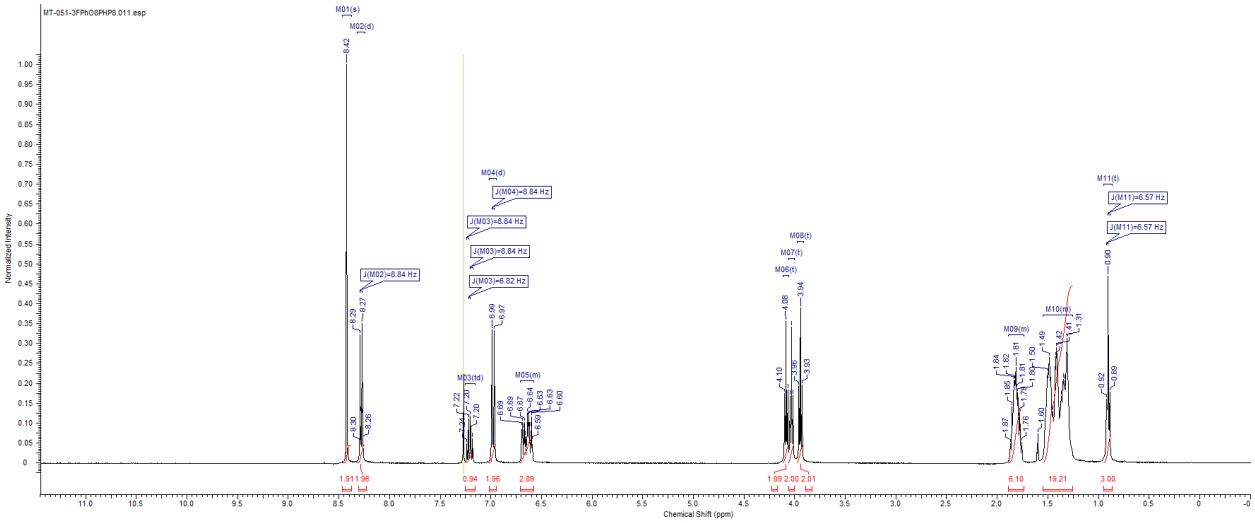

Figure A3-31: 400 MHz ^{1}H NMR spectrum of **QL21-8/8-3F**

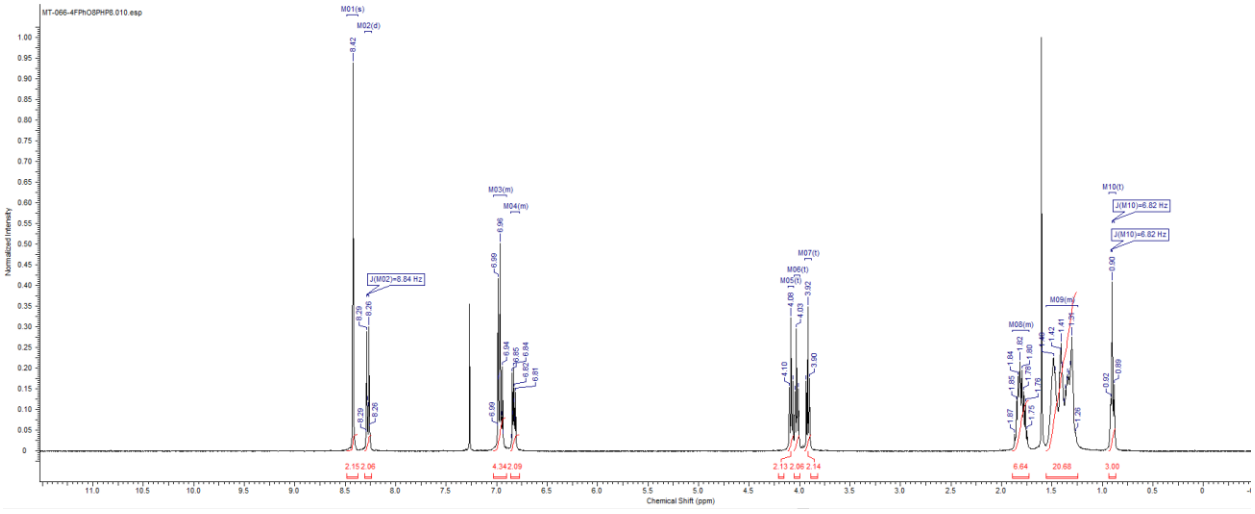

Figure A3-32: 400 MHz ^{1}H NMR spectrum of **QL21-8/8-4F**

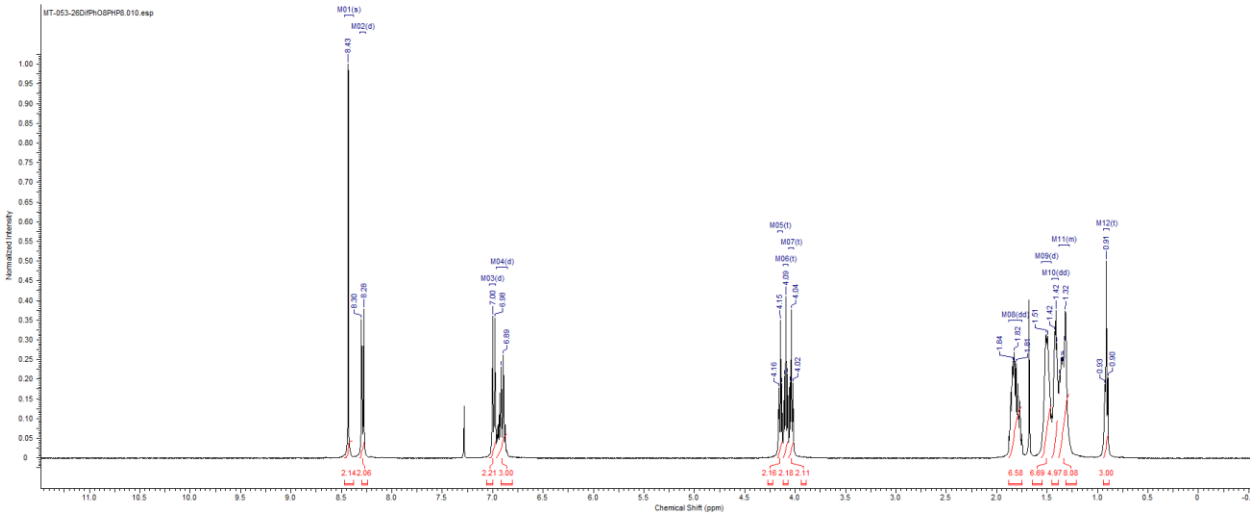

Figure A3-33: 400 MHz ^{1}H NMR spectrum of **QL23-8/8-2,6F$_2$**

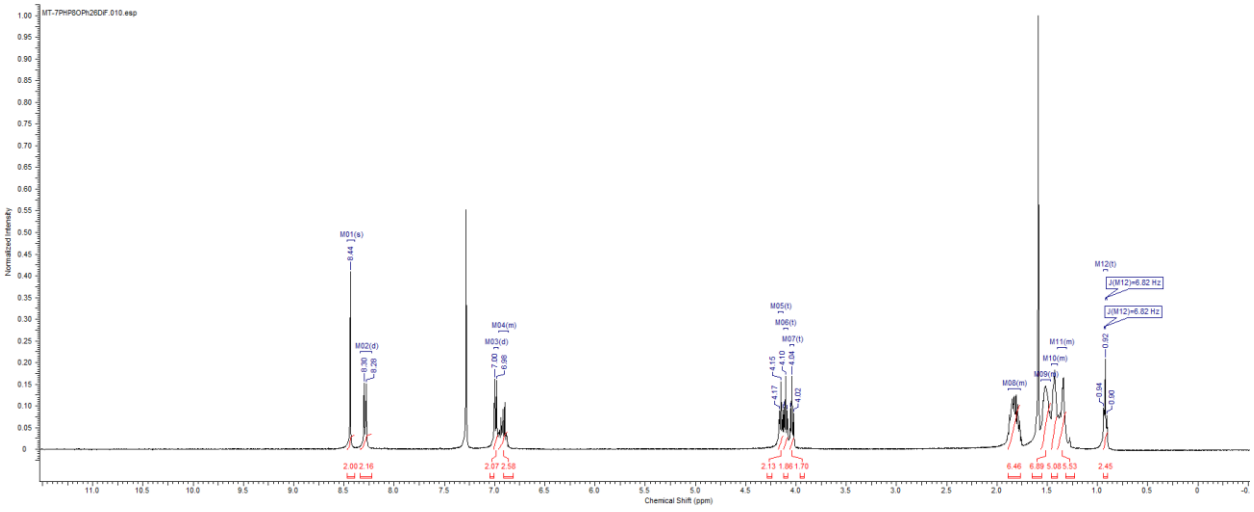

Figure A3-34: 400 MHz ^{1}H NMR spectrum of **QL22-7/8-2,6F$_2$**

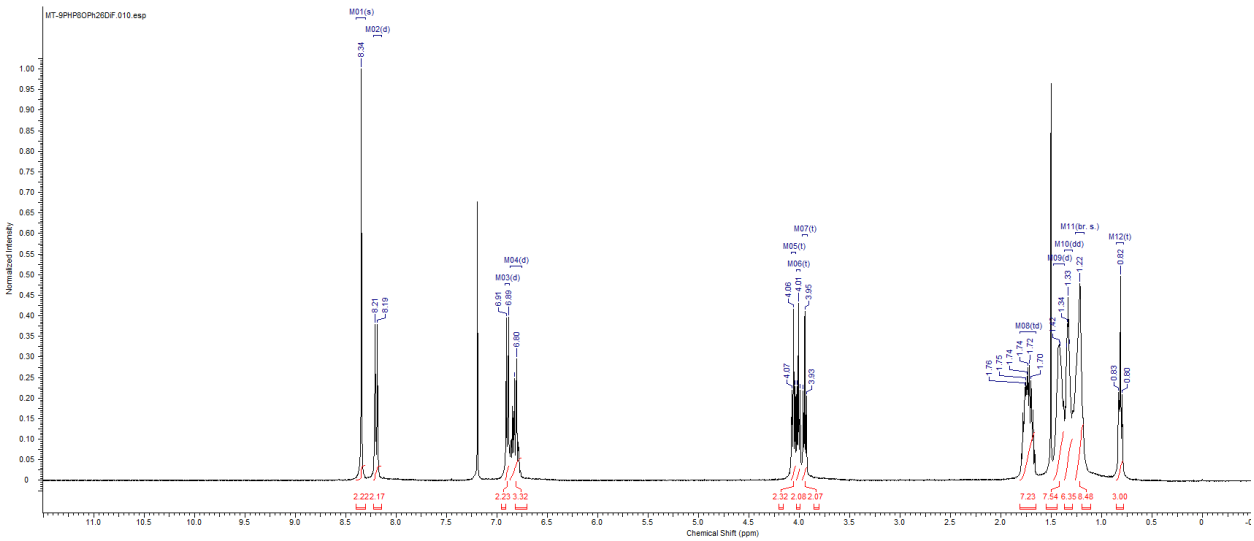

Figure A3-35: 400 MHz ^{1}H NMR spectrum of **QL22-9/8-2,6F$_2$**

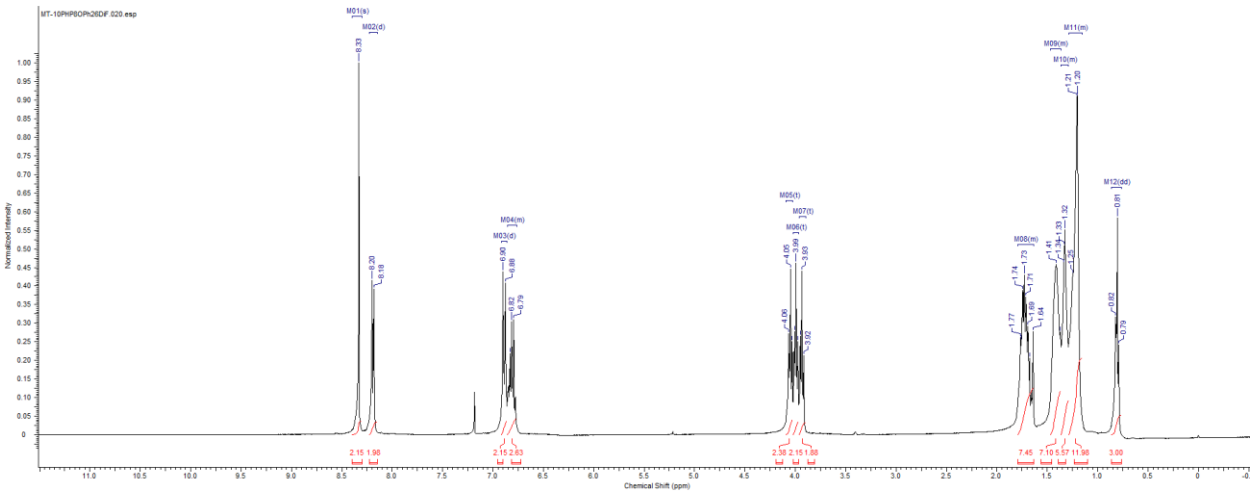

Figure A3-36: 400 MHz ^{1}H NMR spectrum of **QL22-10/8-2,6F$_2$**

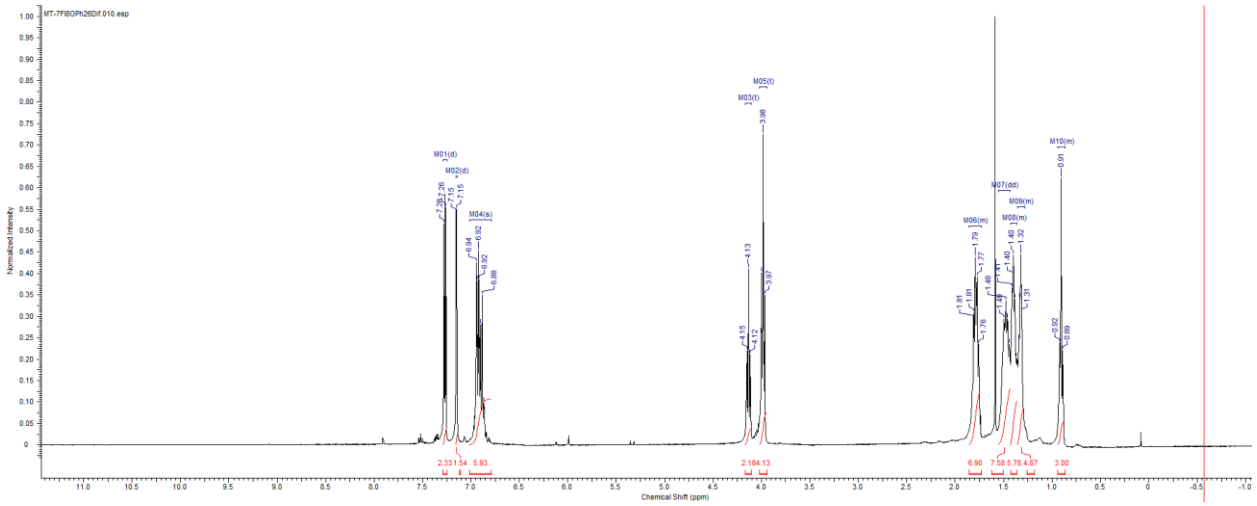

Figure A3-37: 400 MHz ^{1}H NMR spectrum of **QL29-7/8-2,6F$_2$**

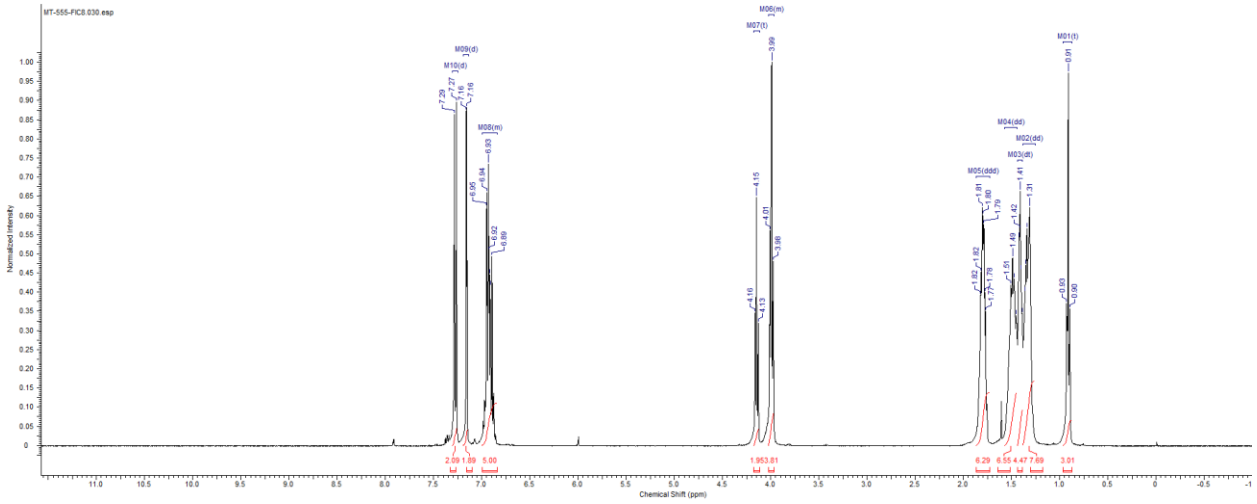

Figure A3-38: 400 MHz ^{1}H NMR spectrum of **QL29-8/8-2,6F$_2$**

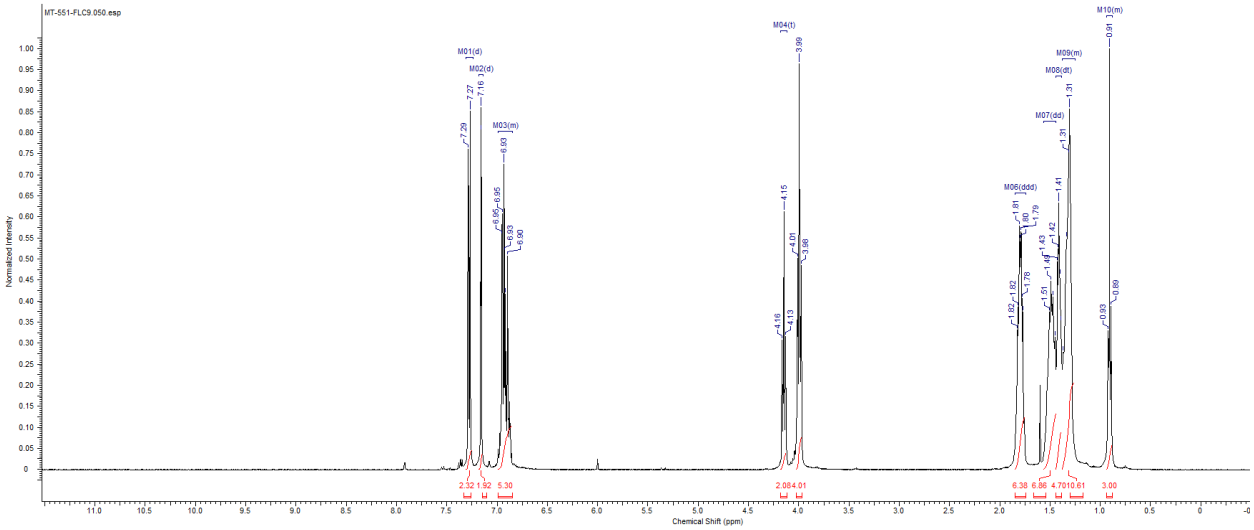

Figure A3-39: 400 MHz ^{1}H NMR spectrum of **QL29-9/8-2,6F$_2$**

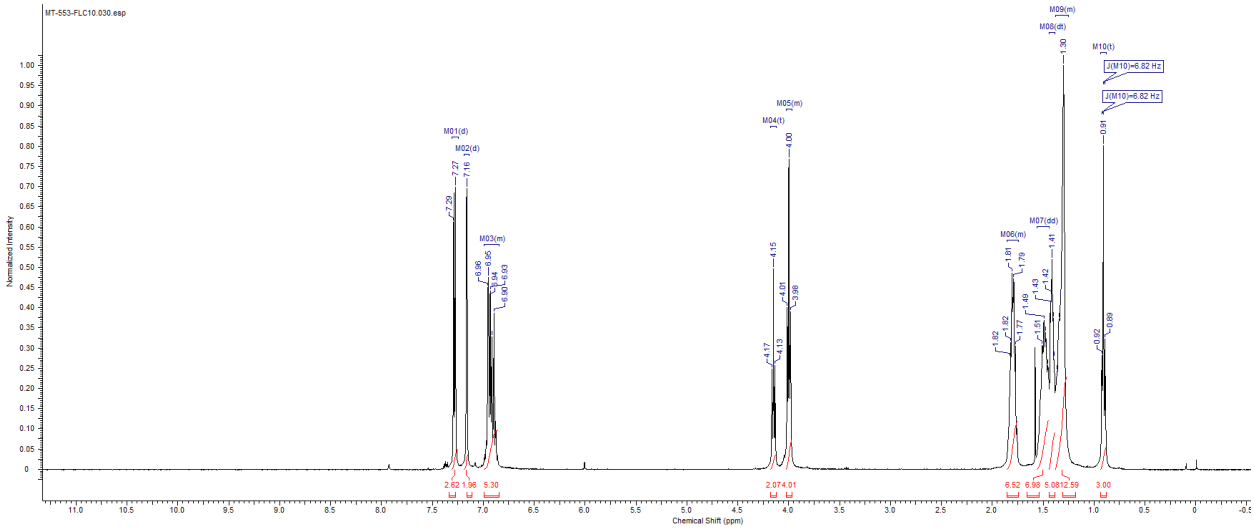

Figure A3-40: 400 MHz ^{1}H NMR spectrum of **QL29-10/8-2,6F$_2$**

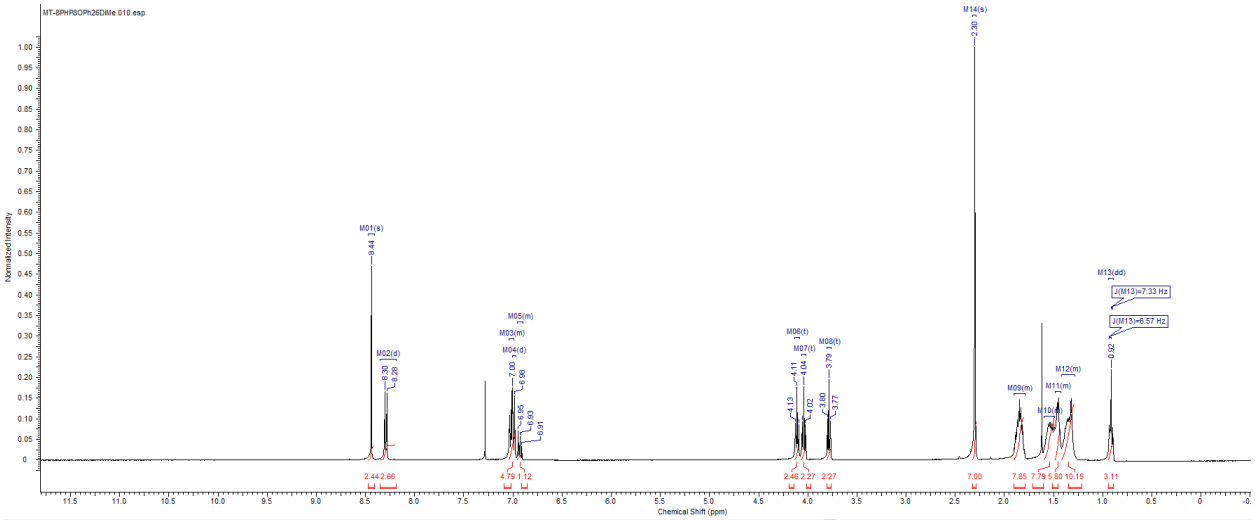

Figure A3-41: 400 MHz ^{1}H NMR spectrum of **QL30-8/8-2,6Me$_2$**

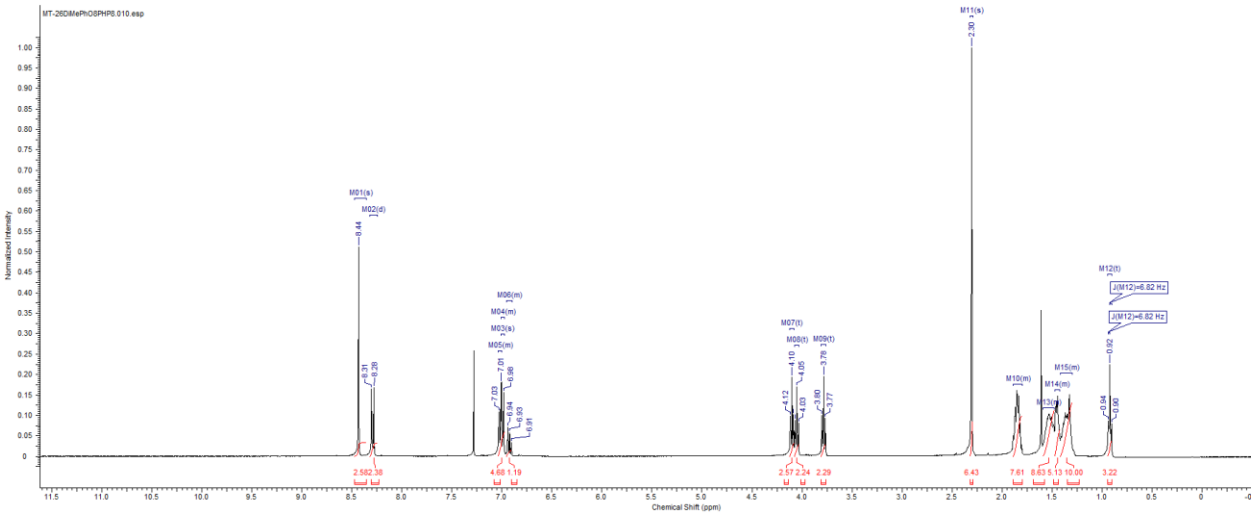

Figure A3-42: 400 MHz ^{1}H NMR spectrum of **QL31-8/8-2,6Me$_2$**

Appendix 4: Michel-Levy Chart

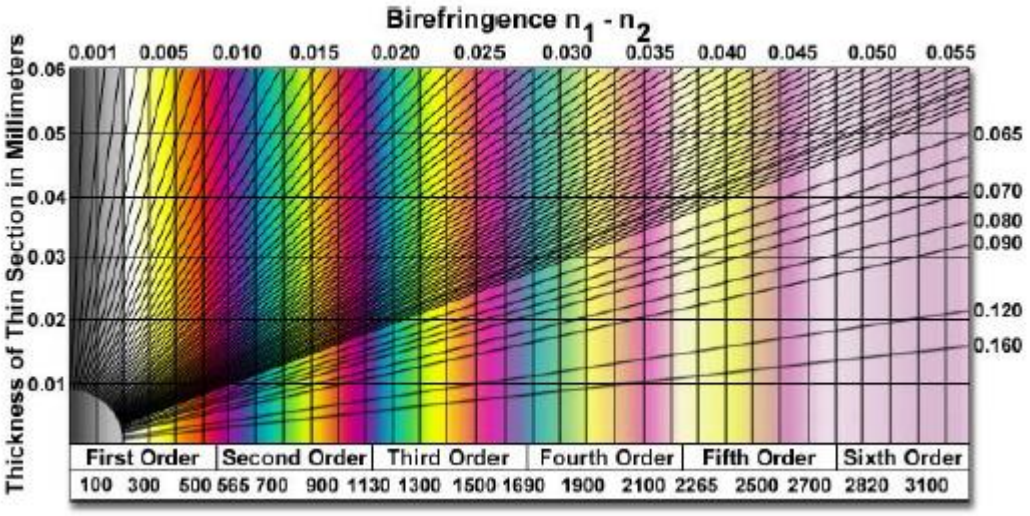

Figure 4A-1: Michel Levy Chart